Structural studies of trans-synaptic complexes

Anna Christina Heroven

St. Hilda's College
University of Oxford

Thesis submitted for the Degree of
Doctor of Philosophy

Trinity 2019



Declaration of authorship

I, Anna Christina Heroven, confirm that the work presented in this thesis is my own. Where information has been derived from other sources, I can confirm that this has been indicated in the thesis.

Date:

Signed:

ABSTRACT

'Structural studies of trans-synaptic complexes'
Anna Christina Heroven, St. Hilda's College
Thesis submitted for the Degree of *Doctor of Philosophy*
Trinity 2019

Neuronal synapses are the functional units of the nervous system, allowing the fast transmission of information between neurons. A plethora of proteins populate the cleft between connecting neurons, and many contribute to the formation of protein complexes than span the synaptic cleft. Such trans-synaptic complexes are of tremendous importance for synaptic function, affecting the neuronal wiring specificity, synaptic plasticity or the differentiation of the pre-and post-synaptic compartments. Two important protein families that form trans-synaptic complexes are ionotropic glutamate receptors (iGluRs) and receptor protein tyrosine phosphatases (RPTPs). In this thesis, I present work conducted on two prototypical protein complexes: the Glutamate Delta 2 (GluD2) receptor, in complex with Cerebellin 1 and β Neurexin 1; and the receptor protein tyrosine phosphatase μ (RPTPμ), which forms a homophilic dimer across cell contacts. Despite previous efforts, it is not well understood how these protein complexes are able to integrate their cell-adhesive properties with their downstream signalling functions. The aim of this thesis is to pave the way towards a mechanistic understanding of the function of these complexes. Using X-ray crystallography and biophysical assays, GluD2-specific nanobodies were identified, leading to the discovery of molecular tools that can stabilize distinct GluD2 conformations. Of particular interest, a nanobody capable of activating the receptor and preventing desensitization was identified, which will be instrumental for unveiling the GluD2 metabotropic signalling mechanism. Single-particle cryo-EM was applied to study the full-length GluD2 receptor, providing the first insights into the general architecture of Delta subtype iGluRs and laying the grounds to obtain a high-resolution structure. RPTPμ-mediated cell-cell contacts were analysed by cryo electron tomography, obtaining data from cells thinned by focused ion beam (FIB) milling. The FIB milled sections revealed unprecedented detail of the architecture of insect cells and allowed the analysis of RPTPμ in a native environment. Subtomogram averaging shed light on a potential higher-order organization of RPTPμ at cell-cell contacts. Finally, a protocol for the purification and crystallization of the complete cytoplasmic region of RPTPμ was developed. This data paves the way towards unravelling the structure of the juxtamembrane domain, an essential part for understanding how type IIb RPTPs are regulated.

ACKNOWLEDGEMENTS

Firstly, I would like to thank Prof Radu Aricescu for the invitation to meet for a quick chat 5 years ago, which led to a 3-hour meeting, many doodles and plans to obtain the atomic structure of a synapse within 4 years. I am thankful for Radu's encouragement to dive into cellular tomography and for the opportunity to learn many new and exciting techniques during this DPhil. His relentless enthusiasm, support and daily *genius*© ideas made all the difference. I also thank Radu for the chance to work at both STRUBI and the MRC-LMB. I have learned so much and met so many talented colleagues at both places. I am thankful to Prof Kay Grünewald, my collaborator and co-supervisor, for providing access to microscopes and for his advice. I thank Prof Peijun Zhang and Prof Christian Siebold for also joining my supervision. I am very grateful to Prof Yvonne Jones and Dr Giulia Zanetti for agreeing to examine this DPhil thesis.

The first year of my DPhil would not have been the same without the mentorship of Dr Jonathan Elegheert and Dr Ester Behiels. I have enjoyed working with our collaborators during my DPhil. I thank Prof Michisuke Yuzaki and his colleagues for outstanding contributions on both the GluD2 and RPTPμ projects. I thank Prof Jan Steyaert's team at VUB for providing us with nanobodies. I am also thankful to the Grünewald laboratory, particularly Dr Michael Grange and Dr Christoph Hagen, who introduced me to electron microscopy, taught me FIB-milling, data collection and data processing.

I thank Dr Patricia Brown, Dr Lina Malinauskaite, Dr Sebastian Bonilla and Prof Radu Aricescu for help with proofreading this thesis. I am also grateful to Dr Suzanne Scott and Dr Sebastian Bonilla for help with analysing BLI data and fixing MATLAB scripts. Life in the lab would be miserable if it weren't for the colleagues, true friends and partners in crime. Both in Oxford and Cambridge, I thank Paul, Suzanne, Holly, Veronica, Duncan, Lina, Patricia, Bianka, Simonas, Kuni, Vikram and of course the 'Young Boys', Jonas and Andrija. Thank you for so many shared meals, occasional consumption of "important experiments cooled at 4°C" and cooperative Krios sessions trying to find elusive blow-up points. Thank you for all the advice and support.

At the MRC-LMB, I thank the EM facility, particularly Giuseppe Cannone, Shaoxia Chen, Christos Savva, Joanna Brown, Anna Yeates and Grigory Sharov. I also thank the X-ray crystallography facility, Minmin Yu, Fabrice Gorrec and Dom Bellini. I would like to thank Dustin Morado for advice on tomography data collection and data processing. I am happy to have met the tomo and FIB milling community, and I thank Wanda, Helen, Vicky, Shirley, Patrick, Michael, Iva, Alicia, and Yangci. It has been a pleasure working with you. I would specially like to thank Dr Nick Ader, who taught me how to do CLEM experiments on plastic sections.

This DPhil would not have been possible without the generous support from the Nuffield Department of Medicine and the EPSRC. The NDM Studentship has been an outstanding opportunity to entirely dedicate 4 years of research to this project.

I would also like to thank Ele, Domi, Fiona, Dan, Nutri, Tata and Cami for the comic relief outside the lab. I thank my parents, Bettina, Cata and Blanca for their relentless support and encouragement. And finally, I would like to thank Sebas. From debugging MATLAB scripts and proofreading, to his unwavering writing discipline, contagious passion for science and loving support, he's been a fantastic partner, in every sense of the word.

Table of Contents

Declaration of authorship 2
ABSTRACT 3
ACKNOWLEDGEMENTS 4
Table of Contents 5
List of Abbreviations 9

1. Introduction 12

1.1 The Neuronal Synapse is the functional unit of the central nervous system 12
1.2 Protein complexes form synaptic nanocolumns that span the synaptic cleft 13
1.3 Ionotropic Glutamate Receptors mediate excitatory synaptic transmission throughout the central nervous system 16
1.4 Glutamate Receptor Delta 2 mediates synaptogenesis and synaptic plasticity through metabotropic mechanisms 19
1.5 Cerebellins populate the synaptic cleft and act as soluble synaptic organizers 20
1.6 Neurexins are synaptic cell-adhesion molecules that control synapse properties 21
1.7 Signalling *via* the trans-synaptic GluD2-Cbln1-βNrx1 complex 23
1.8 Receptor Protein Tyrosine Phosphatases integrate adhesive and signalling functions at cell contact sites 25
1.9 Regulation of RPTP intracellular domains 26
1.10 RPTPμ is a prototypical homophilic adhesion molecule 28
1.11 Aims of this thesis 33

2. Materials and Methods 34

2.1 Mammalian expression and purification of soluble RPTPμ, GluD2, Cbln1 and βNrx1 constructs 34
2.2 Bacterial periplasmic expression and purification of nanobodies 36
2.3 Biolayer Interferometry 38
2.4 Purification and crystallization of GluD2-nanobody complexes 40
2.5 X-ray crystallography data collection, data processing and model building 41
2.6 Expression and purification of membrane scaffold proteins 42
2.7 Coupling of Rho-1D4 antibody onto activated CNBr-sepharose 44
2.8 Preparation of lipid stocks for reconstitution of membrane proteins into nanodiscs 45

2.9 Expression, solubilisation and purification of full-length GluD2 45
2.10 Preparation of GluD2 single particle cryo EM grids 47
2.11 Single particle cryo EM data collection 48
2.12 Single particle cryo EM data processing 48
2.13 Sf9 cell clutstering assay 49
2.14 Resin embedding, sectioning and CLEM imaging of Sf9 cells 49
2.15 Plunge freezing of RPTPμ-induced cell aggregates 50
2.16 Focused Ion Beam Milling 51
2.17 Rebuffering and BSA-coating of gold nanoparticles 51
2.18 Preparation of unilamellar liposomes 52
2.19 EM sample preparation of RPTPμ-decorated liposomes 53
2.20 Cryo-EM Tomography data acquisition 53
2.21 Image processing and tomogram reconstruction 54
2.22 Subtomogram Averaging 55
2.23 Expression and purification of RPTPμ D1-D2 tandem constructs and RACK1 56
2.24 Purification and crystallization of RPTPμ D1D2 constructs 58

3. Generation and characterization of nanobodies against GluD2, Cbln1 and β-Nrx1 59

3.1 Aims of this chapter 59
3.2 Generation of nanobodies against GluD2, Cbln1 and β-Nrx1 60
3.3 Biolayer interferometry reveals high-affinity GluD2 binders 61
3.4 Nanobodies stabilize dimers and bind to domain interfaces 65
3.5 Nanobodies act as crystallization chaperones 66
3.6 GluD2 is locked in an active conformation by Nb399 68
3.7 Nb399 activates GluD2 in mouse brain slices 72
3.8 Nb390 and Nb392 share the same binding mode as Nb399 74
3.9 Nb381 and Nb389 bind to unique binding sites on GluD2^{ATD} 75
3.10 Only Nb389 can access all four binding sites on GluD2 77
3.11 Summary and conclusions drawn from chapter 3 78

4. Single particle cryo-EM studies of GluD2-nanobody complexes 80

4.1 Aims of this chapter 80

4.2 Nanodiscs allow the study of trans-membrane receptors in a lipidic environment .. 80
4.3 Expression and purification optimization leads to a stable and monodisperse GluD2 sample 81
4.4 Nanobody 399 disrupts the tetrameric conformation of GluD2 84
4.5 GluD2 is affected by the air-water interface during cryo-EM grid preparation 88
4.6 Interaction of proteins with the air-water interface leads to preferential orientation and denaturation..... 90
4.7 Immobilization of GluD2 on continuous carbon results in a high-percentage of non-denatured particles 91
4.8 Nanobody 381 stabilizes the GluD2 extracellular region 92
4.9 Summary and conclusions drawn from chapter 4..... 94

5. Analysis of RPTPμ-mediated cell contacts by cryo electron tomography 97

5.1 Aims of this chapter 97
5.2 Establishing a workflow for *in-situ* studies of RPTPμ..... 97
5.3 Overexpression of RPTPμ causes cell clusters that can be targeted by FIB milling 99
5.4 Cell-cell contacts can be observed by TEM 102
5.5 Overexpression of RPTPμ leads to the formation of cytoplasmic membrane stacks 103
5.6 Correlative light and electron microscopy experiments reveal that membrane stacks contain RPTPμ..... 105
5.7 Subtomogram averaging of RPTPμ-mediated membrane stacks 107
5.8 Expression and purification of RPTPμ extracellular region leads to high protein yields 112
5.9 Liposomes decorated with the RPTPμ extracellular region form low-order zippers 113
5.10 Summary and conclusion drawn from chapter 5 115

6. Purification and crystallization of RPTPμ cytoplasmic region and RACK1 119

6.1 Aims of this chapter 119
6.2 Construct design of D1-D2 and RACK1 constructs 120

6.3 Expression and purification of D1-D2 and RACK1 constructs leads to high yields of recombinant protein 121
6.4 RACK1 does not co-elute with RPTPμ$^{777-1452}$ in size-exclusion chromatography experiments..... 124
6.5 RPTPμ D1-D2 forms diffracting crystals..... 125
6.6 Summary and conclusions drawn from chapter 6..... 126
7. Discussion and Outlook 129
8. Appendix 140
References..... 155

List of Abbreviations

Abbreviation	Meaning
2D	2-dimensional
3D	3-dimensional
A, Ala	Alanine
A280	Absorbance measured at a wavelength of 280 nm
AMPA	α-amino-3-hydroxy-5-methyl-4-isoxazolepropionic acid
ATD	Amino-terminal domain
AUC	Analytical Ultracentrifugation
BBE	Bovine Brain Extract
BLI	Biolayer Interferometry
β-Nrx1^{+SS4}	β-Neurexin 1, including splice product from splice site 4
C, Cys	Cysteine
CAM	Cell adhesion molecules
Cbln1	Cerebellin 1
CDR	Complementarity-determining region
CHS	Cholesterol hemisuccinate
CLEM	Correlative light and electron microscopy
CNS	Central nervous system
Cryo-EM	Cryo electron microscopy
Cryo-ET	Cryo electron tomography
CTD	Carboxy-terminal domain
CTF	Contrast transfer function
D-Ser	D-Serine
D, Asp	Aspartate
DDM	n-Dodecyl-beta-D-Maltopyranoside
DLS	Diamond Light Source
DMEM	Dulbecco's Modified Eagle's Medium
DMNG	Decyl maltose neopentyl glycol
E. coli	*Escherichia coli*
E, Glu	Glutamate
ECTO	Extracellular region
EDTA	Ethylenediaminetetraacetic acid
EGFP	Enhanced green fluorescent protein
EndoF1	Endoglycosidase F1
EPSC	Excitatory post-synaptic current
ER	Endoplasmic reticulum
F, Phe	Phenylalanine
FCS	Fetal Calf Serum
FIB-SEM	Focused ion beam-scanning electron microscopy

FN	Fibronectin-like domain
G, Gly	Glycine
GABA	Gamma-Aminobutyric acid
GBM	Glioblastoma multiforme
GluA2	Glutamate Receptor AMPA 2
GluD1	Glutamate Receptor Delta 1
GluD2	Glutamate Receptor Delta 2
GluD2^{Lc}	GluD2 A654T mutation, present in lurcher mice
GluK2	Glutamate Receptor Kainate 2
GluK4	Glutamate Receptor Kainate 4
H, His	Histidine
HEK293	Human embryonic kidney 293 cells
HEPES	4-(2-hydroxyethyl)-1-piperazineethanesulfonic acid
H. sapiens	*Homo sapiens*
HUVEC	Human umbilical vein endothelial cells
I, Ile	Isoleucine
Ig	Immunoglobulin-like domain
iGluR	Ionotropic Glutamate Receptor
IPTG	Isopropyl-β-D-thiogalactoside
ITC	Isothermal Titration Calorimetry
JM	Juxtamembrane domain
K, Lys	Lysine
K_D	Dissociation constant
KO	Knock-out
L, Leu	Leucine
LB	Luria Broth
LBD	Ligand binding domain
LNS	Laminin/neurexin/sex-hormone-binding globulin domain
LRP4	Lipoprotein receptor-related protein 4
LRRTM	Leucine-rich repeat transmembrane protein
LTD	Long-term depression
M, Met	Methionine
MAM	Meprin/A5/μ domain
MSP	Membrane scaffold protein
MWCO	Molecular weight cut-off
N, Asn	Asparagine
NAG	N-acetyl glucosamine
Nb	Nanobody
Nb380	Nanobody CA11380
Nb381	Nanobody CA11381
Nb389	Nanobody CA11389
Nb390	Nanobody CA11390
Nb392	Nanobody CA11392

Nb399	Nanobody CA11399
Nb663	Nanobody CA11663
NDMA	N-methyl-D-aspartate
NEAA	Non-essential amino acids
NTA	Nitrilotriacetic acid
OSER	Organized smooth endoplasmic reticulum
P, Pro	Proline
PBS	Phosphate-buffered saline
PC	Purkinje Cell
PDB	Protein Data Bank
pDNA	Plasmid deoxyribonucleic acid
PEI	Polyethylenimine
PF	Parallel Fiber
PKC-δ	Protein kinase C δ
POPC	2-Oleoyl-1-palmitoyl-*sn*-glycero-3-phosphocholine
PTM	Post-translational modifications
Q, Gln	Glutamine
R, Arg	Arginine
r.m.s.d.	Root-mean-square deviations
RACK1	Receptor for activated protein c kinase
RPM	Revolutions per minute
RPTPμ	Receptor protein tyrosine phosphatase μ
RPTPs	Receptor protein tyrosine phosphatases
RU	Response Units
S, Ser	Serine
SDS-PAGE	Sodium dodecyl sulphate - polyacrylamide gel electrophoresis
SEC	Size-exclusion chromatography
SEM	Scanning electron microscopy
SOC	Super Optimal broth with Catabolite repression
SPR	Surface Plasmon Resonance
STA	Subtomogram averaging
STEM	Scanning transmission electron microscopy
T, Thr	Threonine
TB	Terrific Broth
TCEP	Tris(2-carboxyethyl)phosphine
TEV	Tobacco Etch Virus
TLS	Translation/Libration/Screw
TMD	Transmembrane domain
TNF	Tumor necrosis factor
V, Val	Valine
VGCC	Voltage gated calcium channels
W, Trp	Tryptophan
Y, Tyr	Tyrosine

1. Introduction

1.1 The neuronal synapse is the functional unit of the central nervous system

The mammalian brain and nervous system are composed of billions of neurons (~86 x 10^9 estimated for *H. sapiens* (1)) that form a sophisticated and interconnected network. The connections between neurons, termed neuronal synapses, constitute the fundamental functional units of virtually all cognitive processes. Rapid signal transmission between neurons is passed through electrical and chemical synapses. At electrical synapses, ions fluctuate directly between connected neurons. Chemical synapses, however, rely on neurotransmitters that are released by the pre-synaptic neuron into the synaptic cleft. Receptors localized on the post-synaptic neuron interact with these neurotransmitters to either trigger the influx of ions, depolarizing the membrane (ionotropic signalling), or activate other downstream signalling events (metabotropic signalling) (5). The ability of synapses to strengthen or weaken over time in relation to their activity is termed synaptic

plasticity (6) and is greatly dependent on the molecular composition of the synaptic cleft. Initial electron microscopy (EM) studies of the synaptic cleft identified a dense molecular layer between the apposing membranes of pre- and post-synaptic neurons (7-9). This observation was confirmed by later investigations (10-12) and it has since become apparent that the synaptic cleft is populated with trans-cleft spanning structures (13-15). Lučić *et al.* further reported that the trans-synaptic structures had a non-trivial topology and were highly connected laterally (10), suggesting the presence of a higher-order architecture in the synaptic cleft. The formation of sub-synaptic nanodomains has been observed for glutamate receptors (16, 17) and there is mounting evidence that changes in such supra-molecular arrangements play a significant role in synaptic plasticity and can lead to pathological disorders (18, 19). Moreover, it has been suggested that protein structures spanning the synaptic cleft drive synaptogenesis, lead to the differentiation of pre- and post-synaptic compartments and help to coordinate the alignment of neurotransmitter release sites and post-synaptic receptors (reviewed in (20)).

1.2 Protein complexes form synaptic nanocolumns that span the synaptic cleft

Recently, Tang *et al.* provided evidence for the spatial correlation between synaptic-vesicle docking sites and clusters of post-synaptic PSD-95 scaffold protein (21). The authors suggested the presence of so-called ‘nanocolumns’ that span the synaptic cleft and showed that these structures are involved in regulatory changes in synaptic strength. These findings raised the questions of what proteins are involved in the formation of synaptic nanocolumns and how their assembly is regulated. It also remains unclear whether synaptic nanocolumns fulfil solely an alignment function, maintaining post-synaptic receptors in areas of high

neurotransmitter concentrations, or whether they could also be involved in downstream or retrograde signalling.

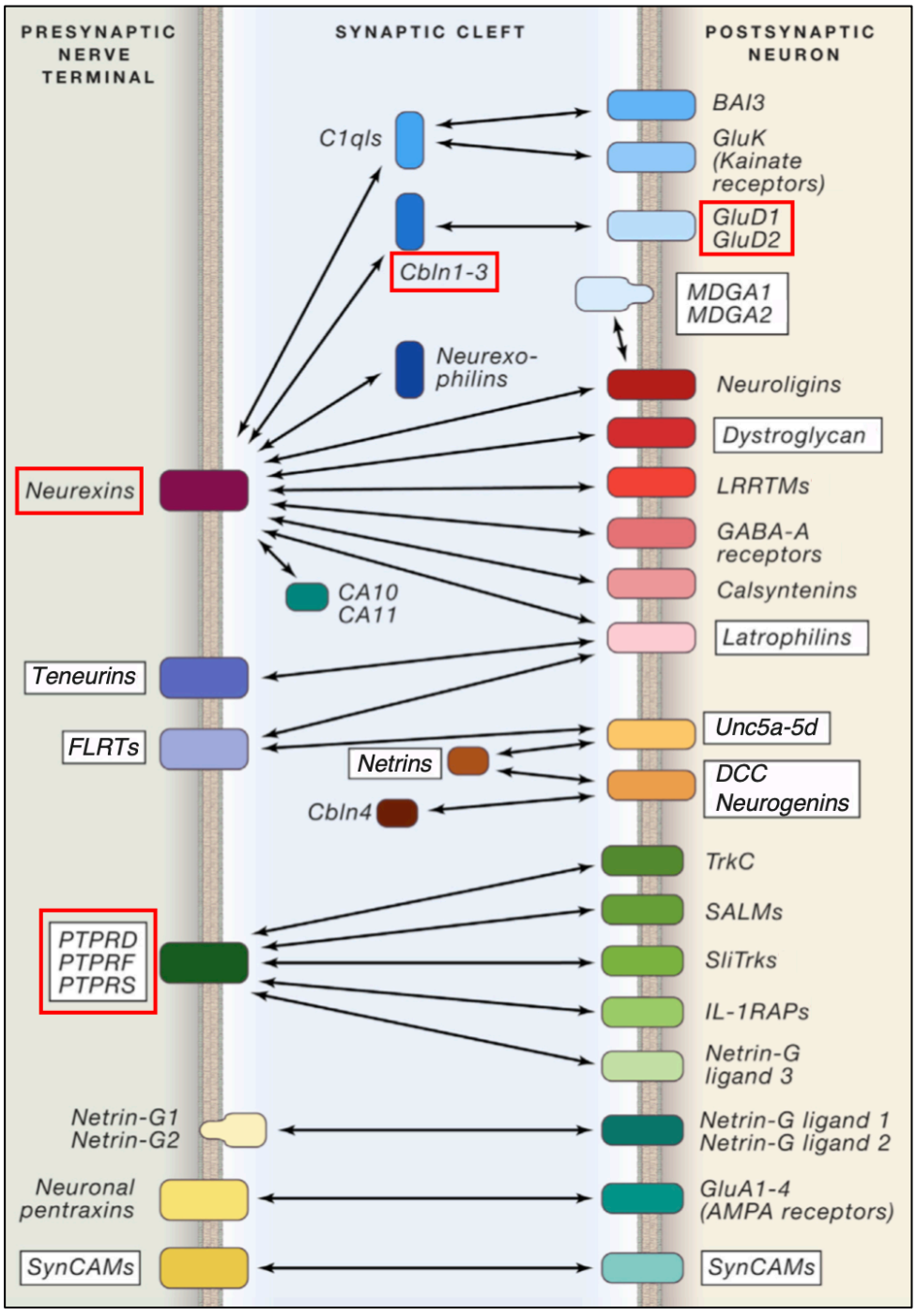

***Figure 1-1* Schematic overview of some trans-synaptic protein complexes.** Modified with permission from Südhof *et al.* (3). A plethora of trans-synaptic complexes have been reported in the last decades, some of which are relevant in neuropsychiatric disorders. Most of these proteins are specifically localized to either the pre- or postsynaptic membrane. For this DPhil thesis, members of the protein families marked in red boxes were studied. RPTPμ (also known as PTPRM) is a member of the PTPR family and is not shown here as its localization within neurons has not yet been established.

A plethora of protein complexes that span the synaptic cleft and could perform such functions have been characterized in the last decades (**Figure 1-1**). These complexes are highly diverse and carry out different functions. The trans-synaptic neurexin-neuroligin complex leads to the differentiation of the pre- and post-synaptic compartments (22-24). Complexes between neuroligin and N-cadherin have been shown to trigger retrograde signalling (25, 26). Neurexin was also found to interact with a leucine-rich repeat transmembrane protein (LRRTM2), acting as a synaptic organizer at excitatory synapses (27). Neurexin complexes with either LRRTM or neuroligin stabilize excitatory synapses (28, 29). Synaptic differentiation is also supported by members of the receptor tyrosine phosphatase LAR family, which interact with post-synaptic Netrin-G ligand 3 (30, 31). RPTPδ is involved in inhibitory synapse development by forming a trans-synaptic complex with Slitrk3 (32). Another high-affinity trans-synaptic receptor pair involved in synaptogenesis is latrophilin 1 and Lasso/teneurin 2 (33). Interestingly, Lasso is proteolytically cleaved and can also activate latrophilin 1 on axonal growth cones, leading to axonal attraction (34).

Apart from the membrane-bound adhesive proteins named before, the synaptic cleft is also populated by soluble secreted proteins that act as synaptic organizers. For instance, the glia-derived neurotrophic factor (GDNF) is a secreted protein that triggers presynaptic differentiation by inducing the *trans*-homophilic binding of its receptor GFRα1 (35), present at both pre- and postsynaptic hippocampal neurons. Another family of synaptic organizers are cerebellins (Cbln1-4), which are expressed in overlapping spatio-temporal patterns across various brain regions (36). Cbln1 forms a trans-synaptic triad by binding pre-synaptic β-Neurexin 1 (Nrx1) (37) and post-synaptic glutamate receptor Delta 2 (GluD2) (38). This complex is involved in synaptogenesis and also regulates synaptic plasticity, since ablation

of individual components lead to impaired long-term depression in the cerebellum (39, 40). Other members of the Cbln family have been found to bind GluD1 (41) and the netrin receptor DCC (42), suggesting that the synaptogenic roles of Cblns could be widespread to other regions of the brain. Moreover, the Nrx-Cbln-GluD2 triad could be representative for complexes formed by other ionotropic glutamate receptors (iGluRs). Indeed, neuronal C1q-like proteins -structurally very similar to Cblns- are able to bind to presynaptic neurexin-3 and the postsynaptic kainate receptors GluK2 and GluK4 and GluA1 containing AMPA receptors (43). The amino terminal domains of GluA receptors (AMPARs) have been found to affect synaptic transmission and plasticity by receptor anchoring (44), suggesting the involvement in a trans-synaptic adhesive complex.

For this DPhil thesis, I set out to study two cell-adhesion complexes that combine both adhesive and downstream signalling functions: the homophilic complex of a receptor protein tyrosine phosphatase, RPTPμ, and the above mentioned trans-synaptic Nrx-Cbln-GluD2 triad.

1.3 Ionotropic Glutamate Receptors mediate excitatory synaptic transmission throughout the central nervous system

L-glutamate is the main neurotransmitter of excitatory signalling in the central nervous system (CNS) (45). Ionotropic glutamate receptors (iGluRs) are activated by pre-synaptically released L-glutamate, triggering the opening of their ion channel, causing the fast depolarization of the post-synaptic membrane and initiating signalling events that control synaptic plasticity. iGluRs are classified into 4 sub-families based on their sequence identity and pharmacological properties: AMPA (GluA1-4), kainate (GluK1-5), NDMA (GluN1, GluN2A-D, GluN3A-B) and Delta (GluD1-2) receptors. All sub-families form tetrameric receptors with the same modular architecture, comprising an amino-terminal

domain (ATD) that reaches into the synaptic cleft; a ligand-binding domain (LBD) which triggers the activation of the receptor; a transmembrane domain (TMD) that forms the central ion channel pore and a carboxy-terminal domain (CTD).

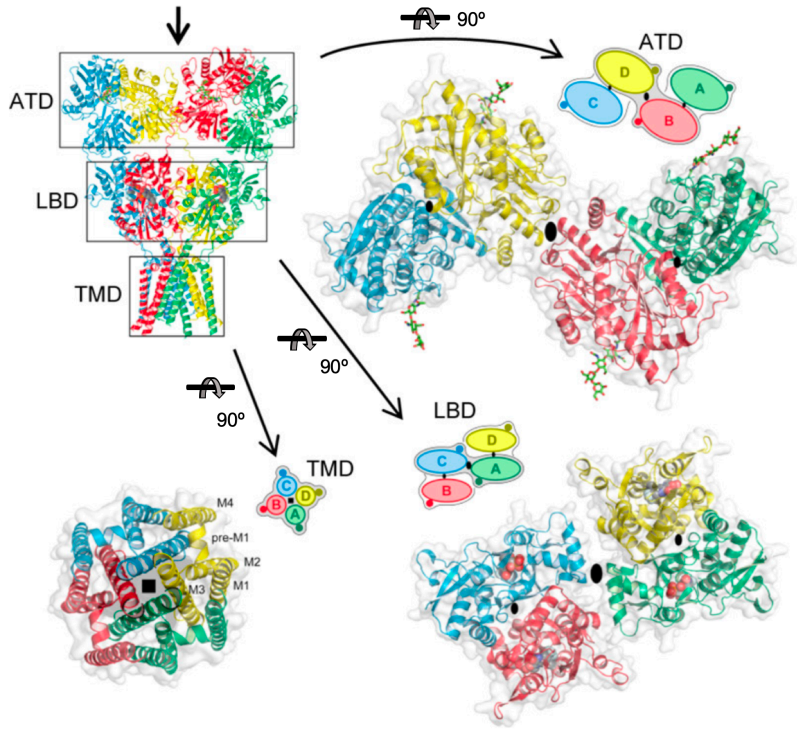

***Figure 1-2* Overall architecture and subunit arrangement of iGluRs.** Modified from Traynelis *et al* (4) and reproduced with permission. iGluRs are tetrameric receptors that are composed of four layers: the amino-terminal domain (ATD), the ligand-binding domain (LBD), the transmembrane domain (TMD) and the carboxy-terminal domain (CTD, not shown here). The TMD has a fourfold-symmetry, while the LBD and ATD layers arrange into dimers of dimers. Domain swapping occurs from the LBD to the ATD layer, where A/D and B/C dimers are rearranged into A/B and C/D dimers.

The four subunits that assemble into one receptor are commonly labelled A, B, C and D, and they form a fourfold-symmetric arrangement in the transmembrane domain. At the LBD layer, the four subunits assemble into a dimer of dimers conformation where the A/D and B/C dimers form contacts between the A and C subunits. At the ATD layer, however, a subunit crossover results in a dimer of dimer conformation where the A/B and C/D subunits form dimers, and contacts between the B and D subunits stabilize the tetrameric conformation (**Figure 1-2**). This symmetry mismatch has important implications for signal transduction and the function of the ion channel (4).

Since the first crystal structure of a full-length iGluR was reported (46), further X-ray crystallography and cryo-EM structures of NMDA, kainate and AMPA receptors have been determined (reviewed in (47)), revealing the general gating mechanism that supports ionotropic signalling. Upon binding of an agonist, the two clamshell lobes (D1 and D2) of the LBDs close, producing a conformational change that is transduced into the opening of the pore. This motion is translated by three short, flexible linkers that connect the LBD to the TMD. Depending on the strength of the agonist, the LBDs will reach a different degree of closure, resulting in a stronger or weaker activation and desensitization (48). If the agonist binding persists, the receptor will enter a desensitized conformation, in which the dimerization interface between the upper (D1) lobes of the LBDs is disrupted, leading to a reorientation of the whole LBD and the relaxation of the strain on the TMD (**Figure 1-3**). This results in the closure of the channel, while the agonist remains bound. Once the agonist is released, the receptor returns to its closed conformation.

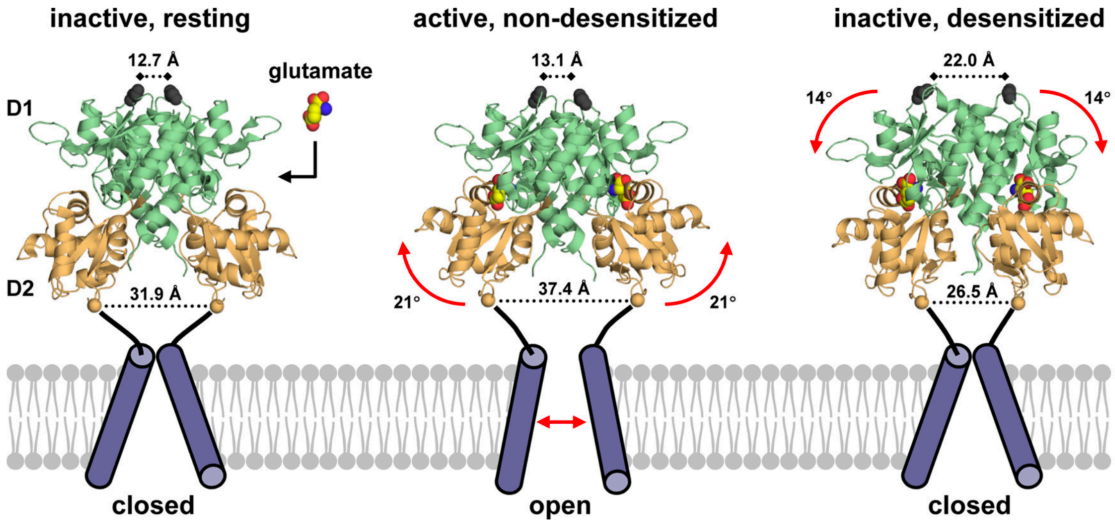

***Figure 1-3* Gating cycle of iGluRs.** As seen in Traynelis *et al*. (4), reproduced with permission. iGluRs cycle through a resting, open and desensitized state, in which conformational changes of the LBD trigger the opening of the ion channel (ATD and CTD are not shown). Upon binding of the agonist, the D2 lobe of the LBD rotates upward by 21°, closing the LBD clamshell. This pulls the ion channel open. If ligand binding persists, the D1 dimerization interface is disturbed, and the closed LBD clamshell rotates 14° downwards, releasing the strain on the TMD and closing the channel. This results in a desensitized receptor.

While iGluRs are mostly studied for their ionotropic function, it appears that many of its family members contribute to synaptogenesis by interacting with other proteins that populate the synaptic cleft (37, 43, 49, 50) and are also involved in metabotropic mechanisms that trigger post-synaptic signalling (51-55). These functions are best understood for the iGluR Delta sub-family.

1.4 Glutamate Receptor Delta 2 mediates synaptogenesis and synaptic plasticity through metabotropic mechanisms

Glutamate Receptor Delta 2 (GluD2) is highly expressed in distal dendrites of Purkinje cells (PC) of the cerebellar cortex (56), where synaptic connections are formed with the parallel fibers (PF) of granule cells. In mice lacking GluD2, the number of PC-PF synapses are greatly reduced and motor coordination and cerebellar long-term depression (LTD) are impaired (40). This finding suggests that GluD2 is involved in synaptic plasticity in the cerebellum. Indeed, GluD2 plays an important role in human disease, with reports linking its malfunction to cerebellar ataxia and atrophy (57-59).

Despite being classified as glutamate receptors due to their sequence similarities to other iGluRs, GluD receptors have not been found to bind or be activated by L-Glutamate (56, 60). However, a study by Kakegawa *et al.* discovered that D-serine (D-Ser) triggers cerebellar LTD and controls motor coordination through GluD2 (61). Structural evidence confirmed that D-Ser binds to the GluD2 LBD and triggers a conformational change (62). D-Ser does not, however, trigger the opening of the GluD2 ion channel and to date no excitatory post-synaptic currents (EPSCs) have been measured from GluD2-transfected cells. Furthermore, mice carrying GluD2 mutations that abolish ion permeation in the putative ion channel show intact cerebellar LTD (63). This raises the question of whether GluD2 is able to form a functional ion channel. Experiments where the GluD2 LBD was

swapped with those LBDs of kainate or AMPA receptors resulted in glutamate-induced channel activities, suggesting that the GluD2 TMD forms a potentially functional ion channel (64, 65). In fact, a single point mutation in GluD2 in *lurcher* mice ($GluD2^{Lc}$), A654T, results in a constitutively open channel in the absence of ligand binding (66). Currents measured from $GluD2^{Lc}$ are reduced upon addition of D-Ser, probably due to desensitization of the ion pore upon closure of the LBD (67). Although D-Ser does not trigger channel opening in GluD2, this finding shows that ligand binding and closure of the LMB clamshell can induce a conformational change in the TMD, potentially transducing a signal. Various groups have reported that both the N- and C-termini of GluD2 are essential for cerebellar LTD (68-71), pointing towards a metabotropic signalling mechanism in which conformational changes in the extracellular regions of GluD2 get transferred to the C-terminus, possibly affecting the interactions to scaffold and signalling proteins.

Further to D-serine, cerebellin-1 (Cbln1), a synaptic organizer molecule secreted by granule cells, was also found to bind to the ATD of GluD2 (38). Cbln1 simultaneously binds presynaptic β-Neurexin 1 (βNrx1), forming a bridge that spans the trans-synaptic cleft (37).

1.5 Cerebellins populate the synaptic cleft and act as soluble synaptic organizers

Cerebellins are soluble, secreted proteins that belong to the C1q/tumor necrosis factor (TNF) superfamily. Vertebrates express four sub-types of cerebellins (Cbln1-4) in characteristic patterns across the brain (36). Cerebellins are composed of a C-terminal C1q-domain, that assembles into trimers, and a N-terminal cysteine-rich sequence that dimerizes two C1q trimers, producing a hexameric cerebellin molecule (72). All cerebellins assemble into homohexamers, with the exception of Cbln3 that requires Cbln1 for secretion, suggesting the formation of heterohexamers (73). Cbln1 knock-out (KO) mice exhibit an identical

phenotype to mice lacking GluD2 (39), which suggests that both proteins are part of the same signalling pathway. In fact, Cbln1 and Cbln2 were found to bind directly to the N-terminal domain of GluD1 and GluD2 (38, 41, 74) and to all neurexins containing the SS4 insert (2, 37, 75). Biophysical measurements indicate that Cbln1 binds to βNrx1 with high affinity ($K_D \sim 40$ nM) in a 1:1 ratio (2), while the affinity of one Cbln1 hexamer to tetrameric GluD2 is about 125 nM. However, the measured affinity between GluD2-Cbln1 is likely the result of an avidity effect resulting from the oligomeric conformation of the proteins. The affinity between the minimal interaction units, monomeric $GluD2^{ATD}$ and trimeric $Cbln1^{C1q}$, was determined to be in the high μM range (2).

1.6 Neurexins are synaptic cell-adhesion molecules that control synapse properties

Neurexins are a family of single-pass transmembrane proteins that are expressed from three genes (NRXN1-3). Neurexin genes contain internal promoters that give raise to different protein variants, labelled α-, β, and γ-neurexins (76-78). The longest subtype, α-neurexins, are composed of 6 laminin/neurexin/sex-hormone-binding globulin (LNS) domains, interspersed by three EGF-like repeats, a juxta-membrane domain containing an O-linked sugar modification sequence and a short cysteine-loop domain, followed by the transmembrane region and a cytoplasmic C-terminal domain with a PDZ-binding motif. β-neurexins, by contrast, are transcribed from an internal promoter in the NRXN1-3 genes, resulting in a truncated form of α-neurexins that contain only the most membrane-proximal LNS domain, with a short N-terminal β-neurexin-specific motif. γ-neurexin is only transcribed from the NRXN1 gene and is the shortest variant, containing only the juxta-membrane domain, transmembrane domain and cytoplasmic C-terminus. This great variety of neurexin proteins is further enhanced by six sites of alternative splicing (labelled SS1 to

SS6) that result in thousands of neurexin isoforms that are widely expressed in different areas of the brain (79, 80). The regulatory mechanisms that drive alternative splicing of neurexins are not well understood, however, Ding *et al*. recently showed that splicing on SS4 is regulated by neuronal activity as a consequence of fear learning in mice (81).

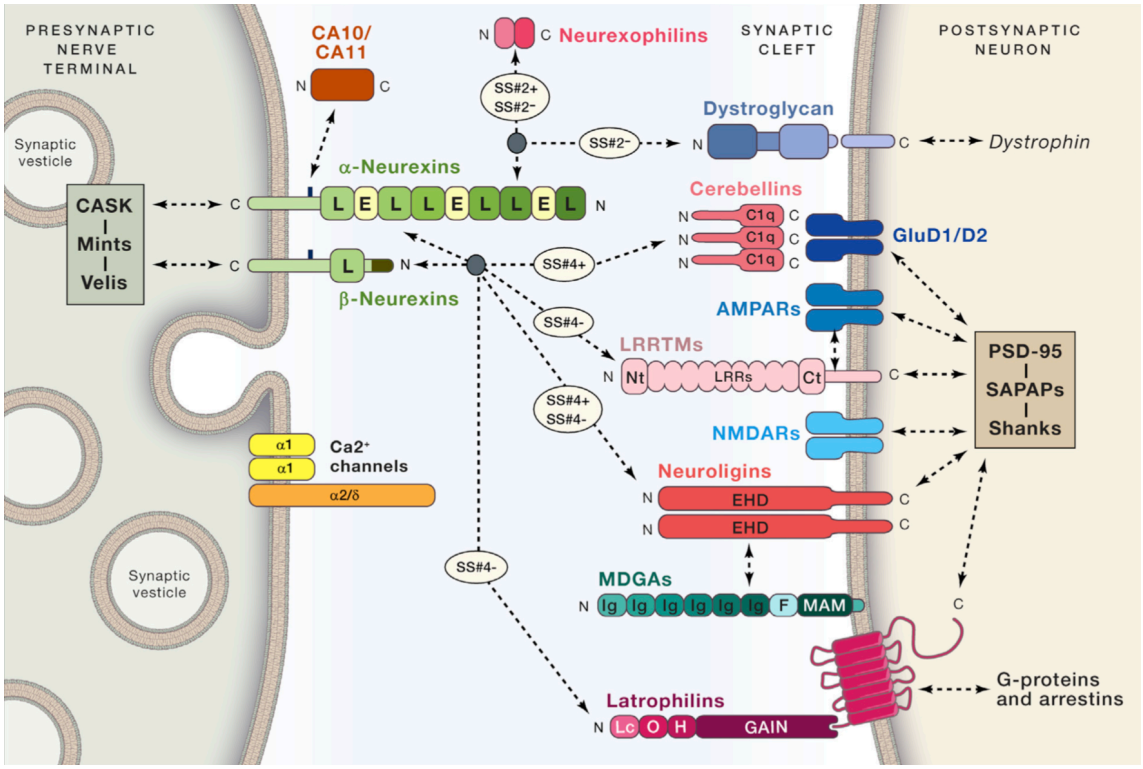

***Figure 1-4* Trans-synaptic interactions of α- and β-Neurexins depend on alternative splicing.** As seen in Südhof *et al*. (3), reproduced with permission. Schematic overview of interaction partners of Neurexin subtypes in the context of the synapse, indicating the requirement of specific splice variants. Where a potential competition between ligands could take place, the junctions are marked with a circle.

Neurexins exert their functions by interacting with a wide range of proteins, most of which are post-synaptic cell-adhesion molecules. Neurexophillins and dystroglycan interact with the LNS2 domains of α-neurexins (82, 83), while neuroligins, LRRTMs, cerebellins and latrophilins bind to the LNS6 domains of α- and β-neurexins (28, 29, 37, 84-86). Recently, the juxta-membrane domain of neurexins have also been shown to bind to C1qls (43), CA10 and CA11 (78). Many of these interactions are dependent on the alternative splicing of

neurexins and of its ligands (**Figure 1-4**). For instance, a splice variant of neuroligin-1 specifically binds to β-neurexins lacking the SS4 insert (87). In contrast, Cerebellin-1 only binds β-Neurexin-1 that contains the SS4 insert (βNrx1 +SS4) (2). Thus, the regulation of neurexin alternative splicing is an important mechanism by which the specificity of neurexins is controlled.

1.7 Signalling *via* the trans-synaptic GluD2-Cbln1-βNrx1 complex

GluD2 forms a trans-synaptic triad with Cbln1 and βNrx1, acting together as bidirectional synaptic organizers. Recently, structural and biophysical studies confirmed the stoichiometry of this complex, where one GluD2 tetramer binds to two Cbln1 hexamers, which in turn bind to two βNrx1 monomers (1:2:2 ratio) (2). GluD2-Cbln1 have been shown to be involved in both pre- and postsynaptic differentiation. On presynaptic sites, GluD2-Cbln1 signalling leads to the accumulation of synaptic vesicle markers and impairment of R-type presynaptic voltage-gated Ca^{2+} channels (R-type VGCCs), probably in a neurexin-dependent fashion (88). On postsynaptic sites of PF-PC synapses, GluD2-Cbln1 contribute to the enrichment of cytoplasmic proteins such as homer, shank and PSD93 (38). The best studied function of the GluD2-Cbln1-βNrx1 triad, however, is related to its role in synaptic plasticity in the cerebellum. In the immature brain, burst stimulation of parallel fibers of the cerebellum lead to the release of D-Serine by Bergmann glia (61). D-Ser binds to the LBD of GluD2, which results in the activation of PTPMEG, a phosphatase that associates to the cytoplasmic C-terminus of GluD2. PTPMEG controls the phosphorylation of tyrosine 876 (Y876) on the GluA2 subunits of AMPA receptors (55), which in turn allows the phosphorylation of a second residue, serine 880 (S880) on GluA2. When long-term depression is triggered, protein kinase C (PKC) phosphorylates GluA2-S880, which releases

AMPA receptors from their anchoring protein glutamate receptor interacting protein 1 (GRIP1), allowing their internalization *via* clathrin-dependent endocytosis (61) (**Figure 1-5**). Interestingly, this signalling mechanism is disrupted in absence of the GluD2 cytoplasmic C-terminus, in mice lacking PTPMEG or Cbln1 or in GluD2 KO mice overexpressing GluD2 containing mutations that hinder D-Ser or Cbln1 binding (2, 61, 70). Furthermore, LTD at PF-PC synapses is also impaired when a glycan linker is added between the LBD and ATD domains of GluD2, disrupting the transmission of any conformational changes between the ATD and LBD layers (2).

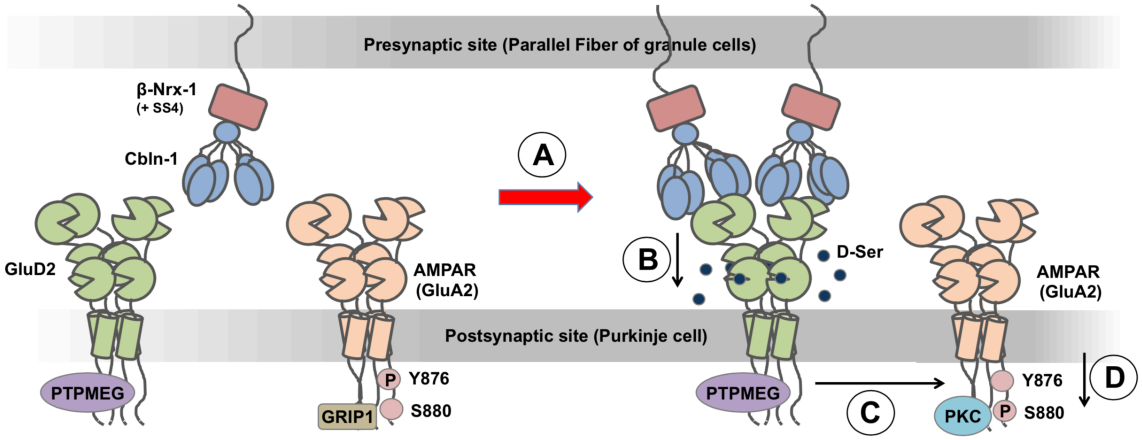

***Figure 1-5* D-Ser signalling via the GluD2-Cbln1-βNrx2 triad leads to internalization of AMPA receptors.** Adapted from Elegheert *et al.* (2), reproduced with permission. Prior to the LTD input, GluA2 subtype of AMPA receptors are phosphorylated at Y876, preventing the phosphorylation of S880 by Protein Kinase C (PKC). This allows for the interaction with GRIP1, which anchors the receptor to the synapse. Upon D-Ser binding at the LBD of GluD2, and anchoring of GluD2 by Cbln1-βNrx1, a signal is transduced to the GluD2 C-terminus, activating PTPMEG (A-B). PTPMEG is a phosphatase that is associated to the GluD2 C-terminus, and dephosphorylates GluA2-Y876 (C). Upon dephosphorylation of GluA2-Y876, PKC phosphorylates S880 and GRIP1 is released. Subsequently, AMPARs diffuse laterally to the perisynaptic area where they are internalized by clathrin-dependent endocytosis (D).

Taken together, these observations suggest that the orchestrated action of D-Ser and Cbln1, binding to the GluD2 LBDs and ATDs respectively, induce a conformational change that is transduced to the GluD2 C-terminus, activating intracellular signalling that leads to the endocytosis of AMPA receptors. Despite previous efforts, it is still unclear how GluD2 transduces signals from its extracellular to its intracellular region, in part due to the lack of a full-length structure of GluD2. Deciphering this metabotropic signalling mechanism

would not only unravel the mode of action of GluD2, but could potentially also shed light on a universal feature of trans-synaptic complexes that integrate iGluRs.

1.8 Receptor Protein Tyrosine Phosphatases integrate adhesive and signalling functions at cell contact sites

The protein phosphorylation of serine, threonine or tyrosine residues is one of the most common and important post-translational modifications (PTMs) and is of fundamental importance for virtually all cellular processes (89, 90).

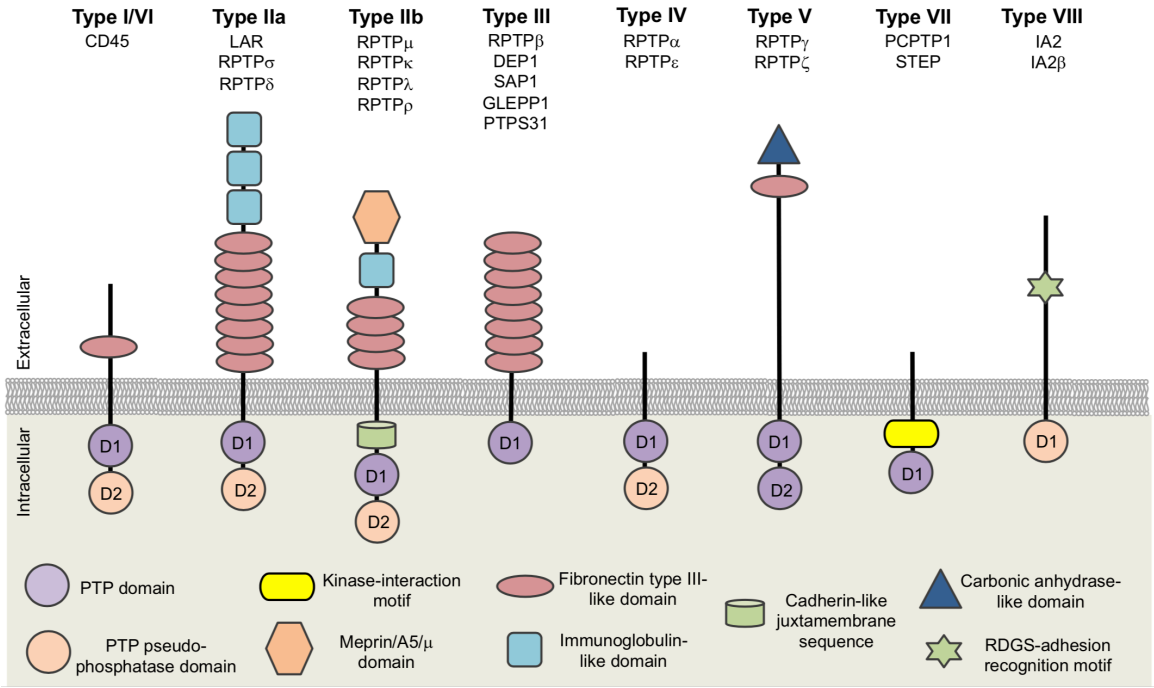

Figure 1-6 **Schematic overview of RPTP subfamilies**. There are eight RPTP subfamilies, classified by the architecture of their extracellular regions. The key for individual domains and structural motifs is provided at the bottom of the figure. All RPTPs contain up to two cytoplasmic tyrosine phosphatase catalytic domains (PTP domains), labelled D1 and D2. In most cases, only the membrane-proximal D1 is catalytically active (depicted in lilac), with the exception of type VIII RPTPs which are believed to be inactive. Type IIb and type VII RPTPs are unusual in that they contain an additional motif between the catalytic domains and the plasma membrane (a cadherin-like juxtamembrane sequence and kinase-interaction motif, respectively). Type IV RPTPs contain the shortest extracellular region, which is often heavily glycosylated.

The fine balance of phosphorylation levels is maintained by the activity of protein kinases and phosphatases, which play an essential role in countless signalling pathways (91).

Receptor Protein Tyrosine Phosphatases (RPTPs) are a large family of single-pass transmembrane proteins that contain up to two phosphatase domains in the cytoplasmic region. While the intracellular domain is conserved among RPTPs, their extracellular region is highly divergent and structurally diverse, giving rise to 8 different sub-families (**Figure 1-6**). This diversity is also observed in the functions that different RPTPs fulfil, performing both overlapping and nonoverlapping roles.

1.9 Regulation of RPTP intracellular domains

Of 21 RPTPs, 12 possess a tandem arrangement of protein tyrosine phosphatases (PTPs), labelled D1 and D2. For all RPTPs, the membrane proximal phosphatase domain D1 is responsible for the catalytic activity (92, 93), while the membrane distal phosphatase D2 is believed to mostly be a platform for protein-protein interactions (94-96). Although D2 is not catalytically active, there is a high degree of sequence and structure conservation between the D1 and D2 domains. In fact, for LAR RPTP, only two point mutations at D2 are needed to convert the domain into an active enzyme (97). There are also cases were the structural integrity of D2 is required for the catalytic activity of D1 (98, 99).

The first RPTP crystal structure to be obtained belonged to the D1 domain of RPTPα, and it revealed that the protein forms dimers (100). In this conformation, a helix-turn-helix motif on one monomer formed a structural wedge that sterically blocked the catalytic site of the other monomer, suggesting that the dimerization of the phosphatase is important for the regulation of its catalytic activity (100). Indeed, further experiments showed that disulphide-bonded RPTPα dimers are catalytically inactive (101) and that RPTPα forms dimers in living cells (102).

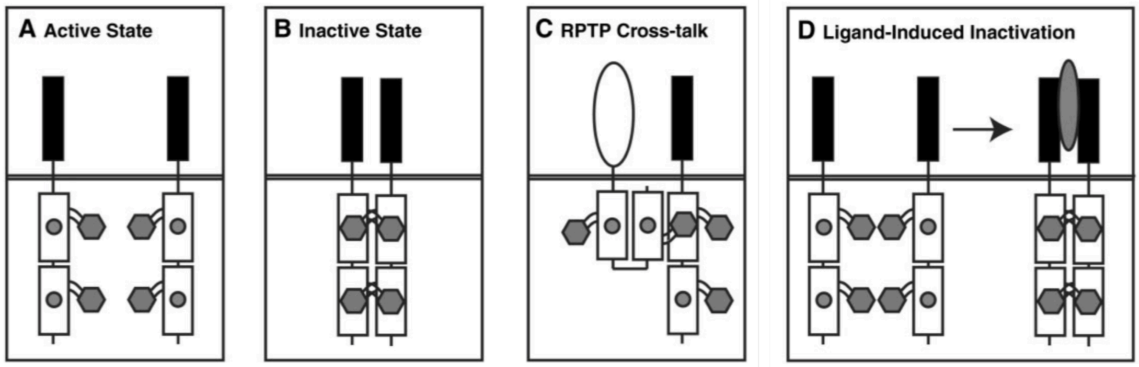

Figure 1-7 **Models for RPTP phosphatase activity regulation.** Adapted from Johnson *et al.* (103), reproduced with permission. Schematic diagrams showing different models for catalytic inhibition. Black rectangles and white oval represent RPTP extracellular regions, while white rectangles stand for the cytoplasmic D1 and D2 phosphatase domains. Grey hexagons depict the inhibitory helix-turn-helix 'wedge' motifs and the grey circles represent the active site of the enzyme. (**A**) Both RPTPs are active, since their active sites are available for catalysis. (**B**) In this model, RPTPs are inhibited by dimerization. The helix-turn-helix motif of the neighbouring RPTP interacts with the active site of the opposing enzyme, sterically hindering catalysis. (**C**) Similar to model depicted in (B), the inhibition by the helix-turn-helix motif happens through a different RPTP type, in which the D2 phosphatase domain blocks the catalytically active D1 domain of the neighbouring molecule. This model would allow cross-talk between RPTPs and different signalling pathways. (**D)** Enzyme inactivation by receptor dimerization is triggered by ligand-binding.

The inhibitory helix-turn-helix structure also plays a regulatory role in other RPTPs. Site-directed mutagenesis on this motif on the RPTP CD45, for instance, leads to autoimmune nephritis and lymphoproliferation (104). A chimeric receptor, in which the cytoplasmic domain of CD45 is combined with the extracellular region of the EGF receptor, displays CD45 phosphatase catalytic activity in the absence of EGF (105). Upon dimerization of the chimeric EGF-CD45 receptor through addition of EGF, the CD45 phosphatase was inactivated, suggesting that extracellular signals regulate the intracellular catalytic activity of RPTPs by affecting their oligomerization state (105).

For some RPTPs, the helix-turn-helix wedge is the basis for regulatory cross-talk between different RPTP family members. The wedge of the second phosphatase of PTPδ, for example, is able to bind and inhibit the D1 phosphatase of RPTPσ (106). RPTPα has also been shown to interact with the D2 phosphatases of RPTPσ, RPTPα, LAR, RPTPδ and RPTPμ (107).

Taken together, the above observations point towards a general mechanism through which RPTP phosphatase activity is regulated by either homo- or hetero-dimerization, and where extracellular cues could be transduced into downstream signalling by directly affecting the RPTP oligomerization state (**Figure 1-7**). This hypothesis remains, however, controversial, since crystal structures of other RPTPs have shown either no dimerization of D1 domains (108); or the impossibility of an inhibitory function of the helix-turn-helix motif due to clashes of the D2 domains (97).

1.10 RPTPμ is a prototypical homophilic adhesion molecule

The IIb subfamily of RPTPs consists of four members: RPTPμ, RPTPρ, RPTPκ and RPTPλ. All four receptors mediate cell adhesion and are highly conserved among family members and across species (109). Despite this similarity, all IIb RPTPs engage in homophilic interactions that are strictly specific to their own type (110), suggesting that IIb RPTPs are involved in cell-cell recognition and play a sorting role in vivo. This notion is confirmed by their layered expression patterns during embryonic development or in the adult mouse cerebellum, where RPTPκ, RPTPμ and RPTPλ are exclusively expressed in the molecular, Purkinje cell and granular layers, respectively (111, 112) (**Figure 1-8**).

The malfunction and expression levels of type IIb RPTPs have been implicated in a number of cancer types, where the proteins adopt both oncogenic and tumor suppressor roles. RPTPρ, for example, presents a high occurrence of somatic mutations across its extra- and intracellular domains in colorectal tumors (113). RPTPμ is down-regulated and acts as a tumor suppressor in glioblastoma multiforme (GBM), a common type of malignant brain tumor (114).

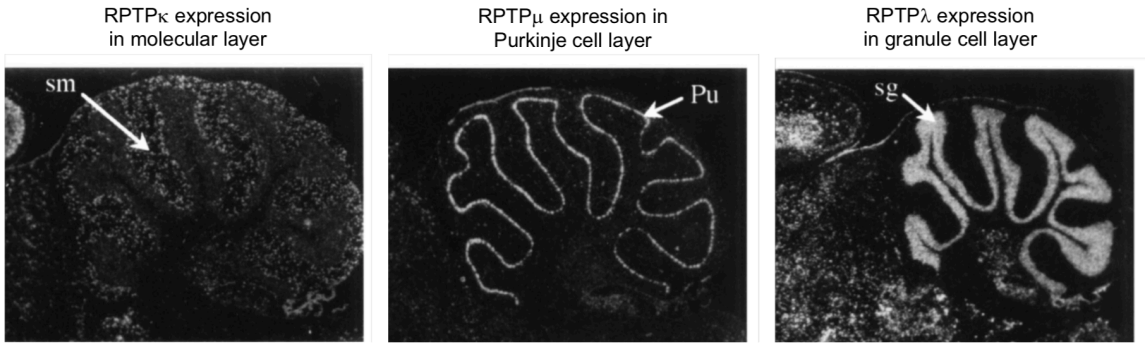

Figure 1-8 **Layered expression pattern of type IIb RPTPs in the adult cerebellum.** Figure adapted with permission from Fuchs *et al*. (111), showing *in situ* hybridization analysis of type IIb RPTPs in parasagittal cryosections of the adult cerebellum. The layered expression pattern of RPTPκ in the molecular layer (stratum moleculare, 'sm'), RPTPμ in the Purkinje cell layer ('Pu') and RPTPλ in the granule cell layer (stratum granulare, 'sg') suggests a cell-sorting and self-recognition role for type IIb RPTPs.

RPTPμ, the focus of this thesis, is further associated with angiogenesis and the formation of tight cell-cell contacts in vascular endothelia (115), in the lung and in the intercalated discs of cardiomyocytes (116). RPTPμ is also found in the nervous system, where it is implicated in neuronal development, axon guidance and retinal lamination (103, 117).

Like all other members of the RPTP IIb subfamily, the extracellular region of RPTPμ consists of a meprin/A5/μ (MAM) domain, one immunoglobulin (Ig)-like domain, and four fibronectin (FN) type III repeats. The crystal structure of the RPTPμ extracellular region revealed a rigid structure, stabilized by an extensive network of interdomain interactions (109). The minimal unit that allows homodimerization comprises the MAM-Ig-FN1-FN2 domains, which form a polar interface that is pH sensitive (118). During the secretory pathway, at acidic pH values, RPTPμ is monomeric. When RPTPμ is exposed to the cell surface, at neutral pH values, the protein is able to homodimerize in *trans* with RPTPμ presented on neighbouring cells.

RPTPμ is processed by a number of proteases at different stages. Protein convertases in the trans-Golgi network produce a cleavage in the membrane-proximal FN4, which potentially adds more flexibility to the extracellular region but does not lead to its dissociation (119,

120). ADAM 10, by contrast, cleaves RPTPμ and results in the shedding of the extracellular region (121). A further intramembrane cleavage by γ-secretase/PS1 releases the cytoplasmic region (120), which is either targeted for proteasomal degradation or is translocated to the nucleus (122).

To date, the only known extracellular ligand of RPTPμ is RPTPμ itself. A number of substrates and interaction partners have been found for its intracellular region. The best described function of RPTPμ relates to its role at cadherin mediated cell-cell contacts, where it interacts with members of the cadherin family (N, E, R, VE cadherins) *via* its intracellular region (123, 124) (**Figure 1-9**). The phosphatase domain of RPTPμ maintains the dephosphorylated state of cadherin-catenin complexes, further stabilizing the cadherin mediated cell-cell contact. A yeast two-hybrid screen further identified that the D1 phosphatase domain of RPTPμ interacts with Receptor for Activated protein C Kinase (RACK1) (125). RPTPμ recruits RACK1 to the plasma membrane at cell-cell contact sites of a lung epithelial cell line, and their association increases at high cell densities (125). RACK1 is an evolutionary conserved scaffolding protein that interacts with multiple signalling molecules and is implicated in shuttling proteins to the plasma membrane, suggesting that RPTPμ could lead to the recruitment of further signalling molecules *via* RACK1. Indeed, RPTPμ and RACK1 are found in complex with protein kinase C δ (PKC-δ) and PKC-δ is required for RPTPμ-dependent neurite outgrowth (126). RACK1 also interacts with other membrane-bound receptors and is part of the eukaryotic ribosome, linking signal-transduction to the regulation of translation (127). This opens the possibility that RPTPμ could be involved in ribosomal recruitment *via* RACK1, activating local translation at cell-cell contact sites in response to extracellular cues.

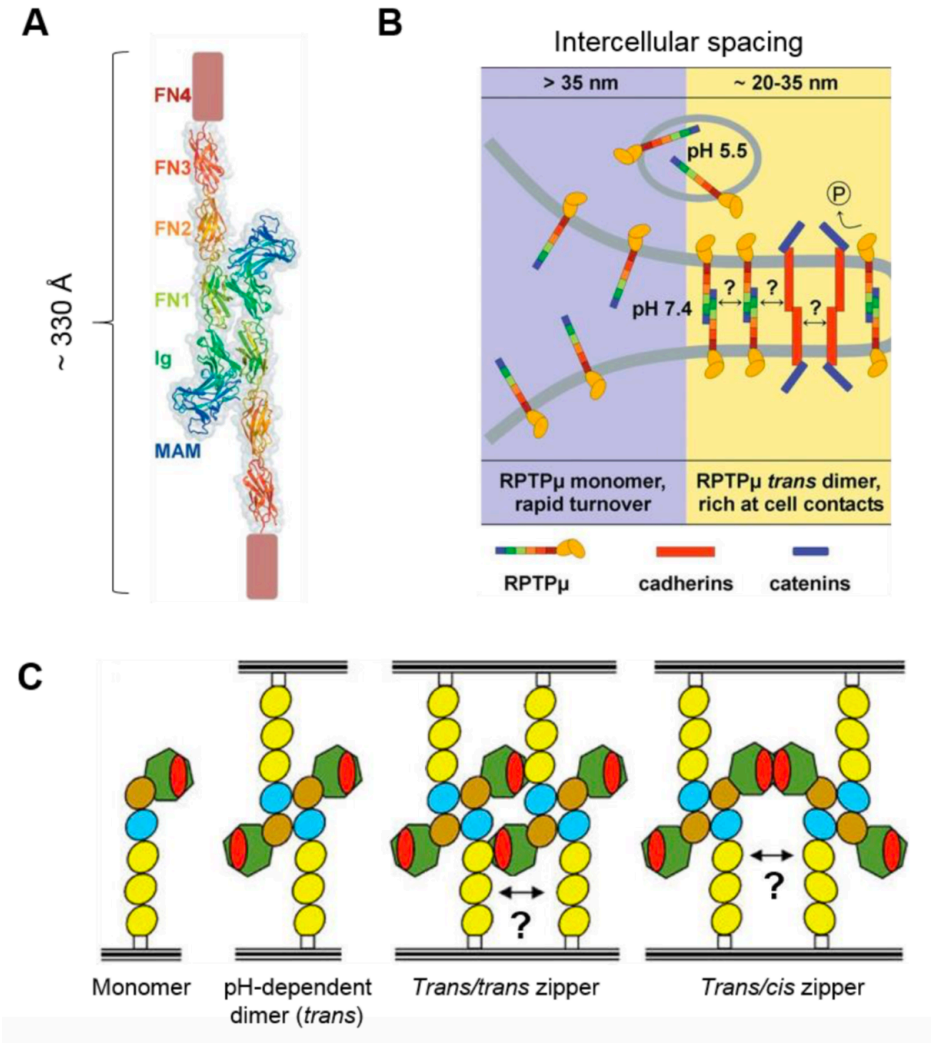

Figure 1-9 **Structure and potential oligomerization states of the RPTPμ ectodomain.** Figures adapted from work published by Aricescu *et al*. (118, 128), reproduced with permission. (**A**) The crystal structure of the RPTPμ ectodomain presents an extended architecture that form a *trans* dimer. The FN4 domain was not well ordered in the crystal packing and is therefore represented as a rectangle. The extensive dimerizing interface (1630 Å^2 per monomer) is formed by residues of the 4 N-terminal MAM, Ig, FN1 and FN2 domains. (**B**) The RPTPμ ectodomain dimerization is a pH-dependent process. In the extracellular, neutral environment, RPTPμ forms *trans* dimers that regulate the spacing between cell membranes. RPTPμ regulates the phosphorylation of cadherin/catenin complexes at cell contacts. Interactions between these proteins' ectodomains (indicated by arrows and question marks) have been proposed but remain to be studied. (**C**) Possible oligomerization arrangements of the RPTPμ ectodomain at cell-cell contacts include 'zipper' conformations by *cis*- or *trans*-dimerization.

Little is known about how type IIb RPTPs integrate their extracellular adhesive function with their intracellular catalytic activity. The simplest explanation suggests that by interacting with extracellular cues (mostly engaging in homophilic *trans* interactions) the receptors locate phosphatase activity at sites of cell-cell contact where they interact with substrates.

In the case of RPTPμ, it seems that homophilic binding is independent of phosphatase activity. For example, constructs lacking the phosphatase domain or containing a catalytically inactive C-S mutant, retain their adhesive properties. On the other hand, both catalytic and adhesive functions are required for neurite outgrowth (129) and retinal lamination (130).

A different model in which extracellular cues could affect catalytic activity involves the extracellular oligomerization of the receptor, leading to dimerization and inactivation of the catalytic phosphatase domains (discussed in section 1.9). This oligomerization could either be the result of the binding of a ligand, or through lateral homophilic interactions in *cis*, posing the question of whether clustering of RPTPs could have a downstream signalling consequence. The formation of signalling clusters has been observed for other complexes spanning cell-cell contacts, like Eph receptor/ephrin (131, 132), β-neurexin/neuroligin (133) and cadherins (134). Recently, a structural study of Slitrk1 and type IIa RPTPs showed that following the formation of a complex in *trans,* lateral oligomerization in *cis* leads to signalling clusters that are functionally relevant (135).

RPTPμ is distributed evenly on the cell surface until the formation of cell-cell contacts, when it is enriched at the contact sites to form large and mostly planar contact surfaces between cells (118, 121, 124). The enrichment of RPTPμ into such clusters opens the question of whether their stability is regulated by lateral oligomerization of RPTPμ, which would require an additional interaction interface (**Figure 1-9**). Modes for RPTPμ interaction in *cis* have been suggested previously (118, 136), however, the packing of the RPTPμ extracellular region crystal lattice revealed no feasible interactions beyond the well-described dimerization in *trans* (109).

Oligomerization of RPTPμ in *cis* could also be affected by the transmembrane and cytoplasmic domains. The RPTPμ transmembrane domain contains a GxxxG motif,

considered a weak predictor of protein dimerization in the membrane (137). Additionally, as described in section 1.9, the D1 and D2 domains of RPTPs have been shown to interact in *cis* (107).

Despite previous efforts, it remains unclear whether RPTPμ forms ordered arrays at cell-cell contacts and how such arrangements would affect the signalling function of the protein. Previous studies have left an imaging gap, in which high resolution information of the protein in a cellular environment is missing. Obtaining such information will be instrumental in understanding how RPTPμ exerts its function, and might also reveal a general mode of action of type IIb RPTPs at cell-cell contact sites.

1.11 Aims of this thesis

During this DPhil thesis, I set out to study two cell-adhesion complexes: the trans-synaptic GluD2-Cbln1-βNrx1 triad and the homophilic dimer of RPTPμ. Using a range of structural biology methods, from X-ray crystallography and single particle cryo-EM, to *in situ* cryo electron tomography, I intend to decipher how these molecules transduce extracellular signals to the cytoplasm.

Specifically, I aim to answer following questions: a) What is the overall structure of GluD2 and how does it compare to other iGluRs? b) How does the GluD2-Cbln1-βNrx1 triad transduce metabotrobic signalling through the GluD2 transmembrane domain? and c) Does RPTPμ form an ordered array at cell-cell contact sites?

2. Materials and Methods

2.1 Mammalian expression and purification of soluble RPTPμ, GluD2, Cbln1 and βNrx1 constructs

For expression and secretion of soluble proteins in HEK293T cells, constructs were cloned into the pHLsec (138) and pHR (139) vectors. All constructs used in this thesis were based on human sequences. GluD2 constructs were based on UniProt ID O43424-1, resulting in constructs for the ligand-binding domain 'GluD2^{LBD}' (residues 440-551 and 664-823), the amino-terminal domain 'GluD2^{ATD}' (residues 24-440) and the extracellular region 'GluD2^{ECTO}' (residues 24-551 and 664-823). Cerebellin-1 constructs were based on UniProt ID P23435-1, resulting in a full-length construct 'Cbln1' (residues 22-193) and a C1q-domain construct 'Cbln1^{C1q}' (residues 59-193). The β Neurexin 1 construct was based on UniProt ID P58400-2, comprising the soluble domain and including the exon resulting from splice site 4 'βNrx1^{+SS4}' (residues 86-295). The extracellular region of RPTPμ resulted from

UniProt ID P28827-2 'RPTPμ^{ECTO}' (residues 1-742). **Table 8-3** in the appendix summarises all constructs.

HEK293T cells were passaged every 2-3 days, splitting 1:10 in Dulbecco's Modified Eagle's Medium (DMEM, Gibco) supplemented with 10% Fetal Calf Serum (FCS, Gibco), 1% non-essential amino acids (NEAA, Gibco) and 1% L-glutamine (L-Gln, Gibco). Where protein samples were intended for crystallization experiments with homogeneous glycans, HEK 293 cells deficient in N-acetylglucosaminyltransferase I were used (HEK293S-GnTI$^{-/-}$) (140). Cultures of adhesive of HEK293 T/S cells were maintained at 37 °C and 5% CO_2. Small scale test expressions were performed in 6-well plates of confluent HEK293T cells. For one well, 4 μg of plasmid DNA (pDNA) were combined with 500 μl of serum-free Dulbecco's Modified Eagle's Medium (DMEM, Sigma). In parallel, 8 μg of polyethylenimine (PEI) were combined with 500 μl of serum-free DMEM. The pDNA and PEI dilutions were mixed and left incubating at room temperature for 15 min. Prior to addition of the transfection mix, the medium of one well was removed and replaced with 1 ml of DMEM, supplemented with 2% FCS, 1% NEAA, 1% L-Gln. Medium containing secreted protein was harvested after 48 h, and analysed by Western Blot. For large scale expression experiments, the cells of 8 confluent T175 flasks were trypsinized, transferred to 8 expanded surface bottles (Corning) and diluted respectively with 200 ml DMEM (10% FCS, 1% NEAA, 1% L-Gln). Once cells reached confluency, transfection was performed similarly as described above. Prior to transfection, large amounts of pDNA (up to 10 mg) were prepared using the Qiagen Plasmid GIGA kit (Qiagen). For sterilization of pDNA, 80 μl chloroform were added to each 1 ml of pDNA and mixed vigorously. The two phases of the pDNA-chloroform mix were separated by centrifugation at 13500 rpm, 10 min at RT. The upper (polar) phase containing the pDNA was collected and used for the next steps. The transfection mix was prepared by combining a) 25 ml of serum-free DMEM with 500 μg

pDNA and b) 25 ml of serum-free DMEM with 1 mg PEI and then mixing both solutions. Before adding the transfection mix, the medium in the roller bottles was replaced by 200 ml of DMEM (2% FCS, 1% NEAA, 1% L-Gln). Adherent cells in roller bottles were incubated at 37 °C, with gentle rotation. Expression of secreted proteins was maintained until cell culture showed signs of cell death (clouding of medium, colour of pH-indicator turning yellow or detachment of adherent cells), typically 6 days after transfection. Medium was harvested and cleared by centrifugation at 5000 RPM, 30 min, 4 °C. Cell debris was further removed by filtering the medium using a 0.2 μm pore membrane. The medium was concentrated and buffer exchanged into 500 mM NaCl, 20 mM Tris-HCl pH 8 and 10 mM imidazole, using either a QuixStand or AKTA Flux (GE Healthcare) system. Purification over nickel affinity chromatography was performed with a pre-packed 5 ml column (GE Healthcare) on an AKTA Pure system. The resin was washed with buffer containing 20 mM and 50 mM imidazole and bound protein was eluted with 500 mM NaCl, 20 mM Tris-HCl pH 8 and 500 mM imidazole. Relevant fractions were pooled, concentrated and further purified by SEC on a Superdex200 column (GE Healthcare). For the production of biotinylated proteins, constructs containing a C-terminal 3C-Avi-6xHis tag were prepared. A plasmid encoding the BirA biotin ligase was co-transfected with the plasmid encoding the protein of interest in a 1:10 ratio (Biotin ligase: protein of interest). The transfection and protein expression were performed as described above, with addition of 100 μM D-biotin (final concentration) to the medium.

2.2 Bacterial periplasmic expression and purification of nanobodies

Nanobodies against the GluD2-Cbln1-βNrx1 complex and against GluD2 alone were raised and selected by Jan Steyaert's laboratory in VUB Belgium. The cDNA sequences encoding

these nanobodies were cloned into the phage display vector pMESy4 (GenBank KF415194), allowing production of 6xHis- and EPEA-tagged soluble nanobodies. A list of the nanobodies generated and their respective amino acid sequences can be seen in **Figure 8-11**. The expression and purification of these nanobodies was performed as described by Pardon *et al* (141). Briefly, ~500 ng of plasmid DNA were mixed with 40 µl of WK6 competent cells (homemade stock) and left incubating on ice for 30 min. Chemical transformation was achieved by heat shock at 42 °C for 45 s, followed by a brief incubation on ice for 2 min. Upon addition of 100 µl of SOC medium (Life technologies), bacteria were left incubating at 37 °C and rotating at 180 RPM for 45 min. Bacterial suspension was streaked on LB agar plates supplemented with 2% glucose and 100 µg/ml ampicillin and left incubating overnight at 37 °C. 20 ml of LB broth, supplemented with 2% glucose, 1mM $MgCl_2$ and 100 µg/ml ampicillin (final concentrations), were inoculated with 1-3 colonies and left incubating for 8 h at 37°C, shaking at 180 RPM. 5 ml of preculture was used to inoculate 500 ml of TB broth, supplemented with 0.1% glucose, 2mM $MgCl_2$ and 100 µg/ml ampicillin (final concentrations). The bacterial culture was incubated shaking at 190 RPM, 37 °C until OD_{600} reached 0.7, upon which expression of nanobodies was induced by addition of IPTG to a final concentration of 1mM. Expression was maintained for 16 h at 28 °C, 190 RPM and cells were harvested by centrifugation in a JLA 8.1 rotor (Beckman Coulter), at 5000 RPM, for 30 min at 4 °C. The bacterial pellet resulting from 500 ml culture was resuspended in 15 ml of TES buffer (0.2 M Tris-HCl pH 8.0, 0.5 mM EDTA, 0.5 M sucrose). The bacterial suspension was left equilibrating in TES buffer by gentle rotation at 4 °C for 3 h. Sucrose osmotic shock was completed by subsequently adding 30 ml TES1/4 (TES buffer diluted 4-fold in MilliQ water) to the suspension, and incubating for further 3 h at 4 °C. Bacterial lysate was cleared by centrifugation for 30 min at 8000 RPM, 4 °C.

Supernatant was mixed with 2 ml of pre-equilibrated Ni-NTA resin (Qiagen) and left rotating gently for 1 h at 4 °C. Ni-NTA resin and immobilized nanobodies were pelleted by centrifugation for 5 min at 500 RPM, 4 °C. Supernatant was removed and resin was washed with subsequent washes of 500 mM NaCl, 50 mM HEPES-NaOH pH 7.2 and increasing concentrations (10, 25 and 50 mM) of imidazole. The final pH of these solutions was adapted for each nanobody preparation, so that the pH was at least one unit apart from the nanobody's pI value. For each washing step, incubation with gentle rotation was allowed for 10 min at 4 °C and resin was pelleted as described above. Elution of nanobodies was achieved with 500 mM NaCl, 50 mM HEPES-NaOH pH 7.2 and 500 mM imidazole. Nanobodies were concentrated and further purified by size-exclusion chromatography in 150 mM NaCl, 20 mM HEPES-NaOH pH 7.2, using a Superdex75 16/60 column (GE Healthcare).

2.3 Biolayer Interferometry

Biolayer Interferometry (BLI) was performed using an Octet RED384 system (ForteBio), where binding of ligand to immobilized receptors is measured by monitoring changes in the biolayer thickness at the tip of the sensors. Biotinylated GluD2 ($GluD2^{ATD}$, $GluD2^{LBD}$ and $GluD2^{\Delta C\text{-}ter}$ constructs) and biotinylated $\beta Nrx1^{+SS4}$-Cbln1 were immobilized on streptavidin coated 'Dip and Read' tips (ForteBio), by dipping the tips in 0.1 mg/ml protein solution at RT for 2 min, reaching a thickness of ~ 3 nm.

For single cycle kinetics experiments, ten-fold dilution series (concentration ranging from 0.1 nM to 1000nM) of each nanobody were prepared, resulting in 5 concentration steps. With this setup, the affinity of 16 nanobodies could be measured in parallel, allowing for the high-throughput characterization of nanobodies. Nanobody dilutions were prepared in 200 mM NaCl and 50 mM HEPES-NaOH pH 7.5 for soluble constructs, and 200 mM NaCl,

50 mM HEPES-NaOH pH 7.5 and 0.007% DMNG:CHS (20:1) for GluD2$^{\Delta C\text{-ter}}$. Each kinetic titration experiment consisted of sequential association periods of 180 s and short dissociation periods of 20 s for each nanobody, followed by a final dissociation length of 600 s. The resulting data was analysed in MATLAB (MathWorks) using scripts written by Dr Suzanne Scott and Dr Sebastian Bonilla, based on previously described methods (142). Briefly, the data is modelled assuming a simple 1:1 binding model, where a ligand (L) binds its receptor (R) to form a complex (RL) with the association rate k_{on} and the dissociation rate k_{off} (

Equation 1).

Equation 1

$$R + L \underset{k_{off}}{\overset{k_{on}}{\rightleftharpoons}} RL$$

The affinity of this interaction, expressed by the dissociation constant at equilibrium K_D, equals the dissociation rate divided by the association rate (**Equation 2**).

Equation 2

$$K_D(M) = \frac{k_{off}(s^{-1})}{k_{on}(M^{-1}s^{-1})}$$

During each injection (or dipping into ligand), the net complex formation rate is given by **Equation 3**, while the dissociation after dipping back into buffer is determined by **Equation 4**.

Equation 3

$$\frac{d[RL]}{dt} = k_{on}[R][L] - k_{off}[RL]$$

Equation 4

$$\frac{d[RL]}{dt} = -k_{off}[RL]$$

In a BLI experiment, the ligand binding is monitored by measuring the increment in the biolayer's thickness, or response R. The concentration of the receptor-ligand complex

formed can be expressed in terms of the response R, where R_{max} represents the maximum ligand binding capacity (**Equation 5**).

Equation 5

$$\frac{dR}{dt} = k_{on}[L]R_{max} - \left(k_{on}[L] + k_{off}\right)R$$

A numerical solution to **Equation 5** was implemented to fit values of k_{on}, k_{off} and R_{max}. The dissociation constant at equilibrium K_D was then derived using **Equation 2**. A coefficient of determination parameter (R^2) was calculated in MATLAB (MathWorks) to determine the quality of the fit.

2.4 Purification and crystallization of GluD2-nanobody complexes

Nanobody nomenclature was adopted from Jan Steyaert's laboratory, typically comprising 'CA', followed by a 5-digit number. For simplicity, hereon all nanobodies are named for the last three digits of their ID number (for example, 'nanobody CA11399' is 'Nb399').

To form complexes of GluD2 domains and nanobodies, the purified components (see previous sections) were combined in a 1:1.5 ratio (GluD2:nanobody). The protein mix was incubated for 5 min at room temperature and then concentrated to 500 µl using centrifugal filters (Millipore, MWCO 5 kDa). The sample was injected onto a Superdex 200 10/300 column, pre-equilibrated in 150 mM NaCl, 20 mM HEPES-NaOH pH 7.5. Size-exclusion chromatography fractions containing the protein complex were pooled and concentrated to 6 mg/ml (LBD complexes) and 8 mg/ml (ATD complexes). Endoglycosidase F1 (EndoF1) was added in a 1:200 w/w ratio to trim N-glycans to one N-acetyl glucosamine (NAG) group. Protein aggregates were removed by centrifuging at 13500 x g at 4 °C for 30 min. 300 nl drops in 1:1 and 1:2 (protein : mother liquor) ratios were set in sitting drop vapour diffusion format using a Mosquito robot (TTB Labtech). Crystals appeared after 3-5 days,

in conditions summarized in **Table 2-1**. All crystals were cryoprotected in their mother liquor supplemented with 30% ethylene glycol (final concentration) and flash frozen in liquid nitrogen.

Table 2-1 **Crystallization conditions for GluD2-Nanobody complexes**

Protein complex	Crystallization condition
GluD2^{ATD} + Nb381	8% (w/v) PEG 8K, 0.1M Tris Hydrochloride pH 8.5 (LMB01-C12/ Hampton Research Screen 1, No 36)
GluD2^{ATD} + Nb389	10% (w/v) PEG 4K, 10% w/v iso-propanol, 0.1 M Sodium Citrate pH 5.6 (LMB08-E3/Jena BioScience Screen 3, No A3)
GluD2^{LBD} + Nb390	30% (w/v) PEG 4K, 0.2 M Ammonium Acetate, 0.1 M Sodium Citrate Tribasic Dihydrate pH 5.6 (LMB01-A9/ Hampton Research Screen 1, No 9)
GluD2^{LBD} + Nb392	22% (w/v) PEG 4K, 0.2 M Ammonium Sulphate, 0.1 M Sodium Acetate (LMB08-F4/ Jena BioScience Screen 3, No C4)
GluD2^{LBD} + Nb399	25% (w/v) PEG 4K, 0.2 M Ammonium Sulphate, 0.1 M Sodium Citrate pH 5.6 (LMB08-F6/ Jena BioScience Screen 3, No C6)

2.5 X-ray crystallography data collection, data processing and model building

X-ray diffraction data were collected at Diamond Light Source (DLS) on beamlines I03 and I04. Datasets were auto-processed using the xia2 package (143) , applying either the dials, 3d or 3dii protocols. Datasets for GluD2^{ATD}+Nb389 and GluD2^{LBD}+Nb392 were integrated and indexed in DIALS and scaled with Aimless (144) (xia2 dials pipeline). The GluD2^{LBD}+Nb390 dataset was integrated and indexed in XDS and scaled with XSCALE (xia2 3d pipeline). Datasets GluD2^{LBD}+Nb399 and GluD2^{ATD}+Nb381 were integrated and indexed in XDS and scaled with XSCALE (xia2 3dii pipeline). Asymmetric Unit composition and solvent content was determined by the Matthews Coefficient (145, 146) of

the CCP4 suite (147) . Phase information was obtained by molecular replacement using Phaser (148). Search models for molecular replacement were derived from previously published structures of GluD2^{ATD} (PDB ID 5KC8) and GluD2^{LBD} in complex with D-Serine (PDB ID 2V3U). Separate lobes of the ligand-binding domain clamshell were used as search models. Nanobody models for molecular replacement were chosen based on a) the highest sequence identity and b) the best model quality (resolution and MolProbity score). For Nb389 and Nb381, PDB entry 5IMM was used as search model. PDB entry 5BOP was used for Nb390, Nb392 and Nb399. Initial rigid body refinement was performed in Refmac (149), defining the two GluD2^{LBD} lobes, GluD2^{ATD} and nanobodies as independent domains, followed by iterative rounds of manual model building in Coot (150) and restrained refinement in Refmac, applying local Non-Crystallographic Symmetry (NCS) restraints where applicable. The model for the GluD2^{ATD}-Nb381 dataset was built in automated manner using ARP/wARP (151, 152). ARP/wARP was also used to model water molecules for the other datasets. Final refinement rounds were performed in Phenix (153), using automated X-ray and atomic displacement parameter (ADP) weight optimisation and Translation/Libration/Screw (TLS) groups determined using the TLSMD Server (154). Final models were submitted for analysis to the MolProbity server (155). Model analysis and figure preparation were performed in Pymol and Chimera (156). Interface analysis was done with the PISA server (157). Domain motions for the GluD2^{LBD} structures were determined with the DynDom server (158). Pymol was used to calculate root-mean-square deviations (r.m.s.d.) *via* the alignment tool.

2.6 Expression and purification of membrane scaffold proteins

Plasmids encoding the membrane scaffold proteins (MSP) MSP1D1 and MSP2N2 were kindly provided by Dr Christiane Kowatsch and were originally purchased from Addgene

(plasmids #29520 and #20061). For cytoplasmic expression of belt protein in *E. coli*, approximately 50 ng of pDNA were chemically transformed into 50 µl of BL21-Gold(DE3) pLysS competent cells (Agilent) and streaked on LB agar plates supplemented with 30 µl/ml kanamycin. 1-3 colonies were used to inoculate 15 ml of LB growth medium containing kanamycin, and the culture was left to grow shaking overnight at 37 °C and 200 rpm. 500 ml of Terrific Broth (TB) growth medium containing kanamycin were mixed with 5 ml of the overnight starter culture, and incubated at 37 °C, 220 rpm until OD_{600} reached 2.5 - 3.0. Expression of belt proteins was induced by addition of IPTG to a final concentration of 1 mM IPTG and cultures were kept shaking at 37 °C, 220 rpm for 3 h. Bacteria were harvested by centrifugation in a JLA8.1 rotor (Beckman Coulter) at 5000 rpm, 4 °C for 30 min. Pellets were flash frozen in liquid nitrogen and kept at -80 °C for storage. For the purification of belt proteins, the pellet from a 1 l culture was thawed and resuspended in 50 ml ice-cold lysis buffer (500 mM NaCl, 20 mM Tris-HCl pH 8, 1% Triton X-100, supplemented with EDTA-free, complete protease inhibitors (Roche)). All subsequent steps were performed on ice or at 4 °C. Lysis of bacteria was achieved by sonication, using a probe operating at 40% amplitude and generating a pulse set to 2 s on and 8 s off for a total of 20 min. Bacterial lysate was cleared by centrifugation using a JA25.50 rotor, operated at 22000 rpm and 4 °C, for 1 h. The supernatant was collected, combined with 3 ml of pre-equilibrated Ni-NTA resin slurry (Qiagen) and incubated for 1 h and 4 °C with gentle rotation. Ni-NTA resin was pelleted by centrifugation at 500 x g, 4 °C for 10 min. Supernatant was discarded and resin was washed in subsequent steps with 25 ml each of the following solutions: a) 500 mM NaCl, 20 mM Tris-HCl pH 8, 1% Triton X-100; b) 500 mM NaCl, 20 mM Tris-HCl pH 8, 50 mM cholate; c) 500 mM NaCl, 20 mM Tris-HCl pH 8 and d) 500 mM NaCl, 20 mM Tris-HCl pH 8, 20 mM imidazole. For each washing step, the resin was allowed to rotate gently for 10 min at 4 °C before being pelleted as described above. Elution of belt proteins

was achieved by addition of 10 ml 500 mM NaCl, 20 mM Tris-HCl pH 8, 500 mM imidazole. Fractions containing MSP belt proteins were concentrated and further purified by SEC on a Superdex 200 16/600 (GE Healthcare) column, previously equilibrated in 100 mM NaCl, 20 mM Tris-HCl pH 7.8. Purified MSP proteins were concentrated to 5 mg/ml, aliquoted and flash frozen in liquid nitrogen.

2.7 Coupling of Rho-1D4 antibody onto activated CNBr-sepharose

1 g of CnBr-activated sepharose 4B (GE Healthcare, Cat No 17-0430-01) were combined with 50 ml of 1 mM HCl under a fume hood and left incubating for 10 min at room temperature. After this incubation step, the material had swelled and formed a homogenous suspension. The beads were pelleted by centrifugation at 500 x g, for 10 min at room temperature. The supernatant was removed under the fume hood and the beads were subsequently washed with 50 ml of 1mM HCl and 50 ml of 500 mM NaCl, 100 mM $NaHCO_3$ pH 8.5. 14 mg of monoclonal Rho-1D4 antibody (University of British Columbia) were dissolved in 10 ml of PBS, added to the sepharose and incubated rotating over night at 4 °C. Sepharose with coupled antibody was pelleted by centrifugation at 500 x g, for 10 min at room temperature. Efficient coupling of antibody was assessed by measuring the supernatants' absorbance at 280 nm. Beads were first washed with 50 ml of 200 mM glycine, pH 8.0 and the incubated with further 50 ml of 200 mM glycine rotating for 2 h at room temperature. The beads were subsequently washed with the following solutions: a) 50 ml of 500 mM NaCl, 100 mM $NaHCO_3$ pH 8.5; b) 50 ml of 500 mM NaCl, 100 mM NaOAc pH 4.0; c) 50 ml of 500 mM NaCl, 100 mM $NaHCO_3$ pH 8.5 and d) 50 ml of PBS, supplemented with 10 mM NaN_3. The beads were resuspended in a final volume of 10 ml PBS, supplemented with 10 mM NaN_3 and stored long term at 4 °C.

2.8 Preparation of lipid stocks for reconstitution of membrane proteins into nanodiscs

1 g of Bovine Brain Extract (BBE, Sigma, Cat. No. B1502) and 500 mg of 2-Oleoyl-1-palmitoyl-*sn*-glycero-3-phosphocholine (POPC, Sigma, Cat. No. 42773) were combined with 50 ml of 3% n-Dodecyl-β-D-Maltopyranoside (DDM, Anatrace, Cat. No. D310), 20 mM HEPES-NaOH pH 7.4, 150 mM NaCl, respectively. The mixtures were maintained rotating at 4 °C for 3 days, before aliquoting for long-term storage at -20 °C. The final concentrations of the stocks were 20 mg/ml BBE and 10 mg/ml POPC. For reconstitution of membrane proteins into nanodiscs, a lipid mix of BBE and POPC was prepared. 30 µl of 20 mg/ml BBE and 170 µl of 10 mg/ml POPC were combined and left rotating at room temperature for 30 min. Large aggregates were removed by centrifugation at 13000 rpm for 5 min at room temperature.

2.9 Expression, solubilisation and purification of GluD2 membrane proteins

GluD2 constructs (UniProt ID O43424-1) were cloned into the pHLsec vector (138), flanked with a C-terminal 1D4 epitope tag (TETSQVAPA) . Extensive screening experiments performed by Dr Ester Behiels (2) determined that constructs lacking the C-terminus were monodisperse and resulted in higher yields. Consequently, all constructs used in this thesis comprise residues GluD2$^{D24\text{-}K870}$. For large scale expression experiments, HEK293F 'Expi' cells (ThermoFisher) were cultured in suspension at 37 °C, 8% CO_2 and 125 RPM, in Expi293 expression medium (ThermoFisher) with no supplements. Cells were split every two to three days, maintaining the cell density at approximately 0.5 x 10^6 cells/ml. Transient transfection was performed at a cell density of 2 x 10^6 cells/ml, using polyethylenimine

'MAX' transfection reagent (PEI 'MAX', Polysciences). Prior to the preparation of transfection mixes, pDNA was purified using Qiagen Plasmid GIGA kits (Qiagen) and chemically sterilized with chloroform. For a 500 ml cell suspension, 550 µg pDNA were mixed with 16 ml of Expi293 expression medium. In parallel, 1.5 mg PEI 'MAX' were mixed with 16 ml Expi293 expression medium. The pDNA and PEI 'MAX' mixes were combined and left to incubate for 15 min at room temperature. Subsequently, the mixture was added to 500 ml of cell suspension. Protein expression was maintained for 72 h at 37 °C, 8% CO_2 and 125 RPM. Cells were harvested by centrifugation at 3000 x g for 15 min at 4 °C, flash frozen in liquid nitrogen and kept at -80 °C for long term storage.

For protein solubilisation and purification, the pellet from one 500 ml culture was thawed and resuspended in 300 mM NaCl, 3 mM $CaCl_2$, 10 mM HEPES-NaOH pH 7.2 and 1% (v/v) mammalian protease inhibitor cocktail (Sigma-Aldrich). Once resuspension was complete, 20:1 (w/w) decyl maltose neopentyl glycol:cholesterol hemisuccinate (DMNG:CHS, Anatrace, Cat. No. NG322 and CH210) was added to reach a final detergent concentration of 1.3% (w/v). Cells were solubilized for 1.5 h at 4 °C with gentle rotation and insoluble material was subsequently removed by centrifugation at 21000 x g, 4 °C for 1 h. The supernatant was diluted with resuspension buffer to lower the detergent concentration to 0.8%, and then combined with 400 µl pre-equilibrated Rho-1D4 bead slurry (monoclonal Rho-1D4 antibody (University of British Columbia) immobilised on cyanogen bromide-activated sepharose agarose (GE Healthcare), preparation described in section 2.7). The protein was allowed to bind for 1.5 h at 4 °C before removing unbound material by centrifugation at 500 x g, 10 min at 4 °C. The resin was washed four times with 1 ml 300 mM NaCl, 3 mM $CaCl_2$, 10 mM HEPES-NaOH pH 7.2 and 0.007% (w/v) 20:1 DMNG:CHS, incubating the beads with buffer 10 min at 4 °C and centrifuging the resin as described above for every step. At this point, reconstitution into nanodiscs was performed

while the protein was still bound to Rho-1D4 resin. This method was performed as described previously (159-161). Briefly, washing buffer was added to the resin pellet to reach 1 ml and the beads were resuspended gently. To this mix, 100 µl of BBE:POPC lipid mix (preparation described in section 2.8) was added and incubated rotating for 30 min at 4 °C. Rho-1D4 resin was pelleted as described above, and 500 µl of the supernatant was removed. Subsequently, 100 µl 5 mg/ml MSP1D1 belt protein solution in 150 mM NaCl, 3 mM $CaCl_2$, 10 mM HEPES-NaOH pH 7.2 was added and left incubating for further 30 min. In order to promote nanodisc formation, the mixture was combined with pre-equilibrated BioBeads SM-2 (Bio-Rad, Cat. No. 152-8920) for 2 h at 4 °C with gentle rotation. After reconstitution into nanodiscs, the Rho-1D4 beads were subjected to further washing steps to remove residual detergent and any empty nanodiscs generated by the excess lipids and MSP1D1 belt protein. The washing steps were carried out as described above, in the absence of detergent. After removing the supernatant from the last washing step, GluD2 was eluted by addition of 150 mM NaCl, 3 mM $CaCl_2$, 10 mM HEPES-NaOH pH 7.2 supplemented with 5 mM TETSQVAPA peptide (Genscript). Monodispersity was analysed by SEC using a Superose 6 3.2/300 column pre-equilibrated in 150 mM NaCl, 3 mM $CaCl_2$, 10 mM HEPES-NaOH pH 7.2, attached to a high-performance liquid chromatography system (HPLC, Shimadzu).

2.10 Preparation of GluD2 single particle cryo EM grids

GluD2 reconstituted into MSP1D1 nanodiscs was concentrated using centrifugal concentrators (500 µl, 100 kDa MWCO) to reach 0.7 mg/ml (nanodrop reading at 280/260 nm). Prior to EM grid preparation, protein samples were spun down to remove large aggregates. Blotting and plunge freezing was performed using a Leica GP2 plunger, set to 10 °C and 95% humidity. 3.5 µl sample were pipetted on UltrAu Foil Gold support 1.3/1.2 grids (Quantifoil) previously glow-discharged for 1 min at 30 mA (Pelco easiGlow), blotted

for 3-5 seconds from the front and plunge frozen into liquid ethane kept at -180 °C. Samples were stored in liquid nitrogen. Alternatively, Quantifoil Cu 1.2/1.3 grids (300 mesh) coated with a 2 nm-thin layer of amorphous carbon were used. These were glow-discharged for 7 s at 35 mA and 3 µl of sample at 0.13 mg/ml were applied to the grids. For the preparation of grids for GluD2 in complex with nanobodies, a 1,5-fold molar excess of nanobody was mixed with GluD2 30 min prior to plunge freezing.

2.11 Single particle cryo EM data collection

Cryo EM data were collected on a Titan Krios IV (ThermoFisher) microscope operating at 300 keV and equipped with a Falcon 3EC direct detector and Volta phase plate (162). Automated data collection was performed using the EPU software (ThermoFisher). Micrographs were collected at a nominal magnification of 75,000x, resulting in a pixel size of 1.07 Å/pixel. Each movie contained 75 frames collected at a dose rate of 0.55 e^-/pix/sec over 60 s, resulting in a total dose of ~ 30 e^-/Å. All datasets presented in this thesis were collected over 24-h sessions, resulting in 381 micrographs for the GluD2-Nb399 (free-standing ice) dataset, 327 micrographs for the GluD2 *apo* (free-standing ice) dataset, and 399 micrographs for the GluD2-Nb381 (continuous carbon) dataset.

2.12 Single particle cryo EM data processing

Cryo EM movies were motion corrected, aligned and dose-weighted with MotionCor2 using a 5 x 5 patch (163). Contrast transfer function (CTF) fitting, defocus and phase-shift estimation was done with Gctf (164), using non-dose-weighted, motion-corrected micrographs. Particle picking was performed in automated manner in RELION 3.0.6 (165, 166) or in semi-automated manner with e2boxer from the EMAN2 package (167). Picked particles where manually inspected prior to further processing. Selected particles (128,508

for GluD2-Nb399, 54,372 for GluD2 *apo*, 100,938 for GluD2-Nb381) were then 2 x binned, resulting in a pixel size of 2.14 Å/pix and subjected to reference-free 2D classification in RELION 3.0.6. In total, 3 rounds of 2D classification where performed and classes that did not contain recognizable GluD2 features were removed. Six representative 2D class averages were employed to generate an initial 3D reference within RELION 3.0.6, which was subsequently low-pass filtered to 60 Å and used as a template for 3D classification rounds. 3D classification was carried out in RELION 3.0.6, using a mask diameter of 260 Å and an angular sampling interval of 7.5°. Owing to the low resolution of the 3D classes obtained, no further processing was performed on the datasets described in this thesis.

2.13 Sf9 cell clustering assay

Sf9 insect cells were cultured at 27ºC, shaking at 150 RPM in conical flasks in serum free SF900II medium (Gibco). The culture density was kept between 3,5 x 10^5 and 1 x 10^6 cells/ml. RPTPμ-mVenus (UniProt ID P28827-2, Residues 1-1465) was overexpressed using a baculoviral system based on pFastBac vectors. Cultures at 1 x 10^6 cells/ml were infected by addition of P2 viral stock (1:500 dilution of P2 stock). Expression of RPTPμ was monitored by observing fluorescence by mVenus and cell-aggregation due to trans-dimerization of RPTPμ. Approximately 19 h after infection, a 1:5 dilution of the cell suspension was seeded on Quantifoil R2/1 Au G200F1 finder grids pre-coated with 0,01 mg/ml fibronectin. Cells were left to adhere to grids for 24-48 h prior to plunge freezing as described in section 2.15.

2.14 Resin embedding, sectioning and CLEM imaging of Sf9 cells

Correlative light and electron microscopy (CLEM) experiments were essentially carried out as described by Ader *et al*. (168). Sf9 insect cells growing in suspension at a cell density of

1 x 10^6 cells/ml were infected by addition of RPTPμ-mVenus (UniProt ID P28827-2, Residues 1-1465) P2 baculoviral stock (1:500 dilution of P2 stock). 19 h post infection, Sf9 cell clumps were seeded on sapphire disks previously coated with 0,01 mg/ml fibronectin. 48 h after seeding, cells on sapphires were high-pressure frozen and then subjected to freeze-substitution with Lowicryl, following procedures published previously (168, 169). Lowicryl blocks with embedded cells were sectioned to 300 nm slices and transferred to EM grids. Fluorescent microspheres (50 nm TetraSpecks, Invitrogen) were added to the slices in order to aid correlation between light and electron microscopy images. Resin sections of Sf9 cells were first documented under a fluorescence microscope, acquiring data from DIC, far red (TetraSpecks) and green (EGFP-RPTPμ) channels. Next, gold fiducials of 20 nm were added to resin sections in order to aid the tomogram reconstruction. Areas of interest identified by light microscopy were documented using a Tecnai F20 electron microscope (ThermoFisher) operating at 200 keV. Low magnification images at 100 μm defocus were stitched together to form a map of the cell of interest. Tomograms of features of interest were collected in STEM mode, at a 1.1 nm/pixel pixel size and acquiring unidirectional tilt-series from -60 to 60 degrees using SerialEM (170). Tomograms were reconstructed using ETOMO from IMOD, and Matlab CLEM algorithms from Martin Schorb (EMBL) were used to correlate images from fluorescence and electron microscopes, as described previously (169).

2.15 Plunge freezing of RPTPμ-induced cell clusters

Prior to plunge freezing, a full fluorescent grid scan was performed using a ZEISS Axio Observer fluorescent microscope. Subsequently, grids were plunge frozen using either a manual plunger or a Leica GP2 plunger. When the Leica GP2 plunger was used, the chamber was maintained at 10 °C and 90 % humidity. Prior to plunge freezing in liquid ethane, 4 μl

of medium was applied to the front of the grids, followed by back-sided blotting for 8 seconds. Vitrified grids were stored in liquid nitrogen until transfer for FIB milling.

2.16 Focused Ion Beam Milling

Focused ion beam (FIB) milling was performed with a Scios FIB-SEM microscope (ThermoFisher), following recommendations by Schaffer *et al* (171). Plunge frozen grids were clipped under liquid nitrogen into ThermoFisher autogrids, mounted on a homemade transfer shuttle (172) and transferred into the FIB-SEM chamber using a Quorum cryo-transfer system. To ensure a constant temperature below -180 °C, a custom-built 360° rotatable cryo-stage cooled by an open nitrogen circuit (173) was used during operation. Prior to FIB milling, samples were coated with a layer of organometallic platinum using a gas injection system (ThermoFisher), with the purpose of protecting the milling front and reducing curtaining artefacts. Lamellae were prepared by targeting cell contacts, aided by fluorescent grid scans taken before plunge freezing. The gallium ion beam was operated at 30 kV and rectangular patterns were milled with progressively decreasing beam currents (0.3 nA for the first, rough steps, and then 0.1 nA, 50 pA and 30 pA for thinning and polishing steps). Thickness and homogeneity of the lamellae were estimated by observing charging effects in the SEM operated at 5 kV (171). Lamellae were produced at an angle of 10-13° (effective angle between the ion beam and the grid surface) and imaged using the SEM at 5-10 kV and 5-50 pA.

2.17 Rebuffering and BSA-coating of gold nanoparticles

975 µl of 5 nm gold nanoparticles (BBI solutions, EM.GC5, $9x10^{10}$ particles/ml) were combined with 25 µl of 200 mM NaH_2PO_4 pH 5.0 and 50 µl of 5 mg/ml Bovine Serum Albumine (BSA, Sigma, dissolved in 5 mM NaH_2PO_4 pH 5.0). The mixture was incubated

rotating overnight at 4 °C. Gold nanoparticles were collected by centrifugation using a TLA55 rotor (Beckman) at 35000 rpm, for 1 h at 4°C. Supernatant was removed and gold nanoparticles resuspended in 1 ml of 150 mM NaCl, 20 mM HEPES-NaOH pH 7.5. The gold nanoparticles were pelleted and resuspended two more times as described above. The final rebuffered stock of nanoparticles was kept at 4 °C.

2.18 Preparation of unilamellar liposomes

For the production of liposomes, a mixture of 95 % egg L-α-phosphatidylcholine (Egg PC, Avanti Polar Lipids, Cat. No. 840051C) and 5 % 18:1 1,2-dioleoyl-sn-glycero-3-[(N-(5-amino-1-carboxypentyl)iminodiacetic acid)succinyl] (nickel salt)) (DGS-NTA(Ni), Avanti Polar Lipids, Cat. No. 790404C) was prepared. 1 ml of the PC chloroform stock (10 mg/ml) were combined with 144 µl of the DGS-NTA(Ni) chloroform stock (5 mg/ml) in a round-bottom glass flask. Chloroform was evaporated under a nitrogen gas flow under constant swirling, until the lipids formed a thin and even film. Full evaporation of chloroform was achieved by using a vacuum desiccator overnight. Lipids were allowed to swell in 2.2 ml of 150 mM NaCl, 20 mM HEPES-NaOH pH 7.5 for 1 h at room temperature (achieving a final lipid concentration of 5 mg/ml). Resuspension of lipids was achieved by submersion in an ultrasonic bath for 15 min. The lipid mix was transferred to microcentrifuge tubes and liposomes were formed by 10 freeze-thaw cycles using liquid nitrogen and a water bath kept at 42 °C. The resulting stock was flash frozen in liquid nitrogen and stored long term at -80 °C. To obtain homogenous and unilamellar liposomes, 200 µl of lipid stock was extruded immediately before sample preparation. The extruder was kept at 65 °C and the lipids were passed 21 times through a 100 nm or 400 nm pore membrane.

2.19 EM sample preparation of RPTPμ-decorated liposomes

For the preparation of RPTP-decorated liposomes, 2 µl of extruded liposomes (at 5 mg/ml, see above) were combined with 31 µl of 150 mM NaCl, 20 mM HEPES-NaOH pH 7.5 and 7 µl of RPTPμ extracellular region (at 4.7 mg/ml). The mixture was incubated for 0, 15, or 30 min at room temperature before the preparation of EM grids. Immediately before freezing EM grids, 0.5 µl of 5 nm gold nanoparticles was added to the sample and mixed thoroughly. A Leica GP2 plunger was used to prepare cryo EM grids. Gold R 2/1 G200 grids with a carbon support (Quantifoil) were glow-discharged for 1 min at 30 mA. 3.5 µl of sample was applied to the front face of these grids, while 1 µl of buffer was applied to the back face, to ensure efficient back-side blotting. The blotting chamber was kept at 95 % humidity and 15 °C, the adsorption time of the sample on the grid was 30 s to 90 s and back-sided blotting time was set to 4 s to 6 s. Cryo EM grids were stored in liquid nitrogen.

2.20 Cryo-EM tomography data acquisition

For data acquisition of cryo-FIB milled lamellae, cryo-TEM imaging was performed on a Tecnai TF30 “Polara” Microscope (ThermoFisher) operating at 300 keV. The microscope was equipped with a Quantum post-column Gatan energy filter operating in zero-loss mode with a 20 eV wide slit. Data was recorded on a K2 Summit direct electron detector (Gatan) in counting mode. Tilt-series were collected with SerialEM (170), using a bi-directional data acquisition scheme and a tilt increment of 3°. The typical tilt range covered between -50° and 60° and data were acquired at a target defoci between -5 and -2 µm, with a pixel size of 3.42 Å/pix or 4.22 Å/pix and a total dose of 60-100 $e^-/Å^2$. During tilt-series acquisition of cryo-FIB lamellae, the 10-13° pre-tilt resulting from the milling angle was considered, so that the acquisition was bi-directional from 0° in respect to the sample. In addition, particular

efforts were made to align the tomographic tilt axis parallel to the pre-tilt axis of the lamellae to prevent tracking and focusing errors.

For data acquisition of liposomes decorated with RPTPμ, cryo-TEM imaging was performed on a Titan Krios microscope (ThermoFisher) operating at 300 keV. The Titan Krios microscope was equipped with a Quantum post-column energy filter (Gatan) operating in zero-loss mode with a 20 eV wide slit. TEM imaging was carried out with a K2 Summit direct electron detector (Gatan) operating in counting mode. Tilt-series were acquired using SerialEM and applying a dose-symmetric acquisition scheme, as described previously by Hagen *et al*. (174). Tilt-series usually covered a range from -60° to 60°, with a 3° tilt increment. Data was recorded with 6 frames per tilt, at a pixel size of 1.08 Å/pix, targeting a defocus range of -5 and -2 μm and with a total dose of about 140 $e^-/Å^2$. AutoCTF (ThermoFisher) was used for Coma-free alignment and objective astigmatism correction.

2.21 Image processing and tomogram reconstruction

Individual frames acquired for each tilt were aligned and combined using the 'alignframes' command from IMOD (175). Tilt-series were inspected manually, "bad" tilts were discarded (for example tilts with large objects obscuring the field of view) and the tilts were dose-filtered according to the cumulative radiation dose (176). Tilt-series alignment and tomographic reconstruction were performed using the IMOD package (175). Due to the lack of gold nanoparticles as fiducial markers in lamellae thinned by FIB, alignment of tilt-series projection images was performed with IMOD patch tracking or by using dirt, ice or spherical biological structures as fiducial markers. For the tilt-series collected from liposomes decorated with RPTPμ, gold fiducials were used for alignment. Contrast transfer function (CTF) parameters were estimated using CTFFIND4 (177) on non-dose-weighted micrographs and CTF correction was performed using the 'ctfphaseflip' command from

IMOD (175). Reconstruction of tomograms was done by weighted back-projection in IMOD, using the CTF-corrected stacks. Volumes were visualized in UCSF Chimera (156) or 3DMOD of IMOD (175). Tomogram segmentation was carried out in Amira (ThermoFisher). Dimitry Tegunov's deconvolution filter was used to improve tomogram contrast for the preparation of **Figure 5-11** (178).

2.22 Subtomogram averaging

For subtomogram averaging, tomograms of FIB-milled lamellae containing either a cell contact or a regular membrane stack were subjected to 4x binning. Initial subtomogram positions were defined using the Dynamo package (179), which allows for the modelling of surfaces *via* a triangulation algorithm. Surfaces were traced in the middle between apposing membranes, such that the derived subtomogram centres were placed at the middle of a RPTPμ *trans* dimer. Subsequently, subtomograms were extracted with a box size of 48 pixels, allowing for the incorporation of the apposing membranes. Further subtomogram averaging, aligning and visualization steps were also carried out within Dynamo (179). As a first step, an alignment with a translation search in *z* was carried out to align the subtomograms in respect to the plasma membranes. An average of 50 subtomograms, low-pass filtered to 50 Å was used as a reference. This initial step resulted in a subtomogram average with very clear densities for both apposing membranes. The two lines of higher density observed in the raw tomograms were also visible in the initial subtomogram average. In subsequent steps, a soft-edged mask was used to exclude the membranes from the alignment, with the purpose to focus the alignment on the protein features. Because the length of the RPTPμ extracellular region dimer is almost equivalent to the distance between membranes, we concluded that the trans-adhesive complexes must be perpendicular to the membrane, with little room for sampling oblique angles. Because of this, multilevel angular

searches were carried out sampling a narrow cone aperture and using fine angular increments. Later stages of subtomogram averaging involved fine azimuthal rotation searches and tighter alignment masks. A distance cut-off filter was applied to remove any oversampled and duplicated particles. Because the data did not reach convergence at the time of writing, further alignments with non-binned data were not carried out.

2.23 Expression and purification of RPTPμ D1-D2 tandem constructs and RACK1

RPTPμ cytoplasmic domain and RACK1 constructs were cloned into the pFastBac vector for baculoviral expression. RPTPμ constructs were based on UniProt entry P28827-1, and boundaries were determined by secondary structure predictions and alignment to other RPTP cytoplasmic domain structures. Three ranges were selected: RPTPμ$^{777\text{-}1452}$, RPTPμ$^{859\text{-}1452}$, RPTPμ$^{879\text{-}1452}$, all including both D1 and D2 phosphatase domains and various lengths of the juxta-membrane domain. Various constructs were generated, in which the proteins were flanked C- or N-terminally by a TEV-protease cleavage site and a 6x His-tag. The RACK1 construct was based on UniProt entry P63244-1, comprising residues RACK1$^{1\text{-}317}$. Generation of bacmids was achieved by transformation of pFastBac plasmids into DH10Bac *E. coli* (ThermoFisher) cells. Blue/white colony selection was used to identify colonies containing the recombinant bacmid. The bacmid DNA was isolated following manufacturer's instructions (Bac-to-Bac Baculovirus System manual, ThermoFisher) and used to generate P1 viral stocks. For this purpose, 0.5 x 10^6 Sf9 cells in serum-free Sf9 Lonza medium were seeded in each well of a 6-well dish and allowed to settle at 28 °C. In the meantime, 250 μl of serum-free Lonza medium were mixed with 5 ng of bacmid DNA. In parallel 250 μl of serum-free Sf9 Lonza medium were combined with 10 μl of FuGene HD transfection reagent (Promega). The DNA and FuGene mixes were combined and left to

incubate for 20 min at room temperature. After corroborating the attachment of Sf9 cells, the medium was removed and replaced by 1 ml of the transfection mix. After 24 h, each well was topped up with an additional 1 ml of serum-free Sf9 Lonza medium. Expression of proteins and production of P1 virus was maintained for 5 days. The medium was stored (P1 viral stock) and adherent cells were lysed and protein expression levels were analysed by Western Blot using anti-His antibodies. 500 µl P1 viral stock were used to infect 50 ml 0.5 x 10^6 cells/ml Sf9 cells. After 72 h, the medium was collected by centrifugation at 1000 x g, 15 min at room temperature and stored (P2 viral stock). For large-scale protein expression, 2 l of Sf9 insect cells at 2 x 10^6 cells/ml were infected with 20 ml of P2 viral stock. Expression was maintained for 72 h and cells were harvested by centrifugation at 5000 rpm, 30 min at 4 °C. For long term storage, cell pellets were flash frozen in liquid nitrogen and stored in -80 °C. For protein purification, the pellet from 1 l Sf9 cell culture was thawed and resuspended in 20 ml ice-cold lysis buffer (200 mM NaCl, 20 mM Tris-HCl pH 7.5, 1 mM TCEP, supplemented with protease inhibitors (Sigma)). Cells were lysed by sonication on ice, operating the probe at 40% intensity, using a 5 s on, 10 s off pulse, for a total sonication time of 10 min. Cell lysate was cleared by centrifugation at 20000 x g, 4 °C for 1 h. The supernatant was combined with 4 ml pre-equilibrated Ni-NTA resin slurry (Qiagen) and incubated for 1 h at 4 °C, with gentle rotation. Ni-NTA resin was pelleted at 1000 rpm, 4 °C for 5 min and the supernatant was discarded. Resin was washed with lysis buffer supplemented with increasing concentrations of imidazole (20, 50, 100 and 200 mM). Bound protein was eluted by addition of 200 mM NaCl, 20 mM Tris-HCl pH 7.5, 1 mM TCEP, 500 mM imidazole. Imidazole concentrations were reduced by buffer exchange using a centrifugal filter. Protein samples were subjected to cleavage by TEV protease overnight, at 4°C, using a 1:50 w/w ratio of home-made protease. Undigested protein and contaminants were removed by reverse Ni-affinity chromatography. Fractions were analysed by SDS-

PAGE and those containing the protein of interest were concentrated to 2 ml for injection on a Superdex 200 16/600 column (GE Healthcare), previously equilibrated in 100 mM NaCl, 20 mM Tris-HCl pH 7.5, 1 mM TCEP.

2.24 Purification and crystallization of RPTPμ D1D2 constructs

Pure RPTPμ D1-D2 samples were concentrated to 8 mg/ml using centrifugal filters. Protein aggregates were removed by centrifugation at 13500 x g at 4 °C for 30 min. 300 nl drops in 1:1 and 1:2 (protein : mother liquor) ratios were set in sitting drop vapour diffusion format using a Mosquito robot (TTB Labtech). Crystals appeared after 3-5 days, in 10% w/v PEG 4000, 20 % v/v glycerol, 0.02 M Monosaccharides mix, 0.1 M MES/imidazole pH 6.5 (Morpheus Screen, Well F3). All crystals were cryoprotected in their mother liquor supplemented with 30% ethylene glycol (final concentration) and flash frozen in liquid nitrogen.

3. Generation and characterization of nanobodies against GluD2, Cbln1 and β-Nrx1

3.1 Aims of this chapter

Nanobodies are stable, 15 kDa, single-domain fragments derived from camelid heavy chain-only antibodies. Due to their shape and ability to bind to clefts on the surface of proteins *via* their complementarity-determining region 3 (CDR3) loop, nanobodies are ideally equipped to recognize different protein conformations or binding interfaces of protein complexes. Their potential as crystallization chaperones and as stabilizing tools for cryo-EM studies has been widely recognized (159, 160, 180-182). We set out to generate nanobodies against the GluD2-Cbln1-β-Nrx1 triad with the aim to obtain tools that would a) stabilize the complex and b) allow us to probe different conformations that are physiologically relevant for signal transduction.

3.2 Generation of nanobodies against GluD2, Cbln1 and β-Nrx1

In collaboration with Prof Jan Steyaert's laboratory at Vrije Universiteit Brussel (VUB), llama immunizations were carried out using samples of a) GluD2$^{\Delta C\text{-}ter}$ and b) the GluD2$^{\Delta C\text{-}ter}$ -Cbln1-β-Nrx1^{+SS4} triad. The protein samples for these injections were prepared by Dr Ester Behiels and Dr Jonathan Elegheert. Subsequent selection of antigen binders by phage display was carried out using three samples: a) GluD2$^{\Delta C\text{-}ter}$, b) Cbln1-βNrx^{+SS4} and c) GluD2$^{\Delta C\text{-}ter}$ -Cbln1-βNrx^{+SS4}. Screening by phage display resulted in the identification of 9 nanobodies against GluD2$^{\Delta C\text{-}ter}$, 19 nanobodies against the GluD2$^{\Delta C\text{-}ter}$ -Cbln1-βNrx^{+SS4} triad and 5 nanobodies against the Cbln1-βNrx^{+SS4} complex (**Table 3-1**). 4 nanobodies were selected during screening with both GluD2$^{\Delta C\text{-}ter}$ and the GluD2$^{\Delta C\text{-}ter}$ -Cbln1-βNrx^{+SS4} triad. The nanobody amino acid sequences can be found in the appendix, **Figure 8-10** and **Figure 8-11**. For simplicity, hereon all nanobodies will be named after their last three digits only (e.g. Nb399 for Nb CA11399).

In order to characterize the library of nanobodies, I produced the total of 37 nanobodies through bacterial periplasmic expression and purification over affinity chromatography (see Materials & Methods, section 2.2). All nanobodies produced medium to high yields, resulting in 1 to 10 mgs of protein from 500 ml *E. coli* culture.

With the aim to determine the nanobody specificity against different domains of the GluD2-Cbln1-βNrx1 triad, I also prepared samples of the GluD2 extracellular region, ATD and LBD soluble domains, and of the Cbln1 C1q domain. The soluble GluD2^{LBD} construct was designed following a similar strategy used previously for other iGluRs and for GluD2 (62), where the linkers to the M1 and M2 transmembrane helices are cleaved and fused *via* a Gly-Thr linker. Soluble GluD2 and Cbln1 proteins were expressed using a mammalian expression system (see Materials & Methods, section 2.2) and purified over affinity and size-exclusion chromatography.

3.3 Biolayer interferometry reveals high-affinity GluD2 binders

Biolayer interferometry was used to determine the binding specificity and approximate affinity of the nanobodies. For this purpose, two kinds of experiments were conducted. First, biotinylated domains of GluD2 (LBD and ATD) and the C1q domain of Cbln1 were immobilized on streptavidin biosensors and dipped into 1 μM nanobody solutions to determine their specificity against these individual domains. This experiment had the purpose to serve as a coarse screening method to narrow down the specificity of the nanobodies. **Table 3-1** contains an overview of these results. Most nanobodies raised against GluD2 bind either the ATD or LBD domains. Nb663 binds to the C1q domain of Cbln1.

Next, single-cycle kinetics experiments were performed, where either biotinylated GluD2$^{\Delta C\text{-}ter}$ or the Cbln1-βNrx1^{+SS4} complex were immobilized on streptavidin biosensors and dipped into increasing concentrations of nanobody to determine binding affinity and kinetics. Single-cycle kinetics experiments are considered less precise than parallel sensor kinetics, because single sensors are more susceptible to drift given the longer measurement times. Nevertheless, this experimental setup allowed for the high throughput characterization of nanobodies and the quick identification of high affinity binders, which was the main objective of the experiment. The data resulting from the single-cycle kinetics experiments were analysed in MATLAB (MathWorks), using scripts written by Dr Suzanne Scott and Dr Sebastian Bonilla. The scripts fit a 1:1 binding model on the data, and the association and dissociation rates (k_{on} and k_{off}) are derived from the fit. The quality of the fit was assessed using the coefficient of determination R^2, where only fits with R^2 greater than 0.9 were considered.

Exemplary curves and fits for the single-cycle kinetics experiments can be seen in **Figure 3-1**, and the corresponding data is shown in **Table 3-2**. All binding curves can be seen in

the appendix (**Figure 8-5**, **Figure 8-6**, **Figure 8-7**, **Figure 8-8**, **Figure 8-9**) and the corresponding analysis are summarized in **Table 8-1** and **Table 8-2**.

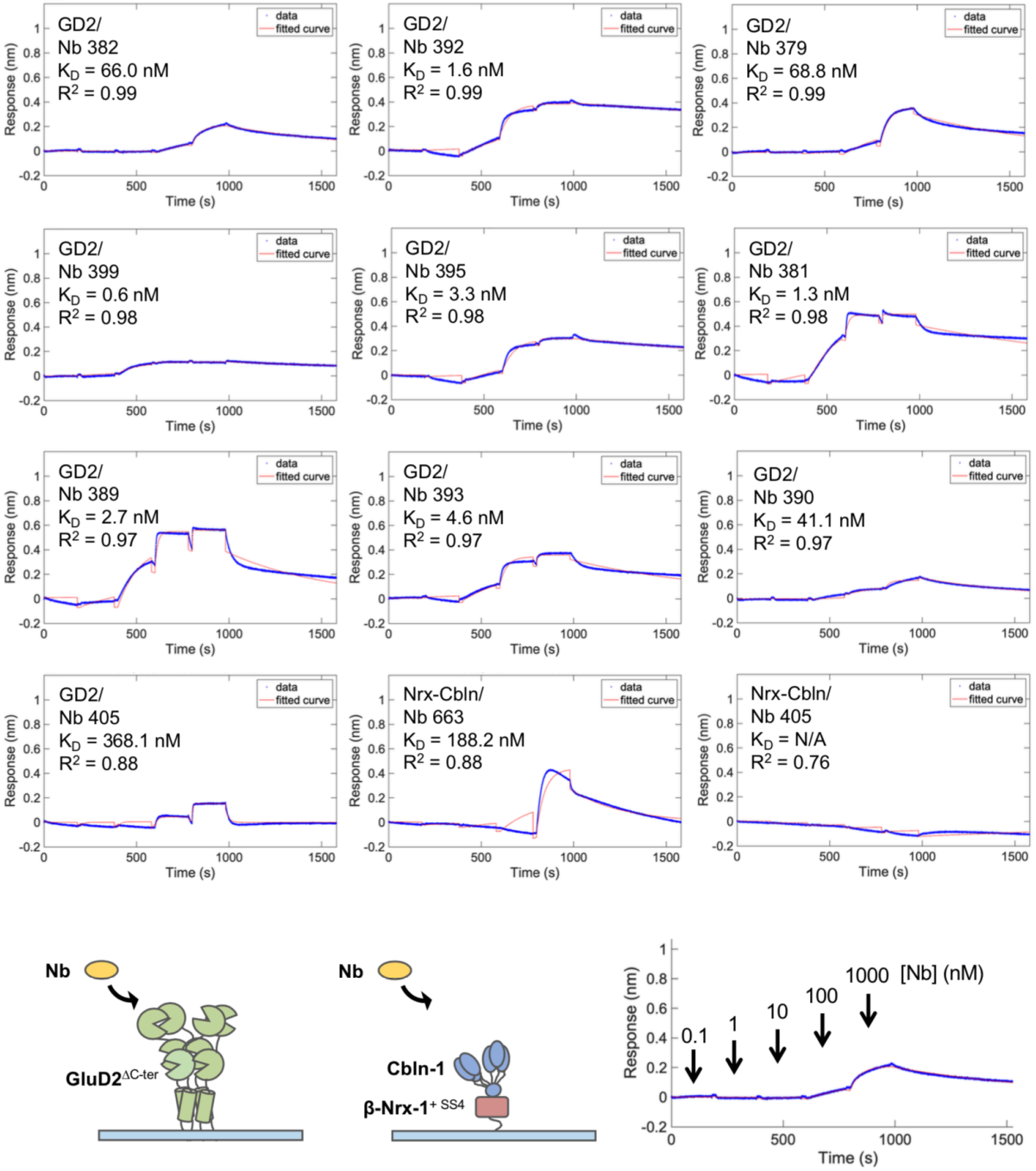

Figure 3-1 **Single-cycle kinetics experiments reveal tight binders against GluD2** Exemplary binding curves (blue data points) and fits (red traces) of single-cycle kinetics experiments, using Biolayer Interferometry. Biotinylated GluD2$^{\Delta C\text{-ter}}$ or Cbln1-βNrx-1^{+SS4} complex were immobilized on streptavidin-coated biosensors (see schematic overview at the bottom) and dipped into increasing concentrations of nanobody samples (0.1, 1, 10, 100, 1000 nM). k_{on} and k_{off} values were derived from the fits, and used to calculate the binding affinity (K_D) (see ***Table 3-2*** and appendix for all data).

Table 3-1* Summary of nanobody binding experiments against GluD2-βNrx1-Cbln1** Phage display screening resulted in 19 nanobodies being selected against the GluD2$^{\Delta C\text{-ter}}$ -Cbln1-βNrx1^{+SS4} triad, 9 against GluD2$^{\Delta C\text{-ter}}$ and 5 against the Cbln1-βNrx1^{+SS4} complex. 4 nanobodies were selected during screening of both GluD2$^{\Delta C\text{-ter}}$ and the GluD2$^{\Delta C\text{-ter}}$ -Cbln1-βNrx1^{+SS4} triad. A coarse screen using Biolayer Interferometry narrowed their specificity, and binders were identified against the GluD2 ATD and LBD domains and extracellular region, and against the Cbln1 C1q domain. K_D values were determined by single-cycle kinetics experiments (see ***Figure 3-1, ***Table 3-2*** and appendix). Nanobody complex formation was confirmed by size-exclusion chromatography. 'GluD2': GluD2$^{\Delta C\text{-ter}}$, 'Cbln': Cbln1, 'Nrx': βNrx1^{+SS4}.

Nanobody ID	Selected against (Phage Display)	Epitope (BLI screen)	K_D (nM) (α GluD2)	K_D (nM) (α Cbln-Nrx)	Co-elution in SEC
CA11379	GluD2	GluD2^{ATD}	68.8	Not tested	GluD2^{ATD}
CA11380	GluD2-Cbln-Nrx	GluD2^{ECTO}	2.6	No binding	GluD2^{ECTO}
CA11381	GluD2/ GluD2-Cbln-Nrx	GluD2^{ATD}	1.3	No binding	GluD2^{ATD}
CA11382	GluD2	GluD2^{LBD}	66.0	Not tested	Not tested
CA11383	GluD2/ GluD2-Cbln-Nrx	GluD2^{LBD}	157.6	No binding	GluD2^{LBD}
CA11384	GluD2-Cbln-Nrx	GluD2^{LBD}	10.0	No binding	GluD2^{LBD}
CA11385	GluD2/ GluD2-Cbln-Nrx	GluD2^{LBD}	151.2	Not tested	GluD2^{LBD}
CA11386	GluD2-Cbln-Nrx	GluD2^{ATD}	332.0	No binding	Not tested
CA11387	GluD2-Cbln-Nrx	GluD2^{ATD}	Poor fit	No binding	GluD2^{ATD}
CA11388	GluD2	GluD2^{ATD}	5.8	Not tested	GluD2^{ATD}
CA11389	GluD2-Cbln-Nrx	GluD2^{ATD}	2.7	No binding	GluD2^{ATD}
CA11390	GluD2	GluD2^{LBD}	41.1	Not tested	GluD2^{LBD}
CA11391	GluD2-Cbln-Nrx	GluD2^{LBD}	5.8	No binding	Not tested
CA11392	GluD2-Cbln-Nrx	GluD2^{LBD}	1.6	No binding	GluD2^{LBD}
CA11393	GluD2-Cbln-Nrx	GluD2^{LBD}	4.6	No binding	Not tested
CA11395	GluD2-Cbln-Nrx	GluD2^{LBD}	3.3	No binding	Not tested
CA11397	GluD2-Cbln-Nrx	GluD2^{LBD}	2.3	No binding	Not tested
CA11399	GluD2/ GluD2-Cbln-Nrx	GluD2^{LBD}	0.6	Not tested	GluD2^{LBD}
CA11400	GluD2-Cbln-Nrx	GluD2^{LBD}	Poor fit	No binding	Not tested
CA11402	Cbln-Nrx	No binding	Not tested	No binding	Not tested
CA11403	GluD2	No binding	No binding	Not tested	Not tested
CA11404	GluD2-Cbln-Nrx	No binding	No binding	No binding	Not tested
CA11405	GluD2-Cbln-Nrx	No binding	No binding	No binding	Not tested
CA11410	GluD2-Cbln-Nrx	GluD2^{LBD}	Poor fit	No binding	Not tested
CA11411	GluD2-Cbln-Nrx	GluD2^{LBD}	Poor fit	No binding	Not tested
CA11412	GluD2	GluD2^{ATD}	Poor fit	Not tested	Not tested
CA11413	GluD2-Cbln-Nrx	No binding	Poor fit	No binding	Not tested
CA11414	GluD2-Cbln-Nrx	No binding	Poor fit	No binding	Not tested
CA11415	GluD2-Cbln-Nrx	GluD2^{LBD}	277.5	No binding	Not tested
CA11416	GluD2	GluD2^{LBD}	121.0	Not tested	GluD2^{LBD}
CA11417	GluD2	No binding	Poor fit	Not tested	Not tested
CA11418	GluD2	GluD2^{LBD}	Poor fit	Not tested	Not tested
CA11419	Cbln-Nrx	No binding	Not tested	No binding	Not tested
CA11420	GluD2-Cbln-Nrx	No binding	Poor fit	No binding	Not tested
CA11661	Cbln-Nrx	No binding	Not tested	No binding	Not tested
CA11662	Cbln-Nrx	No binding	Not tested	No binding	Not tested
CA11663	Cbln-Nrx	Cbln1^{C1q}	Not tested	188.2	Cbln-Nrx

Of 32 nanobodies tested against GluD2, 10 were identified to be tight binders, with K_D values of 10 nM or lower. All these nanobodies bind either the ATD or LBD domains of GluD2. On the contrary, only one nanobody showed binding to the β-Nrx1(+SS4)-Cbln1 complex. Nb663 binds to the C1q domain of Cbln1 with an apparent affinity of 188.2 nM, however, the fit for this binding curve is poor (R^2 = 0.88), so the K_D value is likely inaccurate.

Table 3-2* Single-cycle kinetics results for nanobody binding experiments** Exemplary results for single-cycle kinetics experiments, using Biolayer Interferometry. Binding curves were fitted in MATLAB (see text and Materials & Methods, section 2.3) and association (k_{on}), dissociation (k_{off}) constants and R_{max} values were derived from the fits. K_D values were calculated using equation 2 (see Materials & Methods, section 2.3) and R^2 was determined in MATLAB to evaluate the quality of the fit. The results shown here are derived from the curves in ***Figure 3-1. All results and data can be found in the appendix.

Nanobody ID	Screened against	k_{on} ($M^{-1}s^{-1}$)	k_{off} (s^{-1})	R_{max} (nm)	K_D (nM)	R^2
CA11399	GluD2$^{\Delta C\text{-ter}}$	9.99E+05 ± 1.34E+04	5.65E-04 ± 1.12E-05	1.14E-01 ± 2.77E-04	**5.65E-01** ± 1.88E-02	0.98
CA11381	GluD2$^{\Delta C\text{-ter}}$	5.95E+05 ± 6.93E+03	7.52E-04 ± 1.51E-05	4.98E-01 ± 1.29E-03	**1.26E+00** ± 4.00E-02	0.98
CA11392	GluD2$^{\Delta C\text{-ter}}$	1.72E+05 ± 2.54E+03	2.76E-04 ± 8.88E-06	3.85E-01 ± 1.08E-03	**1.61E+00** ± 7.57E-02	0.99
CA11389	GluD2$^{\Delta C\text{-ter}}$	6.77E+05 ± 9.05E+03	1.84E-03 ± 2.85E-05	5.63E-01 ± 1.71E-03	**2.72E+00** ± 7.86E-02	0.97
CA11395	GluD2$^{\Delta C\text{-ter}}$	1.51E+05 ± 2.45E+03	5.05E-04 ± 1.25E-05	2.98E-01 ± 1.15E-03	**3.34E+00** ± 1.37E-01	0.98
CA11393	GluD2$^{\Delta C\text{-ter}}$	2.51E+05 ± 4.63E+03	1.15E-03 ± 1.74E-05	3.59E-01 ± 1.26E-03	**4.58E+00** ± 1.54E-01	0.97
CA11390	GluD2$^{\Delta C\text{-ter}}$	4.14E+04 ± 1.09E+03	1.70E-03 ± 1.67E-05	1.51E-01 ± 8.75E-04	**4.11E+01** ± 1.49E+00	0.97
CA11382	GluD2$^{\Delta C\text{-ter}}$	2.04E+04 ± 2.70E+02	1.35E-03 ± 7.76E-06	2.23E-01 ± 9.57E-04	**6.60E+01** ± 1.25E+00	0.99
CA11379	GluD2$^{\Delta C\text{-ter}}$	2.10E+04 ± 3.26E+02	1.44E-03 ± 1.14E-05	3.87E-01 ± 2.07E-03	**6.88E+01** ± 1.61E+00	0.99
CA11405	GluD2$^{\Delta C\text{-ter}}$	1.64E+05 ± 1.13E+04	6.03E-02 ± 3.39E-03	2.10E-01 ± 4.25E-03	**3.68E+02** ± 4.62E+01	0.88
CA11663	βNrx1^{+SS4}-Cbln1	1.90E+04 ± 8.85E+02	3.57E-03 ± 9.03E-05	5.18E-01 ± 1.15E-02	**1.88E+02** ± 1.35E+01	0.88
CA11405	βNrx1^{+SS4}-Cbln1	N/A	N/A	N/A	N/A	0.76

3.4 Nanobodies stabilize dimers and bind to domain interfaces

Next, I set out to confirm the interaction of the highest affinity binders *via* analytical size-exclusion chromatography (SEC). The extracellular region of GluD2 ($GluD2^{ECTO}$) co-eluted with Nb380, Nb388 and Nb390, $GluD2^{ATD}$ with Nb379, Nb380, Nb381, Nb387, Nb388 and Nb389 and $GluD2^{LBD}$ with Nb383, Nb384, Nb385, Nb390, Nb392, Nb399 and Nb416 (SEC profiles and SDS-PAGE data can be seen in appendix). As can be seen by SDS-PAGE analysis, the intensity of the bands corresponding to the nanobodies correlated with their binding affinity. High affinity binders resulted in strong bands co-eluting with GluD2 domains, while lower affinity nanobodies resulted in only faint bands. The only nanobody to co-elute with the Cbln1-βNrx1^{+SS4} complex was Nb663.

Some interesting features can be observed from the SEC data. For example, four nanobodies (Nb384, Nb390, Nb392 and Nb399) form a complex with $GluD2^{LBD}$ and elute earlier than complexes of $GluD2^{LBD}$ with Nb383, Nb385 or Nb416 (**Figure 3-2**). The elution volumes of these complexes suggest that these two classes of nanobodies are able to stabilize $GluD2^{LBD}$ in different conformational states by inducing its dimerization or maintaining a monomeric state. The exact oligomeric state will need to be established with a quantitative method (e.g. Size-Exclusion Chromatography-Multiangle Light Scattering (SEC-MALS)).

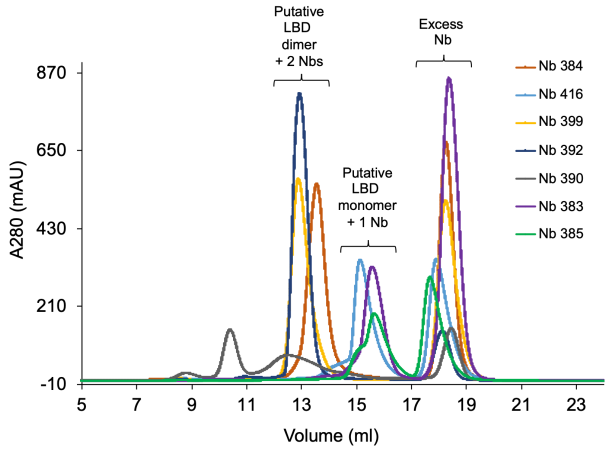

Figure 3-2 **Nanobodies alter the oligomeric state of the GluD2 ligand-binding domain** Overlay of size-exclusion chromatography elution profiles of $GluD2^{LBD}$ in complex with different nanobodies. Nanobodies 399, 392, 390 and 384 co-elute with putative LBD dimers, while nanobodies 416, 383 and 385 bind to putative LBD monomers. The corresponding SDS-PAGE results can be found in the appendix, **Figure 8-3**.

Another nanobody, Nb380, does not co-elute with isolated GluD2^{LBD} and shows only weak binding to GluD2^{ATD}. When combined with GluD2^{ECTO}, however, Nb380 results in a band of higher intensity, suggesting that the intact extracellular region of GluD2 is required for binding (**Figure 3-3**). It is likely that Nb380 binds to the interface between GluD2^{LBD} and GluD2^{ATD}, since this epitope is only available in the GluD2 full-length or GluD2^{ECTO} constructs.

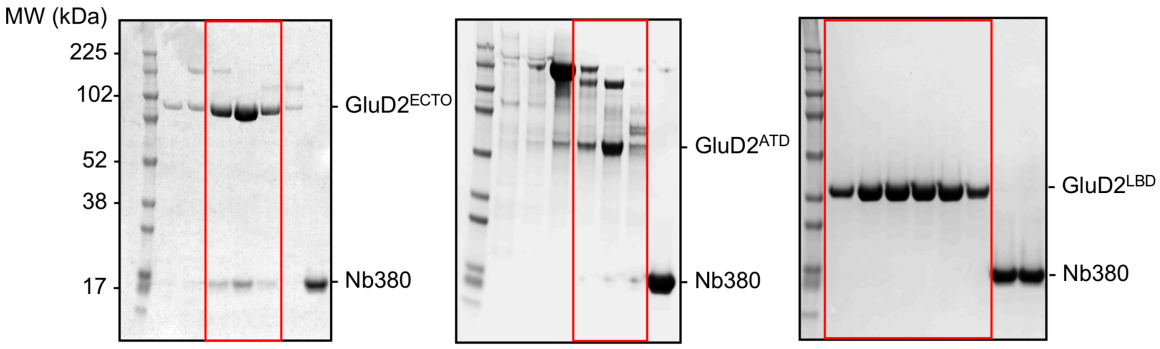

Figure 3-3 **Nanobody 380 binds to the extracellular region of GluD2, but not to the individual ATD or LBD domains** SDS-PAGE analysis from size-exclusion chromatography experiments of nanobody 380 in combination with the extracellular region of GluD2 (GluD2^{ECTO}), GluD2^{ATD} and GluD2^{LBD}. Corresponding elution profiles can be seen in **Figure 8-1**, **Figure 8-2** and **Figure 8-4** in the appendix. GluD2^{LBD} does not co-elute with Nb 380 (gel on the right, red box). GluD2^{ATD} weakly interacts with Nb 380 (gel in the middle, red box). GluD2^{ECTO} co-elutes with Nb 380 (gel on the left, red box).

3.5 Nanobodies act as crystallization chaperones

With the purpose to reveal the precise epitopes of the nanobodies, I next proceeded to obtain X-ray crystal structures of those nanobody complexes that were successfully obtained by analytical and preparative SEC. Well diffracting crystals were obtained for GluD2^{LBD} in complex with Nb390, Nb392 and Nb399 (**Figure 3-4**) and GluD2^{ATD} in complex with Nb381 and Nb389 (**Figure 3-5**) (the conditions in which these complexes were obtained are summarized in Materials and Methods, section 2.4). Phase information was obtained by molecular replacement using deposited structures of the GluD2^{LBD} in complex with D-Ser

(PDB ID 2V3U) and GluD2^{ATD} (PDB ID 5KC8), and of the general nanobody scaffold (PDB IDs: 5IMM and 5BOP) and models were refined to good statistics and geometries. More details about crystallographic data collection and refinement strategies can be found in Materials & Methods, section 2.5. The crystallographic data collection and refinement statistics are summarised in **Table 3-3**.

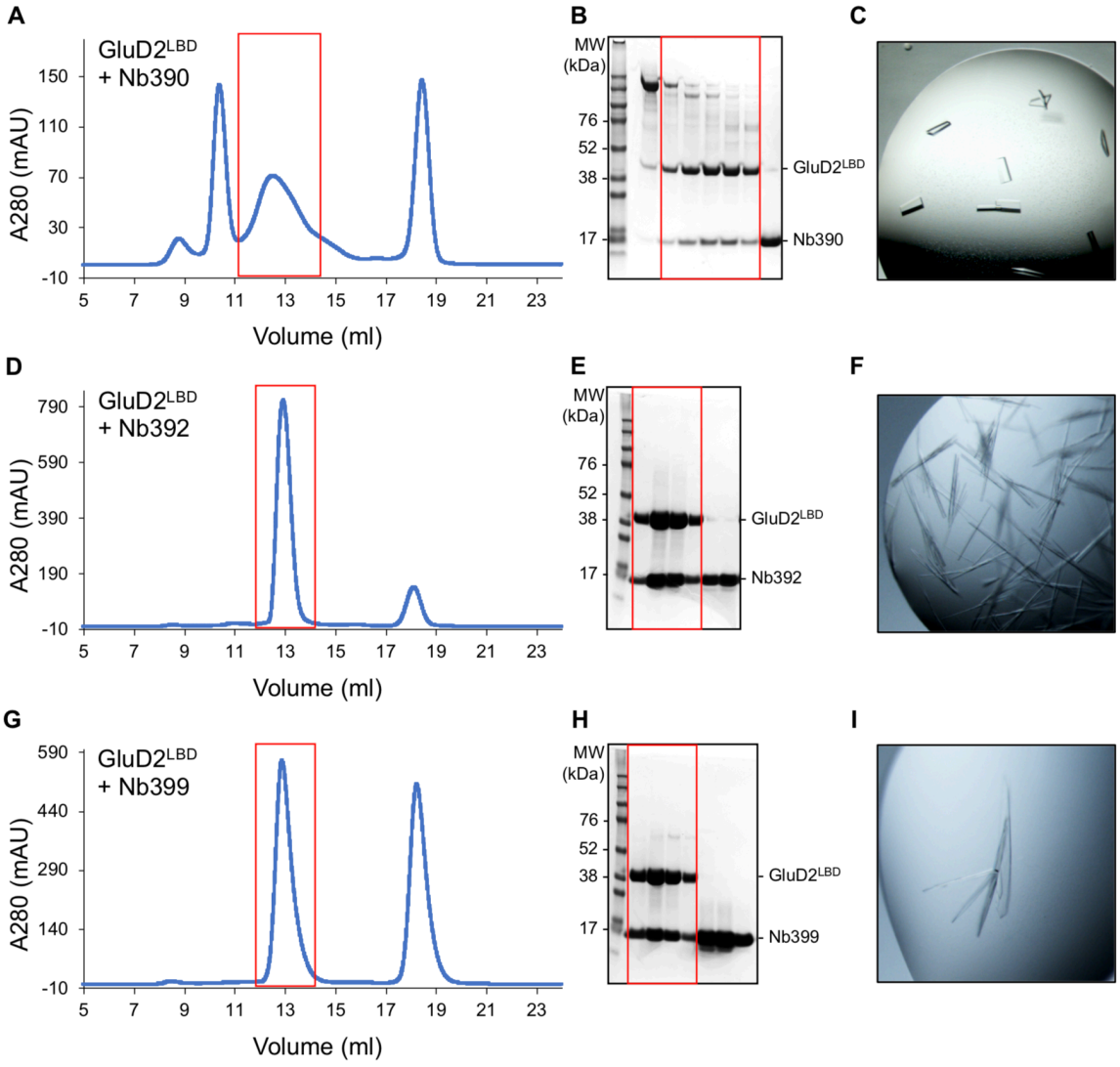

Figure 3-4 **Preparation and crystallization of GluD2^{LBD} – nanobody complexes** (**A**, **D**, **G**) Size-exclusion chromatography (SEC) profiles of GluD2^{LBD} complexes with nanobodies 390, 392 and 399. The peak in the red delineated box corresponds to the complex. The peak at ~18 ml corresponds to excess nanobody. (**B**, **E**, **H**) SDS-PAGE analysis of fractions from SEC runs shown in (A, D, G). Fractions within the red delineated box correspond to the GluD2^{LBD}-nanobody complexes. Numbers on the left of the gel represent the molecular weights in kDa of the protein weight standards. (**C**, **F**, **I**) Exemplary images of crystals resulting from crystallization trials using fractions highlighted in (B, E, H).

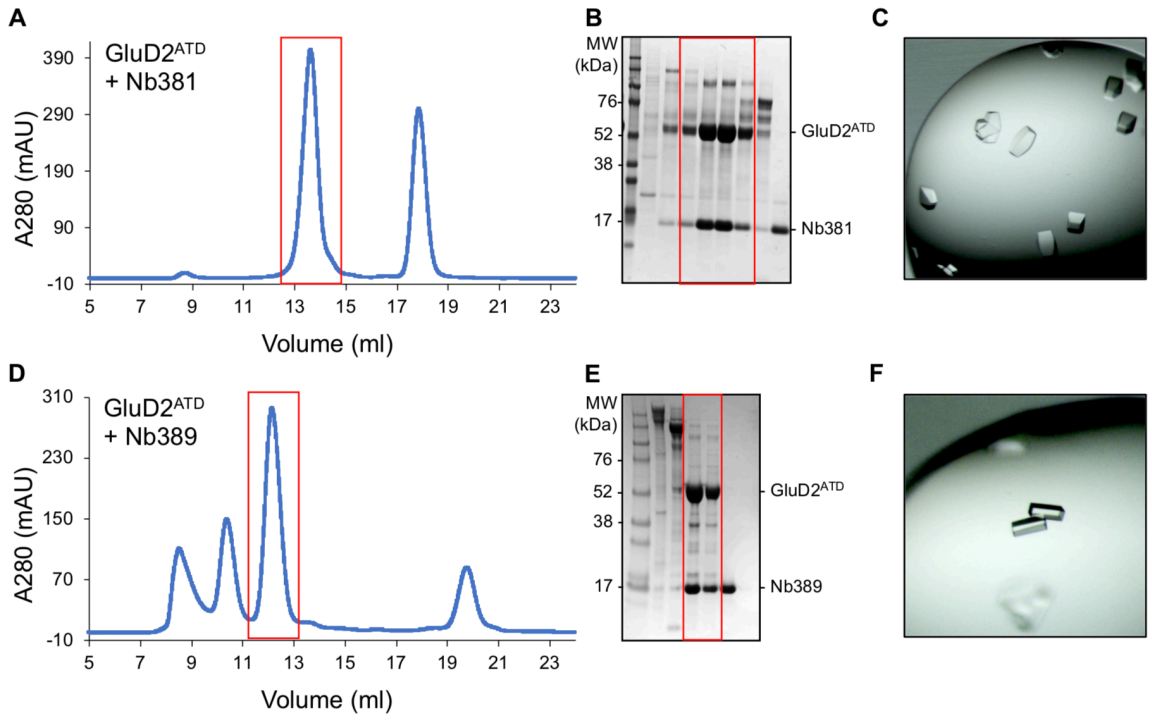

Figure 3-5 Preparation and crystallization of GluD2^{ATD} – nanobody complexes (**A**, **D**) Size-exclusion chromatography (SEC) profiles of GluD2^{ATD} complexes with nanobodies 381and 389. The peak in the red delineated box corresponds to the complex. The peak at 18-20 ml corresponds to excess nanobody. (**B**, **E**) SDS-PAGE analysis of fractions from SEC runs shown in (A, D). Fractions within the red delineated box correspond to the GluD2^{ATD}-nanobody complexes. Numbers on the left of the gel represent the molecular weights in kDa of the protein weight standards. (**C**, **F**) Exemplary images of crystals resulting from crystallization trials using fractions highlighted in (B, E).

3.6 GluD2 is locked in an active conformation by Nb399

The structure of GluD2^{LBD} in complex with Nb399 revealed a dimeric conformation, where one GluD2^{LBD} dimer is stabilized on each side of the interface by one copy of Nb399 (**Figure 3-6**). The GluD2^{LBD} dimerization interface is similar to that observed in the GluD2^{LBD} *apo* structure (PDB ID 2V3T), and most of the inter-molecular hydrogen bonds and salt bridges are maintained. The overall fold of GluD2^{LBD} presents a clamshell-like architecture as described previously for GluD2 (62) and as observed for other iGluRs. When an iGluR is activated, the binding of a ligand at the cleft of the LBD clamshell triggers the upward motion of the LBD lower lobe (D2), leading to the closure of the clamshell and the subsequent opening of the ion channel. In the co-crystal structure with Nb399, GluD2^{LBD} adopts a closed and active-like conformation, resembling the structure of GluD2^{LBD} in complex with its ligand, D-Serine (**Figure 3-7**). A superposition with the D-Serine bound

structure (PDB ID 2V3U) resulted in a root-mean-square (r.m.s) deviation on Cα-positions of 0.771 Å.

For AMPA receptors, the lower lobe upward motion angle (ranging from 20-26°) has been found to correlate with the extent of receptor activation and desensitization (183). In the structures reported by Naur *et al*. (62), a domain closure of 29.9° can be observed when comparing GluD2^{LBD} in its *apo* state and bound to D-Serine.

Table 3-3 **X-ray crystallography data collection and refinement statistics for GluD2-nanobody structures ([a])** Values in parentheses refer to the highest resolution shell. **([b])** Rmeas = ∑h [n/(n-1)]1/2 ∑i ⎪Ih - Ih,i⎪/ ∑h ∑i Ih,i; where Ih is the mean intensity of symmetry-equivalent reflections and n is the redundancy. **([c])** Rwork = ∑h ⎪Fo – Fc⎪/ ∑ Fo (working set, no σ cut-off applied). **([d])** Rfree is the same as Rcryst, but calculated on 5% of the data excluded from refinement.

	GluD2 ATD + Nb381	**GluD2 ATD + Nb389**	**GluD2 LBD + Nb390**	**GluD2 LBD + Nb392**	**GluD2 LBD + Nb399**
Data collection					
Beamline	DLS I03	DLS I03	DLS I03	DLS I04	DLS I04
Space group	$P\,4_32_12$	$P\,1$	$C\,2\,2\,2_1$	$P\,1$	$P\,1$
Wavelength (Å)	0.9762	0.9762	0.9795	0.9795	0.9795
Cell dimensions					
a, *b*, *c* (Å)	85.50, 85.50, 241.86	57.83, 94.91, 112.34	47.69, 138.55, 132.86	52.32, 92.39, 111.31	52.04, 92.94, 112.33
α, β, γ (°)	90.00, 90.00, 90.00	93.12, 90.05, 90.92	90.00, 90.00, 90.00	80.80, 84.08, 82.28	79.93, 83.68, 82.17
Resolution (Å) [a]	80.61-1.88 (1.91-1.88)	74.41-2.19 (2.27-2.19)	47.95-2.25 (2.29-2.25)	51.67-3.64 (3.70-3.64)	65.10-2.91 (2.96-2.91)
R_{merge} [a,b]	0.131 (2.249)	0.171 (1.372)	0.218 (1.506)	0.226 (0.540)	0.157 (0.741)
R_{pim}	0.038 (0.637)	0.110 (0.851)	0.092 (0.629)	0.141 (0.334)	0.157 (0.741)
I / σI [a]	10.41 (1.15)	4.84 (1.02)	7.75 (1.36)	6.18 (3.88)	3.96 (0.84)
Completeness (%) [a]	99.98 (99.95)	97.69 (90.17)	100 (99.71)	99.22 (96.95)	97.81 (97.76)
CC1/2 [a]	0.9947 (0.5880)	0.9621 (0.3011)	0.9915 (0.5068)	0.9397 (0.7475)	0.9715 (0.5581)
Multiplicity [a]	12.81 (13.38)	3.40 (3.46)	6.53 (6.65)	3.50 (3.51)	1.80 (1.85)
Unique reflections [a]	74053 (3668)	119457 (5180)	21392 (1048)	22644 (1145)	43855 (2178)
Refinement					
R_{work} [c] /R_{free} [d]	0.196/0.225	0.231/0.266	0.232/0.271	0.239/0.274	0.242/0.286
No. atoms					
Protein	4103	15314	2933	11177	11446
Water/solvents	216	88	44	-	22
B-factors					
Protein	44.3	48.9	36.2	60.9	64.8
Water/solvents	44.4	34.7	25.8	-	36.2
R.m.s. deviations					
Bond length (Å)	0.0101	0.0017	0.0017	0.0018	0.0018
Bond angles (°)	0.98	0.42	0.44	0.44	0.43
Ramachandran					
Outliers (%)	0.19%	0.00%	0.00%	0.00%	0.00%
Favored (%)	99.03%	98.58%	97.78%	97.05%	96.70%
Molprobity Score	1.16	0.93	1.12	1.38	1.56

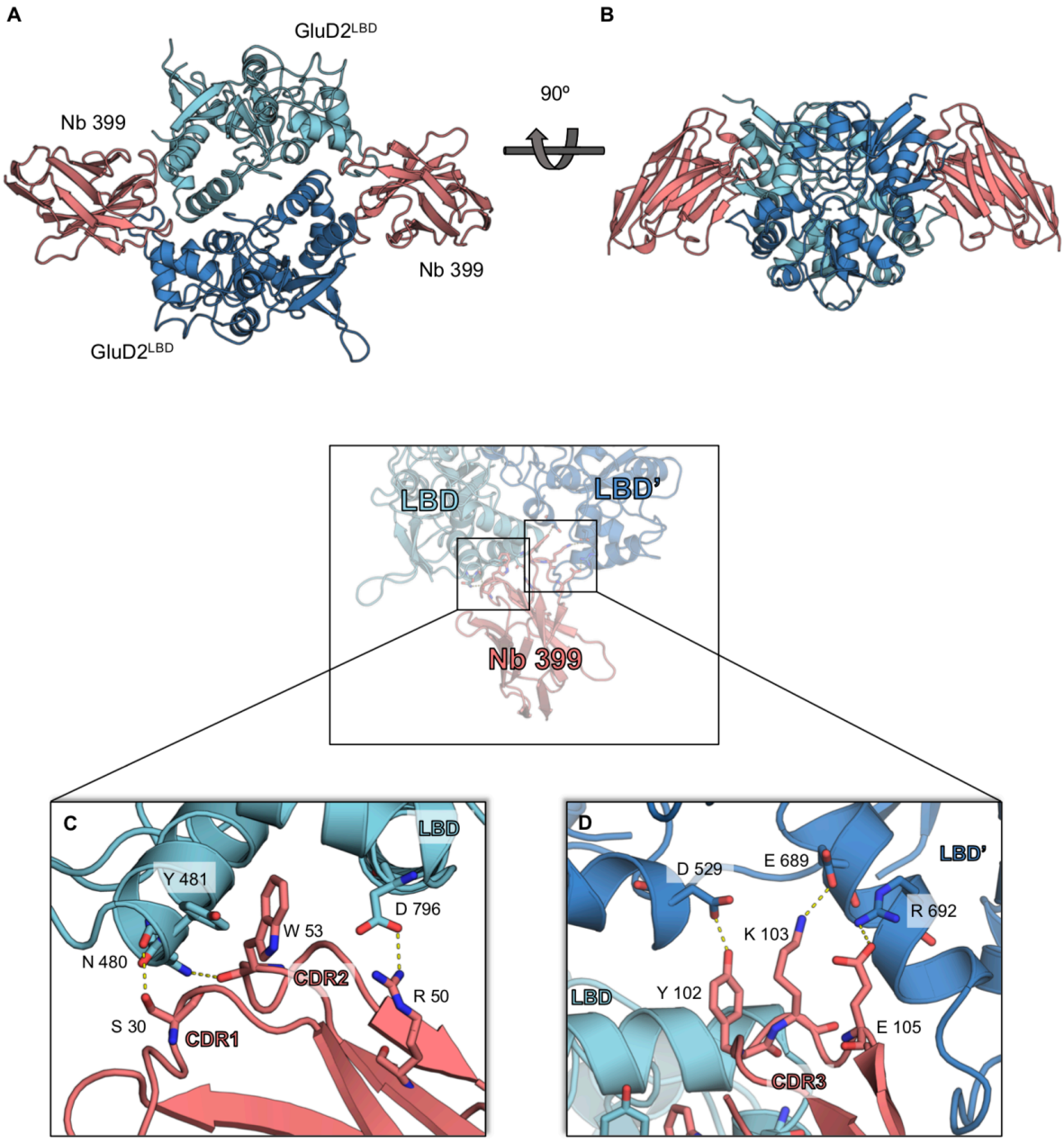

Figure 3-6 **Nanobody 399 stabilizes the GluD2^{LBD} in an active and dimerized conformation** (**A**) Top view of the crystal structure of GluD2^{LBD} (LBD), in complex with nanobody 399 (Nb 399). Nb 399 (pink) binds at the edge of the LBD-LBD' interface (dark and light blue), stabilizing the dimer. (**B**) Side view of the LBD-Nb399 structure shown in (A). (**C**) Close-up view of the interactions between Nb399 CDR1 and CDR2 (pink) to the upper lobe of LBD (light blue). Ser 30 of the CDR1 loop forms a hydrogen bond to the backbone carbonyl of Tyr 481. Trp 53 of the CDR2 loop forms a further hydrogen bond to Asn 480 and Arg 50 engages in a salt bridge with Asp 796. (**D**) The stabilization of the LBD-LBD' interface is mediated by the Nb399 CDR3 loop (pink), which binds to both the upper and lower lobes of LBD' (dark blue). Nb399 Tyr 102 forms a hydrogen bond with Asp 529 of the upper lobe of LBD'. Nb399 Lys 103 and Glu 105 form salt bridges with Glu 689 and Arg 692 of the lower lobe of LBD', respectively.

This extensive domain closure, combined with the observation that addition of D-Serine leads to the near-complete reduction of currents measured from GluD2^{Lc}, led the authors to suggest that binding of D-Serine causes the desensitization of the GluD2^{Lc} receptor (62). Binding of Nb399 to GluD2^{LBD} introduces a lower lobe motion of 24.3°, indicating that Nb399 activates GluD2 but is a weaker agonist that D-Serine. The resulting interface between the upper and lower lobes of the closed clamshell bury a surface area of 641 Å^2.

In the iGluR gating cycle, if ligand binding persists, the receptor will collapse into a desensitized state in which the LBD upper lobes rotate downwards, breaking apart the LBD dimerization interface. In the GluD2^{LBD}-Nb399 structure, however, the dimerization of the LBD upper lobes persists. If the gating mechanism of other iGluRs is conserved in GluD2, this would indicate that Nb399 is capable of maintaining the LBDs in a non-desensitized state.

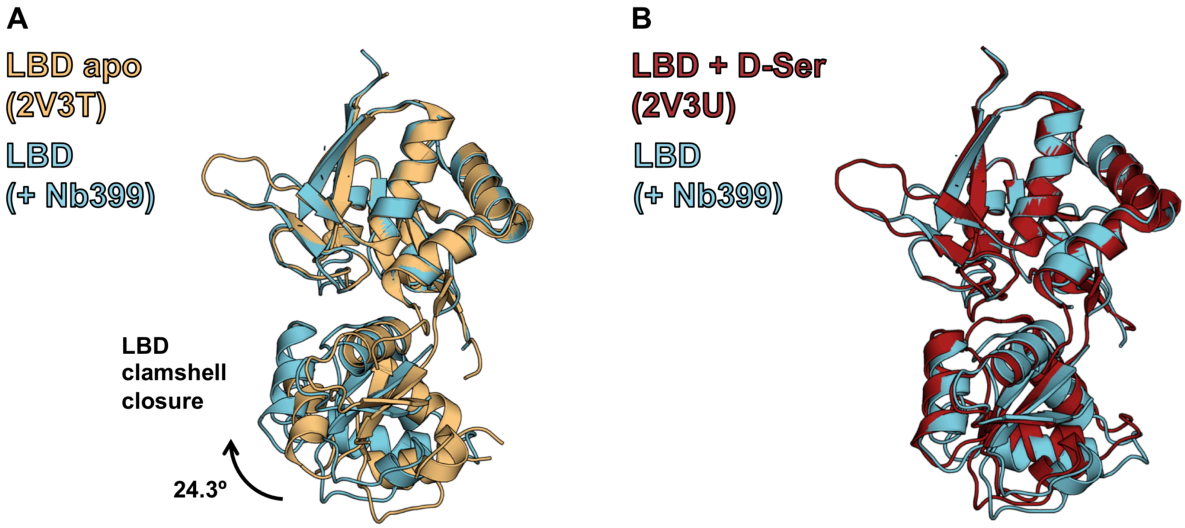

Figure 3-7 **Nb399 induces the closure of the GluD2^{LBD} clam-shell, mimicking the binding of D-Ser** (**A**) Structures of GluD2^{LBD} in complex with Nb 399 (light blue, nanobody not shown) and GluD2^{LBD} in *apo* form (orange, PDB ID 2V3T, from Naur *et al*. (62)), superposed using the lower lobe. Nb 399 triggers the downward movement of the upper lobe by 24.3°, leading to the closure of the GluD2^{LBD} clamshell. (**B**) Structures of GluD2^{LBD} in complex with Nb 399 (light blue, nanobody not shown) and GluD2^{LBD} in complex with D-Serine (red, PDB ID 2V3U, from Naur *et al*. (62)), superposed using the lower lobe. Nb 399 induces a conformation which is comparable to the ligand-bound state.

Nb399 accomplishes GluD2 activation by binding simultaneously to two GluD2^{LBD} monomers (termed LBD and LBD' for simplicity), with a total binding interface area of 998

Å^2. The interface is composed of two sub-areas: the first between Nb399 CDR loops 1 and 2 and the LBD upper lobe (590 Å^2) and the second one between Nb399 CDR loop 3 and the LBD' upper and lower lobes (408 Å^2) (**Figure 3-6**).

The Nb399 CDR1 contributes one hydrogen bridge between the side-chain hydroxyl group of Ser 30 and the backbone carbonyl of Tyr 481 of the LBD upper lobe. The backbone carbonyl of Trp 53 on CDR2 forms an additional hydrogen bond with the side-chain amide of Asn 480, while the guanidinium group of Arg 50 engages in a salt bridge with the carboxylate of Asp 796 (**Figure 3-6**).

On the other hand, CDR loop 3 forms one hydrogen bond between the side-chain hydroxyl group of Tyr 102 and the carboxylate of the LBD' Asp 529 (on the upper lobe) and engages in two salt bridges to the LBD' lower lobe: one between the amino group of Lys 103 and the carboxylate group of Glu 689, and one between the carboxylate group of Glu 105 and the guanidinium group of Arg 692 (**Figure 3-6**). This extensive network of hydrogen bonds and salt bridges is in accordance with the high affinity of 0.6 nM measured for Nb399.

3.7 Nb399 activates GluD2 in mouse brain slices

Having identified a nanobody that locks the GluD2^{LBD} in an active conformation, I next asked whether Nb399 is able to activate GluD2 in a physiologically relevant environment. In collaboration with Prof Michisuke Yuzaki's laboratory at Keio University, the effect of Nb399 was tested on organotypic slices of mouse cerebella.

Although no direct currents can be measured from GluD2, the downstream signalling effects of GluD2 can be observed by measurement of parallel fiber-evoked excitatory post-synaptic currents (PF-EPSCs). When GluD2 is activated upon D-Serine binding, a signal is transmitted downstream, leading to dephosphorylation of the C-terminus of GluA2 receptors and their subsequent internalization (see Introduction, section 1.4) (61). The decrease of

GluA2 receptors on the cell surface leads to a reduction in PF-EPSCs, and hence GluD2 activity can be measured indirectly by observation of these currents.

When Nb399 was added to mouse cerebellar slices of wild-type mice, a decrease in PF-EPSCs was observed (**Figure 3-8**, red points, data kindly provided by Prof Michisuke Yuzaki) in comparison to the negative control (**Figure 3-8**, empty vehicle, black points). The decrease in PF-EPSCs is comparable to that observed for D-Serine in previous studies (61). Nb399 had no effect on GluD2-knock out mice, demonstrating that the Nb399-induced reduction of PF-EPSCs is GluD2-dependent.

Taken together, these results show that Nb399 not only locks the $GluD2^{LBD}$ in an active conformation, but also triggers GluD2 signalling in a physiologically relevant environment. Nb399 is hence a valuable tool to study GluD2 function, particularly due to its specificity, very high affinity and capacity to prevent receptor desensitization.

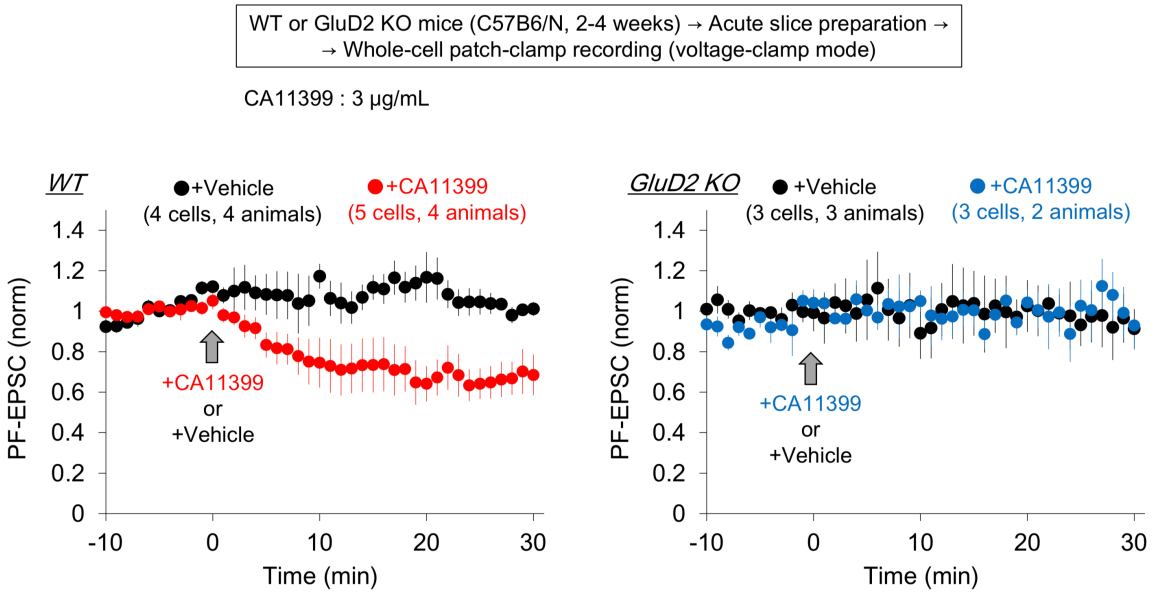

Figure 3-8 **Nb399 induces a GluD2-dependent decrease in excitatory post-synaptic currents** Experiments conducted and data kindly provided by Prof Michisuke Yuzaki and Takahiro Aimi. Organotypic slices were prepared from wild-type or GluD2-knock out mice and whole-cell patch clamp recordings were taken from Purkinje cells. The plots display averaged amplitudes of parallel fiber-evoked excitatory post-synaptic currents (PF-EPSCs), against time (t= 0 min corresponds to application of Nb399 or empty vehicle). The addition of Nb399 activates GluD2, leading to downstream signalling and the internalization of AMPA receptors. This results in the decrease of PF-EPSCs (see plot on the left). This phenomenon is dependent on GluD2, since recordings from GluD2 knock out mice brain slices display no effect upon addition of Nb399 (see plot on the right). The decrease of EPSCs as a result from Nb399 addition is comparable to the effects observed for D-Serine addition (61).

3.8 Nb390 and Nb392 share the same binding mode as Nb399

The structures of GluD2^{LBD} in complex with Nb390 and Nb392 reveal the same binding mechanism as observed for Nb399 (**Figure 3-9**). As described above for Nb399, Nb390 and Nb392 bind to either side of a GluD2^{LBD} dimer, stabilizing the GluD2^{LBD} in a closed and active conformation. The degree of clamshell closure differs slightly from nanobody to nanobody: as described above, Nb399 triggers a closure of 24.3°. Nb390 introduces a closure of 27.9°, Nb392 a motion of 25.8° (all measured using the DynDom Server (158)). Although these motions clearly indicate that all nanobodies lead to the activation of the ligand-binding domain, the degrees of closure are lower than that triggered by D-Ser (29.9°, discussed above), suggesting that Nb390, Nb392 and Nb399 are weaker agonists than D-Ser.

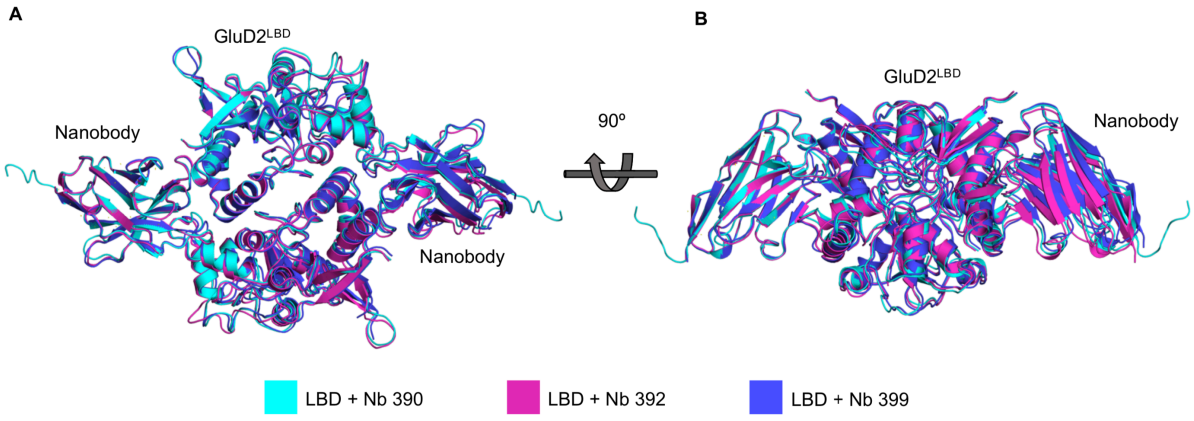

Figure 3-9 **Nanobodies 390 and 392 share the same binding mode as Nanobody 399** (**A**) Top view of structures of GluD2^{LBD} dimers in complex with nanobodies 390 (cyan), 392 (pink) and 399 (purple), superposed using one nanobody copy. (**B**) Side view of structures shown in (A). Nanobodies 390 and 392, as observed for nanobody 399, induces the dimerization of GluD2^{LBD}, locking the receptor in an active state.

In the structures of GluD2^{LBD} in complex with Nb390 and Nb392, the CDR1 and CDR2 loop residues that engage in the interaction with the upper lobe of one LBD are maintained, and indeed the same hydrogen bonds and salt bridge can be observed on that side of the interface (see **Figure 3-6** for reference). However, a proline following Tyr 102 in the CDR3

loop of Nb390 and Nb392 introduces a hairpin structure that disrupts the hydrogen bond between Tyr 102 and Asp 529 observed in the GluD2^{LBD}-Nb399 structure. The additional salt bridges that are formed by the CDR3 loop are also missing in the Nb390 and Nb392 structures (**Figure 3-10**). The absence of these bonds is reflected in the drop in binding affinity for these nanobodies (~70-fold weaker for Nb390, and ~3 fold weaker for Nb392, in comparison to Nb399). The stabilization of the GluD2^{LBD} dimer by Nb390 and Nb392 is still achieved by hydrophobic interactions between their CDR3 loop and the lower lobe of the opposing GluD2^{LBD} monomer.

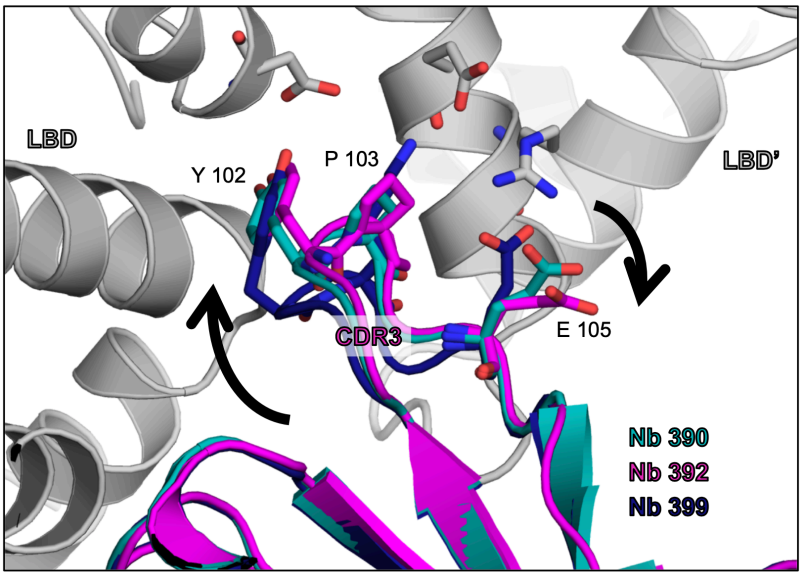

Figure 3-10 **Comparison of CDR3 loop binding mode for Nanobodies 390, 392 and 399.** A proline in the CDR3 loop of Nanobodies 390 and 392 (Pro 103) introduces a hairpin structure that disrupts the hydrogen bond between the preceding tyrosine (Tyr 102) and Asp 259 of the LBD. This conformational change also prevents the salt bridge formation between the CDR3 Glu 105 and LBD Arg 692.

3.9 Nb381 and Nb389 bind to unique binding sites on GluD2^{ATD}

Crystal structures were obtained for GluD2^{ATD} in complex with Nb381 and Nb389. Like other iGluRs, the ATDs of GluD2 form dimers, with an extensive total dimerization interface of 1637 Å^2. Both Nb381 and Nb389 were found to bind on either side of the GluD2^{ATD} dimer, without affecting its oligomerization state (**Figure 3-11**).

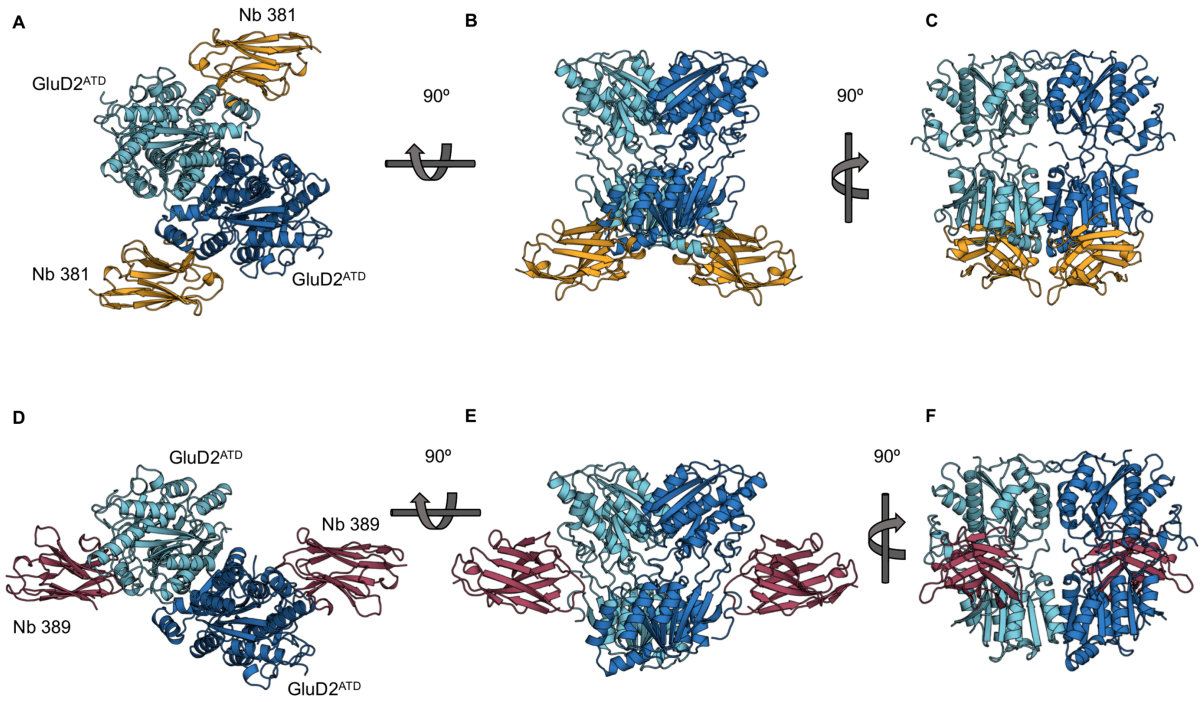

Figure 3-11 **Nanobodies 381 and 389 bind to different sites on the GluD2^{ATD} dimer** (**A**) Top view of the structure of a GluD2^{ATD} dimer (light and dark blue), in complex with Nb 381 (orange). (**B-C**) Side views of the structure depicted in (A). Nb 381 binds to the base of the GluD2^{ATD} dimer, where it could possibly interact with the neighbouring GluD2 ligand-binding domains (not shown). (**D**) Top view of the structure of a GluD2^{ATD} dimer (light and dark blue), in complex with Nb 389 (red). (**E-F**) Side views of the structure depicted in (A). Nb 389 binds to the GluD2^{ATD} clamshell cleft.

Nb381 binds at the membrane-proximal end of the ATD clamshell, in close proximity to where the adjacent ligand-binding domains would be placed in a GluD2 tetrameric conformation. This opens the question of whether Nb381 could bind to both GluD2^{ATD} and GluD2^{LBD} in a full-length receptor, bridging both domains and hence rigidifying the extracellular region. All CDR loops of Nb381 contribute to the binding to GluD2^{ATD}, forming hydrogen bonds and salt bridges with residues of GluD2 α-helix 7, the loop connecting β-sheets 13 and 14, and α-helix 6', which is unique to GluD receptors. The total buried surface area of the interface is 679 Å^2. The structure of GluD2^{ATD} in complex with Nb389 revealed a different binding site. Nb389 binds to the cleft of the ATD clamshell, wedging in between the upper and lower lobes. The interaction is mainly driven by CDR loops 1 and 3, which form hydrogen bonds to residues on the loop connecting β-sheets 12 and 13, and on α-helix 10. The total buried surface area of the interface is 718 Å^2.

3.10 Only Nb389 can access all four binding sites on GluD2

The structures of nanobodies 390, 392, 399, 381 and 389 were all obtained in complex with either isolated ligand-binding or amino-terminal domains. All structures unveiled binding mechanisms in which two nanobodies bind on either side of LBD or ATD dimers. In a full-length, tetrameric receptor, however, not all of these binding sites would be available. Those sides of LBD or ATD dimers facing toward the centre of the receptor are occluded from binding partners due to steric clashes.

By superposing the obtained GluD2^{ATD}- and GluD2^{LBD}-nanobody structures on the structure of a full-length iGluR (the crystal structure of an AMPA receptor was used, PDB ID 3KG2), it is possible to visualize what nanobody binding sites might be available in a full-length GluD2 receptor (**Figure 3-12**).

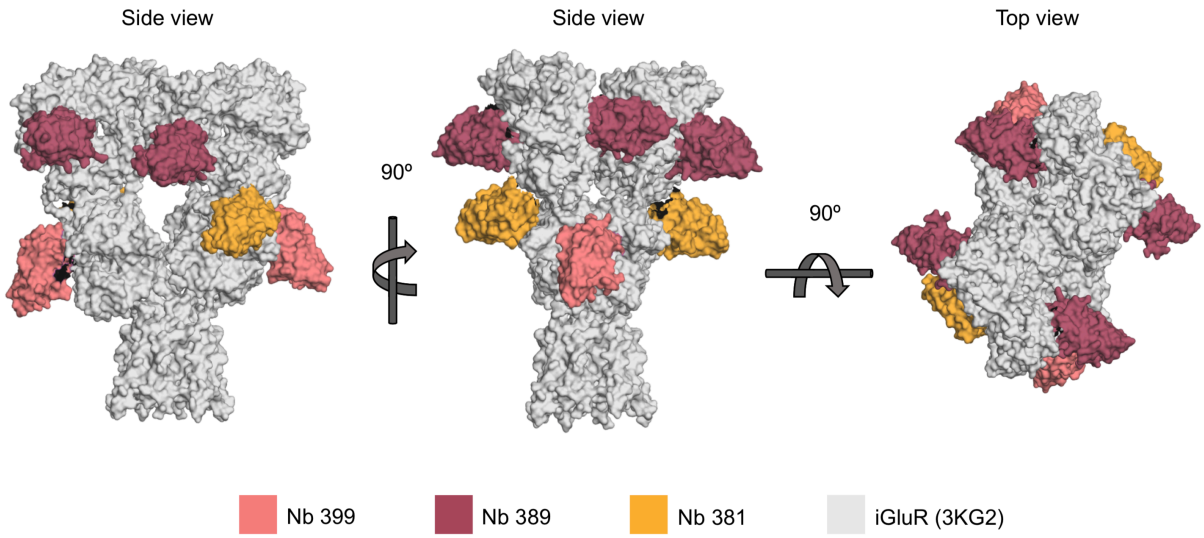

Figure 3-12 **Overview of nanobody binding sites on the GluD2 tetramer** Surface representation of nanobodies 399 (pink), 381 (orange) and 389 (red) and their respective binding sites. The structure of an AMPA receptor (PDB ID 3KG2) was used as a model for the iGluR tetramer conformation. GluD2^{LBD} and GluD2^{ATD} structures in complex with the respective nanobodies were superposed on 3KG2 using either the amino-terminal or ligand-binding domains (not shown). Nanobodies 390 and 392 are not depicted since their binding mode is equivalent to Nb 399. In a tetrameric conformation, only nanobody 389 is able to bind all four binding sites (see top view, on the right). Nanobodies 399 and 381 only have access to two, outward-facing binding sites.

Nbs 390, 392, 399 and 381 only have access to two of their respective binding sites, while the other two are sterically occluded when superposed on the tetrameric AMPA receptor structure. Nb389, on the other hand, is able to access all four binding sites on the ATD clamshell clefts.

3.11 Summary and conclusions drawn from chapter 3

With the aim to generate tools that would enable us to study the function of the GluD2-Cbln1-βNrx1^{+SS4} triad, we raised specific nanobodies against this complex. After characterization of these nanobodies, 10 high affinity binders were identified to bind GluD2, while only one nanobody was found to bind Cbln-1 with lower affinity. No nanobodies against -βNrx1^{+SS4} were identified. Crystal structures of nanobodies binding the GluD2^{LBD} revealed that Nb390, Nb392 and Nb399 lock the domain in a closed and active conformation. Interestingly, the GluD2^{LBD} dimerization interface is maintained, which is associated with a non-desensitized state in other iGluRs. Nb399 was further tested in mouse cerebellar slices, where it induced a decrease in measured parallel fiber-evoked EPSCs, mimicking the effect observed for the GluD2 ligand, D-Serine. Taken together, these data show that Nb399 is not only able to induce the closure of the ligand-binding domain, but also acts as a true agonist by triggering GluD2-specific downstream signalling. Hence, the discovery of Nb399 results in a valuable molecular tool to study the function of GluD2, conduct structural studies on the receptor and understand its signalling mechanism. Moreover, given the fact that Nb399 stabilizes the active, non-desensitized state of GluD2^{LBD}, Nb399 widens the time frame to analyse the structure of an active receptor (normally limited to the millisecond range).

Three nanobodies, Nb383, Nb385 and Nb416, were found to bind GluD2^{LBD} in its monomeric state, suggesting that they stabilize different GluD2^{LBD} conformations to those

induced by Nb390, Nb392 and Nb399. Efforts to obtain crystal structures of GluD2^{LBD} in complex with Nb383, Nb385 and Nb416 are ongoing. These monomerizing nanobodies will be particularly useful as control samples in functional experiments testing the effect of e.g. Nb399.

Crystal structures of nanobodies in complex with GluD2^{ATD} revealed further useful molecular tools. Nb381 binds at the very base of the GluD2^{ATD}, possibly bridging the GluD2^{ATD} to the adjacent GluD2^{LBD} and rigidifying the tetrameric receptor. Nb389 binds to the cleft of the GluD2^{ATD} clamshell, and is the only nanobody that is theoretically able to access all four binding sites in a tetrameric conformation. Although no functional studies were performed with Nb381 and Nb389, it is possible to rationalize that they would not affect GluD2 function. These nanobodies do not affect the ligand-binding domain and do not occlude the binding sites of any known binding partners (Cbln1, for instance, binds at the very membrane-distal side of GluD2^{ATD}). Hence, Nb381 and Nb389 would be good molecular tools for, e.g., nanobody-based purification techniques, for labelling GluD2 on cell surfaces or stabilizing the receptor for structural studies.

4. Single particle cryo-EM studies of GluD2-nanobody complexes

4.1 Aims of this chapter

Following the discovery of nanobodies that stabilize different functional conformations of GluD2, I next set out to use these tools to elucidate the structural basis of GluD2 signalling. In order to understand how the extracellular region and transmembrane domain coordinate to enable signal transduction, I aimed to obtain a full-length structure of GluD2 by single particle cryo-EM analysis.

4.2 Nanodiscs allow the study of trans-membrane receptors in a lipidic environment

Traditionally, the study of membrane proteins has involved their solubilization with detergents, resulting in detergent-protein-lipid micelles. Although the structures of many membrane proteins solubilized in detergents have successfully been determined (including all iGluR structures to date, summarised in (47)), there is mounting evidence that detergents

pose a hazard to membrane protein stability and can ultimately lead to artificial protein conformations. This phenomenon is particularly evident for $GABA_A$ receptors, where the presence of detergents leads to the collapse of the ion channel (reviewed in (184)). In addition, many membrane proteins require specific phospholipids to perform their function, an environment which is not reproduced when using detergent micelles. Thus, membrane proteins are ideally studied in a lipidic environment. The development of nanodiscs allowed the preparation of membrane proteins in a solubilized state, but maintaining a small disc of lipidic bilayer surrounding the trans-membrane domains of the protein of interest (161). Nanodiscs consist of amphipathic helical protein belts (named membrane scaffold proteins (MSPs)) that encircle a phospholipid bilayer and in which the membrane protein is embedded. The size of the resulting nanodiscs is largely controlled by the length of the MSP, but also varies with the concentrations of phospholipid used during nanodisc assembly. For GluD2, which has 16 transmembrane helices and a predicted footprint diameter of 6 nm (based on measurements done on PDB ID 3KG2), the belt protein MSP1D1 was used. MSP1D1 produces a nanodisc of ~9.7 nm diameter and hence provides sufficient surface area for GluD2 reconstitution.

4.3 Expression and purification optimization leads to a stable and monodisperse GluD2 sample

Initial expression and purification tests carried out by Dr Ester Behiels showed increased expression levels for GluD2 constructs lacking the carboxy-terminal cytoplasmic tail. Hence, all GluD2 constructs used for this thesis are C-terminal truncations comprising residues D24 to K870, followed by a C-terminal 1D4 epitope tag (TETSQVAPA).

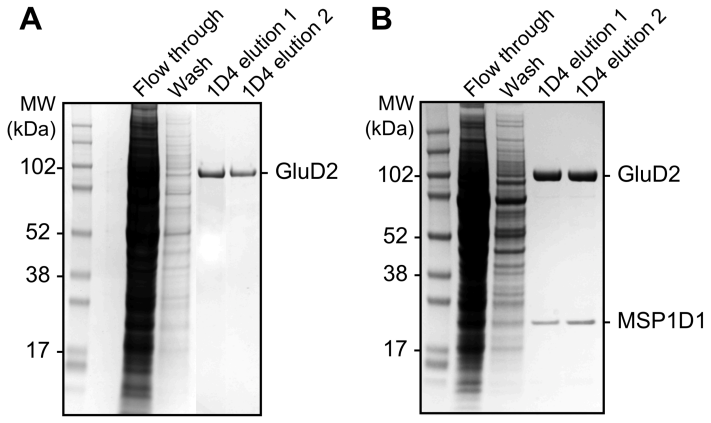

Figure 4-1 **GluD2 purification over the 1D4 epitope tag** (**A**) Purification of GluD2 in DMNG:CHS. SDS-PAGE analysis of flow through, wash after cell debris removal and elution fractions, stained with Coomassie. GluD2 was eluted over night with 5 mM 1D4 peptide (elution 1), followed by another elution step for 5 h (elution 2). (**B**) Reconstitution of GluD2 in MSP1D1 nanodiscs, on 1D4 resin. SDS-PAGE analysis of flow through, wash after cell debris removal and elution fractions, stained with Coomassie. Elution steps took place as described for (A). Numbers on the left of the gel represent the molecular weights in kDa of the protein weight standards.

In order to devise the best strategy to reconstitute GluD2 in nanodiscs, I first performed small-scale expression and purification tests. GluD2 was expressed in HEK 293 'Expi' cells, using a mammalian expression system (more details can be found under section 2.9 in Materials and Methods). Cells were harvested and GluD2 was solubilized by addition of DMNG:CHS (20:1).

Upon removal of insoluble material and cell debris, GluD2 was purified by affinity chromatography using monoclonal Rho-1D4 antibody resin, resulting in a pure GluD2 sample (**Figure 4-1 A**). At this stage, the sample was divided for three different strategies.

First, GluD2 was eluted from the Rho-1D4 resin and nanodisc reconstitution was performed in solution. This has the advantage that the GluD2 concentration can be measured, and hence the quantities of lipid and MSP that are added can be adjusted accordingly. On the other hand, this method produces a large amount of 'empty' nanodiscs that do not contain GluD2, which introduces the need for a second purification step to remove such nanodiscs.

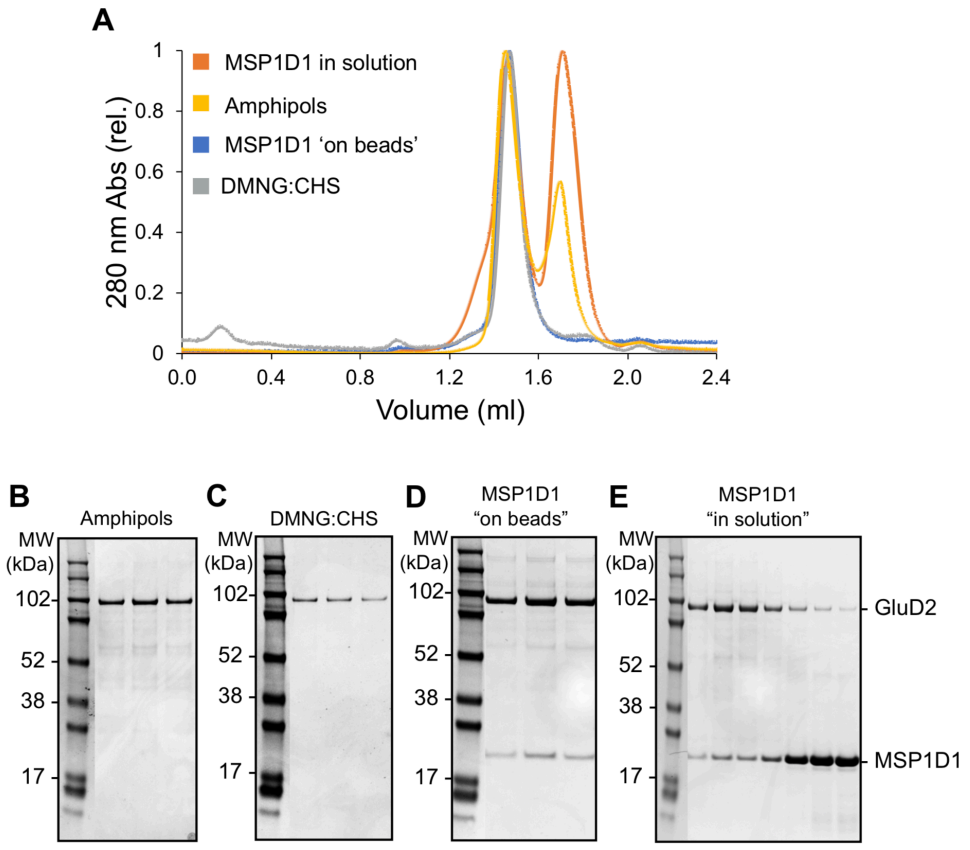

Figure 4-2 **GluD2 purification tests and reconstitution into nanodiscs** (**A**) Size-exclusion chromatography (SEC) elution profiles of GluD2, purified over 1D4-resin with four different strategies: in DMNG:CHS (grey curve), reconstituted in solution into amphipols (yellow curve), reconstituted in solution into MSP1D1 nanodiscs (orange curve) and reconstituted into MSP1D1 nanodiscs on 1D4 resin, prior to 1D4 elution (orange curve). Absorbance measurements at 280 nm are normalized and relative to a maximum of 1. (**B-E**) SDS-PAGE analysis of fractions obtained from SEC runs shown in (A). Fractions shown correspond to GluD2 peak (at ~ 1.4 ml), while the gel on (E) also shows fractions for empty MSP1D1 nanodiscs (second peak at ~ 1.7 ml). Numbers on the left of the gel represent the molecular weights in kDa of the protein weight standards.

The second aliquot of GluD2 was also eluted from the Rho-1D4 resin, and reconstituted in amphipols. Amphipols, or amphiphilic polymers, are another alternative to detergents and are able to form soluble complexes with membrane proteins by adsorbing to the protein transmembrane helices (185). As for protein reconstituted with nanodiscs in solution, the caveat of reconstitution of membrane proteins in amphipols in solution, is the large amount of excess amphipols which needs to be removed prior to cryo EM sample preparation.

The third aliquot of GluD2 was maintained bound to the Rho-1D4 resin, and nanodisc reconstitution was done on the beads. For this strategy, excess amounts of lipids and belt proteins were added to the Rho-1D4 slurry and nanodisc formation was triggered by addition

of hydrophobic beads that adsorb the detergent. With this method, excess nanodiscs that do not contain GluD2, leftover lipids, detergent and belt protein can be washed off, without the necessity of a second purification step (**Figure 4-1 B**).

The results of the three purification strategies can be observed in **Figure 4-2**. All GluD2 samples, in DMNG:CHS, reconstituted in amphipols or in nanodiscs, produce a single monodisperse GluD2 peak, indicating that all methods maintain protein stability. For reconstitution of GluD2 in solution in amphipols or nanodiscs, a second peak is observed, corresponding to excess amphipols or excess "empty" nanodiscs. Since nanodiscs provide the closest approximation to a native, lipidic environment, all further GluD2 sample preparations were reconstituted in nanodiscs, using the "on beads" assembly method.

4.4 Nanobody 399 disrupts the tetrameric conformation of GluD2

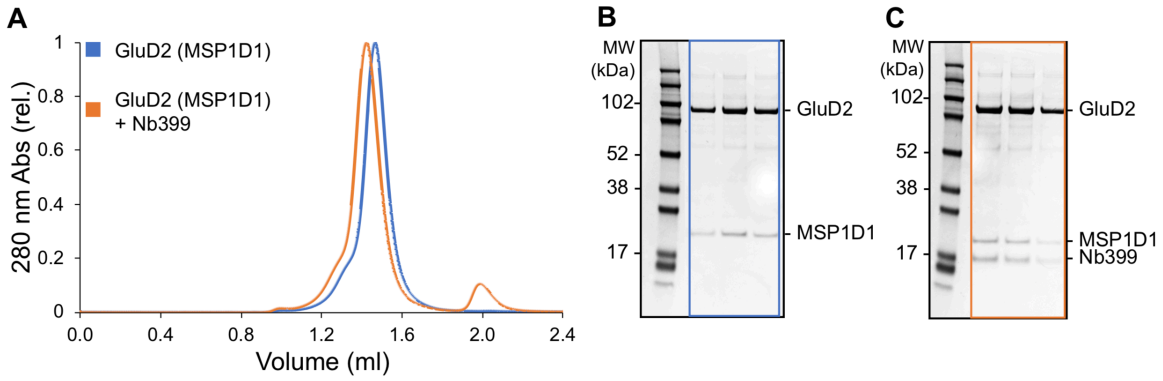

Figure 4-3 **Nanobody 399 interacts with GluD2 reconstituted in MSP1D1 nanodiscs** (**A**) Size-exclusion chromatography (SEC) elution profiles of GluD2 reconstituted in MSP1D1 nanodiscs, with and without bound nanobody 399 (Nb 399). Absorbance measurements at 280 nm are normalized and relative to a maximum of 1. (**B-C**) SDS-PAGE analysis of fractions obtained from SEC runs shown in (A), stained with Coomassie. Fractions shown correspond to the respective GluD2 peaks. Numbers on the left of the gel represent the molecular weights in kDa of the protein weight standards.

Having determined that nanobody 399 (Nb399) dimerizes the GluD2 LBD and mediates GluD2-dependent signalling, I next aimed to study the effect of Nb399 on the full-length receptor by cryo-EM. GluD2 reconstituted in nanodiscs was combined with Nb399 with a

1,5-fold molar excess. Analytical size-exclusion confirmed that Nb399 binds to GluD2 (**Figure 4-3**).

Cryo-EM grids prepared with the sample at 0.6 mg/ml resulted in good distribution across free-standing ice. These grids were then used for data collection on a Titan Krios, applying parameters summarized in Materials & Methods, section 2.11. Micrographs were motion corrected using MotionCor2 (163) and the CTF was estimated with Gctf (164). An exemplary micrograph is shown in **Figure 4-4**. Automated particle picking and subsequent data processing was done within RELION (165).

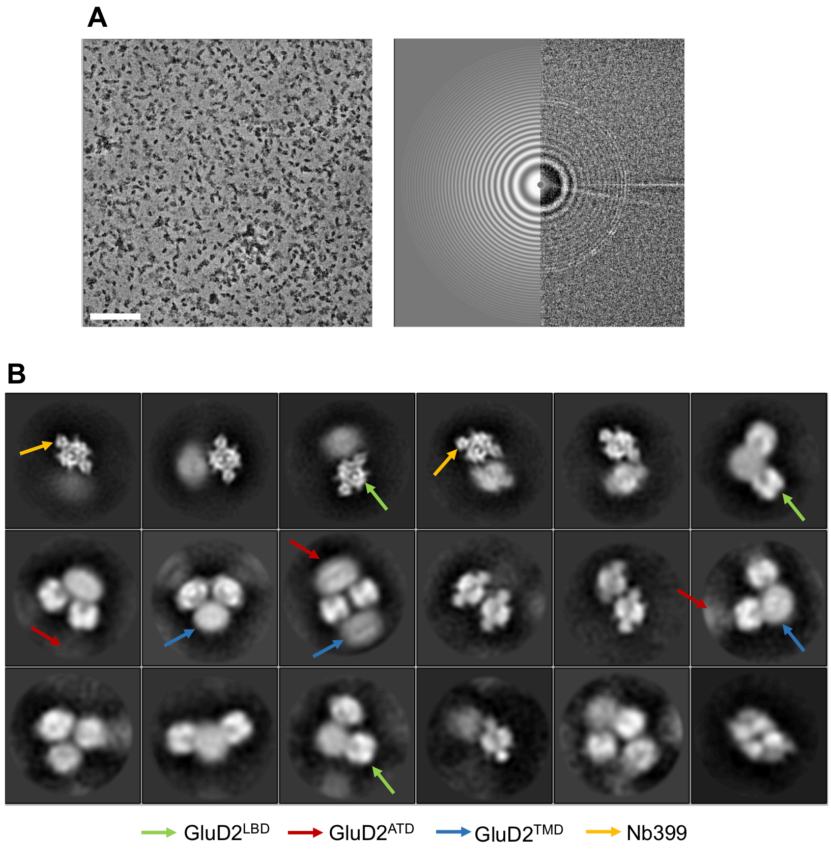

Figure 4-4 **Exemplary micrograph and 2C class averages of GluD2 in complex with nanobody 399** (**A**) Exemplary dose-weighted, motion-corrected micrograph and corresponding fitted power spectrum of GluD2 in complex with Nb 399 in free-standing ice. Scale bar: 60 nm. (**B**) Exemplary 2D class averages (obtained in RELION) of particles picked from motion-corrected micrographs. Most prominent classes show top views of $GluD2^{LBD}$ dimers (green arrows) in complex with Nb 399 (yellow arrows). The $GluD2^{TMD}$ and nanodisc belt (blue arrows) are distinguishable in side views, while $GluD2^{ATD}$ (red arrows) is blurry and absent from most classes. Mask diameter: 220 Å.

The 2D classification results from the GluD2-Nb399 dataset can be seen in **Figure 4-4**. Features corresponding to the nanodisc belt, the LBD and ATD layers can be recognized. The most predominant classes, however, constitute top views of two LBD dimers in complex with four nanobodies, greatly resembling the arrangement observed in the LBD-Nb399 crystal structure (**Figure 4-5**). This observation disproves the initial assumption that only two binding sites for Nb399 would be available in the tetrameric GluD2 receptor, where the binding sites facing the centre of the receptor are sterically occluded by the dimerization of the ATDs in the upper molecular layer. From this cryo-EM dataset it becomes apparent that Nb399 is able to disrupt the tetrameric conformation, wedging the LBD dimers apart and occupying all four binding sites. A high degree of flexibility between the LBD and TMD of GluD2 is also observed, evidenced by the wide range of relative orientations of the LBD dimers in a single receptor (**Figure 4-5**).

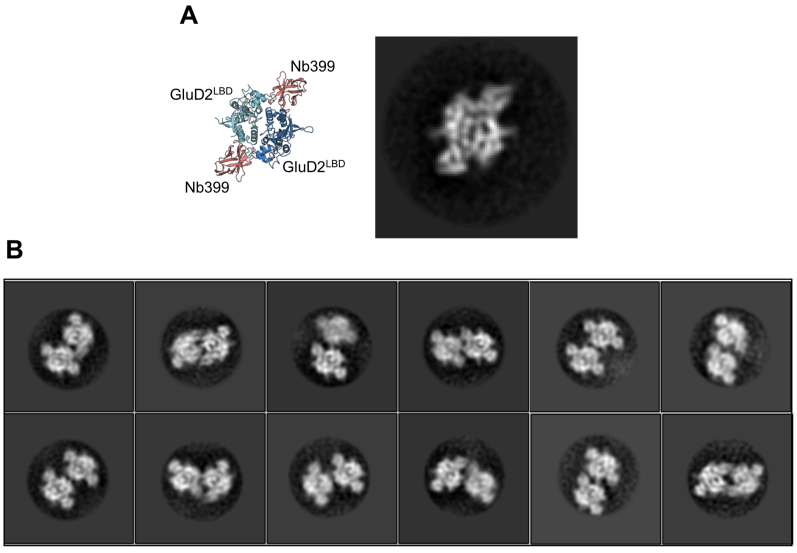

Figure 4-5 **Nanobody 399 binds to four sites on the tetrameric GluD2 receptor** (**A**) Comparison of the $GluD2^{LBD}$-Nb399 crystal structure (see chapter 3) and an exemplary 2D class average of a $GluD2^{LBD}$ dimer top view. (**B**) Selected 2D class averages of the GluD2-Nb399 dataset, showing top views of $GluD2^{LBD}$ dimers in complex with a total of four nanobodies (one on each side of the dimers). The wide range of relative orientations of $GluD2^{LBD}$ dimers (in parallel, perpendicular or diagonal to each other) indicates that the TMD-LBD linkers are flexible and allow many conformations. Mask diameter: 160 Å.

The fact that most particles are classified into LBD top views suggests that this sample displays a preferred particle orientation. The main cause for preferential orientation in cryo-

EM is the interaction of particles with the air-water interface during cryo-EM grid preparation, which in severe cases can lead to the denaturation of the protein sample (186). This raises the question of whether the access of Nb399 to the occluded binding sites on GluD2 becomes available only once the receptor is destabilized due to partial denaturation at the air-water interface, or whether Nb399 already binds to four sites when GluD2 is in solution. Although a significant shift in the size-exclusion elution profile can be observed for GluD2 in complex with Nb399, the resolution of the Superose 6 column is not high enough to distinguish between the addition of 30 kDa (equivalent to two nanobodies) or 60 kDa (equivalent to four nanobodies).

As is known from other iGluRs, the ATDs usually sample many conformations, owing to the flexibility of the linkers between the LBD and ATD layers (47). This phenomenon is also observed here for GluD2, where 2D classes mostly contain a distinct nanodisc belt and LBD layers, but the ATDs are only visible as a haze on top of the LBD layer (**Figure 4-6**). As discussed before, the lack of defined ATD densities could also be due to adsorption to the air-water interface.

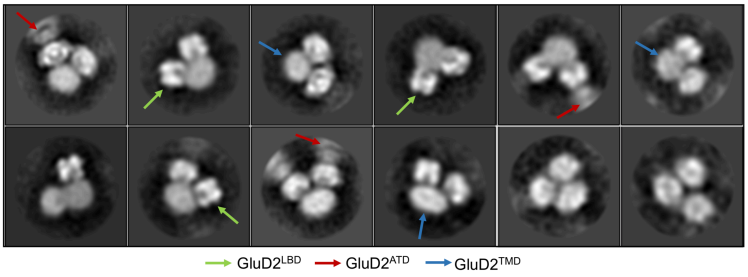

Figure 4-6 **Side views of GluD2-Nb399 reveal flexibility in the GluD2^{ATD} layer** Selected 2D class averages (obtained in RELION) showing side views of GluD2 in complex with Nb 399. The GluD2^{TMD} (blue arrows) and GluD2^{LBD} (green arrows) domains are distinguishable. Only in some classes it is possible to discern GluD2^{ATD} (red arrows), mostly as a haze above the GluD2^{LBD} domains. Mask diameter: 220 Å.

4.5 GluD2 is affected by the air-water interface during cryo-EM grid preparation

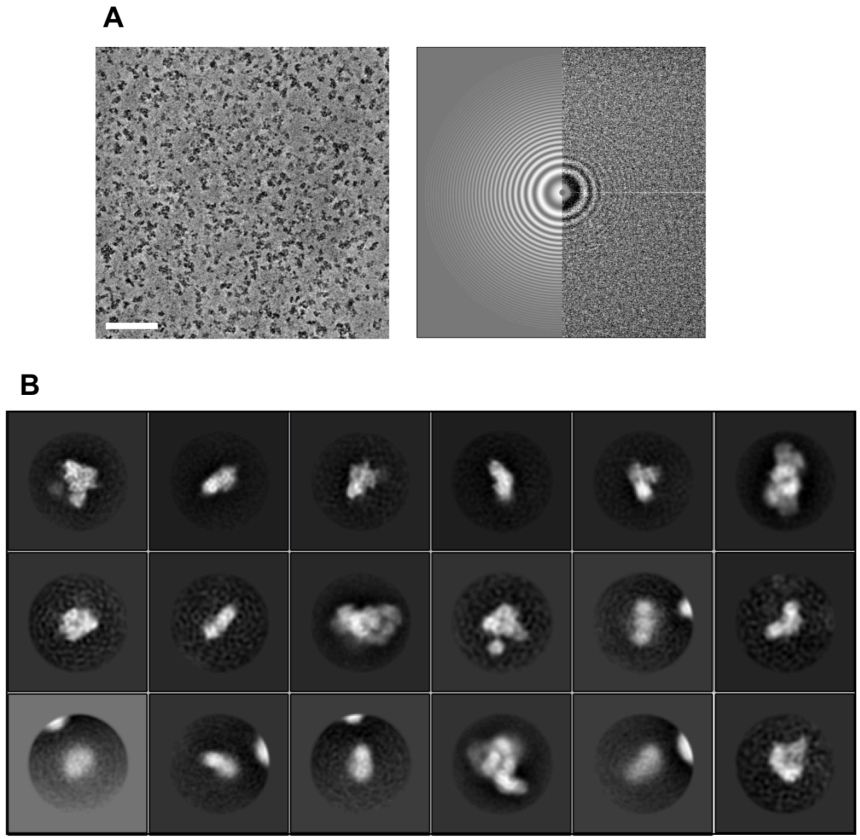

Figure 4-7 **Exemplary micrograph and 2D class averages of GluD2 *apo*** (**A**) Exemplary dose-weighted, motion-corrected micrograph and corresponding fitted power spectrum of GluD2 *apo* in free-standing ice. Scale bar: 60 nm. (**B**) Exemplary 2D class averages (obtained in RELION) of particles picked from the GluD2 *apo* dataset. Most classes display very small particles that do not resemble GluD2, suggesting that these correspond to GluD2 fragments following GluD2 denaturation at the air-water interface. Mask diameter: 220 Å.

After establishing that Nb399 might have a destabilizing effect on GluD2, I next explored whether GluD2 behaves differently in its *apo* state. Cryo-EM grids were prepared at similar protein concentrations, using UltrAuFoil 1.2/1.3 grids and equivalent data collection parameters. An exemplary micrograph and corresponding power spectrum are shown in **Figure 4-7 A**. 2D class averages of particles picked from this dataset revealed that most particles were too small to correspond to GluD2 (~40 Å in diameter, see **Figure 4-7 B**). Since the sample is very pure (see **Figure 4-3 B**) and there is no detectable protein

degradation (even after one week at 4°C), it is likely that these small particles correspond to fragments of denatured GluD2 resulting during the preparation of cryo-EM grids. Of 54,372 picked particles, only 4% resulted in 2D classes that contained features resembling GluD2 (**Figure 4-8 A**). These classes were used for the generation of an initial 3D reference model within RELION, which was subsequently low-pass filtered and used as a reference for 3D classification. Due, in part, to the low number of particles available at this stage (2,279), the resulting 3D class averages displayed no high-resolution features (**Figure 4-8 B**). However, it was still possible to discern the general architecture of GluD2, which displays three layers for the amino-terminal, ligand-binding and transmembrane domains.

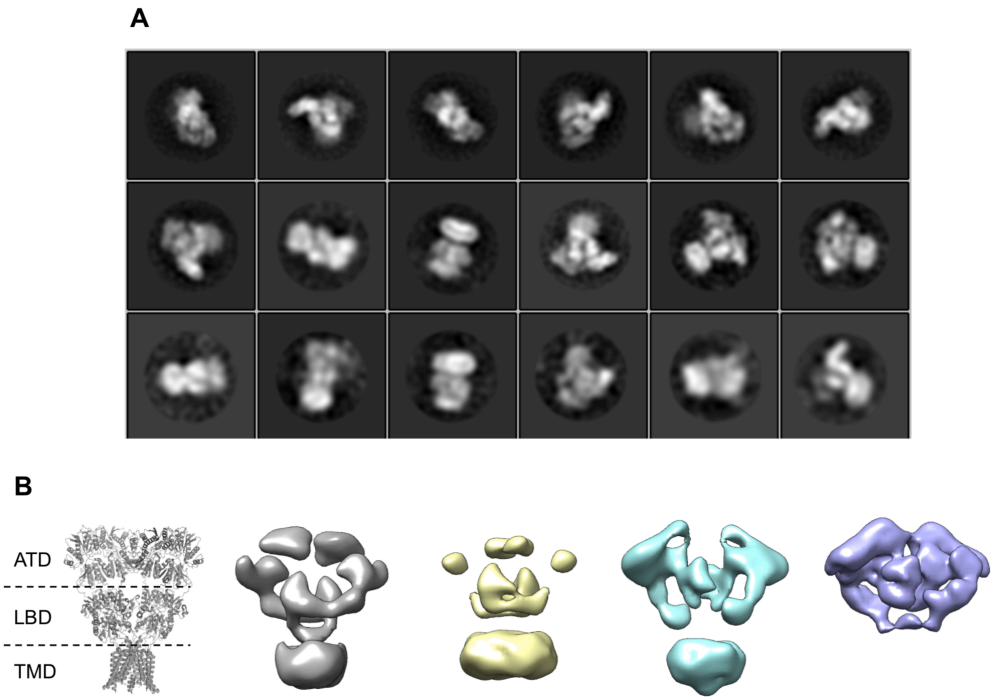

Figure 4-8 **2D and 3D class averages of selected GluD2 *apo* particles** (**A**) Exemplary 2D class averages of subset selection of particles from the GluD2 *apo* dataset in free-standing ice. Only ~4% of particles (2,279) represent non-denatured GluD2. GluD2 TMD, LBD and ATD layers are easily recognizable in side, top and bottom views. Mask diameter: 220 Å. (**B**) 3D classification in RELION from 2D classes depicted in (A). For comparison, the GluA1 crystal structure (3KG2) is shown on the left, indicating the ATD, LBD and TMD layers.

4.6 Interaction of proteins with the air-water interface leads to preferential orientation and denaturation

As mentioned before, the interaction of proteins to the air-water interface poses an important problem for structural studies by cryo-EM (186). Proteins adsorbing to this interface typically display a preferential orientation, which limits the angular information obtained, resulting in biased three-dimensional maps. In severe cases, the adsorption to the air-water interface leads to the denaturation of the protein of interest, as can be observed for GluD2.

During purification and subsequent cryo-EM grid preparation, protein molecules are estimated to interact with air-water interfaces up to 1000 times (187). The probability of these interactions is increased with smaller volumes and large surface areas, a situation which is exacerbated when excess protein solution is removed to form a thin film (50-100 nm thick) in the holes of grids, immediately before vitrification in liquid ethane. It has been shown that decreasing the delay between formation of the sample film to vitrification to ~100 ms, can decrease the number of molecules that adsorb to the air-water interface (188). This, however, requires plunge freezing technology that is currently unavailable in our laboratory.

Different methods to prevent the adsorption of proteins to the air-water interface include the addition of detergents or surfactants that change the properties of this interface (189). This method, however, has mostly been tested with soluble proteins and their applicability for transmembrane proteins remains to be tested. Another technique to avoid the interaction of protein to the air-water interface involves the use of support films that sequester protein molecules to the cryo-EM grid, preventing them from reaching the surface of the aqueous film.

4.7 Immobilization of GluD2 on continuous carbon results in a high-percentage of non-denatured particles

In order to circumvent denaturation of GluD2 at the air-water interface, I next set out to prepare cryo-EM grids of GluD2 using grids with a thin (~2nm), continuous carbon layer. Additionally, Nb381 was added with 1,5-fold molar excess to the sample, with the purpose to rigidify the extracellular region of GluD2. Application of protein at a concentration of 0.13 mg/ml resulted in grids with good particle distribution. These grids were then used for data collection on a Titan Krios microscope, using equivalent parameters as described above. An exemplary micrograph and corresponding power spectrum can be seen in **Figure 4-9 A**.

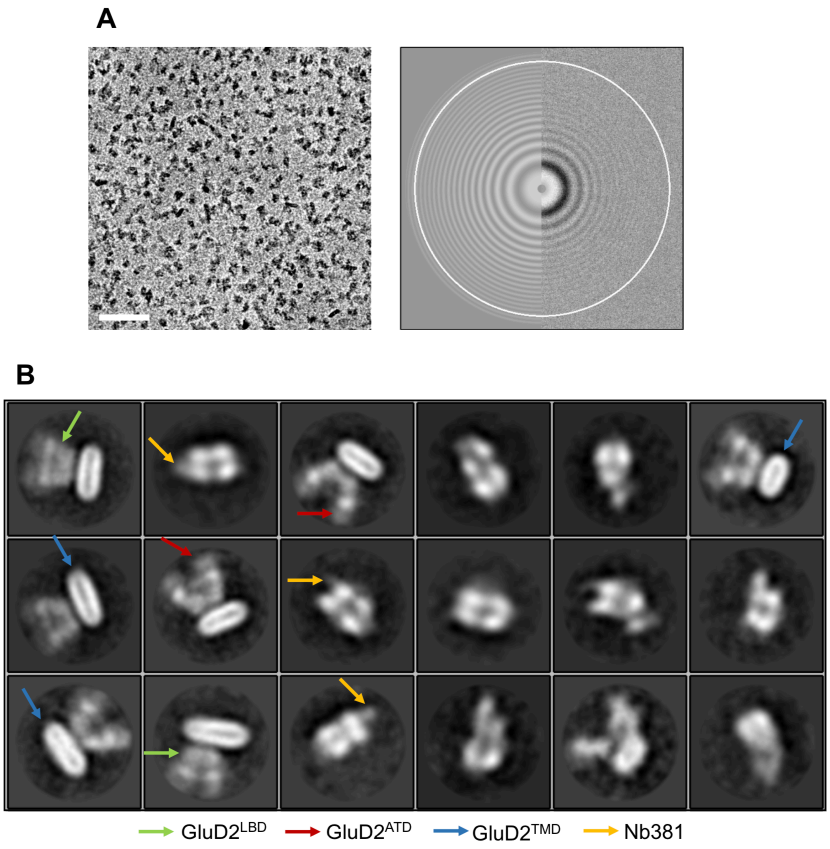

Figure 4-9 **Exemplary micrograph and 2D class averages of GluD2 in complex with nanobody 381** (**A**) Exemplary dose-weighted, motion-corrected micrograph and corresponding fitted power spectrum of GluD2 in complex with Nb381 on a continuous carbon layer. Scale bar: 60 nm. (**B**) Exemplary 2D class averages (obtained in RELION) of particles picked from the GluD2+Nb381 dataset. Density for Nb381 can be observed in top views of the receptor, protruding sideways (yellow arrows). As opposed to the dataset obtained in complex with Nb399, the amino-terminal domains are better defined and less flexible (red arrows). The most prominent features correspond to the nanodisc surrounding the transmembrane domain (blue arrows). Mask diameter: 260 Å.

Data were processed as described for the previous datasets, resulting in 2D class averages that are depicted in **Figure 4-9 B**. Of 100,938 particles picked, 80% resemble GluD2, suggesting that the use of continuous carbon is indeed an effective method to avoid denaturation by contact with the air-water interface.

4.8 Nanobody 381 stabilizes the GluD2 extracellular region

In the previous chapter, the crystal structure of GluD2^{ATD} in complex with Nb381 revealed that the nanobody binds to the membrane-proximal side of the ATD, in close proximity to the adjacent ligand-binding domains. I hence hypothesized that Nb381 would be able bridge both domains, potentially rigidifying the GluD2 extracellular region. The 2D class averages resulting from the dataset obtained from GluD2 in complex with Nb381 seem to confirm this hypothesis (see **Figure 4-9 B**). Particularly in comparison to the GluD2-Nb399 dataset, the amino-terminal domains are better defined and less flexible when Nb381 is added during the preparation of cryo-EM grids. The differences between both datasets could however also stem from the different cryo-EM grid preparation techniques. The GluD2-Nb399 dataset was obtained from cryo-EM grids without carbon support, where the protein particles are more vulnerable to denaturation at the air-water interface. The high degree of flexibility observed for GluD2 in complex with Nb399, in comparison to GluD2-Nb381, could hence be a consequence of this denaturation.

In the 2D classes obtained from the GluD2-Nb381 dataset, the nanobody can be vaguely distinguished in top views of GluD2, as two densities protruding sideways. In contrast to Nb399, which disrupts the tetrameric receptor and binds to 4 sites, Nb381 only accesses the two outward-facing binding sites. The preference of Nb381 for these sites might be due to steric clashes, but most likely stems from an increased affinity due to association to the neighbouring ligand-binding domains. Due to the subunit crossover at the iGluR ATD-LBD

interface, the Nb381 binding sites facing the centre of the receptor are not symmetric to the outer sides, and they do not provide the proximity to the ligand-binding domains because the ATD-LBD linkers necessarily adopt an extended conformation.

2D classes containing features that resembled an iGluR were used for 3D classification. A low-pass filtered map from a GluK2 receptor, kindly provided by Dr Patricia Brown, was used as a reference for initial rounds of 3D classification. At the time of writing, the resulting 3D classes did not yet converge to high-resolution maps. The best 3D class average is depicted in **Figure 4-10 A-C**, revealing the general architecture of GluD2, consistent with a tetrameric assembly.

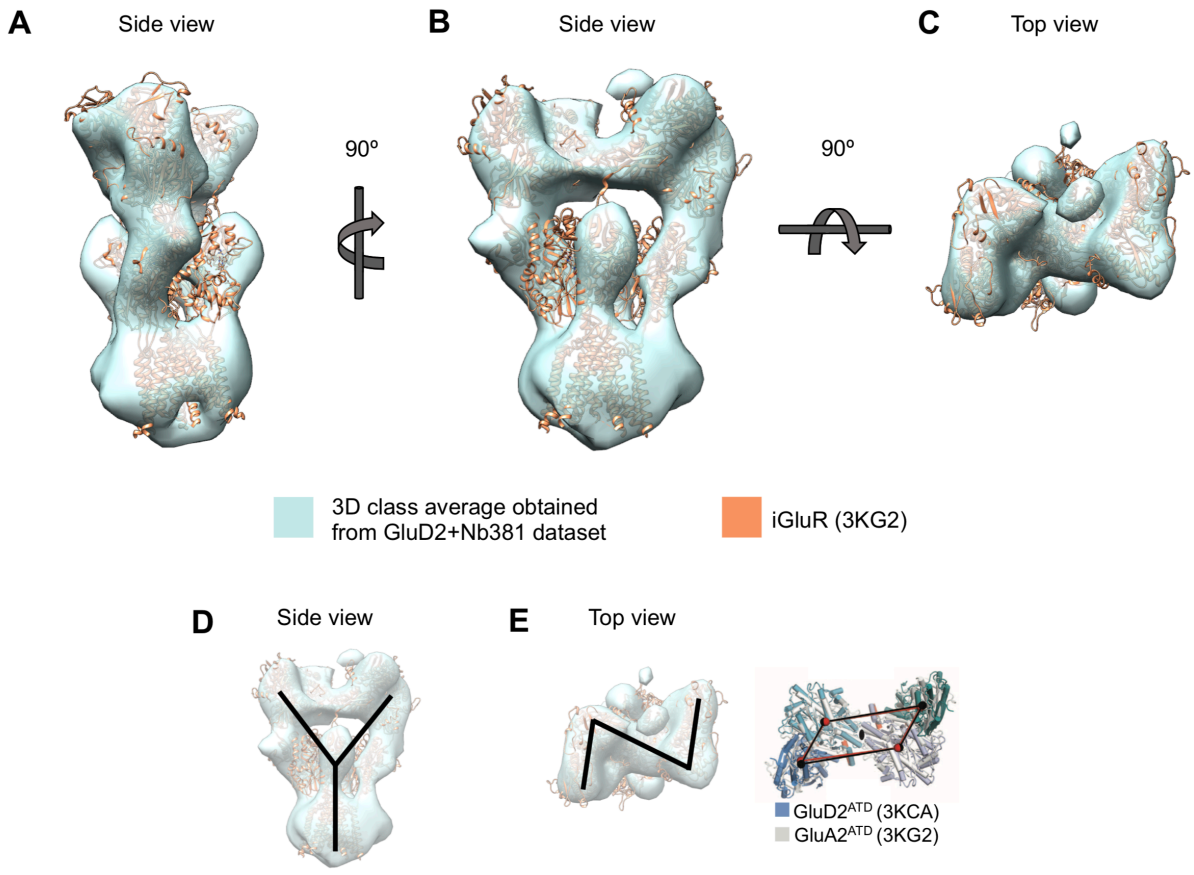

Figure 4-10 **3D class average of the GluD2-Nb381 dataset** (**A-C**) Side and top views of a reconstructed cryo-EM map obtained from the GluD2-Nb381 dataset, with the crystal structure of an AMPA receptor (3KG2) fitted into the map (fitting was done within Chimera (156)). (**D**) As has been observed for AMPA receptors, GluD2 also adopts an extended 'Y' conformation. (**E**) Top view of the GluD2-Nb381 3D class average, compared to the superposed crystal structures of GluD2 (PDB 3KCA) and GluA2 (PDB 3KG2) (figure adapted from Elegheert *et al*. (2)). The GluD2-Nb381 map displays an N-shaped ATD layer, in accordance with the crystal structure of $GluD2^{ATD}$.

As previously reported for AMPA receptors (46, 190, 191), the extracellular region of GluD2 adopts an extended, 'Y'-shaped conformation (**Figure 4-10 D**). This is in agreement with the relative domain arrangement observed in the GluD2^{ATD}-Cbln1 crystal structure (2), where the amino-terminal domains form a dimer of dimers and adopt an 'N'-shape when viewed from the top (**Figure 4-10 E**). Fitting the crystal structure of GluA2 (PDB 3KG2) into the reconstructed cryo-EM map of GluD2-Nb381 results in an overall good correlation, with the exception of the ligand-binding domains, where the observed density does not fit the model (**Figure 4-10 A-C**).

4.9 Summary and conclusions drawn from chapter 4

In this chapter, I set out to study the full-length GluD2 receptor by single-particle cryo-EM and to investigate the effect of the nanobodies characterized in chapter 3. In order to obtain structural information of GluD2 in a lipidic environment, I established a protocol to purify GluD2 and reconstitute the receptor in a lipidic bilayer, surrounded by membrane scaffold proteins (nanodiscs). This protocol resulted in pure, stable and monodisperse GluD2 samples, which were suitable for the preparation of cryo-EM grids.

The crystal structure of GluD2^{LBD} in complex with Nb399 revealed that Nb399 is able to stabilize the GluD2^{LBD} dimers and lock the GluD2^{LBD} lobes in a closed and active conformation. Due to steric clashes, I hypothesized that Nb399 would only bind to the two outward-facing binding sites in a tetrameric receptor. However, 2D class averages obtained from a GluD2-Nb399 cryo-EM dataset, revealed that Nb399 is able to disturb the GluD2 tetrameric conformation and binds to all four binding sites. The increased conformational heterogeneity resulting from addition of Nb399 prevented further analysis of this data.

Next, I set out to obtain cryo-EM data on GluD2 in its *apo* form. This dataset revealed that GluD2 suffers a severe case of denaturation at the air-water interface, since 2D classes

representing only 4% of particles contained features resembling GluD2. To circumvent this problem, the following cryo-EM grids were prepared using grids with a thin and continuous carbon layer. A high percentage of particles that resembled GluD2 were obtained from these grids, confirming that sequestering the particles to a support film is an effective method to avoid denaturation at the air-water interface.

A dataset of GluD2 in complex with Nb381, using continuous carbon support, was obtained. 2D class averages revealed that the GluD2 amino-terminal domains are well defined and less flexible than observed for the GluD2-Nb399 dataset. This observation confirms that Nb381 is able to stabilize the GluD2 extracellular region, making it an extremely useful tool for the structural analysis of GluD2. Furthermore, and contrary to Nb399, Nb381 does not disturb the tetrameric conformation of GluD2 and is only found to occupy the two outer binding sites. 3D class averages obtained from this dataset revealed the general architecture of the GluD2 receptor, which adopts an extended, 'Y'-conformation. Owing to the low resolution of the maps obtained, further interpretation of the data was not possible. Nevertheless, the work presented in this chapter paves the way towards obtaining a single particle cryo-EM structure of GluD2, stabilized in different conformations by the use of nanobodies.

Immediate steps toward this goal will be to explore alternative methods to avoid particle interactions with water surfaces. One successful approach to tackle preferential orientations of particles in ice is the use of so called 'megabodies'. Megabodies are enlarged nanobodies, were the scaffold is extended by fusion to the extracellular adhesin domain of *Helicobacter pylori* (HopQ). Although the mechanism is not well understood, the addition of megabodies has proved effective in preventing the adsorption of $GABA_A$ receptors to the ice surface, leading to their random orientation in ice (159, 160). For GluD2, the generation of

megabodies based on Nb381 or Nb389 could provide useful tools to prevent interactions with the air-water interface.

In addition, the recent development of gold grids with a functionalized monolayer of graphene have delivered promising results in regards to specimen preparation reliability (192). These specimens might prove beneficial in the preparation of GluD2 cryo-EM grids.

As mentioned above, the time elapsed between blotting of the EM grids and freezing has been reported to influence the interactions of particles with the air-water interface (188). The prototype of a rapid plunge-freezing robot as proposed by Noble *et al.* (188) has recently become available, and might aid in the preparation of grids where GluD2 is less exposed to the air-water interface.

Finally, strategies involving mild fluorinated detergents have been reported to ameliorate the preferential orientation of particles in ice (193) and might also hold the potential of avoiding denaturation of particle by their interaction with the air-water interface.

5. Analysis of RPTPμ-mediated cell contacts by cryo electron tomography

5.1 Aims of this chapter

Chapters 3 and 4 were dedicated to study the trans-synaptic GluD2-Cbln1-βNrx1 triad, particularly the signalling mechanism of GluD2. For the next two chapters of this thesis, I focused my attention on another class of cell-adhesion molecules, the class IIb Receptor Protein Tyrosine Phosphatase μ (RPTPμ). The aim of this chapter is to a) establish the overall architecture of the RPTPμ homophilic dimer in a native environment and b) investigate whether RPTPμ forms ordered clusters on the surface of cell-cell interfaces.

5.2 Establishing a workflow for *in-situ* studies of RPTPμ

Studying protein complexes in their native environment by cryo transmission electron microscopy (cryo-TEM) poses a number of difficulties.

Firstly, TEM imposes a sample thickness limitation to about 500 nm, above which objects are not electron transparent enough to be imaged. Furthermore, samples of about 100 nm or below are preferred, since thinner samples will inherently have a better contrast and allow for the collection of higher resolution information. Obtaining vitreous samples is a pre-requisite for cryo-EM, and this imposes a further thickness limitation. Currently, the most common methods to achieve vitreous ice are limited to 10 μm (by plunge-freezing grids in liquid ethane) and 200 μm (by high-pressure freezing). Due to the thickness limitation imposed by freezing methods, biological material to be imaged needs to be derived from slices of tissue, or from cell-culture systems.

Another difficulty when studying protein complexes in a native environment stems from a biological limitation. Obtaining and culturing primary cells (Purkinje neurons or endothelial cells, in the case of RPTPμ) is not straightforward and requires highly specialized protocols, limiting the availability of biological material. The lack of fluorescently tagged proteins of interest in a native sample precludes the possibility to selectively target areas during sample preparation and cryo-EM data collection. In addition, the molecular heterogeneity and complexity of a cell-cell contact makes it more difficult to identify the protein of interest during analysis of cryo-EM data.

To circumvent the above-mentioned difficulties, I devised a simpler system to study RPTPμ in a cellular context. Although this system does not reflect the native environment of RPTPμ in human tissue, it is an important stepping stone to understand the architecture of cell-spanning receptor complexes *in situ*. In this simpler system, fluorescently tagged human RPTPμ is overexpressed in Sf9 insect cells, which are grown on cryo-EM grids. RPTPμ-mediated cell-cell contacts are then targeted for cryo-EM data collection. The motivation to use Sf9 insect cells as a model to study cell-cell interactions is based on two reasons. Firstly, Sf9 insect cells can be grown in suspension and they normally form no cell clusters. This is

an important pre-requisite to assess specific clustering events induced by the expression of cell adhesion molecules (CAMs) on cell surfaces. The specificity of CAMs has traditionally been studied by clustering assays using insect cells. Secondly, Sf9 insect cells typically have a diameter of about 10 µm and hence are suitable for plunge-freezing in liquid ethane.

5.3 Overexpression of RPTPµ causes cell clusters that can be targeted by FIB milling

The first step towards studying RPTPµ-induced cell-cell contacts was to obtain Sf9 cell clusters. Using a Baculovirus expression system, C-terminally mVenus-tagged RPTPµ was overexpressed in Sf9 insect cells (more details can be found in Materials & Methods, section 2.13). As demonstrated previously (109, 118, 121), the presence of RPTPµ on SF9 cell surfaces led to the formation of cell clusters (**Figure 5-1**). The size of the clusters increased with time, until the replication of the baculovirus particles resulted in Sf9 cell death.

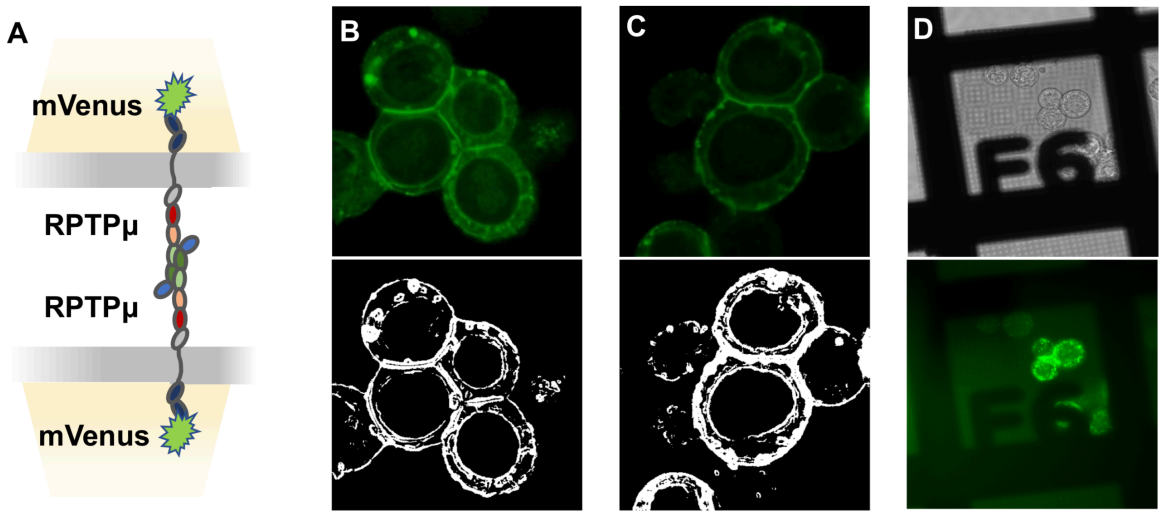

Figure 5-1 **Overexpression of RPTPµ leads to the formation of cell clusters** (**A**) Schematic representation of a RPTPµ homophilic dimer in trans, mediating a cell contact. (**B-C**) Confocal microscopy images of Sf9 cells, green signal corresponds to RPTPµ-mVenus fluorescence (top panels). RPTPµ overexpression leads to the formation of cell clusters, where RPTPµ is enriched at sites of cell-cell contacts. The interfaces between cells are remarkably flat (see cartoon representation in lower panels). (**D**) Cell clusters were grown in suspension and then seeded on EM grids, previously coated with fibronectin.

Because of the size limitation imposed by freezing techniques discussed previously, I aimed to obtain clusters of about 2-4 cells which could then be grown as monolayers on cryo-EM grids. Sf9 cell clusters of this size were obtained 19 h after baculoviral infection. The clusters were then seeded on EM grids, previously coated with fibronectin to promote cell attachment. The cell density was adjusted so that cell confluency on the EM grid reached about 40%. The cell confluency was particularly important for two reasons. Firstly, removing excess growth medium from a grid with a fully confluent culture is less effective, which results in a thicker sample and high probabilities to obtain non-vitreous ice. Secondly, identifying suitable cell-cell contacts for cryo-FIB milling and data collection is easier when cell-clumps are sparse. Upon seeding of Sf9 cell clusters on EM grids, the expression of RPTPμ was maintained for further 24h prior to grid freezing. Inspection of Sf9 cells overexpressing mVenus-tagged RPTPμ by light microscopy showed that RPTPμ is predominantly located on the cell surface **Figure 5-1**. Specks of RPTPμ were also visible in the cytoplasm. In cells forming clusters, RPTPμ is greatly enriched at the cell contacts and the interfaces appear to be planar and continuous. The enrichment of RPTPμ at cell contacts has been observed previously by Gebbink *et al.* (121), leading the authors to suggest that RPTPμ associates laterally on cell-cell surfaces, in addition to their homophilic interaction in *trans*.

EM grid freezing was done by plunge-freezing into liquid ethane, either manually or using the GP2 plunger (Leica) and excess growth media was removed by back-side blotting to avoid damaging the cells. As discussed above, one of the main limitations of TEM is the requirement of a thin (< 500 nm) sample. In order to obtain samples that are suitable for cryo-TEM imaging, I used focused ion beam (FIB) milling to produce thin (~ 100 nm) sections. By targeting the junctions of cell clusters on the cryo-EM grids, it was possible to obtain lamellae of cell-cell contacts (**Figure 5-2**).

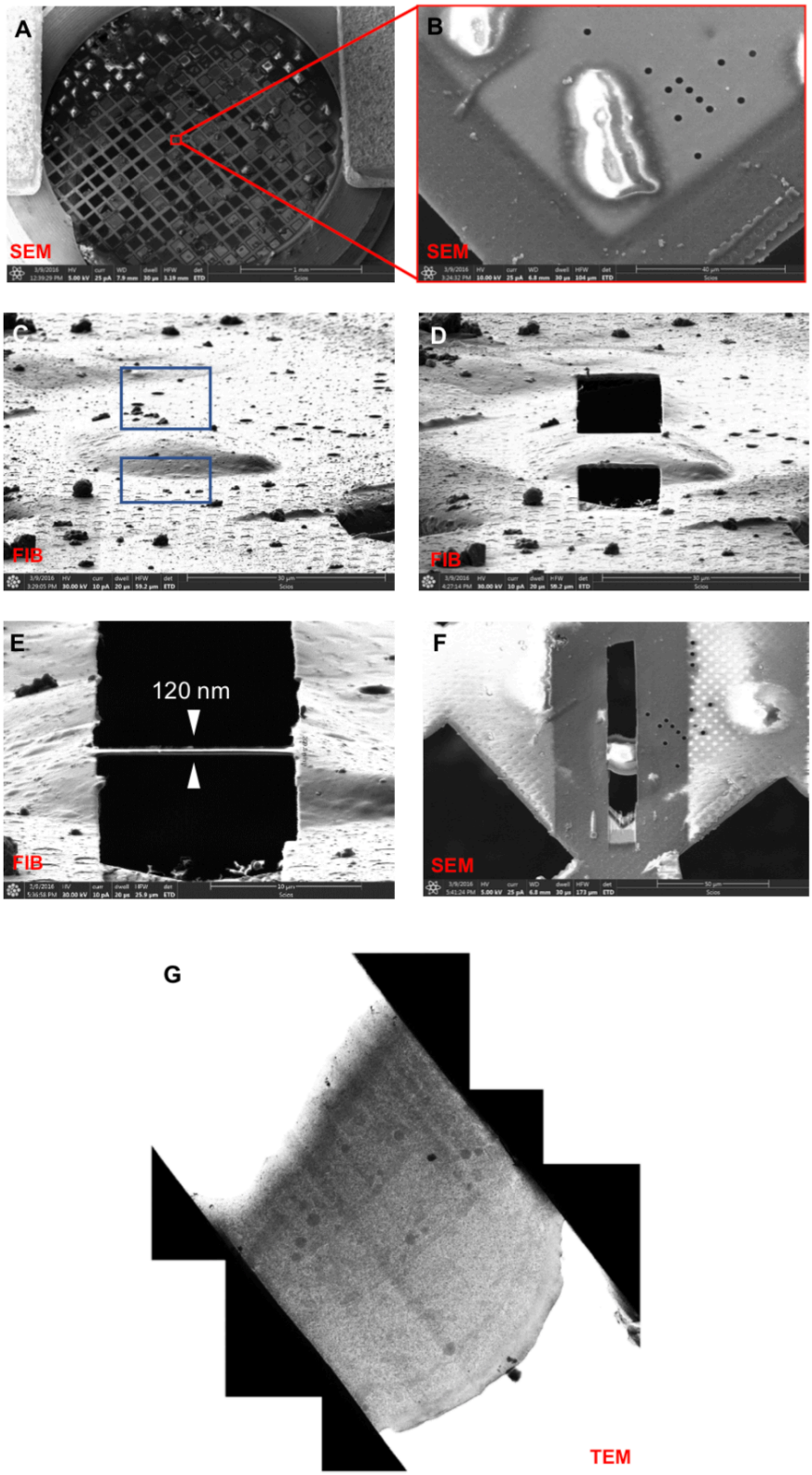

Figure 5-2 **Focused Ion Beam milling of cell-cell contacts lead to thin sections that can be imaged by TEM** (**A**) Scanning Electron Microscopy (SEM) overview of a representative cryo EM grid, seeded with Sf9 cell clusters. (**B**) Representative cluster of two cells, imaged by SEM. (**C**) Cluster of cells depicted in (B) but imaged with the Focused Ion Beam (FIB). The blue rectangles represent the areas that are removed by the FIB during coarse milling steps. (**D**) Same view as in (C), after the marked areas were removed by coarse milling. (**E**) Consecutive fine milling steps lead to the generation of a thin (100-150 nm) section, depicted in the FIB from the front. (**F**) Same section as seen in (E), imaged from the top with the SEM. (**G**) Stitched TEM images, depicting an representative section through a Sf9 cell.

5.4 Cell-cell contacts can be observed by TEM

Upon inspection of the FIB milled lamellae by cryo-TEM, it was possible to distinguish several characteristic features of insect cells. The nuclei of Sf9 cells take up most of the cell's volume, pushing all other organelles into close proximity of the plasma membrane. Among other features, it is possible to clearly distinguish centrioles, polyhedral virion assemblies derived from the Baculovirus, peroxisome crystals, mitochondria, microtubules, various vesicles and the phospholipid bilayers of the plasma membrane.

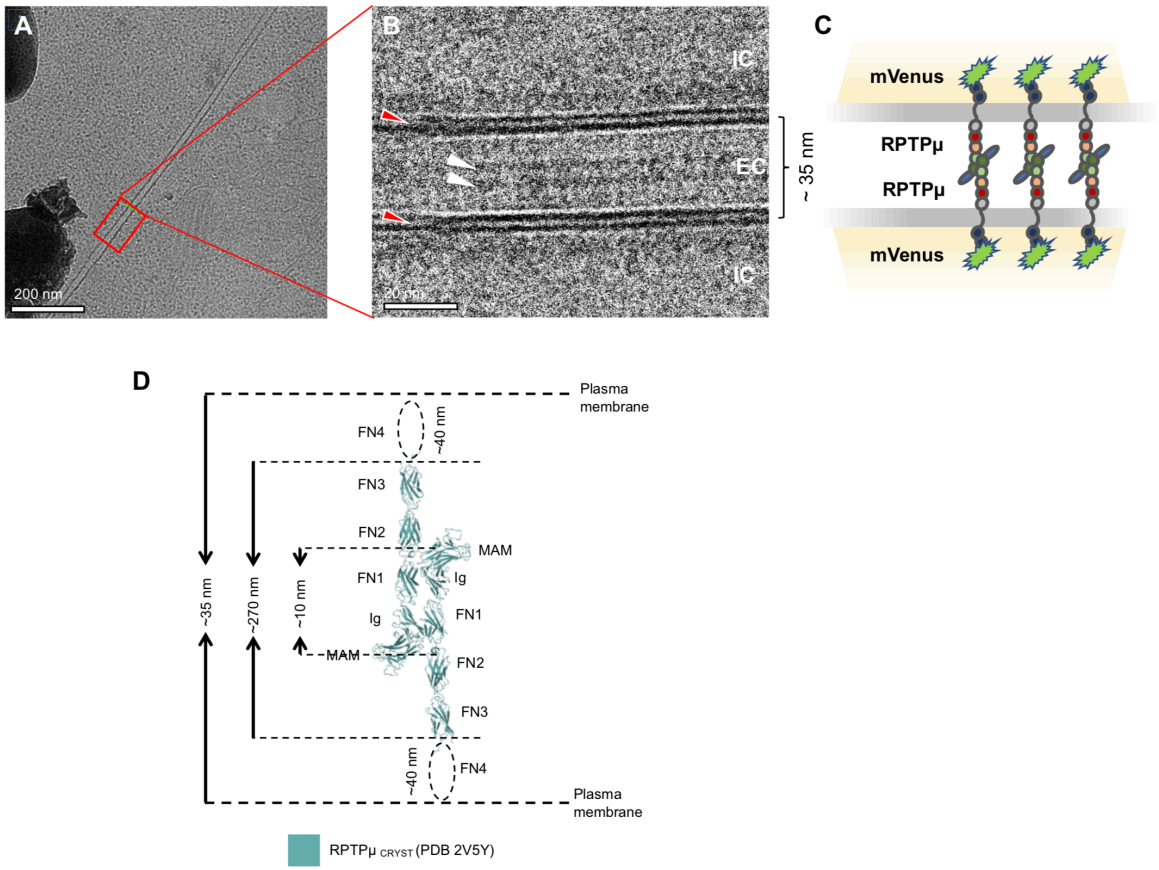

Figure 5-3 **RPTPμ-mediated cell contacts can be imaged by TEM** (**A**) Low magnification micrograph of a Sf9 cell section, displaying a cell-cell contact. (**B**) High magnification micrograph of cell-cell contact, representing the area marked with a red rectangle in (A). The lipid bilayers of the cell membranes are clearly distinguishable (red arrowheads) and they maintain a regular spacing of ~35 nm. Two, parallel lines of higher density can be observed between the cell membranes (white arrowheads). EC: extracellular space. IC: intracellular space. (**C**) Schematic representation of a RPTPμ-mediated cell contact, where RPTPμ trans-dimers maintain apposing cell membranes at a regular spacing. (**D**) Crystal structure of the extracellular region of RPTPμ (PDB ID 2V5Y). The distance observed between plasma membranes accommodates for the length of the crystal structure, in addition of two fibronectin domains which were not modelled.

Of particular interest, it was also possible to identify several cell contacts. The membrane-to-membrane spacing of these cell contacts was highly regular, with an average distance of ~35 nm (**Figure 5-3**). This spacing accommodates the length of a RPTPμ extracellular region *trans*-dimer (~ 27 nm), as determined previously by X-ray crystallography (109). The crystal structure does not account for the entire gap between the membranes, since the membrane-proximal fibronectin domain was not modelled into the crystal structure due to weak electron density. In addition, two central, parallel lines of higher electron density could be observed between apposing cell membranes. These lines also maintain a regular spacing of ~10 nm between each other, which matches the distance between the protruding MAM domains in the RPTPμ extracellular region crystal structure (**Figure 5-3 D**). These observations suggest that the density observed between apposing cell membranes corresponds to RPTPμ, and that the regular cell-cell contacts are indeed a consequence of RPTPμ overexpression. Interestingly, the fact that the two central lines of higher density (attributed to RPTPμ MAM domains) are continuous, suggests a dense arrangement of RPTPμ molecules at the cell-cell contact. Whether or not such a tight arrangement is supported by specific lateral oligomerization interactions is not clear.

5.5 Overexpression of RPTPμ leads to the formation of cytoplasmic membrane stacks

Apart from the features named in the previous section, the cryo-FIB milled lamellae also revealed the presence of extensive (300-800 nm long), regularly spaced membrane stacks extending from the endoplasmic reticulum (ER) (**Figure 5-4**). The spacing between these ER membranes alternates between thinner (~25 nm) and wider (~35 nm) gaps. As observed for the cell contacts, the wider gaps also display two central, parallel lines of higher density, separated by a ~10 nm gap. An overlay of intensity plots derived from sections of cell

contacts and ER membrane stacks revealed an identical profile (**Figure 5-5**), suggesting that RPTPμ is also present in the ER membrane stacks and leads to their regular arrangement.

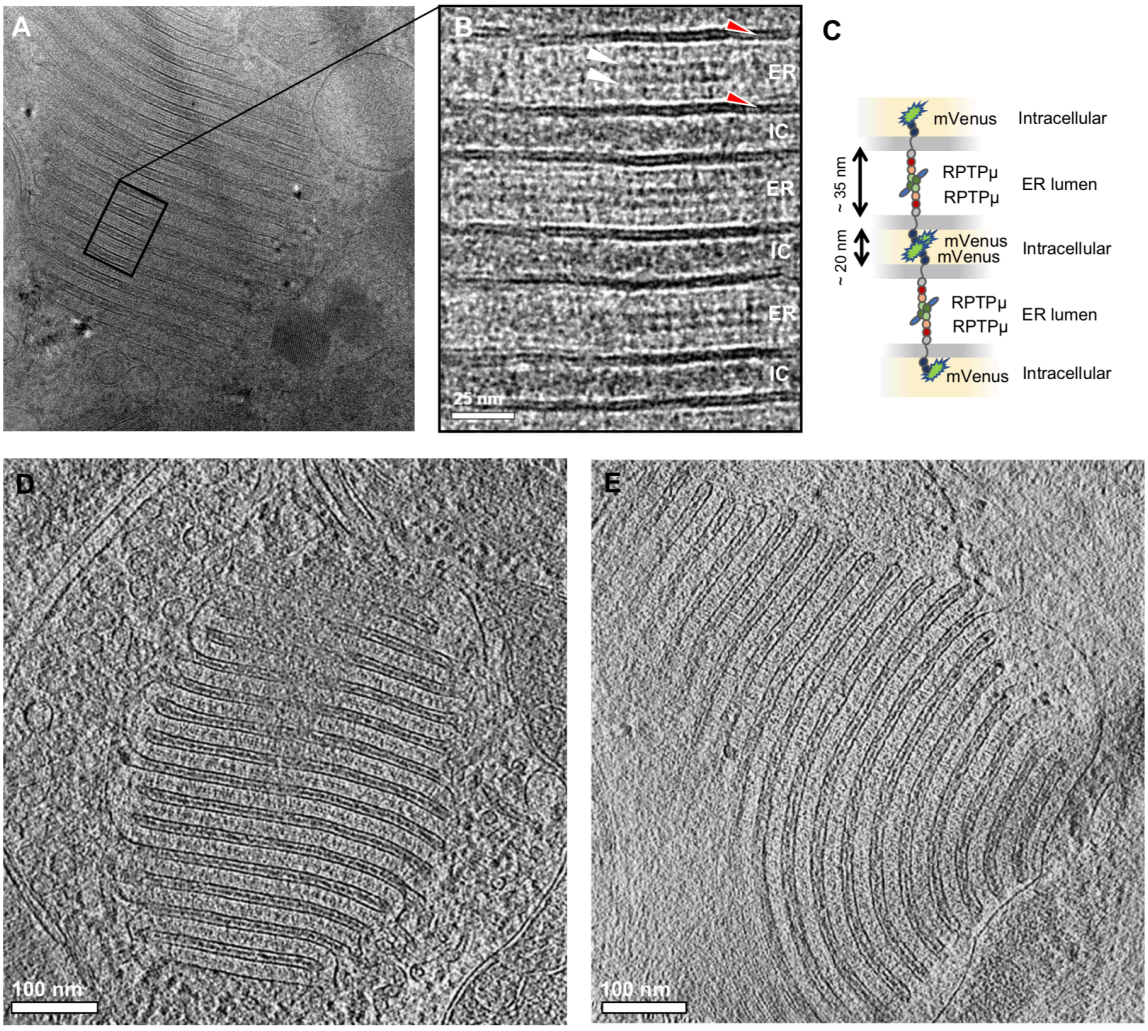

Figure 5-4 **Overexpression of RPTPμ leads to the formation of regularly spaced ER membrane stacks in the cytoplasm** (**A**) Micrograph of a FIB milled section through a Sf9 cell overexpressing RPTPμ. A pattern of regularly spaced membranes can be observed in the cytoplasm. (**B**) Enlarged view of the area marked in a black rectangle shown in (A). Membranes are clearly distinguishable (red arrowheads). Two parallel lines of higher density can be observed between apposing membranes (white arrowheads). ER: endoplasmic reticulum lumen. IC: intracellular space. (**C**) Schematic representation of the regularly spaced membranes stacks shown in (A-B). Overexpression of RPTPμ leads to the association of apposing membranes in the secretory pathway. (**D-E**) Tomographic slices (4.22 Å/pix) of Sf9 cells thinned by cryo-FIB milling, displaying regularly spaced membrane stacks in the cytoplasm.

The origin of these extensive membranous structures is not clear; however, I hypothesize that they are a result from the overexpression of RPTPμ-mVenus. High concentrations of the protein could lead to a premature dimerization of the extracellular region in the lumen of the ER, resulting in the association of apposing ER membranes and the restructuring of

the tubular ER network. This phenomenon has been observed previously for other dimerizing, membrane bound proteins (194, 195).

The pH in the ER lumen (corresponding to the wider, ~35 nm gaps in the membrane stacks) is neutral (196), which offers a favourable environment for the dimerization of the RPTPμ extracellular regions. The thinner, ~25 nm gaps correspond to the cytoplasm, containing the RPTPμ C-terminal phosphatase domains and mVenus tag. These thinner gaps also maintain a regular spacing throughout the membrane stacks, raising the question of whether the association of their apposing membranes could also be regulated by the specific interaction of proteins.

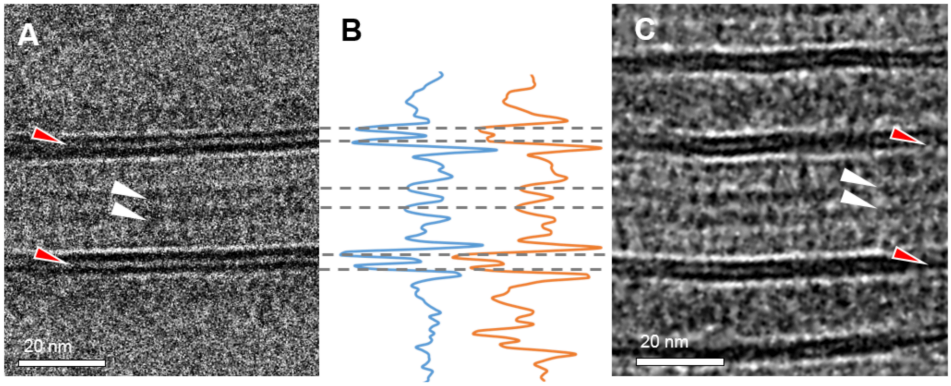

Figure 5-5 **Comparison of RPTPμ-mediated cell contacts and regularly spaced ER membrane stacks** (**A**) Micrograph of a cell contact, displaying the cell membranes (red arrowheads) and two parallel lines of higher density between the apposing membranes (white arrowheads). (**B**) Intensity plots of the cell contact shown in (A) (blue trace) and of the membrane stacks shown in (C) (orange trace). The dotted lines indicate the position of the intensity peaks, which correspond to the lipid bilayers of the plasma membranes (or ER membranes) and to the two central parallel lines between apposing membranes. (**C**) Micrograph of a regularly-spaced membrane stack, displaying lipid bilayers (red arrowheads) and two parallel lines of higher density between the apposing membranes (white arrowheads).

5.6 Correlative light and electron microscopy experiments reveal that membrane stacks contain RPTPμ

To confirm that the observed membrane stacks contain RPTPμ, I next performed correlative light and electron microscopy (CLEM) experiments of plastic-embedded Sf9 cells overexpressing RPTPμ. Cell clusters were high-pressure frozen, subjected to freeze-substitution with lowicryl and sectioned to 300 nm thick slices.

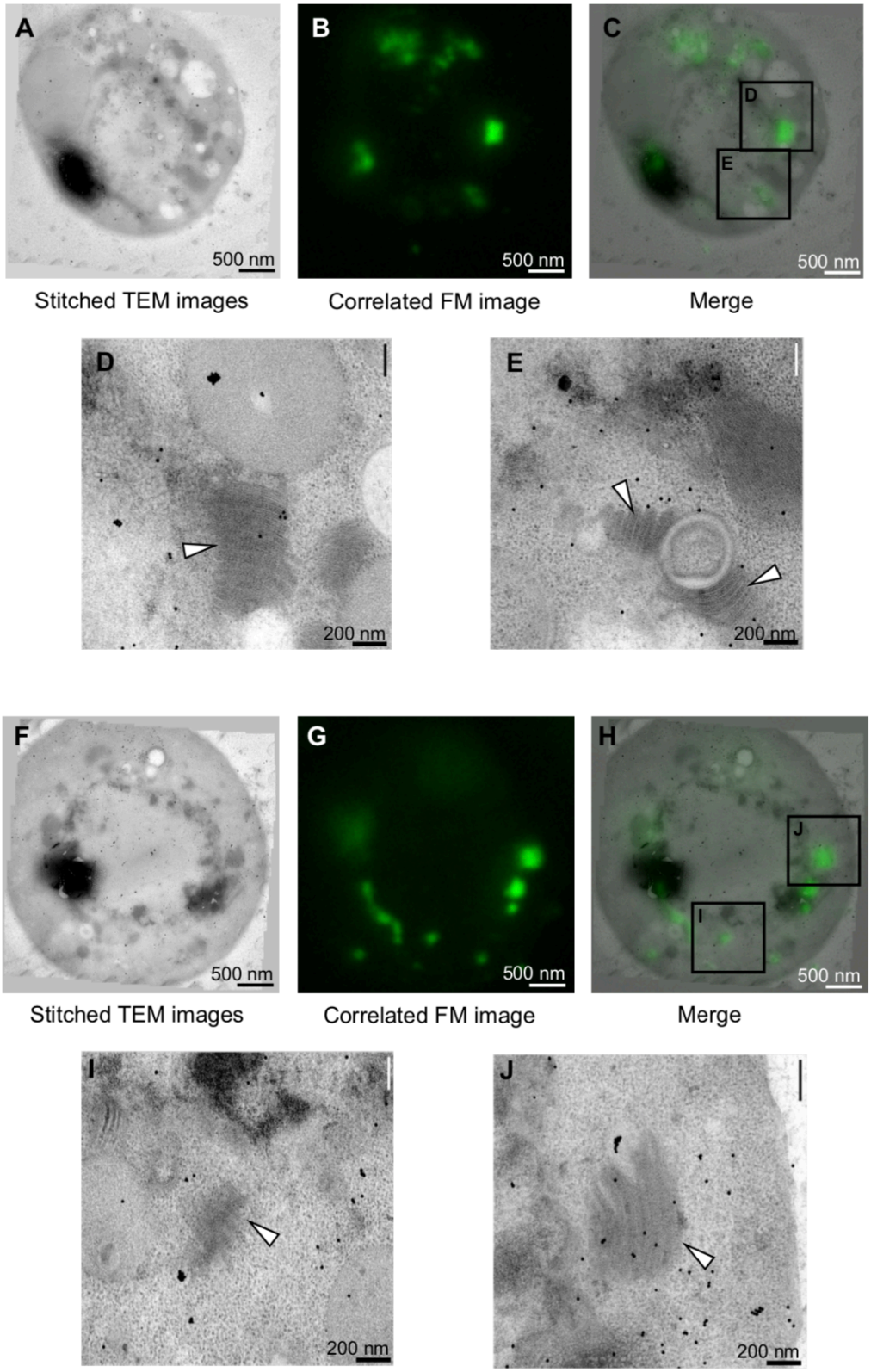

Figure 5-6 **Correlative light and electron microscopy experiments confirm that membrane stacks contain RPTPμ** (**A** and **F**) Stitched, low magnification STEM images of 300 nm slices of lowicryl-embedded Sf9 cells, frozen after 67h of RPTPμ expression. (**B** and **G**) Fluorescence microscopy images of the Sf9 cells depicted in (A) and (F), respectively. Green signal corresponds to fluorescence of RPTPμ-mVenus. (**C** and **H**) Merged image of the electron and fluorescence microscopy images shown in (A), (B), (F) and (G). (**D, E, I, J**) Enlarged micrographs corresponding to the rectangular insets shown in (C) and (H). Membrane stacks (white arrowheads) correlate with areas of increased green fluorescence, confirming that they contain RPTPμ.

Plastic sections were then imaged under a fluorescence microscope (detecting signals for RPTPμ-mVenus and fluorescent tracking markers) and subsequently analysed by electron microscopy. Areas that presented high levels of green fluorescence were selected for the acquisition of electron tomograms.

The CLEM experiments revealed that spots of increased RPTPμ concentrations (evidenced by bright specks of green fluorescence in the cytoplasm) correlate with regular membrane stacks observed by EM (**Figure 5-6**). Although EM data obtained from plastic sections is inherently less detailed and of lower resolution than data obtained from cryo-preserved samples, the membrane stacks that were detected in the plastic-embedded cells have a similar spacing to those observed in cryo-FIB milled lamellae. These observations confirm that the regular membrane stacks observed in Sf9 cells are caused by the *trans*-dimerization of RPTPμ.

5.7 Subtomogram averaging of RPTPμ-mediated membrane stacks

Having confirmed that the observed ER membrane stacks contain RPTPμ, I considered that these cytoplasmic stacks would be a good model for the structural analysis of RPTPμ-mediated cell contacts. Obtaining cryo electron tomograms from membrane stacks offers the important advantage of greatly increasing the number of particles available for subtomogram averaging.

In order to subtract subtomograms, surface models were traced in the middle of apposing membranes using Dynamo (179) (**Figure 5-7 A-B**). Particle positions were seeded along the modelled surfaces, such that the particle centres were placed at the middle of a RPTPμ trans-dimer (**Figure 5-7 C**). Extracted subtomograms had a height of 65 nm, which accommodated for the length of a RPTPμ *trans*-dimer and the apposing membranes.

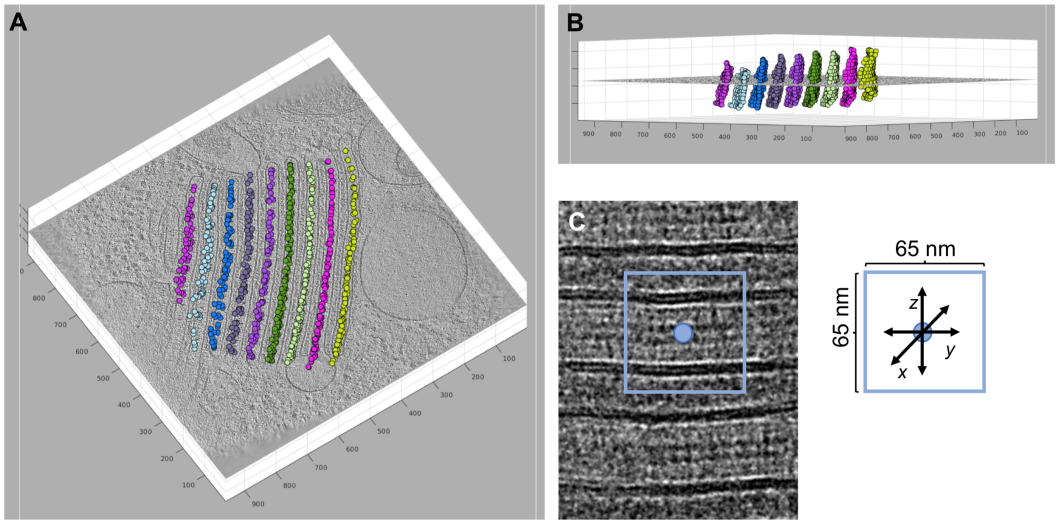

***Figure 5-7* RPTPμ particle picking in Dynamo for subtomogram averaging** (**A**) Tomographic slice through a regularly spaced membrane stack, showing coloured spheres for manually placed positions. These positions are then used within Dynamo (179) to generate surface models between apposing membranes. (**B**) Side view of the tomographic slice shown in (A), displaying positions for 9 surface models. (**C**) Voxels extracted using surface models produced in dynamo. The centre of the "particle" (represented by blue sphere) is placed between apposing membranes and at the centre of the RPTPμ homophilic trans-dimer. The extracted voxel has side lengths of 65 nm. The z-axis is set to be perpendicular to the membrane.

Initial subtomogram averaging stages involved a coarse translation search in *z*, in order to align the membranes of the subtomograms. The resulting averages after this initial round of alignment displayed a strong signal for the membranes, and also showed density for the two parallel lines observed previously in micrographs and tomographic slices (**Figure 5-8 A-B**). Because the membranes represented such strong features, subsequent rounds of processing required the use of masks that would exclude the membranes and focus the alignment on protein features. A multilevel angular search was applied at this stage, where coarse angular searches were followed by local searches around the best angular orientation deriving from the previous step (**Figure 5-8 C-D**). The next stage in the subtomogram averaging pipeline involved alignments with fine azimuthal rotation searches and tighter alignment masks (**Figure 5-8 E-F**). The final subtomogram average is depicted in **Figure 5-8 G**. Densities for the apposing membranes and the two central planes are clearly distinguishable. At the centre of the subtomogram, about 2-3 pillars of density can be observed, connecting the two central planes and extending towards the membranes.

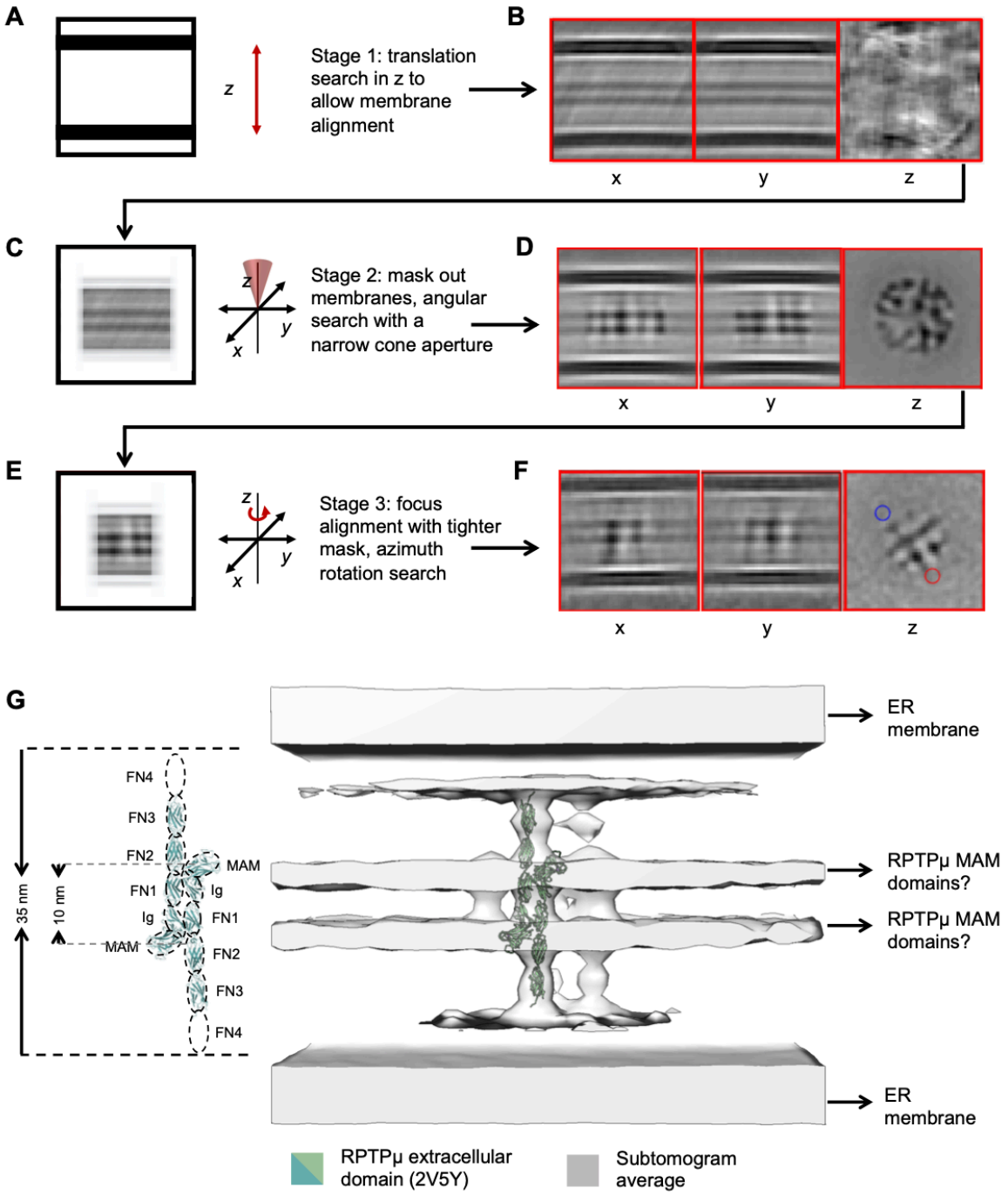

Figure 5-8 **Subtomogram averaging workflow for the RPTPμ-mediated membrane contacts** (**A**) The initial subtomogram averaging steps involved translation searches in *z* to allow for the alignment of the membranes. (**B**) First subtomogram average obtained upon aligning membranes. Images depict 1 pixel-thick slices through the average, in x, y and z orientations. The voxel is 48 pixels wide. (**C**) Subsequent rounds of processing involved using a cylindrical alignment mask that excluded the membranes and applying a multilevel angular search with a narrow cone aperture. (**D**) Representative average obtained after applying processing described in (C). Images depict 1 pixel-thick slices through the average, in x, y, z orientations. (**E**) Final stages of subtomogram averaging applied tighter alignment masks and applying azimuth rotation searches. (**F**) Average obtained from processing described in (E). Images depict 1 pixel-thick slices through the average, in x, y, z orientations. (**G**) Subtomogram average obtained in (E-F), displaying densities for the plasma/ER membranes, for the putative RPTPμ MAM domains (smeared laterally from neighbouring molecules) and for the RPTPμ trans dimer. The crystal structure of the RPTPμ extracellular region (PDB 2V5Y) was manually placed in the map for comparison. All subtomogram averaging was done within Dynamo (179). The 3D map was depicted with Chimera (156).

The crystal structure of the RPTPμ extracellular region fits loosely into one pillar. Interestingly, the protruding MAM domains match the position of the two central planes, suggesting that these densities could be attributed to this region of RPTPμ. If there is a dense packing of RPTPμ at the sites of cell-cell contacts, the MAM domains would form a seemingly continuous layer of protein density, giving rise to the lines observed in the tomograms or the parallel planes obtained in the subtomogram average. The other domains of RPTPμ, which would protrude like rods on either side of the smeared "MAM-domain-layer", would be less densely packed, since their footprint is smaller. However, outside of the volume allowed by the alignment mask, no pillars corresponding to the rest of RPTPμ could be observed in the subtomogram average. This could be explained in three ways.

Firstly, as a general rule, correct alignment of particles embedded in the continuous density of a membrane should result in an average where the density extends beyond the boundaries of the alignment mask. The fact that no pillars corresponding to RPTPμ are observed beyond the mask indicate that the alignments shown here are either incorrect or based on noise.

If, however, the alignments are correct, there are two further ways in which the lack of ordered RPTPμ densities can be explained.

Firstly, either the Ig and 4 fibronectin domains are so flexible- sampling diagonal conformations in relation to the membrane -that the alignment cannot reach convergence. Or secondly, RPTPμ is indeed a rigid rod, but the positions of RPTPμ molecules are random, and hence these densities are averaged out. Considering that the spacing between membranes is highly regular (35 nm) and that the length of the RPTPμ crystal structure in addition of the two missing fibronectin domains matches this spacing quite accurately, the RPTPμ molecules likely need to adopt a perpendicular orientation to the membrane in order to bridge the gap. Since there is little flexibility to adopt diagonal conformations, the first hypothesis cannot fully explain the lack of density for the fibronectin and Ig-like domains.

This conclusion brings us to the second hypothesis, which suggests that RPTPμ adopts random orientations when densely packed at membrane contact sites. The obtained subtomogram average depicted in **Figure 5-8 G** only displays pillar-like densities at the core of the map, within the volume allowed by the mask during alignment. If there was an ordered clustering of RPTPμ, rod-like densities should theoretically appear outside of the mask at regular spacings from those observed in the core of the map. This suggests that RPTPμ, despite adopting a dense arrangement at cell contact sites and in between apposing ER membranes, does not form ordered clusters.

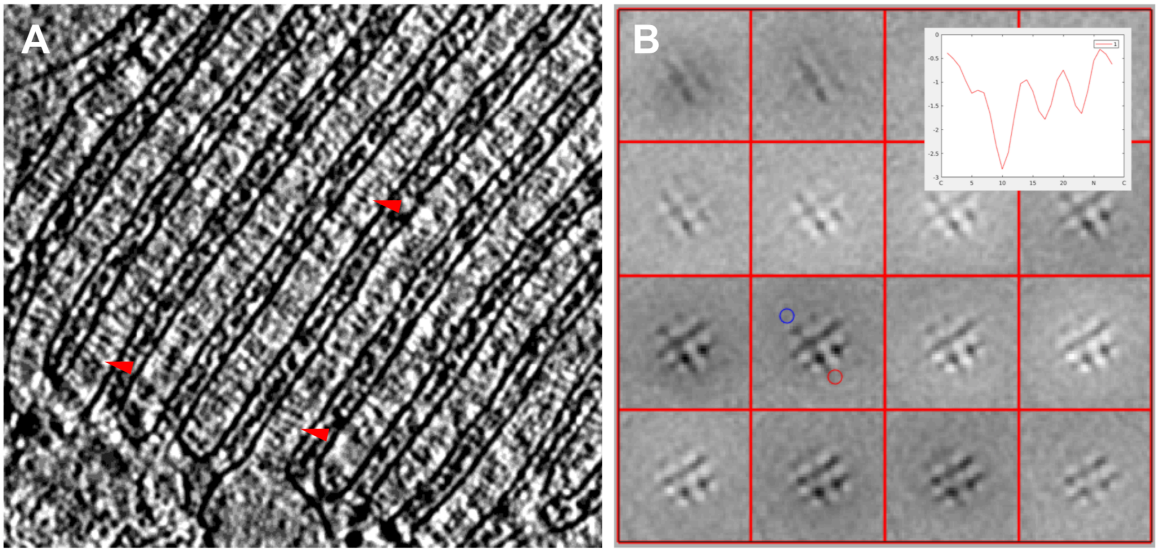

***Figure 5-9* RPTPμ homophilic dimers form sporadic regularly spaced zippers** (**A**) Tomographic slice of a cytoplasmic membrane stack, upon applying very strong contrast. Red arrowheads point to areas of highly ordered RPTPμ dimers, as evidenced by regularly-spaced rods connecting apposing membranes. (**B**) 1 pixel-thick slices in z through the subtomogram average depicted in ***Figure 5-8* E-G**. Images shown correspond to selected slices (17 to 32) of a total of 45 pixels. Plot in the upper right corner shows intensity cross-section between the red and blue circles, displaying regularly spaced intensity peaks.

Conversely, there are some observations that support the notion of an ordered RPTPμ array. Firstly, when analysing highly filtered tomographic slices of the ER membrane stacks, it is possible to discern patches of regularly spaced RPTPμ molecules forming zippers (**Figure 5-9 A**, red arrowheads). Secondly, the subtomogram average depicted in **Figure 5-8 G**,

displays evenly spaced densities at the core of the map. The images shown in **Figure 5-9 B** are 1 pixel-thick slices in *z* through the average, portraying 'top' views of the putative RPTPμ densities. A profile across these top views reveals a regular spacing between the intensity peaks.

Unfortunately, maps obtained by subtomogram averaging of RPTPμ at the ER membrane stacks did not reach high enough resolution to be able to conclusively reveal the higher-order architecture of RPTPμ in a native environment. I next decided to address this question by using a simpler model to study RPTPμ-induced contact sites.

5.8 Expression and purification of RPTPμ extracellular region leads to high protein yields

Following the methodology used to study protocadherins (197), I devised a strategy in which the soluble extracellular region of RPTPμ is used to decorate liposomes, which in turn form membrane-to-membrane contacts mediated by the RPTPμ homodimers.

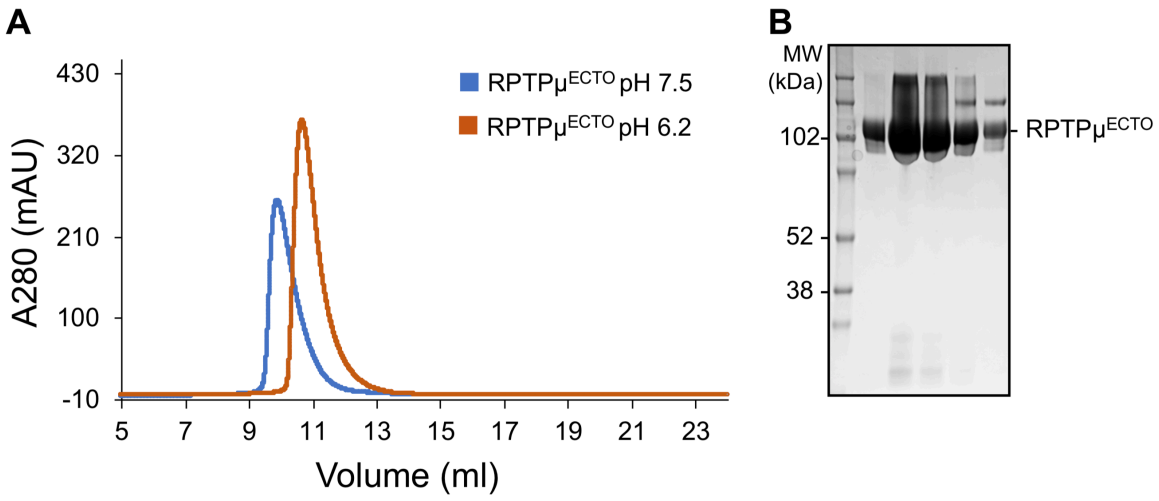

Figure 5-10 **The dimerization of the RPTPμ extracellular region is pH-dependent** (**A**) Size-exclusion chromatography (SEC) elution profiles of the RPTPμ extracellular region at pH 7.5 (blue trace) and pH 6.2 (orange trace). RPTPμ forms dimers at neutral pH, while the protein runs as a monomer at acidic pH values. (**B**) SDS-PAGE analysis of peak fractions obtained from the SEC run depicted in (A) (blue trace). Numbers on the left of the gel represent the molecular weights in kDa of the protein weight standards.

The resulting liposome clusters were then used for the preparation of cryo-EM grids and cryo-ET data collection. This strategy offers many advantages, including the possibility for high-throughput data collection, simpler sample preparation, the possibility to add tracking fiducials and a consistent ice quality.

The first step towards obtaining RPTPμ decorated liposomes, was to obtain a soluble RPTPμ extracellular region sample. A plasmid encoding the full extracellular region, comprising the MAM, Ig and fibronectin 1-4 domains was used for mammalian expression experiments, resulting in high protein yields. The RPTPμ extracellular region was then purified by Ni^{2+}-affinity chromatography and subsequent gel filtration, leading to >90% pure sample.

Previously, it has been reported that the dimerization of the RPTPμ extracellular region is pH dependent, where a neutral pH of 7.5 is compatible with the dimer, but an acidic pH of 6.2 leads to the monomerization of RPTPμ (109). This finding was confirmed by size-exclusion chromatography, as depicted in **Figure 5-10**.

5.9 Liposomes decorated with the RPTPμ extracellular region form low-order zippers

Upon obtaining a pure sample of RPTPμ extracellular region, liposomes were prepared by combining L-α-phosphatidylcholine with lipids that are modified to chelate Ni^{2+} (DGS-NTA(Ni)) (further details can be found in Materials & Methods, section 2.18). The immobilized nickel ions on the liposome surfaces were then used to capture the extracellular region of RPTPμ, which contained a membrane-proximal polyhistidine tag. In this way, it was possible to generate RPTPμ-decorated liposomes, that formed membrane-to-membrane contacts at neutral pH. The resulting liposome clusters were used for the preparation of cryo-EM grids and cryo electron tomography data was acquired.

Representative tomographic slices are depicted in **Figure 5-11**. The first observation that can be made is that individual RPTPμ molecules are easily discernible and that they indeed bridge the gap between neighbouring liposomes. However, the spacing between liposomes is less regular than the spacing observed at cell contacts or between apposing ER membranes. In accordance, the RPTPμ dimers do not appear to be strictly perpendicular to the membrane, but also adopt diagonal orientations.

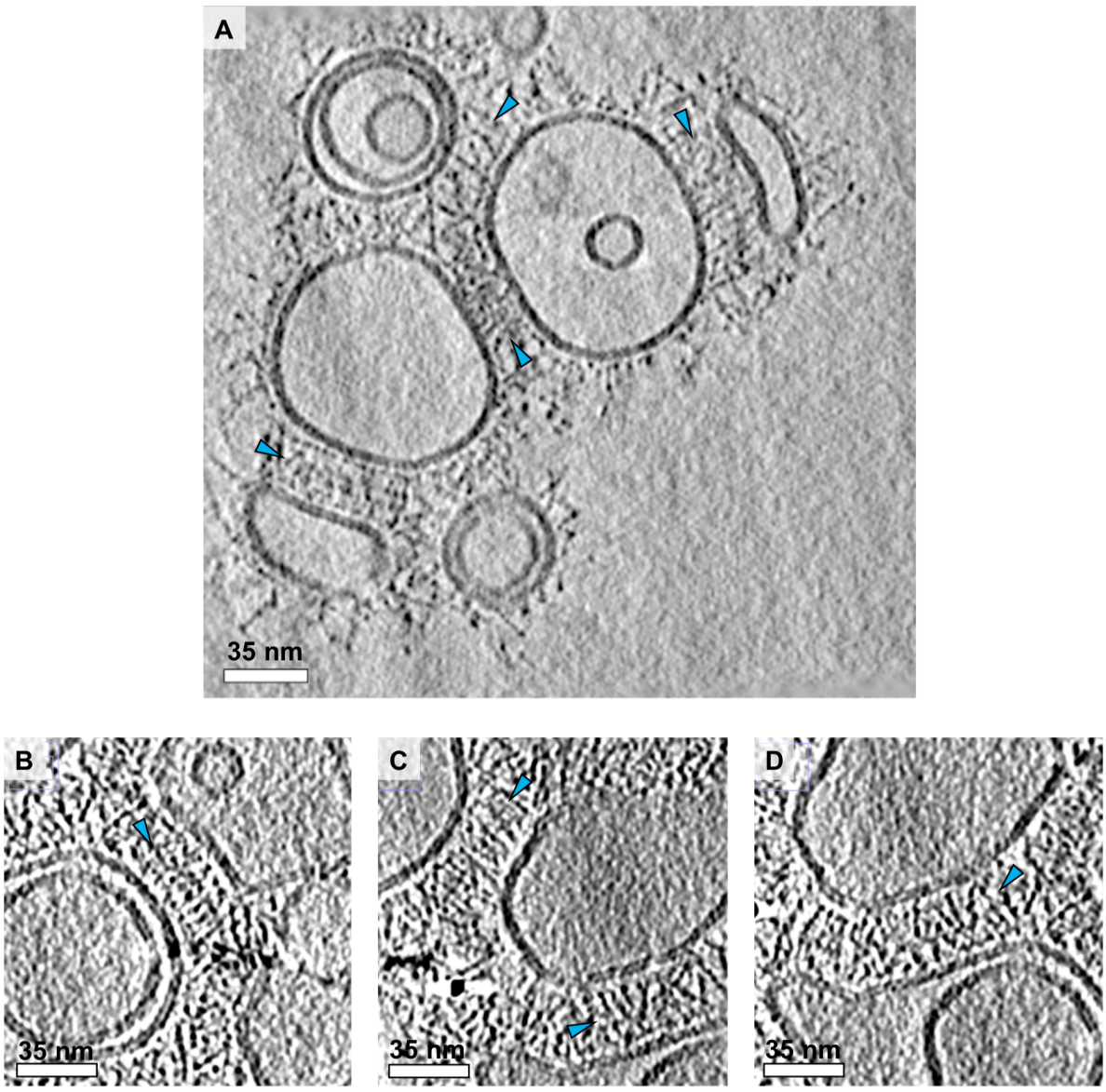

Figure 5-11 **Liposomes decorated with the extracellular region of RPTPμ form less ordered zippers** (**A-D**) Tomographic slices (1.08 Å/pix) of liposomes decorated with the extracellular region of RPTPμ. The dimerization of RPTPμ leads to the formation of liposome clusters. The membrane-to-membrane contacts (blue arrowheads) are less ordered than those observed in cells. Scale bar: 35 nm. The tomogram depicted in (A) was processed with a deconvolution filter (178).

Furthermore, the two lines of higher density observed in the cellular tomograms and attributed to the MAM domains cannot be observed in the contacts between liposomes. In general, the RPTPμ-mediated membrane-to-membrane contacts seem less regular in the liposome dataset, opening the question of whether this simpler strategy is a good representation of RPTPμ under physiological conditions.

An interesting possibility would be that the transmembrane domain and cytoplasmic region are needed in order for RPTPμ to form a dense arrangement at contact sites. To test this hypothesis, further experiments where full-length RPTPμ is reconstituted into liposomes will need to be carried out.

5.10 Summary and conclusion drawn from chapter 5

In this chapter, I set out to study the higher-order architecture of RPTPμ-mediated cell contacts. Specifically, the main aim was to determine whether RPTPμ forms ordered clusters at contact sites, and whether specific interaction in *cis* contribute to the formation of such clusters. In order to study RPTPμ in a native environment, I devised a strategy to study cell-cell contacts in a model system. Fluorescently tagged RPTPμ was overexpressed in Sf9 insect cells, which led to cell clustering due to the dimerization of RPTPμ on the cell surfaces. The cell clusters were then targeted by cryo FIB milling in order to render them suitable for cryo TEM imaging. This workflow proved to be successful, since several cell sections displaying cell contacts could be imaged in this way. Apart from cell contacts, extensive and regularly spaced membrane stacks could be observed in the cytoplasm. CLEM experiments using lowicryl-embedded cells confirmed that these stacks contained RPTPμ. Because the membrane spacing and the general features between cell contacts and membrane stacks were identical, they were deemed structurally equivalent for subsequent data analysis. Subtomogram averaging was conducted in order to obtain the higher-order

structure of RPTPμ at contact sites. Unfortunately, averaging of subtomograms obtained from the membrane stacks did not converge to an average of high enough resolution in order to assign the densities conclusively. However, the crystal structure of the RPTPμ extracellular region could be approximately fit into a pillar-shaped density at the core of the average. The fact that no further pillar-shaped densities could be observed outside of the volume of focused alignment, suggests that RPTPμ does not form a regular array at cell contact sites. On the other hand, when contemplating the raw tomograms of ER membrane stacks it was possible to discern areas that display regular zippers of RPTPμ molecules. Further experiments will be needed to address this question conclusively. Lastly, another strategy to study cell-adhesion molecules was tested. The purified extracellular region of RPTPμ was used to decorate liposomes, which in turn formed clusters due to the *trans*-dimerization of RPTPμ. The liposome clusters could be imaged directly by TEM, without the need of thinning by cryo FIB milling, which increased the amount of biological material available for data collection. Another advantage of this strategy was the possibility to introduce gold fiducials for tilt-series alignment, improving the quality of the tomogram reconstructions. However, the RPTPμ-mediated contacts between liposomes appeared to be more heterogenous than the cell contacts observed in cellular tomograms. This observation led us to the conclusion that, despite the many advantages, the strategy involving liposomes and the extracellular region alone is not a good model to study RPTPμ-mediated cell contacts.

Following this conclusion, future experiments will include the reconstitution of full-length RPTPμ into liposomes, which should provide a better model to study the assembly of potential higher-order structures at sites of membrane contacts.

Apart from the difficulties mentioned earlier in this chapter, subtomogram averaging of RPTPμ from FIB milled cells poses a challenge related to a “preferential orientation” of

particles in the tomograms. When selecting areas for tomogram acquisition, low magnification images of the cell sections taken at zero-degree tilt are analysed. For RPTPμ, I selected areas where cell contacts or ER membrane stacks were visible, clearly distinguishable due to high-contrast membranes. However, I observed that such membranes were only visible when viewed perpendicularly and not, for example, when the membrane surface was parallel or diagonal to the field of view. This has the consequence that data is only acquired at areas were the membrane surfaces are perpendicular to the field of view. Since RPTPμ also adopts a strictly perpendicular orientation between cell contacts or ER membrane stacks, the data acquisition strategy employed predominantly results in the imaging of RPTPμ "side views". The lack of RPTPμ "top views" in the dataset hence biases the angular distribution of the information obtained.

Strategies to overcome this problem will need to be developed for future experiments involving FIB-milled cell contacts. One approach could be to acquire low magnification images of the cell sections at medium to high tilt angles (a compromise between good contrast and the highest possible tilt will need to be found), in order to detect areas of cell-contacts or ER membrane stacks that are not perpendicular to the field of view at zero-degree tilt.

Having established a workflow that allows the imaging of cell contacts *via* FIB milling, exciting opportunities to study RPTPμ in a native environment arise. For example, experiments targeting lung epithelial cells, the adherens junctions in HUVEC cells or the intercalated discs of cardiomyocytes- where RPTPμ is highly enriched at cell contact sites- would provide important insights into the function of RPTPμ. In order to identify untagged RPTPμ in a native environment, it will be of utmost importance to obtain methods of attaching electron-dense labels to RPTPμ. For this purpose, antibodies against RPTPμ have been generated in collaboration with Masahiko Watanabe (Hokkaido University, Sapporo).

In parallel, we are currently in the pipeline to obtain nanobodies against RPTPμ. The attachment of uniform, water-soluble gold nanoparticles to antibodies have been reported to be an effective way of labelling proteins of interest in cellular samples intended for cryo-EM experiments (198). Following the protocols developed by Azubel *et al.* (199), our lab has been able to produce homogeneous gold particles and attach these to nanobodies displaying surface exposed cysteines (work carried out by Andrija Sente). Using gold-labelled nanobodies targeting RPTPμ is hence a promising technique available in the lab that will help us study RPTPμ in a native environment. Furthermore, the introduction of electron-dense particles in the area of data collection might also improve the alignment of tilt series obtained from FIB milled samples, since the gold nanoparticles could be used as tracking fiducials.

From a functional perspective, we are conducting experiments in collaboration with the Yuzaki laboratory to study the role of RPTPμ in the cerebellum. Initial data shows that RPTPμ knock-down in mouse embryos results in migration defects of Purkinje neurons into the Purkinje cell layer of the developing cerebellum (experiments carried out by Michisuke Yuzaki and colleagues, data not shown and acquired by personal communication). Of those Purkinje cells that reached their corresponding cell layer, defects in the planarity of the Purkinje cells could be observed. Although these preliminary results highlight the relevance of RPTPμ in the cerebellum, further experiments are needed to fully understand the implications of RPTPμ knock-down.

6. Purification and crystallization of RPTPμ cytoplasmic region and RACK1

6.1 Aims of this chapter

Chapter 5 of this thesis was dedicated to revealing the overall architecture of the extracellular region of RPTPμ on cell surfaces by cryo electron tomography. Next, I aimed to study how RPTPμ is able to transduce cues into downstream signalling events. A mechanistic understanding of RPTPμ-mediated signal transduction is hampered by lack of structural information of the cytoplasmic region of RPTPμ, comprising a juxtamembrane domain and two phosphatase domains. Although the crystal structure of the membrane-proximal phosphatase (D1) domain is known (108), structural data on the juxtamembrane and second phosphatase (D2) domains are still lacking. Previously, it has been reported for other RPTPs that the catalytic activity of D1 is dependent on the structural integrity of the second (catalytically inactive) D2 domain (98, 99) and also requires a large part of the juxtamembrane domain (200). Yeast two-hybrid screens have revealed intramolecular

interactions between these domains (200), however, a detailed mode of action and the consequences of these interactions are not known.

Additionally, yeast two-hybrid screens have also identified that the RPTPμ D1 phosphatase domain interacts with RACK1 (125), possibly linking local translation to signalling at cell-cell contact sites. Although RPTPμ is able to recruit RACK1 to the plasma membrane and the proteins have been co-precipitated from insect cell cultures (125), a mechanistic understanding of their interaction is still missing. In this chapter, I set out to obtain structural information of the cytoplasmic domain of RPTPμ and characterize a potential interaction with RACK1.

6.2 Construct design of D1-D2 and RACK1 constructs

With the aim to conduct structural studies of the cytoplasmic region of RPTPμ and of RACK1, I set out to generate recombinant protein samples. Construct boundaries for RPTPμ were defined by considering the predicted secondary structure elements and by comparison to the LAR D1-D2 tandem crystal structure (97). Three constructs were generated, comprising residues 879-1452, 859-1452, and 777-1452. RPTPμ$^{879\text{-}1452}$ comprises both phosphatase domains D1 and D2. RPTPμ$^{859\text{-}1452}$ and RPTPμ$^{777\text{-}1452}$ additionally contain different lengths of the juxta-membrane domain. The RACK1 construct boundaries were based on an available crystal structure, comprising residues 2-317 (201) (**Figure 6-1**).

In previous studies, the interaction between RPTPμ D1-D2 and RACK1 was reported after co-immunoprecipitation of the proteins from recombinant co-expression in insect cells. To mimic this experimental setup, I also prepared constructs that would enable co-expression of RPTPμ$^{777\text{-}1452}$ and RACK1 using the Baculovirus Bac-to-Bac system (Invitrogen).

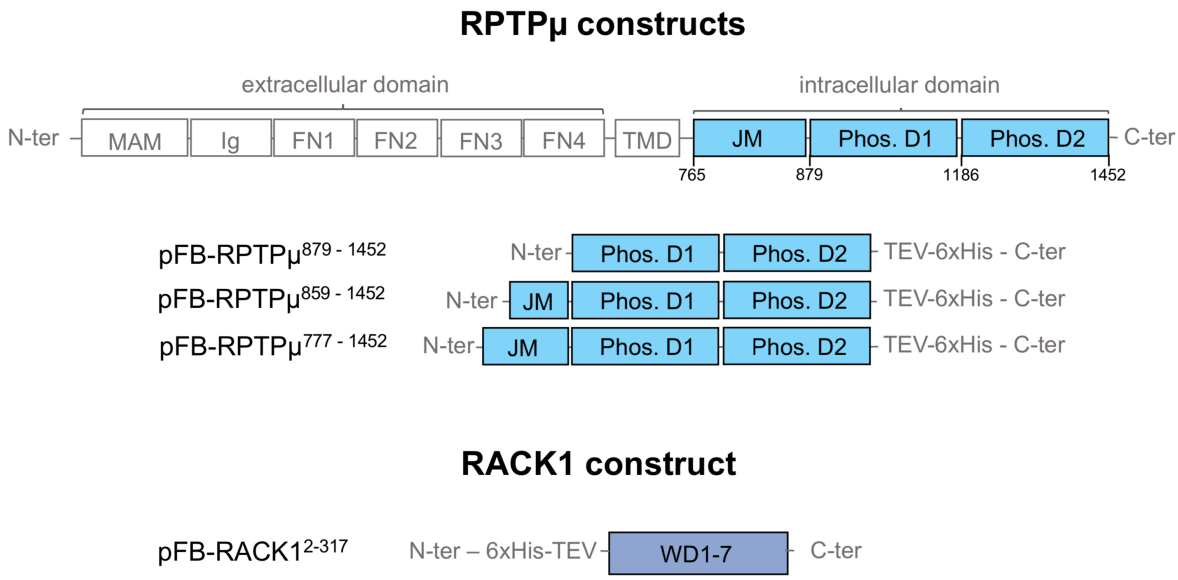

***Figure 6-1* Construct design for RPTPμ intracellular region and RACK1** The intracellular region of RPTPμ consists of a juxtamembrane domain and two phosphatase domains, D1 and D2. Constructs for baculoviral expression tests comprised the D1 and D2 phosphatases, with various lengths of the juxtamembrane domain, based on secondary structure predictions. RACK1 consists of seven WD repeats. The construct designed for expression experiments comprised the full-length sequence.

6.3 Expression and purification of D1-D2 and RACK1 constructs leads to high yields of recombinant protein

All constructs (RPTPμ$^{777-1452}$, RPTPμ$^{859-1452}$, RPTPμ$^{879-1452}$, RACK1 and co-expression of RPTPμ$^{777-1452}$ and RACK1) were produced using the baculovirus expression system in Sf9 cells, resulting in good yields of soluble protein (**Figure 6-2**). Nickel affinity chromatography was used as a first step to purify the proteins, leading to enriched samples. His-tag cleavage through TEV protease and a second purification step over a His-trap column removed most of the contaminants. A final purification over size-exclusion chromatography resulted in ~90% pure protein and revealed that all protein samples are monodisperse and monomeric (**Figure 6-3**).

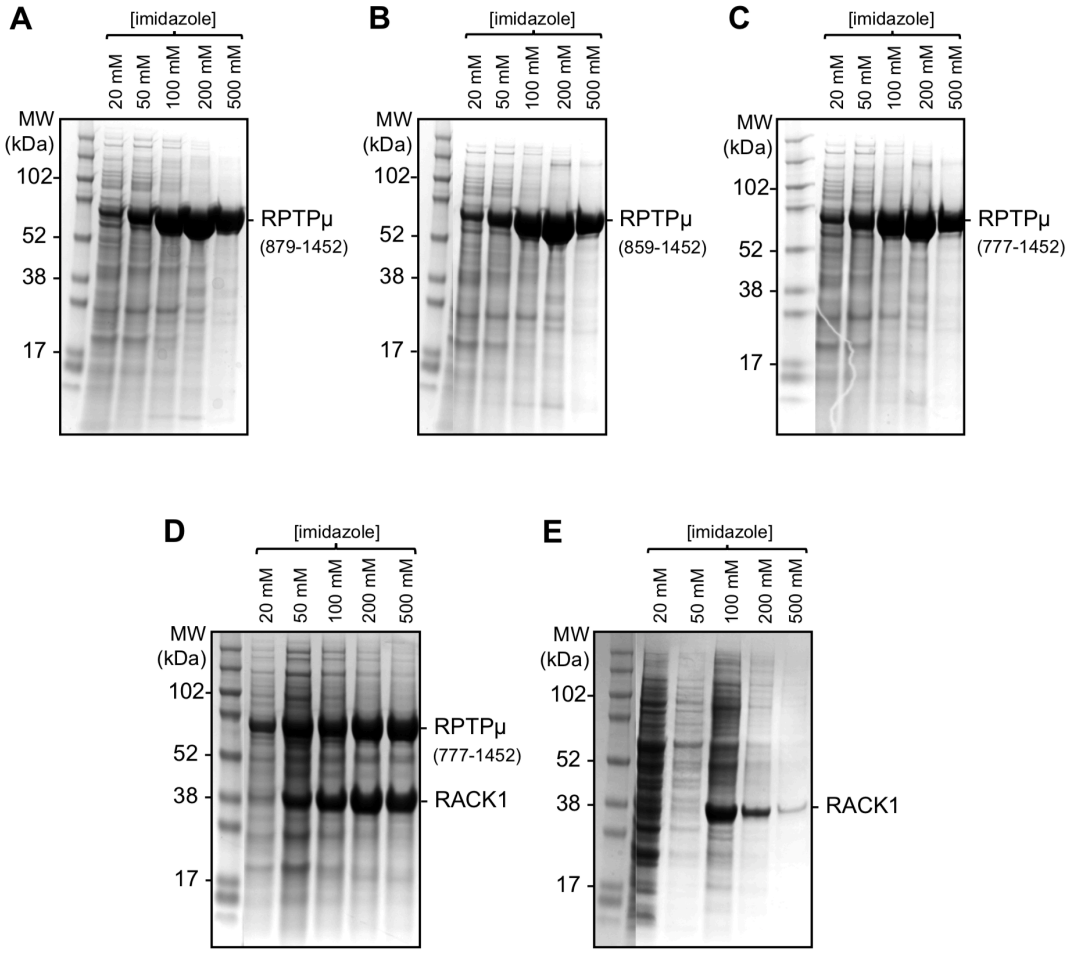

Figure 6-2 **Affinity purification of RPTPμ D1D2 and RACK1 constructs** SDS-PAGE analysis of fractions obtained from Ni^{2+}-affinity purifications of RPTPμ D1D2 and RACK1 constructs. Elution of target proteins was enabled by increasing concentrations of imidazole. Gels correspond to purifications of RPTPμ $D1D2^{879-1452}$ (**A**), RPTPμ $D1D2^{859-1452}$ (**B**), RPTPμ $D1D2^{777-1452}$ (**C**), co-expression and co-purification of RPTPμ $D1D2^{777-1452}$ and RACK1 (**D**) and purification of RACK1 alone (**E**). Numbers on the left of the gel represent the molecular weights in kDa of the protein weight standards.

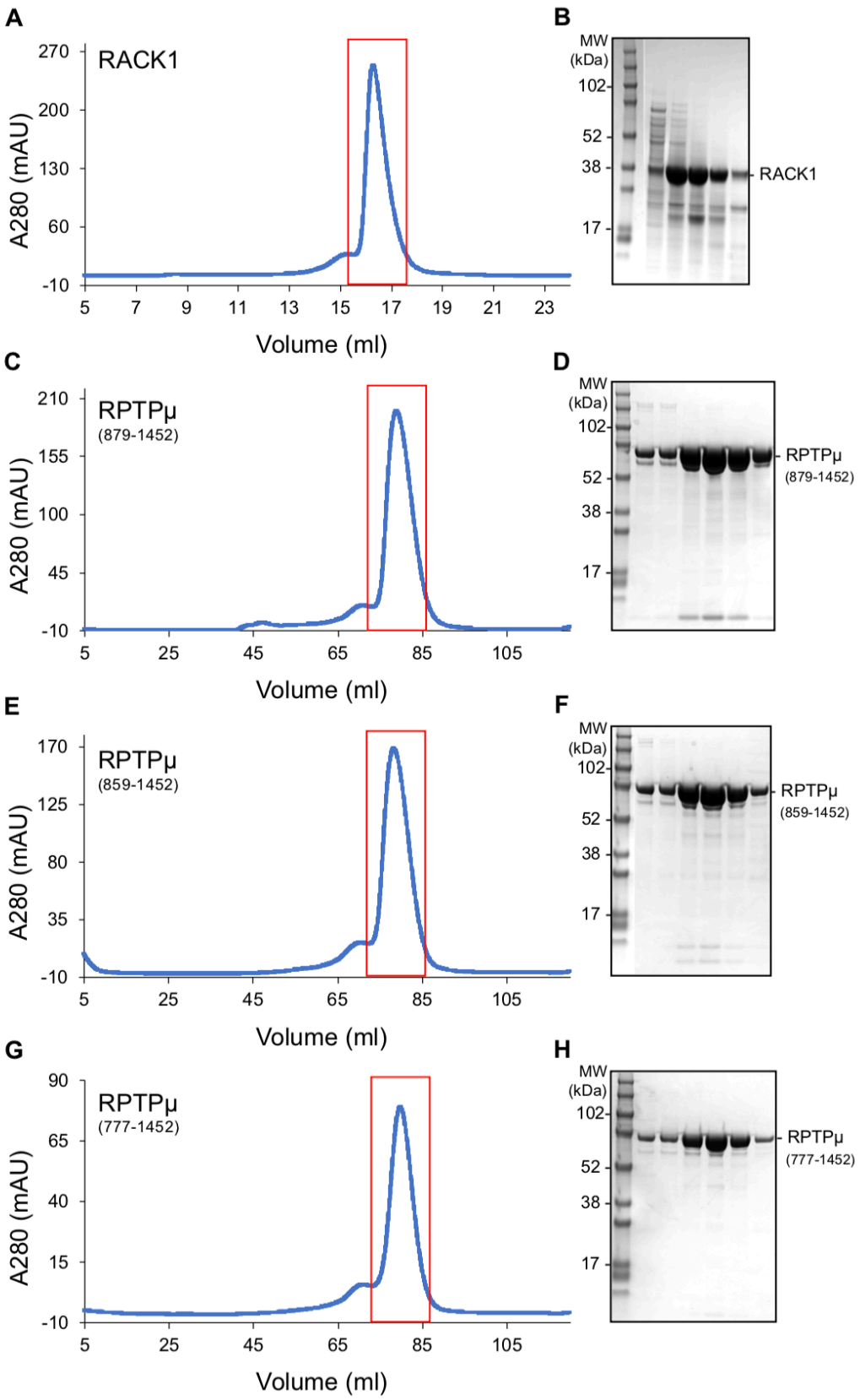

Figure 6-3 **All RPTPμ cytoplasmic domain and RACK1 constructs lead to stable and monodisperse samples** (**A**, **C**, **E**, **G**) Size-exclusion chromatography (SEC) elution profiles of RACK1 and RPTPμ D1-D2 constructs 1 (residues 879-1452), 2 (859-1452) and 3 (777-1452). Peak in red delineated box corresponds to fractions analysed by SDS-PAGE. (**B**, **D**, **F**, **H**) SDS-PAGE analysis of SEC peak fractions highlighted in (A, C, E, G). Numbers on the left of the gel represent the molecular weights in kDa of the protein weight standards.

6.4 RACK1 does not co-elute with RPTPμ$^{777-1452}$ in size-exclusion chromatography experiments

After having obtained pure samples of the RPTPμ cytoplasmic domain and RACK1, I next asked whether both proteins interact. Since all RPTPμ constructs resulted in soluble protein samples, I decided to use the longest construct (RPTPμ$^{777-1452}$) for interaction studies.

As a first step, I ran analytical size-exclusion chromatography (SEC) experiments of RPTPμ$^{777-1452}$ alone and in combination with RACK1. As can be seen in **Figure 6-4**, the proteins do not co-elute and there is no shift in the elution volume of RPTPμ$^{777-1452}$. This suggests that either RACK1 does not bind to RPTPμ directly, or that the interaction is too weak to withstand SEC. Another possibility is that post-translational modifications (PTMs) are needed for the interaction to take place.

The same results were obtained when RPTPμ$^{777-1452}$ and RACK1 (both His-tagged) where co-expressed, co-purified *via* Nickel affinity chromatography and then analysed by SEC (data not shown).

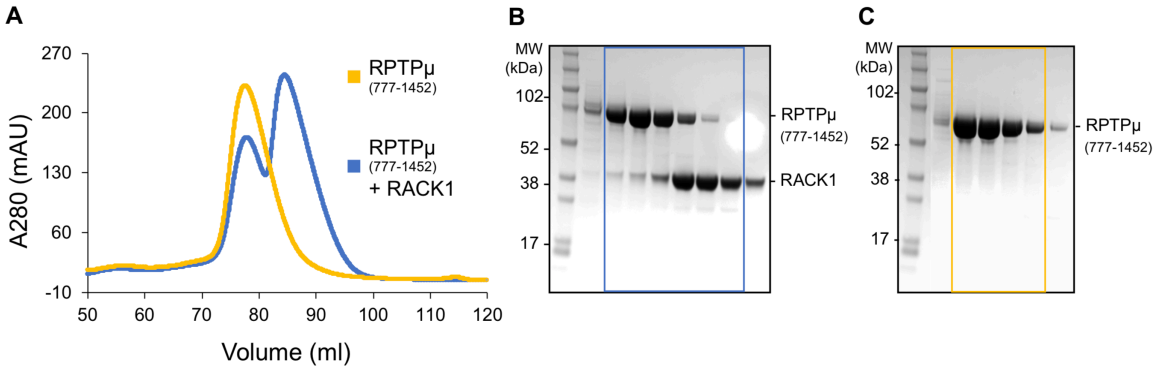

Figure 6-4 **RPTPμ D1D2$^{777-1452}$ does not co-elute with RACK1 in size-exclusion chromatography** (**A**) Size-exclusion chromatography (SEC) elution profiles of RPTPμ D1D2$^{777-1452}$ (yellow curve) and RPTPμ D1D2$^{777-1452}$ in combination with RACK1 (blue curve). (**B**) SDS-PAGE analysis of fractions obtained from SEC of RPTPμ D1D2$^{777-1452}$ in combination with RACK1. Fractions for both peaks were analysed. (**C**) SDS-PAGE analysis of peak fractions obtained from SEC of RPTPμ D1D2$^{777-1452}$. Numbers on the left of the gel represent the molecular weights in kDa of the protein weight standards.

6.5 RPTPμ D1-D2 forms diffracting crystals

In order to obtain structural information of the cytoplasmic domain of RPTPμ and of the potential interaction with RACK1, I set up crystallisation trials of all RPTPμ constructs and of RPTPμ$^{777-1452}$ in combination with RACK1. All of these experiments led to the formation of microcrystals. However, microcrystals obtained from RPTPμ$^{777-1452}$ in combination with RACK1 only appeared in the same conditions as observed for crystals of RPTPμ$^{777-1452}$ alone. It is hence likely that these crystals do not contain a putative complex with RACK1, but RPTPμ$^{777-1452}$ on its own. Since all RPTPμ constructs lead to microcrystals, I proceeded with the longest construct (RPTPμ$^{777-1452}$) for optimization experiments.

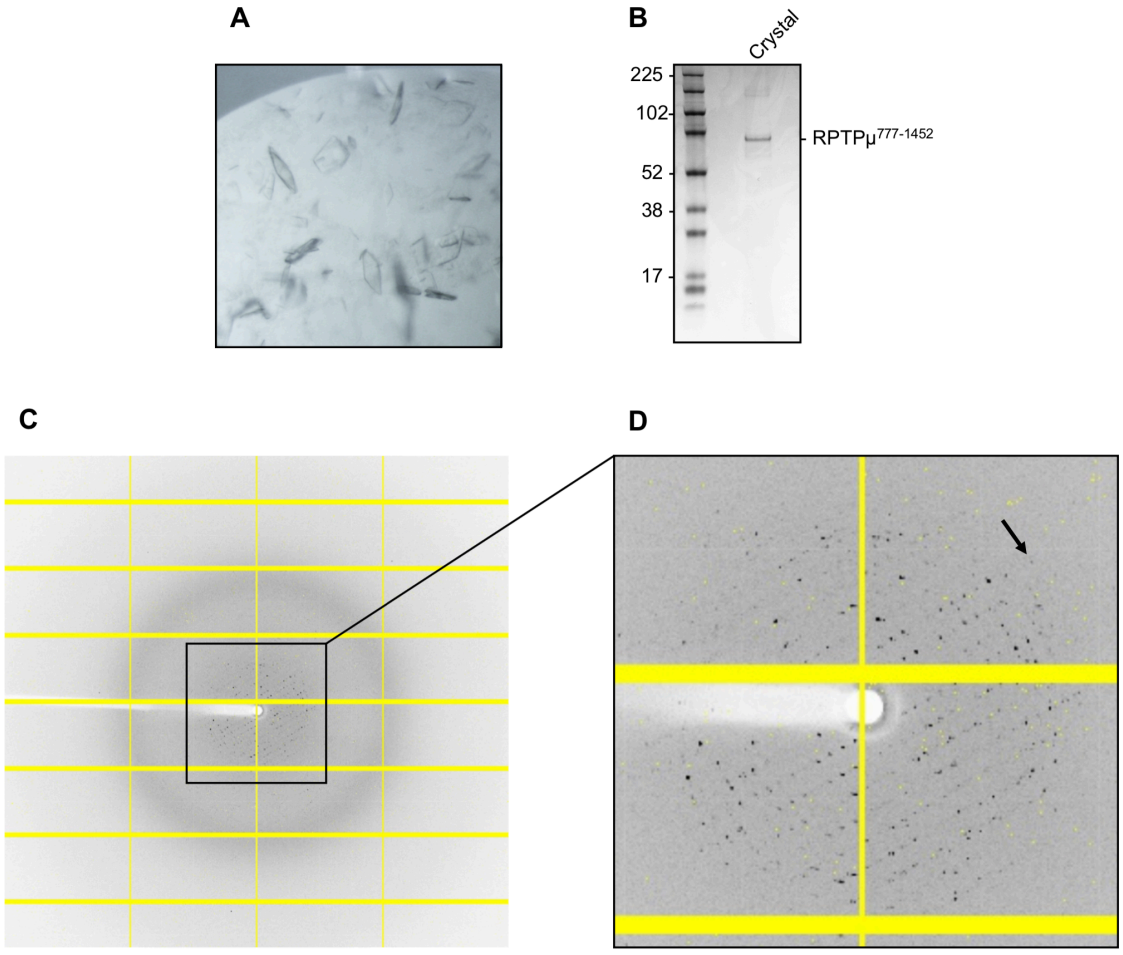

Figure 6-5 **RPTPμ D1D2$^{777-1452}$ forms crystals diffracting to 7 Å** (**A**) RPTPμ$^{777-1452}$ crystallized to thin plates in the Morpheus Screen E3, F3 and G3 conditions (see Material & Methods, section 2.4). (**B**) SDS-PAGE analysis of obtained crystals results in a band of similar size as that obtained after purification of RPTPμ$^{777-1452}$. Numbers on the left of the gel represent the molecular weights in kDa of the protein weight standards. (**C**) Diffraction image of RPTPμ$^{777-1452}$ crystals. (**D**) Close-up view of the diffraction image shown in (C). Black arrow points at 7Å diffraction spot.

Crystals obtained from RPTPμ$^{777-1452}$ optimization trials were analysed by SDS-PAGE, resulting in a band of similar molecular weight as observed during the purification of RPTPμ$^{777-1452}$ (~ 80 kDa) (**Figure 6-5 A-B**). This result confirms that the crystals obtained contain the complete construct and are not a product of RPTPμ degradation.

RPTPμ$^{777-1452}$ crystals were mounted and subjected to diffraction tests. As can be seen in **Figure 6-5 C-D**, the crystals diffracted to ~7 Å. Due to the high anisotropy of the crystal, however, it was not possible to collect a complete dataset and hence no structural information could be obtained from this experiment at the time of writing. Further crystal optimisation experiments are currently ongoing.

6.6 Summary and conclusions drawn from chapter 6

In this chapter, I set out to obtain structural insight into the RPTPμ cytoplasmic region and to characterize the interaction between RPTPμ and RACK1. A baculovirus expression system was employed to express RPTPμ and RACK1 constructs, resulting in high yields of soluble protein samples. Size-exclusion chromatography (SEC) experiments confirmed that the samples were monodisperse and ran as monomers. This finding is particularly interesting in the context of RPTPμ, since the dimerization of the cytoplasmic domain of other RPTPs is considered to be relevant for the regulation of their catalytic activity. In the case of RPTPμ, it appears that, in solution, the cytoplasmic domain either does not dimerize, or does not form dimers of high enough affinity to withstand SEC. Further experiments will be needed to address this question, using, for example, analytical ultracentrifugation to study the oligomeric states of the RPTPμ cytoplasmic domain.

Previously, the RPTPμ D1 domain has been reported to interact with RACK1 in yeast two-hybrid screens. RPTPμ led to the recruitment of RACK1 to the plasma membrane, and both

proteins were co-precipitated from lung epithelial cell lysates or when co-expressed in insect cells (125). To validate this interaction, I set out to study RPTPμ and RACK1 by analytical SEC. The addition of RACK1 did not produce a shift in the elution volume of RPTPμ, and the proteins did not co-elute when loaded together on SEC, showing that RPTPμ and RACK1 either form a weak complex that cannot be detected by SEC or that the proteins do not interact directly. Hence, the potential interaction between RPTPμ and RACK1 needs to be further studied by other methods that would detect a weak binding event, such as surface plasmon resonance (SPR) or isothermal titration calorimetry (ITC).

In order to obtain structural information of the cytoplasmic domain of RPTPμ, I set up crystallisation trials of all RPTPμ constructs. The best crystals were obtained for RPTPμ$^{777-1452}$, which diffracted to about 7 Å. SDS-PAGE analysis of the crystals confirmed that they were not a result of RPTPμ degradation, but that the crystals contained the complete construct (RPTPμ$^{777-1452}$). Although no structural information could be obtained from this experiment, the established purification and crystallisation protocols will be instrumental for further crystal optimisation attempts. In order to obtain a more stable protein sample and increase the crystallisation success, it will be worth considering the addition of a catalytic substrate or conversely the inactivation of the D1 phosphatase domain.

Taken together, the work presented in this chapter paves the way towards a better understanding of the RPTPμ cytoplasmic region function and mechanism.

Future work towards obtaining the structure of the cytoplasmic region of RPTPμ could involve other methods. During crystallization experiments, microcrystals were obtained in various conditions, but these were not suitable for data collection experiments at synchrotron beamlines. With the recent software and hardware development for the acquisition of electron diffraction (ED) data using standard electron microscopes (202), ED is a promising technique to obtain structural information from microcrystals.

In addition, the RPTPμ cytoplasmic region could be a target for single particle cryo EM studies. Despite its small size (~ 80 kDa), the improvements in data collection and processing techniques are expanding the range of protein sizes that can be studied by cryo EM, exemplified by the recent report of the Lander laboratory (203).

7. Discussion and Outlook

For this thesis, I set out to study two protein classes that are involved in the formation of trans-adhesive complexes at inter-cellular contacts: receptor protein tyrosine phosphatases (RPTPs) and ionotropic glutamate receptors in complex with cerebellins and neurexins. Specifically, my research focused on two prototypical complexes shown to integrate both cell-adhesion and downstream signalling functions: the GluD2-Cbln1-βNrx1^{+SS4} triad and the homophilic RPTPμ complex.

As a first step towards studying the GluD2-Cbln1-βNrx1^{+SS4} triad, we aimed to generate specific nanobodies that would enable us to probe different conformational states of the complex. In collaboration with the Steyaert laboratory (VIB Brussels), nanobodies were raised against GluD2-Cbln1-βNrx1^{+SS4}. Subsequent characterization identified 10 nanobodies that bound to GluD2 with K_D values of 10 nM or lower. Only one nanobody was found to bind Cbln1 and no nanobodies were found to bind βNrx1^{+SS4}. Analytical size exclusion chromatography revealed that a subset of nanobodies bound to the ligand-binding

domain (LBD) of GluD2, and that these nanobodies bound distinctively to either monomeric or dimeric forms of the GluD2^{LBD}. Nanobodies (Nbs) 399, 392, 390 and 384 co-eluted with GluD2^{LBD} dimers, while nanobodies 416, 383 and 385 were bound to GluD2^{LBD} monomers. Other nanobodies were identified to bind the GluD2^{ATD}, without affecting the dimeric state of the protein.

The crystal structure of GluD2^{LBD} in complex with Nb399 revealed a dimeric conformation, where Nb399 stabilizes the GluD2^{LBD} lobes in a closed state. In comparison to the GluD2^{LBD} *apo* crystal structure, the GluD2^{LBD}-Nb399 complex displays a domain closure of 24.3°, indicating that Nb399 is able to activate GluD2. Nanobodies 390 and 392 were also found to lock the GluD2^{LBD} in a dimeric and closed state, introducing domain closures of 27.9° and 25.8° respectively. Previously, the degree of domain closure has been correlated with the extent of AMPA receptors activation and desensitization (183). Following this line, nanobodies 390, 392 and 399 could hence be considered weaker agonists than the GluD2 ligand, D-Serine, which introduces an LBD closure of 29.9°.

To test whether nanobodies 390, 392 or 399 are indeed able to trigger GluD2 signalling, we collaborated with the Yuzaki laboratory (Keio University) to test the functional effect of Nb399 addition to mouse cerebellar slices. As has been observed previously for D-Serine, the application of Nb399 led to the decrease of parallel fiber-evoked excitatory post-synaptic currents (PF-EPSCs) in a GluD2-depedendent fashion. This finding confirms that Nb399 (and probably Nb390 and Nb392 too, although these nanobodies were not yet tested), is able to not only stabilize the GluD2^{LBD} in an active state, but also trigger GluD2-specific signalling. Future experiments will determine whether Nb399 activation displays the same features as D-Ser-dependent signalling. For example: a) Does GluD2 activation through Nb399 depend on Cerebellin-1? Or b) Does the ablation of the GluD2 C-terminus or of the downstream signalling partner PTPMEG disrupt Nb399-induced activation?

The crystal structures of the LBDs of other iGluRs have revealed the general motions that lead to the channel gating cycle. When the receptor is inactive, the LBD clamshells are open and the LBDs form dimers. When a ligand binds, the clamshells close, triggering a motion transduction that leads to the opening of the ion channel. If ligand binding persists, the LBD upper lobes undergo a downward motion that breaks the LBD dimerization interface, leading to the desensitization of the receptor. These findings are also applicable to GluD2: in its *apo* form, the GluD2^{LBD} crystallizes as a dimer, while the GluD2^{LBD} structure in complex with D-Serine is monomeric. Interestingly, nanobodies 390, 392 and 399 trigger the closure of the GluD2^{LBD} but simultaneously stabilize the GluD2^{LBD} dimerization interface, preventing the downward motion of the GluD2^{LBD} upper lobes. This suggests that nanobodies 390, 392 and 399 are not only able to activate GluD2, but also prevent receptor desensitization. Such tools would be extremely valuable for the structural analysis of the active receptor, since they would stabilize a conformational state that is usually very short-lived (in the millisecond range). Whether or not nanobodies 390, 392 and 399 are indeed able to prevent or diminish GluD2 desensitization, will need to be tested in further experiments. Currents measured from GluD2^{Lc} are nearly completely reduced upon addition of D-Serine, indicating a strong desensitization induced by ligand-binding. A comparative study with Nb399 would reveal whether the nanobody is able to maintain GluD2^{Lc} in an open state for a longer period of time.

Crystal structures were also determined for GluD2^{ATD} in complex with nanobodies 381 and 389, respectively. The structures revealed unique binding sites, where the nanobodies bound to either site of one ATD dimer, without affecting its oligomeric state. Nb389 binds to the cleft of the ATD clamshell, and is the only nanobody (of those whose structures were determined) that is theoretically able to probe all four binding sites in a tetrameric receptor. Nb381 binds at the membrane-proximal side of GluD2^{ATD}, in close proximity to the adjacent

ligand-binding domains. This opens the question of whether Nb381 would be able to bridge the ATD and LBD in a full-length receptor, stabilizing the extracellular region. In order to test this hypothesis, binding experiments between the isolated GluD2^{LBD} and Nb381 will need to be carried out. Further tests will also be required to establish whether or not Nb381 has a functional effect on GluD2-dependent downstream signalling. Previously, the introduction of glycan linkers between the GluD2 ATD and LBD layers has been observed to disrupt D-Serine-dependent long-term depression (LTD). In the same line, one could argue that the stabilization of the ATD-LBD interface through the binding of Nb381 also impacts the motion transduction between these layers, ultimately affecting downstream signalling.

Having obtained nanobodies that are able to stabilize GluD2 in different conformational states, I next set out to determine a full-length structure of the receptor by cryo electron microscopy and single-particle analysis. A dataset of GluD2 in complex of Nb399 revealed that, contrary to the initial assumption that only two binding sites are available in the tetrameric receptor, four copies of Nb399 bind to GluD2. 2D class averages showed that Nb399 is able to access both sides of the LBD dimers, leading to the disruption of the tetrameric conformation of the GluD2 extracellular region. The high percentage of LBD-Nb399 top views among the 2D class averages reveals a preferential orientation of particles in the ice, likely due to interactions with the air-water interface. This observation opens the question of whether Nb399 destabilizes the tetrameric conformation of GluD2 by binding to four sites, or whether the additional binding sites only become available upon partial denaturation at the air-water interface during blotting. To answer this question, comparative tests involving GluD2 in detergent (hence avoiding interactions with the air-water interface) will need to be carried out.

Another important consideration is whether Nb399 also disrupts GluD2 in a physiologically relevant environment and whether this could have implications for GluD2 function. Is Nb399 inducing a non-native GluD2 conformation? According to Pardon *et al*. (141), nanobodies will preferentially sample energetically favoured protein conformations. Immature B cells expressing antibodies that stabilize native conformations have an advantage over those that express antibodies that induce an energetically expensive conformational change.

Although Nb399 is an invaluable tool to study the function of GluD2 due to its high affinity, specificity and capacity to activate the receptor, the potential to induce a non-native disruption of the native tetrameric conformation will need to be addressed.

Further single-particle cryo-EM studies revealed that GluD2 undergoes a severe degree of denaturation at the air-water interface, resulting in less than 4% of intact particles. The factors that lead to the adsorption of proteins to air-water interfaces are not well understood, however, it is believed that the exposed hydrophobicity of the protein, molecular crowding and the chemical reactivity of solvent-exposed groups may play a role in this phenomenon (204, 205).

One strategy to circumvent the denaturation at the air-water interface, is to use grids with thin carbon supports that sequester the protein molecules. Cryo-EM grids prepared this way indeed resulted in a high percentage of (>80%) of intact particles. A dataset of GluD2 in complex with Nb381 provided the first insights into the general GluD2 architecture. First, it becomes apparent that GluD2 adopts an extended, Y-shaped conformation as is common for AMPA receptors. This is in accordance with previously obtained crystals structures of the $GluD2^{ATD}$ in complex with Cerebellin-1, where the ATDs adopt an N-shaped dimer of dimers conformation (2). Only two copies of Nb381 are found to bind to the sides of the tetrameric GluD2, as the other two binding sites face the centre of the receptor and are hence

sterically occluded. The extracellular region displays a decreased degree of flexibility, as can be assessed from the 2D class averages. This observation suggests that Nb381 is indeed contributing to the stabilization of the extracellular region of GluD2. Although an initial map was obtained from the GluD2 dataset in complex with Nb381, its low resolution hampered further interpretation of the data. Further data collections of this sample will lead to an improved map, hopefully allowing the determination of the first Delta subtype iGluR structure.

Taken together, research conducted on the GluD2-Cbln1-βNrx1^{+SS4} triad resulted in the discovery and characterization of nanobodies that are able to stabilize GluD2 in distinct conformational states. These tools will be instrumental for understanding the function of the GluD2-Cbln1-βNrx1^{+SS4} triad at a molecular and cellular level. Furthermore, the work presented here lays the ground for the determination of the GluD2 structure, and of unveiling the structural basis of iGluR metabotropic signalling.

The second part of this thesis involved the study of a receptor protein tyrosine phosphatase, RPTPμ. RPTPμ forms trans-homophilic interactions across cell-cell contacts and simultaneously exerts a signalling function through its cytoplasmic phosphatase domains. The aims of the second part of my thesis were to identify whether RPTPμ forms higher-order assemblies on the surface of cells and to obtain structural information of the RPTPμ cytoplasmic domain and potential binding partners.

In order to study the RPTPμ-mediated cell-cell contacts in their native environment, I devised a strategy in which mVenus-tagged RPTPμ was overexpressed in insect cells and the cell-cell contacts were targeted by FIB milling for subsequent cryo electron tomography data collection. This workflow proved to be successful, and it was possible to obtain tomograms of cell-cell contacts at molecular resolution. To our knowledge, this is the first

cryo-FIB data obtained from cell-cell contacts and it could potentially provide valuable insight into the organization of cell-adhesion molecules at cell surfaces.

RPTPμ-mediated cell-cell contacts were observed to be highly regular, with a constant spacing of ~ 35 nm. This distance is in accordance with the length of the RPTPμ extracellular region dimer, which measures 27 nm (based on the crystal structure by Aricescu *et al*. (109)). Parallel to the cell membrane, the cell-cell contacts displayed two lines of higher density, with a regular spacing of ~ 10 nm. This spacing matches the distance between protruding MAM domains in the RPTPμ dimer. The fact that RPTPμ-mediated cell contacts are so regular and that the two central lines attributed to the RPTPμ MAM domains are continuous, point towards a tight arrangement of RPTPμ molecules.

To our surprise, extensive, regularly spaced membrane stacks were also observed in the cytoplasm. These stacks presented the same features and membrane distances as the cell contacts, leading us to the conclusion that RPTPμ also mediates the association of these membranes. Similar membranous structures have been observed previously, where the endoplasmic reticulum (ER) transforms from a tubular network into a system of stacked cisternae to increase the available surface area. This phenomenon is commonly seen in cells that play secretory functions or require the storage of enzymes in the ER. Due to the ordered patterns of these ER structures, they have been termed ‘organized smooth endoplasmic reticulum’ (OSER) (194). Because the membrane stacks containing RPTPμ shared similar characteristic to those described for the OSER, we concluded that RPTPμ causes the structural transformation of the ER in Sf9 cells. Further experiments will need to be carried out to understand the formation and function of the RPTPμ-induced OSER.

Subtomogram averaging of RPTPμ-mediated ER membrane contacts did not lead to a high-resolution structure so far. Nevertheless, some conclusions can already be drawn from the obtained average. A pillar-like density at the core of the average resembled the crystal

structure of the extracellular region of RPTPμ. The crystal structure does not account for the entire length between apposing membranes, but this is partially explained by the missing fibronectin-like domain. The membrane-proximal domain was not modelled in the crystal structure obtained by Aricescu *et al* (109), due to weak electron densities in this part of the map.

The subtomogram average further reveals the presence of two planes extending between the apposing membranes, in accordance with lines of higher density observed in micrographs and reconstructed tomograms. These planes match the positions of the protruding MAM domains of the fitted RPTPμ crystal structure. If the planes of continuous density can indeed be attributed to the MAM domains, this would suggest that RPTPμ forms a tightly-packed arrangement at cell contacts or between ER membranes. Is such an arrangement supported by specific intermolecular RPTPμ interaction in *cis*? And does RPTPμ form regular arrays? The work presented here provides evidence in favour and against these hypotheses. On one hand, the fact that no further pillar-shaped densities can be observed beyond the masked volume of the subtomogram average suggests that the positions of RPTPμ are random and are hence do not form regular patterns. In this line, the crystal packing observed for the extracellular region of RPTPμ (109) suggested no additional intermolecular interaction interfaces that could be physiologically compatible (apart from the well described homodimerization in *trans*). For proteins that have been observed to form zipper-like clusters, the supporting *cis* and *trans* interactions could generally be identified in the crystal packing (197).

On the other hand, some observations from the data obtained do support the notion of an ordered RPTPμ array. When contemplating tomographic slices of ER membrane stacks with a strong contrasting filter, it is possible to discern patches that display RPTPμ molecules at regular intervals. In addition, slices in z through the subtomogram average of RPTPμ-

mediated ER membrane contacts revealed RPTPμ top views that appear to be at regular spacings.

Further experiments will need to be carried out in order to conclusively address whether or not RPTPμ forms ordered arrays at cell contact sites. Most importantly, improving the subtomogram averaging pipeline and obtaining higher resolution information from the supramolecular structure of RPTPμ at cell contacts would provide important insights.

Although cryo FIB milling of cell contacts provides unprecedented possibilities to study molecules in their native environment, this method also introduces important challenges for downstream processing and subtomogram averaging. Firstly, molecular crowding and the low concentration of the protein of interest usually makes it very difficult to identify the molecules for subtomogram averaging. Fortunately, RPTPμ is easily recognizable on cell membranes due to the specific cell contact spacing it induces. Further to this issue, FIB milling is a low-throughout technique, resulting in 4-8 sections on one grid. Collecting cryo electron tomography data on these samples usually entails manual data collection, greatly limiting the data acquisition throughput. The ice quality and thickness obtained from freezing cells and FIB milling is also varied, frequently resulting in sections that are not thin enough or do not consist of vitreous ice. Lastly, cryo FIB milling of cells does not allow the use of gold nanospheres as fiducials. This has the consequence that tilt-series obtained from FIB milled sections need to be aligned through patch-tracking and not *via* the alignment of gold particles. In our hands, patch-tracked tilt series were more difficult to align, resulting in worse tomogram reconstructions. Errors in these reconstructions can greatly limit the success of downstream subtomogram averaging.

In order to circumvent the challenges imposed by subtomogram averaging of FIB milled lamellae, I next went on to develop an *in vitro* reconstitution system, following the methodology used to study clustered protocadherins by Brasch *et al*. (197). Previously,

subtomogram averaging experiments carried out from data obtained with reconstituted samples have resulted in high resolution structures, as reported by Schur *et al*. (206) and Hutchings *et al*. (207). These reports motivated us to study RPTPμ using decorated liposomes.

Cryo-ET data obtained from liposomes confirmed that RPTPμ mediates their aggregation, leading to liposome clusters. Rigid rods corresponding to RPTPμ dimers could be observed between apposing liposome membranes. However, the spacing between liposomes varied substantially, unlike the highly regular spacing observed for cell contacts. Moreover, the two parallel lines of increased density previously observed between apposing membranes could not be detected in liposomes. Taken together, the data obtained from liposomes revealed that they are more heterogenous, and might hence not be a good model system to study RPTPμ.

This finding could have interesting implications. The liposome assays were carried out with the extracellular region of RPTPμ, immobilized on lipids *via* a poly-histidine tag. This prompts the question of whether the missing transmembrane and cytoplasmic domain of RPTPμ contribute to the arrangement of RPTPμ oligomers on cell surfaces. Further experiments where full-length RPTPμ is reconstituted into liposomes will be needed to address this question.

Having dedicated chapter 5 to study the arrangement of the extracellular region of RPTPμ, I next went on to gain insight into the downstream signalling driven by the cytoplasmic domain. The cytoplasmic domains of all type IIb RPTPs consists of a juxtamembrane domain and two phosphatase domains. The function of the juxtamembrane domain is poorly understood, however, its structural integrity is required for the catalytic activity of the D1 phosphatase (200). Despite previous efforts, no structural information of the type IIb RPTPs

juxtamembrane domains are available. In this chapter, I set out to determine the RPTPμ cytoplasmic domain structure and to study its potential interaction to RACK1.

Using a baculoviral expression system, high yields of protein were obtained for RPTPμ and RACK1. Crystallisation trials for the cytoplasmic domain of RPTPμ resulted in crystals that diffracted to about 7Å. Optimisation experiments done until completion of this thesis did not yield better diffracting crystals. Further tests involving limited proteolysis, the addition of stabilizing agents or changes in the purification methods might yield better results.

Previously, RPTPμ has been reported to interact with RACK1 (125), a ribosomal protein that participates in the recruitment of signalling molecules to the plasma membrane. This exciting finding suggested that RPTPμ might be responsible for recruiting translation machinery to sites of cell-cell contacts. In order to characterize the putative interaction between RPTPμ and RACK1, I conducted analytical size-exclusion chromatography experiments. No binding could be detected *via* this method, suggesting that the proteins do not interact or that they form a low-affinity complex. Future tests applying methods that are able to detect weak binding events (e.g. ITC or SPR) will hence be needed to characterize this putative complex.

Taken together, the work presented in this chapter lays the ground towards obtaining a crystal structure of the cytoplasmic domain of RPTPμ and characterizing the putative interaction to RACK1. The protocols established to obtain large quantities of pure protein samples will enable analysis *via* other methods, providing valuable insight into the function and regulation of type IIb RPTPs.

8. Appendix

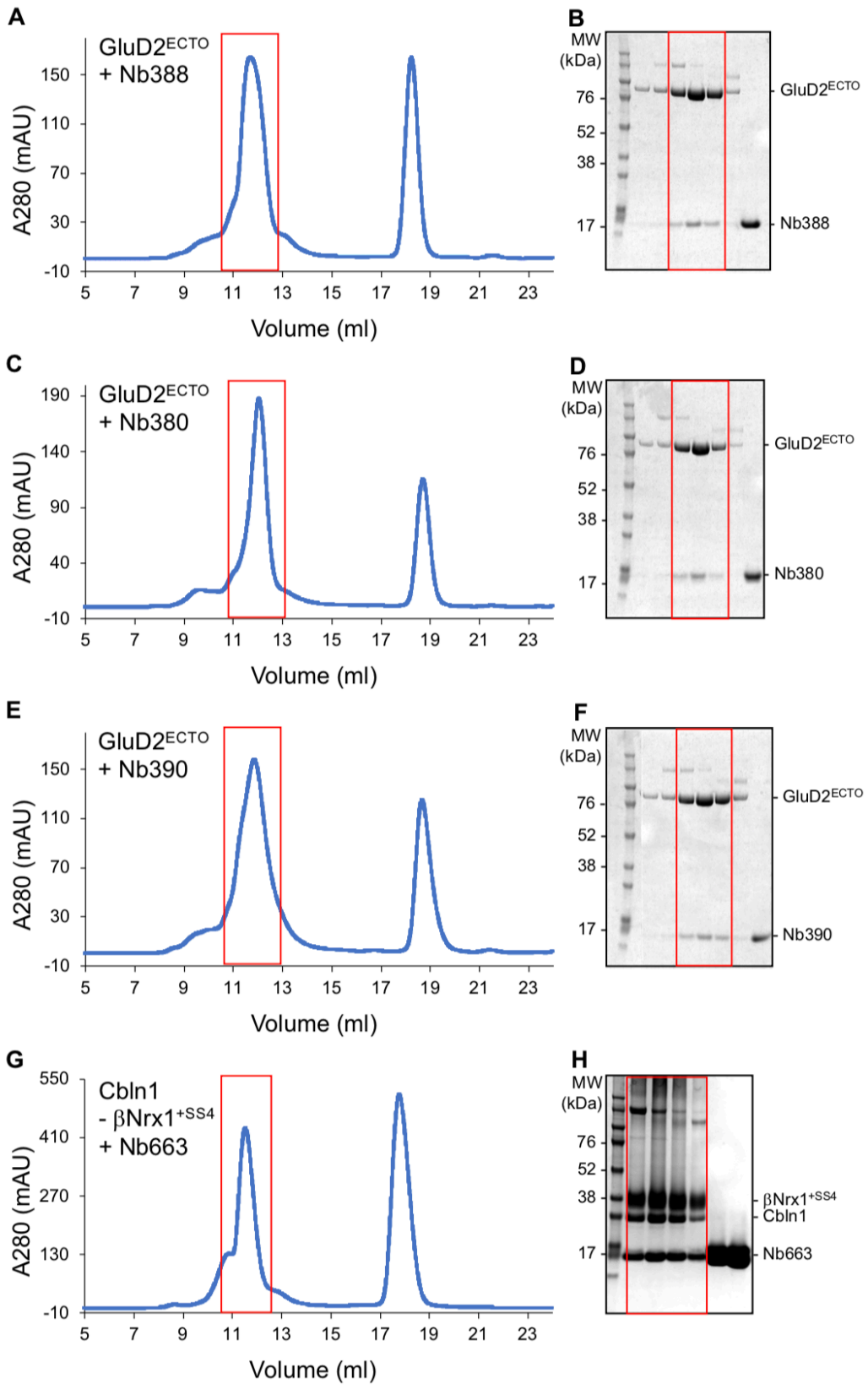

Figure 8-1 **Gelfiltration interaction studies of nanobodies against GluD2^{ECTO} and βNrx1-Cbln1** (**A**, **C**, **E**, **G**) Gelfiltration elution profiles of nanobody complexes with the GluD2 extracellular region (GluD2^{ECTO}) and βNrx-1-Cbln1. All profiles show an excess of nanobody (peak at ~18 ml elution volume). Red rectangles represent complex peak fractions. (**B**, **D**, **F**, **H**) SDS-PAGE analysis of relevant gelfiltration fractions. Red rectangles represent fractions on complex peak.

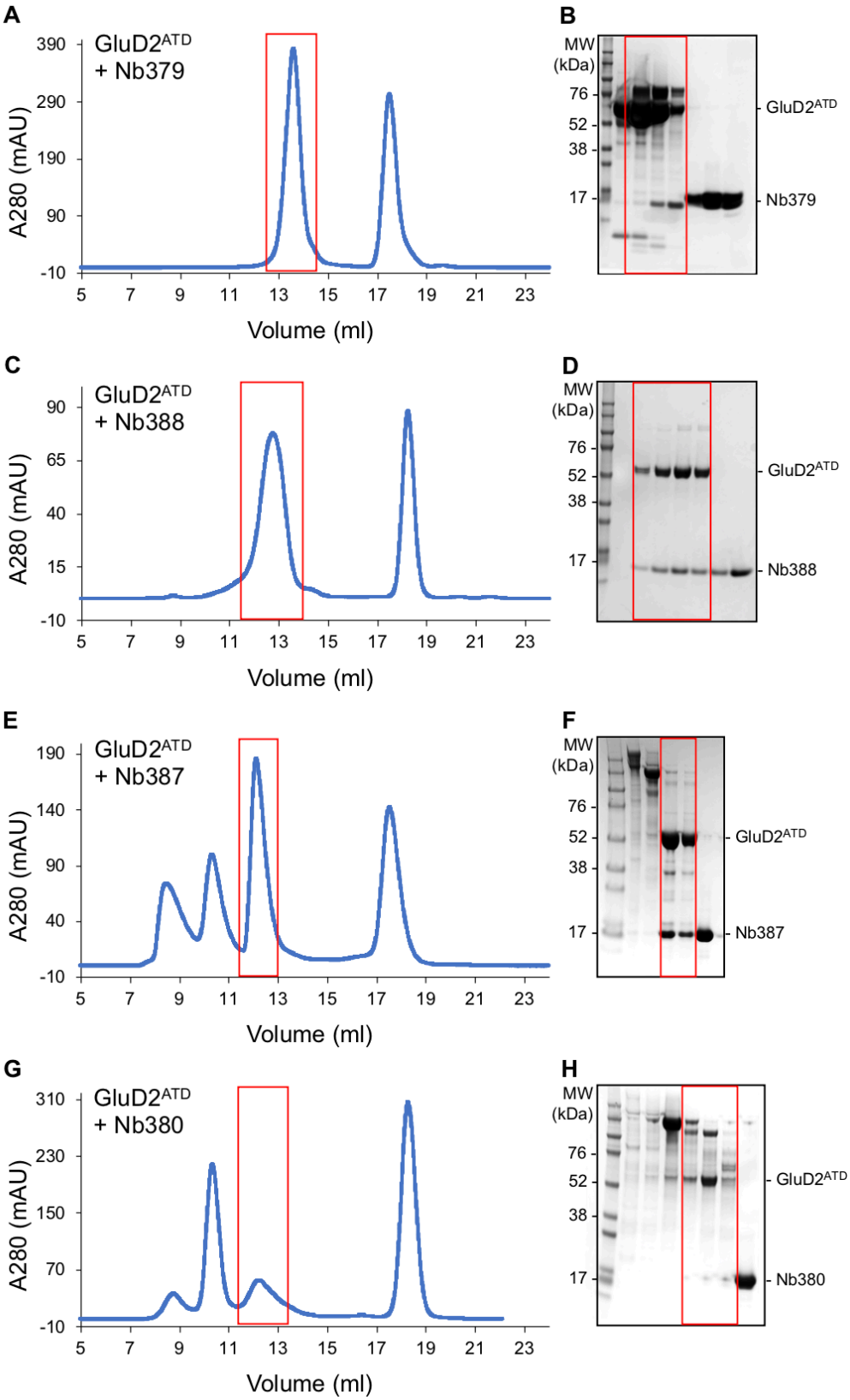

Figure 8-2 **Gelfiltration interaction studies of nanobodies against GluD2^{ATD}** (**A**, **C**, **E**, **G**) Gelfiltration elution profiles of nanobody complexes with the GluD2 amino-terminal domain (GluD2^{ATD}). All profiles show an excess of nanobody (peak at ~18 ml elution volume). Red rectangles represent complex peak fractions. (**B**, **D**, **F**, **H**) SDS-PAGE analysis of relevant gelfiltration fractions. Red rectangles represent fractions on complex peak.

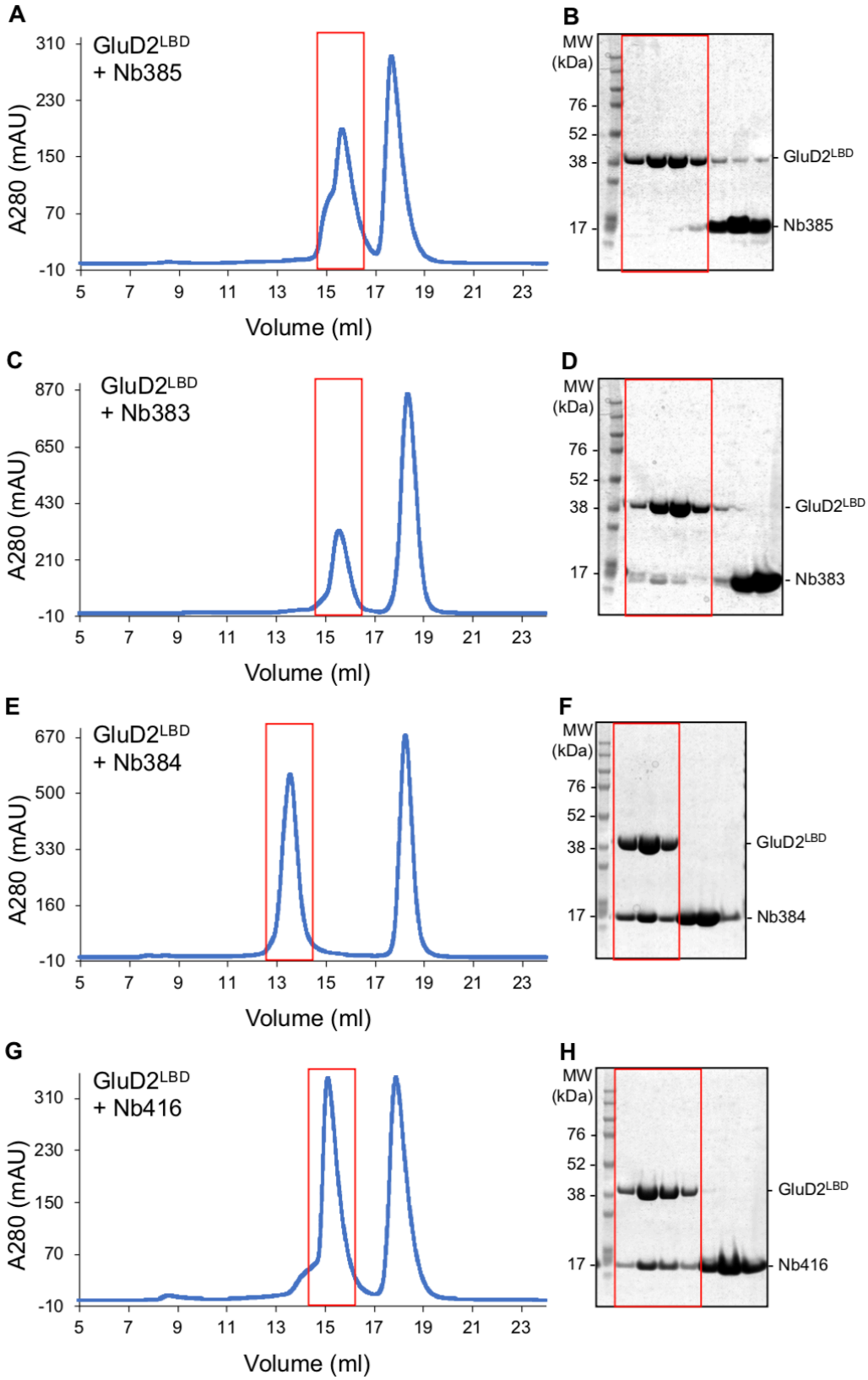

Figure 8-3 **Gelfiltration interaction studies of nanobodies against GluD2^{LBD}** (**A**, **C**, **E**, **G**) Gelfiltration elution profiles of nanobody complexes with the GluD2 ligand-binding domain (GluD2^{LBD}). All profiles show an excess of nanobody (peak at ~18 ml elution volume). Red rectangles represent complex peak fractions. (**B**, **D**, **F**, **H**) SDS-PAGE analysis of relevant gelfiltration fractions. Red rectangles represent fractions on complex peak.

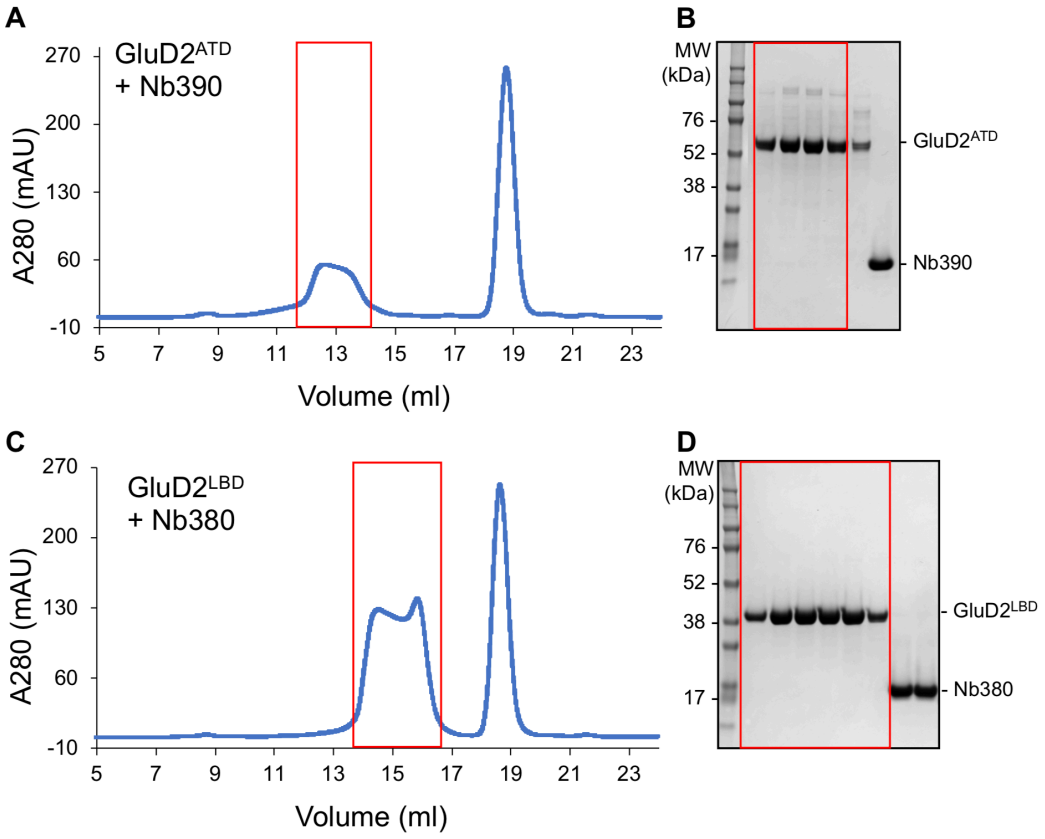

Figure 8-4 **Gelfiltration interaction studies of nanobodies against GluD2^{ATD} and GluD2^{LBD}** (**A**, **C**, **E**, **G**) Gelfiltration elution profiles of nanobody complexes with the GluD2 amino-terminal domain (GluD2^{ATD}) and GluD2 ligand-binding domain (GluD2^{LBD}). All profiles show an excess of nanobody (peak at ~18 ml elution volume). Red rectangles represent complex peak fractions. (**B**, **D**, **F**, **H**) SDS-PAGE analysis of relevant gelfiltration fractions. Red rectangles represent fractions on complex peak.

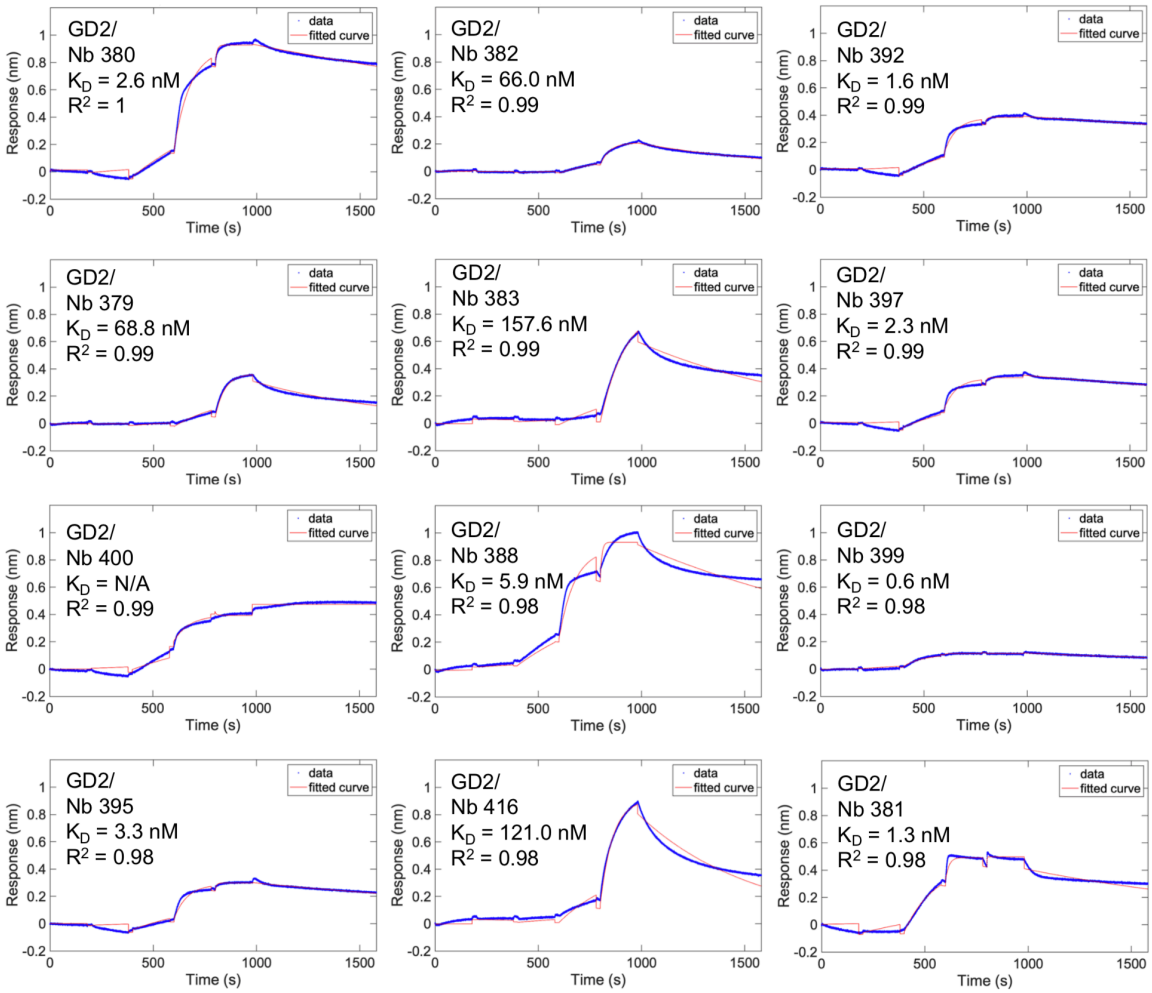

Figure 8-5* Single-cycle kinetics experiments of nanobody library against GluD2** Binding curves (blue data points) and fits (red traces) of single-cycle kinetics experiments, using Biolayer Interferometry. Biotinylated GluD2$^{\Delta C\text{-ter}}$ was immobilized on streptavidin-coated biosensors and dipped into increasing concentrations of nanobody samples (0.1, 1, 10, 100, 1000 nM). k_{on} and k_{off} values were derived from the fits, and used to calculate the binding affinity (K_D) (see ***Table 8-1 for all data and section 2.3 for fitting method).

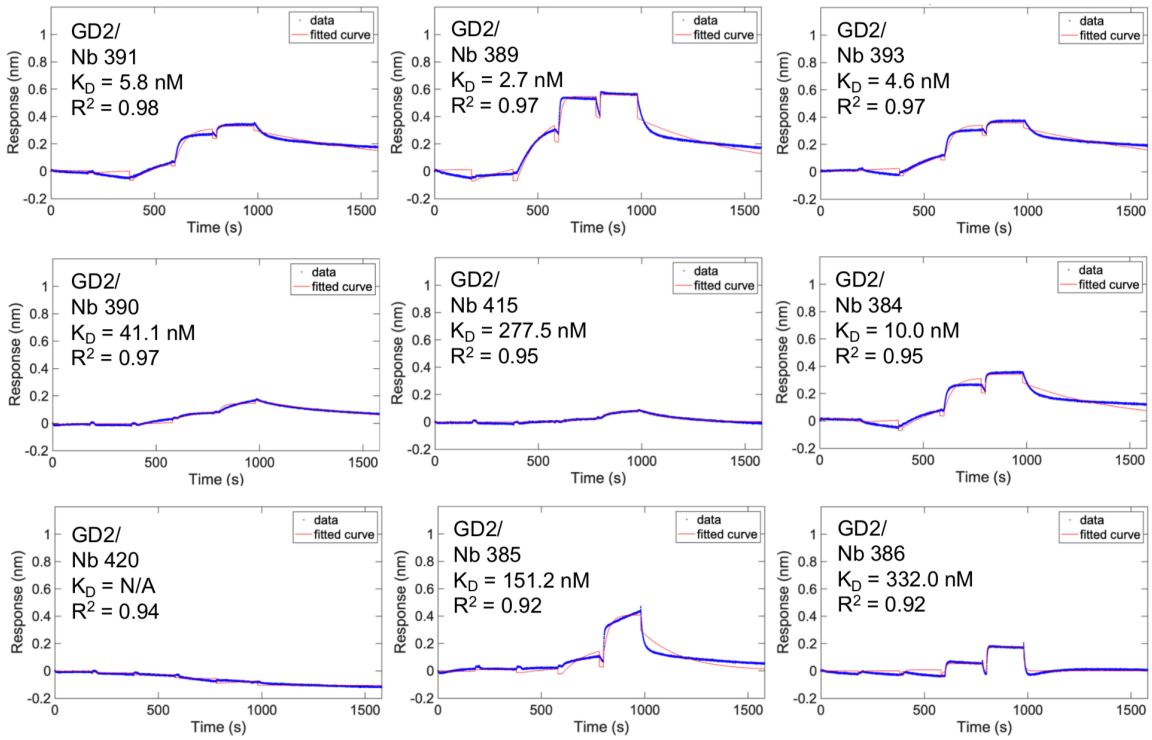

Figure 8-6* Single-cycle kinetics experiments of nanobody library against GluD2** Binding curves (blue data points) and fits (red traces) of single-cycle kinetics experiments, using Biolayer Interferometry. Biotinylated GluD2$^{\Delta C\text{-ter}}$ was immobilized on streptavidin-coated biosensors and dipped into increasing concentrations of nanobody samples (0.1, 1, 10, 100, 1000 nM). k_{on} and k_{off} values were derived from the fits, and used to calculate the binding affinity (K_D) (see ***Table 8-1 for all data and section 2.3 for fitting method).

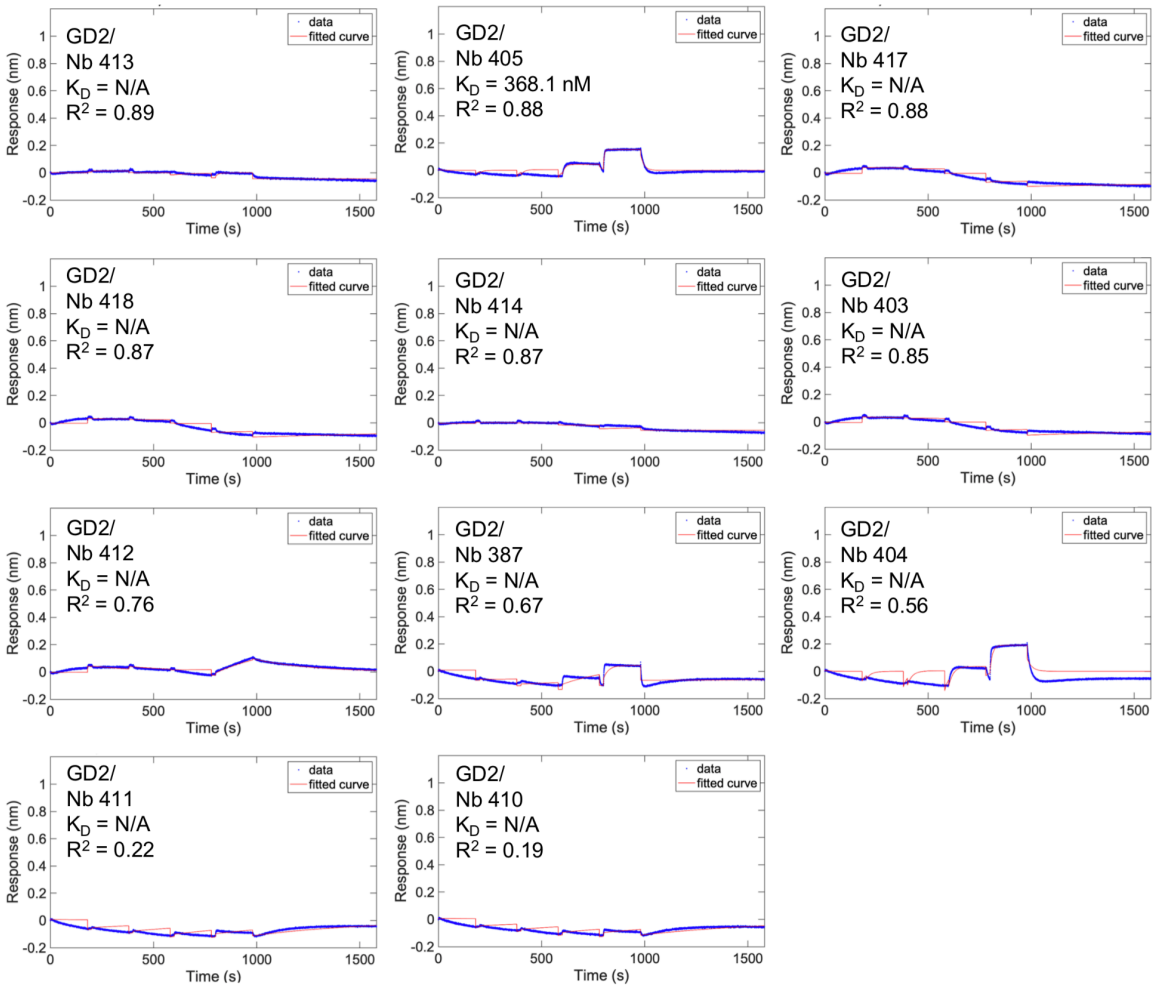

Figure 8-7* Single-cycle kinetics experiments of nanobody library against GluD2** Binding curves (blue data points) and fits (red traces) of single-cycle kinetics experiments, using Biolayer Interferometry. Biotinylated GluD2$^{\Delta C\text{-ter}}$ was immobilized on streptavidin-coated biosensors and dipped into increasing concentrations of nanobody samples (0.1, 1, 10, 100, 1000 nM). k_{on} and k_{off} values were derived from the fits, and used to calculate the binding affinity (K_D) (see ***Table 8-1 for all data and section 2.3 for fitting method).

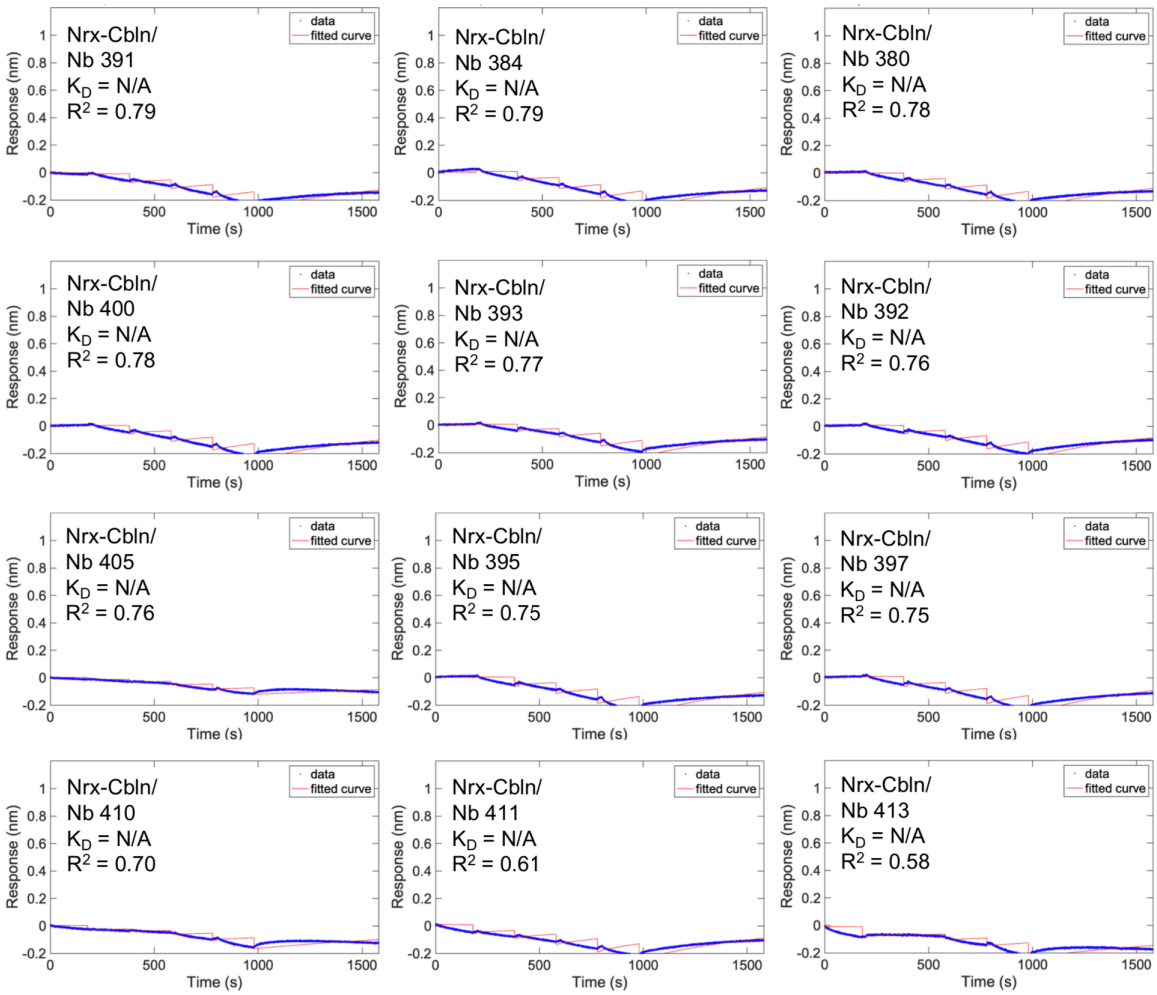

Figure 8-8 **Single-cycle kinetics experiments of nanobody library against Cbln1-βNrx1^{+SS4}** Binding curves (blue data points) and fits (red traces) of single-cycle kinetics experiments, using Biolayer Interferometry. Biotinylated Cbln1-βNrx1^{+SS4} was immobilized on streptavidin-coated biosensors and dipped into increasing concentrations of nanobody samples (0.1, 1, 10, 100, 1000 nM). k_{on} and k_{off} values were derived from the fits, and used to calculate the binding affinity (K_D) (see ***Table 8-2*** for all data and section 2.3 for fitting method).

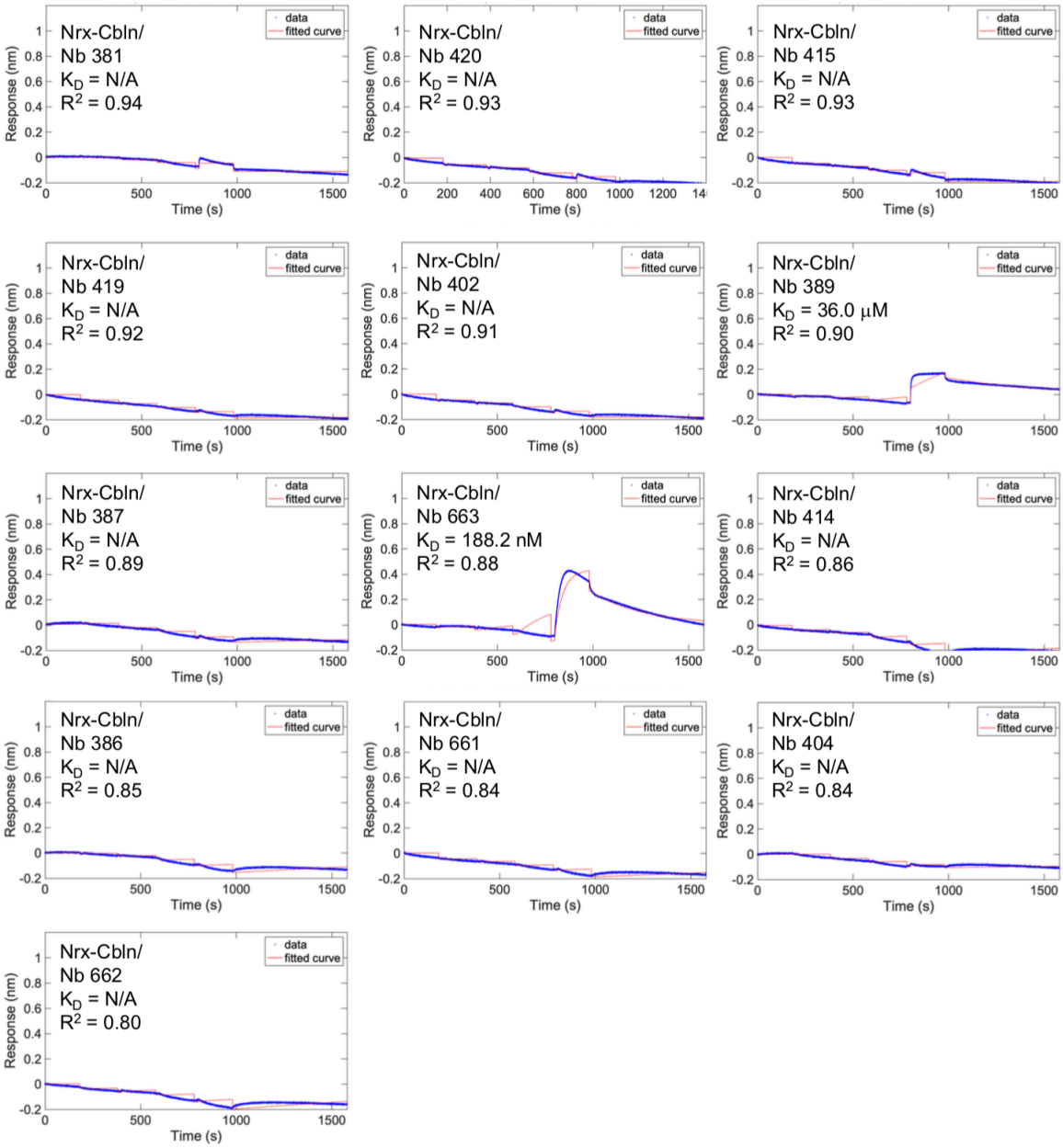

Figure 8-9* Single-cycle kinetics experiments of nanobody library against Cbln1-βNrx1^{+SS4}** Binding curves (blue data points) and fits (red traces) of single-cycle kinetics experiments, using Biolayer Interferometry. Biotinylated Cbln1-βNrx1^{+SS4} was immobilized on streptavidin-coated biosensors and dipped into increasing concentrations of nanobody samples (0.1, 1, 10, 100, 1000 nM). k_{on} and k_{off} values were derived from the fits, and used to calculate the binding affinity (K_D) (see ***Table 8-2 for all data and section 2.3 for fitting method).

Table 8-1 **Single-cycle kinetics results for nanobody binding experiments against GluD2** Results for single-cycle kinetics experiments using Biolayer Interferometry, based on binding curves shown in ***Figure 8-5***, ***Figure 8-6*** and ***Figure 8-7***. Binding curves were fitted in MATLAB (see text and section 2.3) and association (k_{on}), dissociation (k_{off}) constants and R_{max} values were derived from the fits. K_D values were calculated using equation 2 (see section 2.3) and R^2 was determined in MATLAB to evaluate the quality of the fit.

Nb ID	k_{on} ($M^{-1}s^{-1}$)		k_{off} (s^{-1})		R_{max} (nm)		K_D (nM)		R^2
CA11399	**9.99E+05**	±1.34E+04	**5.65E-04**	±1.12E-05	**1.14E-01**	±2.77E-04	**5.65E-01**	±1.88E-02	**0.98**
CA11381	**5.95E+05**	±6.93E+03	**7.52E-04**	±1.51E-05	**4.98E-01**	±1.29E-03	**1.26E+00**	±4.00E-02	**0.98**
CA11392	**1.72E+05**	±2.54E+03	**2.76E-04**	±8.88E-06	**3.85E-01**	±1.08E-03	**1.61E+00**	±7.57E-02	**0.99**
CA11397	**1.66E+05**	±2.97E+03	**3.83E-04**	±1.08E-05	**3.36E-01**	±1.15E-03	**2.31E+00**	±1.06E-01	**0.99**
CA11380	**1.24E+05**	±9.97E+02	**3.17E-04**	±5.52E-06	**9.30E-01**	±1.71E-03	**2.57E+00**	±6.54E-02	**1.00**
CA11389	**6.77E+05**	±9.05E+03	**1.84E-03**	±2.85E-05	**5.63E-01**	±1.71E-03	**2.72E+00**	±7.86E-02	**0.97**
CA11395	**1.51E+05**	±2.45E+03	**5.05E-04**	±1.25E-05	**2.98E-01**	±1.15E-03	**3.34E+00**	±1.37E-01	**0.98**
CA11393	**2.51E+05**	±4.63E+03	**1.15E-03**	±1.74E-05	**3.59E-01**	±1.26E-03	**4.58E+00**	±1.54E-01	**0.97**
CA11391	**1.97E+05**	±3.56E+03	**1.14E-03**	±1.79E-05	**3.32E-01**	±1.29E-03	**5.77E+00**	±1.95E-01	**0.98**
CA11388	**1.25E+05**	±1.82E+03	**7.23E-04**	±1.07E-05	**9.37E-01**	±2.95E-03	**5.78E+00**	±1.70E-01	**0.98**
CA11384	**2.20E+05**	±5.08E+03	**2.19E-03**	±3.49E-05	**3.44E-01**	±1.75E-03	**9.97E+00**	±3.89E-01	**0.95**
CA11390	**4.14E+04**	±1.09E+03	**1.70E-03**	±1.67E-05	**1.51E-01**	±8.75E-04	**4.11E+01**	±1.49E+00	**0.97**
CA11382	**2.04E+04**	±2.70E+02	**1.35E-03**	±7.76E-06	**2.23E-01**	±9.57E-04	**6.60E+01**	±1.25E+00	**0.99**
CA11379	**2.10E+04**	±3.26E+02	**1.44E-03**	±1.14E-05	**3.87E-01**	±2.07E-03	**6.88E+01**	±1.61E+00	**0.99**
CA11416	**1.48E+04**	±3.44E+02	**1.79E-03**	±1.31E-05	**1.02E+00**	±9.73E-03	**1.21E+02**	±3.70E+00	**0.98**
CA11385	**3.41E+04**	±1.04E+03	**5.15E-03**	±8.77E-05	**4.69E-01**	±4.67E-03	**1.51E+02**	±7.21E+00	**0.92**
CA11383	**7.15E+03**	±2.58E+02	**1.13E-03**	±1.02E-05	**1.00E+00**	±2.29E-02	**1.58E+02**	±7.13E+00	**0.99**
CA11415	**2.10E+04**	±1.03E+03	**5.84E-03**	±6.92E-05	**9.68E-02**	±1.71E-03	**2.78E+02**	±1.68E+01	**0.95**
CA11386	**3.95E+05**	±3.18E+04	**1.31E-01**	±9.93E-03	**2.32E-01**	±3.32E-03	**3.32E+02**	±5.19E+01	**0.92**
CA11400	**1.34E+05**	±3.10E+03	**2.47E-14**	N/A	**3.93E-01**	±1.41E-03	**1.84E-10**	±1.88E-10	**0.99**
CA11420	**1.21E+03**	±8.39E+01	**2.22E-14**	N/A	**1.06E-08**	N/A	N/A	N/A	**0.94**
CA11413	**6.65E+04**	±6.55E+03	**2.22E-14**	N/A	**6.74E-10**	N/A	N/A	N/A	**0.89**
CA11414	**5.01E+01**	±2.67E+03	**5.67E-12**	±5.67E-12	**6.31E-01**	±3.57E+01	**1.13E-04**	±6.14E-03	**0.87**
CA11387	**3.98E+04**	±1.95E+03	**8.59E-05**	±6.76E-05	**4.36E-02**	±1.96E-03	**2.16E+00**	±1.80E+00	**0.67**
CA11405	**1.64E+05**	±1.13E+04	**6.03E-02**	±3.39E-03	**2.10E-01**	±4.25E-03	**3.68E+02**	±4.62E+01	**0.88**
CA11404	**4.18E+04**	±9.13E+03	**4.21E-02**	±4.10E-03	**3.83E-01**	±5.20E-02	**1.01E+03**	±3.17E+02	**0.56**
CA11412	**3.97E+01**	±9.73E+02	**3.66E-03**	±7.23E-05	**1.75E+01**	±4.28E+02	**9.20E+04**	±2.26E+06	**0.76**
CA11417	**3.21E-09**	N/A	**2.64E-04**	±2.91E-05	**7.41E-12**	N/A	N/A	N/A	**0.88**
CA11411	**3.04E-10**	N/A	**1.83E-03**	±6.67E-05	**8.59E-12**	N/A	N/A	N/A	**0.22**
CA11403	**1.88E-11**	N/A	**4.68E-04**	±3.28E-05	**1.15E-09**	N/A	N/A	N/A	**0.85**
CA11418	**1.19E-11**	N/A	**4.02E-04**	±2.99E-05	**8.90E-10**	N/A	N/A	N/A	**0.87**
CA11410	**4.37E-14**	N/A	**1.51E-03**	±5.52E-05	**5.18E-14**	N/A	N/A	N/A	**0.19**

Table 8-2 **Single-cycle kinetics results for nanobody binding experiments against Cbln1-βNrx1^{+SS4}** Results for single-cycle kinetics experiments using Biolayer Interferometry, based on binding curves shown in ***Figure 8-8*** and ***Figure 8-9***. Binding curves were fitted in MATLAB (see text and section 2.3) and association (k_{on}), dissociation (k_{off}) constants and R_{max} values were derived from the fits. K_D values were calculated using equation 2 (see section 2.3) and R^2 was determined in MATLAB to evaluate the quality of the fit.

Nb ID	k_{on} ($M^{-1}s^{-1}$)		k_{off} (s^{-1})		R_{max} (nm)		K_D (nM)		R^2
CA11381	**1.78E-09**	N/A	**2.94E-14**	N/A	**3.91E-12**	N/A	**1.65E+04**	±3.30E+04	**0.94**
CA11389	**5.70E+01**	±9.50E+02	**2.05E-03**	±5.17E-05	**1.64E+01**	±2.71E+02	**3.60E+04**	±6.01E+05	**0.90**
CA11402	**3.34E-10**	N/A	**2.26E-14**	N/A	**1.87E-09**	N/A	**6.75E+04**	±1.35E+05	**0.91**
CA11419	**3.55E-11**	N/A	**2.28E-14**	N/A	**6.95E-14**	N/A	**6.41E+05**	±1.28E+06	**0.92**
CA11415	**1.68E-11**	N/A	**2.22E-14**	N/A	**6.13E-12**	N/A	**1.32E+06**	±2.65E+06	**0.93**
CA11420	**1.37E-11**	N/A	**2.22E-14**	N/A	**4.63E-10**	N/A	**1.62E+06**	±3.24E+06	**0.93**
CA11663	**1.90E+04**	±8.85E+02	**3.57E-03**	±9.03E-05	**5.18E-01**	±1.15E-02	**1.88E+02**	±1.35E+01	**0.88**
CA11397	**2.31E-07**	±1.70E+02	**1.71E-03**	±3.85E-05	**1.05E-09**	N/A	N/A	N/A	**0.75**
CA11392	**9.97E-08**	±1.67E+02	**1.75E-03**	±3.79E-05	**2.58E-10**	N/A	N/A	N/A	**0.76**
CA11400	**7.82E-08**	±1.61E+02	**1.49E-03**	±3.47E-05	**4.99E-09**	N/A	N/A	N/A	**0.78**
CA11393	**7.55E-08**	±1.67E+02	**1.62E-03**	±3.60E-05	**4.10E-09**	N/A	N/A	N/A	**0.77**
CA11391	**4.93E-08**	±1.44E+02	**1.21E-03**	±2.95E-05	**2.29E-09**	N/A	N/A	N/A	**0.79**
CA11413	**8.17E-09**	N/A	**7.69E-04**	±3.04E-05	**4.29E-14**	N/A	N/A	N/A	**0.58**
CA11405	**5.66E-09**	N/A	**5.76E-04**	±2.86E-05	**1.11E-11**	N/A	N/A	N/A	**0.76**
CA11662	**2.74E-09**	N/A	**6.17E-04**	±2.51E-05	**6.37E-09**	N/A	N/A	N/A	**0.80**
CA11661	**4.47E-10**	N/A	**3.45E-04**	±2.08E-05	**4.80E-12**	N/A	N/A	N/A	**0.84**
CA11414	**2.39E-11**	N/A	**4.72E-04**	±2.08E-05	**1.35E-12**	N/A	N/A	N/A	**0.86**
CA11410	**2.12E-11**	N/A	**8.53E-04**	±3.15E-05	**2.40E-10**	N/A	N/A	N/A	**0.70**
CA11384	**2.15E-11**	N/A	**1.45E-03**	±3.44E-05	**2.50E-14**	N/A	N/A	N/A	**0.79**
CA11411	**7.82E-12**	N/A	**1.67E-03**	±3.92E-05	**3.23E-13**	N/A	N/A	N/A	**0.61**
CA11395	**2.67E-12**	N/A	**1.52E-03**	±3.68E-05	**2.31E-13**	N/A	N/A	N/A	**0.75**
CA11386	**4.11E-13**	N/A	**5.71E-04**	±2.50E-05	**3.86E-11**	N/A	N/A	N/A	**0.85**
CA11387	**4.44E-14**	N/A	**2.62E-04**	±2.30E-05	**2.80E-11**	N/A	N/A	N/A	**0.89**
CA11380	**1.67E-13**	N/A	**1.34E-03**	±3.26E-05	**2.92E-14**	N/A	N/A	N/A	**0.78**
CA11404	**2.22E-14**	N/A	**1.84E-04**	±2.55E-05	**2.05E-10**	N/A	N/A	N/A	**0.84**

Nanobodies selected against GluD2 -Cbln1-βNrx1^{+SS4}

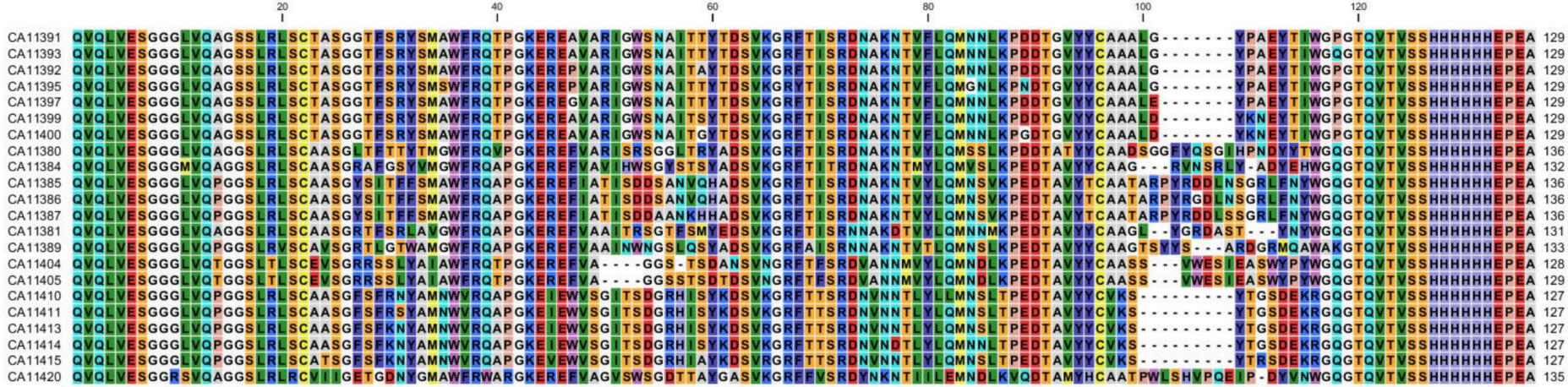

Nanobodies selected against GluD2

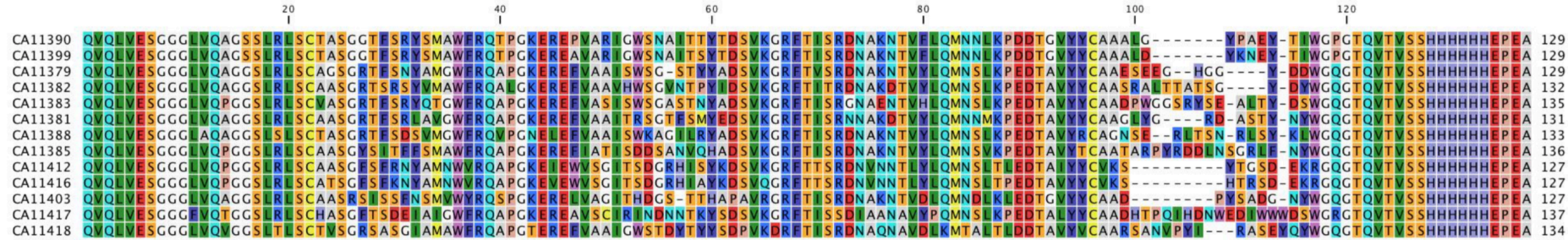

Figure 8-10 **Sequences of nanobodies screened against the GluD2-Cbln1-βNrx1^{+SS4} triad and GluD2 alone** Sequences and alignments obtained from Material Transfer Sheets made available by Jan Steyaert and Els Pardon. Llamas were immunized against two samples: GluD2 alone and GluD2 in complex with Cbln1-βNrx1^{+SS4}. Resulting nanobodies were then screened for binding against the triple complex, against GluD2 alone, and against Cbln1-βNrx1^{+SS4}.

Nanobodies selected against Cbln1-βNrx1^{+SS4}



Figure 8-11 **Sequences of nanobodies screened against CBln1-βNrx1^{+SS4}** Sequences and alignments obtained from Material Transfer Sheets made available by Jan Steyaert and Els Pardon. Llamas were immunized against two samples: GluD2 alone and GluD2 in complex with Cbln1-βNrx1^{+SS4}. Resulting nanobodies were then screened for binding against the triple complex, against GluD2 alone, and against Cbln1-βNrx1^{+SS4}.

Table 8-3 **Table of constructs**

Vector	Protein	Uniprot ID	Boundaries	N-ter tag	C-ter tag
pHLsec	GluD2^{LBD}	O43424-1 *(H. sapiens)*	440-551, GT linker, 664-823	-	2xGGS-Avi-6xHis
pHLsec	GluD2^{ATD}	O43424-1 *(H. sapiens)*	24-440	-	2xGGS-Avi-6xHis
pHLsec	GluD2^{ECTO}	O43424-1 *(H. sapiens)*	24-551, GT linker, 664-823	-	2xGGS-Avi-6xHis
pHLsec	Cbln1	P23435-1 *(H. sapiens)*	22-193	-	2XGGS-Avi-6xHis
pHLsec	Cbln1^{C1q}	P23435-1 *(H. sapiens)*	59-193	-	2xGGS-Avi-6xHis
pHLsec	β-Nrx1^{+SS4}	P58400-2 *(H. sapiens)*	86-295	-	Rho1D4
pHR	GluD2$^{\Delta C\text{-ter}}$	O43424-1 *(H. sapiens)*	24-870	-	Rho1D4
pMESy4	Nanobodies	See figure 10 *(L. glama)*	See figure 10	-	6xHis-CaptureSelect (EPEA)
pHLsec	Nanobodies	See figure 10 *(L. glama)*	See figure 10	-	3C-Avi-6xHis
pFastBac	RPTPμ-mVenus	P28827-2 *(H. sapiens)*	1-1465	-	2xGGS-mVenus
pHLsec	RPTPμ^{ECTO}	P28827-2 *(H. sapiens)*	1-742	-	6xHis
pFastBac	RPTPμ$^{D1\text{-}D2}$	P28827-2 *(H. sapiens)*	879-1452	-	TEV-6xHis
pFastBac	RPTPμ$^{D1\text{-}D2}$	P28827-2 *(H. sapiens)*	859-1452	-	TEV-6xHis
pFastBac	RPTPμ$^{D1\text{-}D2}$	P28827-2 *(H. sapiens)*	777-1452	-	TEV-6xHis
pFastBac	RACK1	P63244-1 *(H. sapiens)*	2-317	6xHis-TEV	-
pFastBacDual	RPTPμ$^{D1\text{-}D2}$ (under p10 promoter)	P28827-2 *(H. sapiens)*	777-1452	-	TEV-6xHis
	RACK1 (under polyhedrin promoter)	P63244-1 *(H. sapiens)*	2-317	6xHis-TEV	-

References and Permissions

1. Herculano-Houzel S. The human brain in numbers: a linearly scaled-up primate brain. Front Hum Neurosci. 2009;3:31.
2. Elegheert J, Kakegawa W, Clay JE, Shanks NF, Behiels E, Matsuda K, et al. Structural basis for integration of GluD receptors within synaptic organizer complexes. Science. 2016;353(6296):295-9.
3. Sudhof TC. Synaptic Neurexin Complexes: A Molecular Code for the Logic of Neural Circuits. Cell. 2017;171(4):745-69.
4. Traynelis SF, Wollmuth LP, McBain CJ, Menniti FS, Vance KM, Ogden KK, et al. Glutamate receptor ion channels: structure, regulation, and function. Pharmacol Rev. 2010;62(3):405-96.
5. Shepherd GM. The Synaptic Organization of the Brain, Chapter 1: Introduction to Synaptic Circuits. 5th Edition ed: Oxford University Press; 2003.
6. Citri A, Malenka RC. Synaptic plasticity: multiple forms, functions, and mechanisms. Neuropsychopharmacology. 2008;33(1):18-41.
7. Peters A PS, deF Webster H. The Fine Structure of the Nervous System. Oxford University Press. 1991.
8. Gray EG. Axo-somatic and axo-dendritic synapses of the cerebral cortex: an electron microscope study. J Anat. 1959;93:420-33.
9. Gray EG. Electron microscopy of synaptic contacts on dendrite spines of the cerebral cortex. Nature. 1959;183(4675):1592-3.
10. Lucic V, Yang T, Schweikert G, Forster F, Baumeister W. Morphological characterization of molecular complexes present in the synaptic cleft. Structure. 2005;13(3):423-34.

11. Burette AC, Lesperance T, Crum J, Martone M, Volkmann N, Ellisman MH, et al. Electron tomographic analysis of synaptic ultrastructure. J Comp Neurol. 2012;520(12):2697-711.
12. Fernandez-Busnadiego R, Schrod N, Kochovski Z, Asano S, Vanhecke D, Baumeister W, et al. Insights into the molecular organization of the neuron by cryo-electron tomography. J Electron Microsc (Tokyo). 2011;60 Suppl 1:S137-48.
13. High B, Cole AA, Chen X, Reese TS. Electron microscopic tomography reveals discrete transcleft elements at excitatory and inhibitory synapses. Front Synaptic Neurosci. 2015;7:9.
14. Tao CL, Liu YT, Sun R, Zhang B, Qi L, Shivakoti S, et al. Differentiation and Characterization of Excitatory and Inhibitory Synapses by Cryo-electron Tomography and Correlative Microscopy. J Neurosci. 2018;38(6):1493-510.
15. Perez de Arce K, Schrod N, Metzbower SWR, Allgeyer E, Kong GK, Tang AH, et al. Topographic Mapping of the Synaptic Cleft into Adhesive Nanodomains. Neuron. 2015;88(6):1165-72.
16. MacGillavry HD, Song Y, Raghavachari S, Blanpied TA. Nanoscale scaffolding domains within the postsynaptic density concentrate synaptic AMPA receptors. Neuron. 2013;78(4):615-22.
17. Nair D, Hosy E, Petersen JD, Constals A, Giannone G, Choquet D, et al. Super-resolution imaging reveals that AMPA receptors inside synapses are dynamically organized in nanodomains regulated by PSD95. J Neurosci. 2013;33(32):13204-24.
18. Fromer M, Pocklington AJ, Kavanagh DH, Williams HJ, Dwyer S, Gormley P, et al. De novo mutations in schizophrenia implicate synaptic networks. Nature. 2014;506(7487):179-84.
19. Volk L, Chiu SL, Sharma K, Huganir RL. Glutamate synapses in human cognitive disorders. Annu Rev Neurosci. 2015;38:127-49.
20. Chia PH, Li P, Shen K. Cell biology in neuroscience: cellular and molecular mechanisms underlying presynapse formation. J Cell Biol. 2013;203(1):11-22.
21. Tang AH, Chen H, Li TP, Metzbower SR, MacGillavry HD, Blanpied TA. A trans-synaptic nanocolumn aligns neurotransmitter release to receptors. Nature. 2016;536(7615):210-4.
22. Scheiffele P, Fan J, Choih J, Fetter R, Serafini T. Neuroligin expressed in nonneuronal cells triggers presynaptic development in contacting axons. Cell. 2000;101(6):657-69.
23. Chih B, Engelman H, Scheiffele P. Control of excitatory and inhibitory synapse formation by neuroligins. Science. 2005;307(5713):1324-8.
24. Graf ER, Zhang X, Jin SX, Linhoff MW, Craig AM. Neurexins induce differentiation of GABA and glutamate postsynaptic specializations via neuroligins. Cell. 2004;119(7):1013-26.
25. Stan A, Pielarski KN, Brigadski T, Wittenmayer N, Fedorchenko O, Gohla A, et al. Essential cooperation of N-cadherin and neuroligin-1 in the transsynaptic control of vesicle accumulation. Proc Natl Acad Sci U S A. 2010;107(24):11116-21.
26. Aiga M, Levinson JN, Bamji SX. N-cadherin and neuroligins cooperate to regulate synapse formation in hippocampal cultures. J Biol Chem. 2011;286(1):851-8.
27. Linhoff MW, Lauren J, Cassidy RM, Dobie FA, Takahashi H, Nygaard HB, et al. An unbiased expression screen for synaptogenic proteins identifies the LRRTM protein family as synaptic organizers. Neuron. 2009;61(5):734-49.
28. de Wit J, Sylwestrak E, O'Sullivan ML, Otto S, Tiglio K, Savas JN, et al. LRRTM2 interacts with Neurexin1 and regulates excitatory synapse formation. Neuron. 2009;64(6):799-806.

29. Ko J, Fuccillo MV, Malenka RC, Sudhof TC. LRRTM2 functions as a neurexin ligand in promoting excitatory synapse formation. Neuron. 2009;64(6):791-8.
30. Woo J, Kwon SK, Choi S, Kim S, Lee JR, Dunah AW, et al. Trans-synaptic adhesion between NGL-3 and LAR regulates the formation of excitatory synapses. Nat Neurosci. 2009;12(4):428-37.
31. Kwon SK, Woo J, Kim SY, Kim H, Kim E. Trans-synaptic adhesions between netrin-G ligand-3 (NGL-3) and receptor tyrosine phosphatases LAR, protein-tyrosine phosphatase delta (PTPdelta), and PTPsigma via specific domains regulate excitatory synapse formation. J Biol Chem. 2010;285(18):13966-78.
32. Takahashi H, Katayama K, Sohya K, Miyamoto H, Prasad T, Matsumoto Y, et al. Selective control of inhibitory synapse development by Slitrk3-PTPdelta trans-synaptic interaction. Nat Neurosci. 2012;15(3):389-98, S1-2.
33. Silva JP, Lelianova VG, Ermolyuk YS, Vysokov N, Hitchen PG, Berninghausen O, et al. Latrophilin 1 and its endogenous ligand Lasso/teneurin-2 form a high-affinity transsynaptic receptor pair with signaling capabilities. Proc Natl Acad Sci U S A. 2011;108(29):12113-8.
34. Vysokov NV, Silva JP, Lelianova VG, Suckling J, Cassidy J, Blackburn JK, et al. Proteolytically released Lasso/teneurin-2 induces axonal attraction by interacting with latrophilin-1 on axonal growth cones. Elife. 2018;7.
35. Ledda F, Paratcha G, Sandoval-Guzman T, Ibanez CF. GDNF and GFRalpha1 promote formation of neuronal synapses by ligand-induced cell adhesion. Nat Neurosci. 2007;10(3):293-300.
36. Miura E, Iijima T, Yuzaki M, Watanabe M. Distinct expression of Cbln family mRNAs in developing and adult mouse brains. Eur J Neurosci. 2006;24(3):750-60.
37. Uemura T, Lee SJ, Yasumura M, Takeuchi T, Yoshida T, Ra M, et al. Trans-synaptic interaction of GluRdelta2 and Neurexin through Cbln1 mediates synapse formation in the cerebellum. Cell. 2010;141(6):1068-79.
38. Matsuda K, Miura E, Miyazaki T, Kakegawa W, Emi K, Narumi S, et al. Cbln1 is a ligand for an orphan glutamate receptor delta2, a bidirectional synapse organizer. Science. 2010;328(5976):363-8.
39. Hirai H, Pang Z, Bao D, Miyazaki T, Li L, Miura E, et al. Cbln1 is essential for synaptic integrity and plasticity in the cerebellum. Nat Neurosci. 2005;8(11):1534-41.
40. Kashiwabuchi N, Ikeda K, Araki K, Hirano T, Shibuki K, Takayama C, et al. Impairment of motor coordination, Purkinje cell synapse formation, and cerebellar long-term depression in GluR delta 2 mutant mice. Cell. 1995;81(2):245-52.
41. Yasumura M, Yoshida T, Lee SJ, Uemura T, Joo JY, Mishina M. Glutamate receptor delta1 induces preferentially inhibitory presynaptic differentiation of cortical neurons by interacting with neurexins through cerebellin precursor protein subtypes. J Neurochem. 2012;121(5):705-16.
42. Iijima T, Miura E, Matsuda K, Kamekawa Y, Watanabe M, Yuzaki M. Characterization of a transneuronal cytokine family Cbln--regulation of secretion by heteromeric assembly. Eur J Neurosci. 2007;25(4):1049-57.
43. Matsuda K, Budisantoso T, Mitakidis N, Sugaya Y, Miura E, Kakegawa W, et al. Transsynaptic Modulation of Kainate Receptor Functions by C1q-like Proteins. Neuron. 2016;90(4):752-67.
44. Watson JF, Ho H, Greger IH. Synaptic transmission and plasticity require AMPA receptor anchoring via its N-terminal domain. Elife. 2017;6.
45. Meldrum BS. Glutamate as a neurotransmitter in the brain: review of physiology and pathology. J Nutr. 2000;130(4S Suppl):1007S-15S.

46. Sobolevsky AI, Rosconi MP, Gouaux E. X-ray structure, symmetry and mechanism of an AMPA-subtype glutamate receptor. Nature. 2009;462(7274):745-56.
47. Greger IH, Mayer ML. Structural biology of glutamate receptor ion channels: towards an understanding of mechanism. Curr Opin Struct Biol. 2019;57:185-95.
48. Sun Y, Olson R, Horning M, Armstrong N, Mayer M, Gouaux E. Mechanism of glutamate receptor desensitization. Nature. 2002;417(6886):245-53.
49. Sia GM, Beique JC, Rumbaugh G, Cho R, Worley PF, Huganir RL. Interaction of the N-terminal domain of the AMPA receptor GluR4 subunit with the neuronal pentraxin NP1 mediates GluR4 synaptic recruitment. Neuron. 2007;55(1):87-102.
50. Saglietti L, Dequidt C, Kamieniarz K, Rousset MC, Valnegri P, Thoumine O, et al. Extracellular interactions between GluR2 and N-cadherin in spine regulation. Neuron. 2007;54(3):461-77.
51. Auger C, Ogden D. AMPA receptor activation controls type I metabotropic glutamate receptor signalling via a tyrosine kinase at parallel fibre-Purkinje cell synapses. J Physiol. 2010;588(Pt 16):3063-74.
52. Rodriguez-Moreno A, Sihra TS. Metabotropic actions of kainate receptors in the CNS. J Neurochem. 2007;103(6):2121-35.
53. Dore K, Aow J, Malinow R. Agonist binding to the NMDA receptor drives movement of its cytoplasmic domain without ion flow. Proc Natl Acad Sci U S A. 2015;112(47):14705-10.
54. Weilinger NL, Lohman AW, Rakai BD, Ma EM, Bialecki J, Maslieieva V, et al. Metabotropic NMDA receptor signaling couples Src family kinases to pannexin-1 during excitotoxicity. Nat Neurosci. 2016;19(3):432-42.
55. Kohda K, Kakegawa W, Matsuda S, Yamamoto T, Hirano H, Yuzaki M. The delta2 glutamate receptor gates long-term depression by coordinating interactions between two AMPA receptor phosphorylation sites. Proc Natl Acad Sci U S A. 2013;110(10):E948-57.
56. Araki K, Meguro H, Kushiya E, Takayama C, Inoue Y, Mishina M. Selective expression of the glutamate receptor channel delta 2 subunit in cerebellar Purkinje cells. Biochem Biophys Res Commun. 1993;197(3):1267-76.
57. Van Schil K, Meire F, Karlstetter M, Bauwens M, Verdin H, Coppieters F, et al. Early-onset autosomal recessive cerebellar ataxia associated with retinal dystrophy: new human hotfoot phenotype caused by homozygous GRID2 deletion. Genet Med. 2015;17(4):291-9.
58. Coutelier M, Burglen L, Mundwiller E, Abada-Bendib M, Rodriguez D, Chantot-Bastaraud S, et al. GRID2 mutations span from congenital to mild adult-onset cerebellar ataxia. Neurology. 2015;84(17):1751-9.
59. Hosaka T, Nakamagoe K, Takahashi Y, Mamada N, Tamaoka A. Opsoclonus associated with autoantibodies to glutamate receptors delta2. Neurol Sci. 2015;36(9):1741-2.
60. Lomeli H, Sprengel R, Laurie DJ, Kohr G, Herb A, Seeburg PH, et al. The rat delta-1 and delta-2 subunits extend the excitatory amino acid receptor family. FEBS Lett. 1993;315(3):318-22.
61. Kakegawa W, Miyoshi Y, Hamase K, Matsuda S, Matsuda K, Kohda K, et al. D-serine regulates cerebellar LTD and motor coordination through the delta2 glutamate receptor. Nat Neurosci. 2011;14(5):603-11.
62. Naur P, Hansen KB, Kristensen AS, Dravid SM, Pickering DS, Olsen L, et al. Ionotropic glutamate-like receptor delta2 binds D-serine and glycine. Proc Natl Acad Sci U S A. 2007;104(35):14116-21.

63. Kakegawa W, Kohda K, Yuzaki M. The delta2 'ionotropic' glutamate receptor functions as a non-ionotropic receptor to control cerebellar synaptic plasticity. J Physiol. 2007;584(Pt 1):89-96.
64. Schmid SM, Kott S, Sager C, Huelsken T, Hollmann M. The glutamate receptor subunit delta2 is capable of gating its intrinsic ion channel as revealed by ligand binding domain transplantation. Proc Natl Acad Sci U S A. 2009;106(25):10320-5.
65. Orth A, Tapken D, Hollmann M. The delta subfamily of glutamate receptors: characterization of receptor chimeras and mutants. Eur J Neurosci. 2013;37(10):1620-30.
66. Zuo J, De Jager PL, Takahashi KA, Jiang W, Linden DJ, Heintz N. Neurodegeneration in Lurcher mice caused by mutation in delta2 glutamate receptor gene. Nature. 1997;388(6644):769-73.
67. Hansen KB, Naur P, Kurtkaya NL, Kristensen AS, Gajhede M, Kastrup JS, et al. Modulation of the dimer interface at ionotropic glutamate-like receptor delta2 by D-serine and extracellular calcium. J Neurosci. 2009;29(4):907-17.
68. Hirai H, Miyazaki T, Kakegawa W, Matsuda S, Mishina M, Watanabe M, et al. Rescue of abnormal phenotypes of the delta2 glutamate receptor-null mice by mutant delta2 transgenes. EMBO Rep. 2005;6(1):90-5.
69. Kakegawa W, Miyazaki T, Emi K, Matsuda K, Kohda K, Motohashi J, et al. Differential regulation of synaptic plasticity and cerebellar motor learning by the C-terminal PDZ-binding motif of GluRdelta2. J Neurosci. 2008;28(6):1460-8.
70. Kohda K, Kakegawa W, Matsuda S, Nakagami R, Kakiya N, Yuzaki M. The extreme C-terminus of GluRdelta2 is essential for induction of long-term depression in cerebellar slices. Eur J Neurosci. 2007;25(5):1357-62.
71. Torashima T, Iizuka A, Horiuchi H, Mitsumura K, Yamasaki M, Koyama C, et al. Rescue of abnormal phenotypes in delta2 glutamate receptor-deficient mice by the extracellular N-terminal and intracellular C-terminal domains of the delta2 glutamate receptor. Eur J Neurosci. 2009;30(3):355-65.
72. Lee SJ, Uemura T, Yoshida T, Mishina M. GluRdelta2 assembles four neurexins into trans-synaptic triad to trigger synapse formation. J Neurosci. 2012;32(13):4688-701.
73. Bao D, Pang Z, Morgan MA, Parris J, Rong Y, Li L, et al. Cbln1 is essential for interaction-dependent secretion of Cbln3. Mol Cell Biol. 2006;26(24):9327-37.
74. Wei P, Pattarini R, Rong Y, Guo H, Bansal PK, Kusnoor SV, et al. The Cbln family of proteins interact with multiple signaling pathways. J Neurochem. 2012;121(5):717-29.
75. Joo JY, Lee SJ, Uemura T, Yoshida T, Yasumura M, Watanabe M, et al. Differential interactions of cerebellin precursor protein (Cbln) subtypes and neurexin variants for synapse formation of cortical neurons. Biochem Biophys Res Commun. 2011;406(4):627-32.
76. Ushkaryov YA, Petrenko AG, Geppert M, Sudhof TC. Neurexins: synaptic cell surface proteins related to the alpha-latrotoxin receptor and laminin. Science. 1992;257(5066):50-6.
77. Ushkaryov YA, Sudhof TC. Neurexin III alpha: extensive alternative splicing generates membrane-bound and soluble forms. Proc Natl Acad Sci U S A. 1993;90(14):6410-4.
78. Sterky FH, Trotter JH, Lee SJ, Recktenwald CV, Du X, Zhou B, et al. Carbonic anhydrase-related protein CA10 is an evolutionarily conserved pan-neurexin ligand. Proc Natl Acad Sci U S A. 2017;114(7):E1253-E62.
79. Ullrich B, Ushkaryov YA, Sudhof TC. Cartography of neurexins: more than 1000 isoforms generated by alternative splicing and expressed in distinct subsets of neurons. Neuron. 1995;14(3):497-507.

80. Schreiner D, Nguyen TM, Russo G, Heber S, Patrignani A, Ahrne E, et al. Targeted combinatorial alternative splicing generates brain region-specific repertoires of neurexins. Neuron. 2014;84(2):386-98.
81. Ding X, Liu S, Tian M, Zhang W, Zhu T, Li D, et al. Activity-induced histone modifications govern Neurexin-1 mRNA splicing and memory preservation. Nat Neurosci. 2017;20(5):690-9.
82. Sugita S, Saito F, Tang J, Satz J, Campbell K, Sudhof TC. A stoichiometric complex of neurexins and dystroglycan in brain. J Cell Biol. 2001;154(2):435-45.
83. Missler M, Hammer RE, Sudhof TC. Neurexophilin binding to alpha-neurexins. A single LNS domain functions as an independently folding ligand-binding unit. J Biol Chem. 1998;273(52):34716-23.
84. Boucard AA, Ko J, Sudhof TC. High affinity neurexin binding to cell adhesion G-protein-coupled receptor CIRL1/latrophilin-1 produces an intercellular adhesion complex. J Biol Chem. 2012;287(12):9399-413.
85. Ichtchenko K, Nguyen T, Sudhof TC. Structures, alternative splicing, and neurexin binding of multiple neuroligins. J Biol Chem. 1996;271(5):2676-82.
86. Siddiqui TJ, Pancaroglu R, Kang Y, Rooyakkers A, Craig AM. LRRTMs and neuroligins bind neurexins with a differential code to cooperate in glutamate synapse development. J Neurosci. 2010;30(22):7495-506.
87. Tanaka H, Nogi T, Yasui N, Iwasaki K, Takagi J. Structural basis for variant-specific neuroligin-binding by alpha-neurexin. PLoS One. 2011;6(4):e19411.
88. Yamashita M, Kawaguchi SY, Hirano T. Contribution of postsynaptic GluD2 to presynaptic R-type Ca(2+) channel function, glutamate release and long-term potentiation at parallel fiber to Purkinje cell synapses. Cerebellum. 2013;12(5):657-66.
89. Sacco F, Perfetto L, Castagnoli L, Cesareni G. The human phosphatase interactome: An intricate family portrait. FEBS Lett. 2012;586(17):2732-9.
90. Li X, Wilmanns M, Thornton J, Kohn M. Elucidating human phosphatase-substrate networks. Sci Signal. 2013;6(275):rs10.
91. Lemmon MA, Schlessinger J. Cell signaling by receptor tyrosine kinases. Cell. 2010;141(7):1117-34.
92. Pot DA, Woodford TA, Remboutsika E, Haun RS, Dixon JE. Cloning, bacterial expression, purification, and characterization of the cytoplasmic domain of rat LAR, a receptor-like protein tyrosine phosphatase. J Biol Chem. 1991;266(29):19688-96.
93. Streuli M, Krueger NX, Tsai AY, Saito H. A family of receptor-linked protein tyrosine phosphatases in humans and Drosophila. Proc Natl Acad Sci U S A. 1989;86(22):8698-702.
94. Wills Z, Bateman J, Korey CA, Comer A, Van Vactor D. The tyrosine kinase Abl and its substrate enabled collaborate with the receptor phosphatase Dlar to control motor axon guidance. Neuron. 1999;22(2):301-12.
95. Serra-Pages C, Kedersha NL, Fazikas L, Medley Q, Debant A, Streuli M. The LAR transmembrane protein tyrosine phosphatase and a coiled-coil LAR-interacting protein co-localize at focal adhesions. EMBO J. 1995;14(12):2827-38.
96. Debant A, Serra-Pages C, Seipel K, O'Brien S, Tang M, Park SH, et al. The multidomain protein Trio binds the LAR transmembrane tyrosine phosphatase, contains a protein kinase domain, and has separate rac-specific and rho-specific guanine nucleotide exchange factor domains. Proc Natl Acad Sci U S A. 1996;93(11):5466-71.
97. Nam HJ, Poy F, Krueger NX, Saito H, Frederick CA. Crystal structure of the tandem phosphatase domains of RPTP LAR. Cell. 1999;97(4):449-57.

98. Streuli M, Krueger NX, Thai T, Tang M, Saito H. Distinct functional roles of the two intracellular phosphatase like domains of the receptor-linked protein tyrosine phosphatases LCA and LAR. EMBO J. 1990;9(8):2399-407.
99. Felberg J, Johnson P. Characterization of recombinant CD45 cytoplasmic domain proteins. Evidence for intramolecular and intermolecular interactions. J Biol Chem. 1998;273(28):17839-45.
100. Bilwes AM, den Hertog J, Hunter T, Noel JP. Structural basis for inhibition of receptor protein-tyrosine phosphatase-alpha by dimerization. Nature. 1996;382(6591):555-9.
101. Jiang G, den Hertog J, Su J, Noel J, Sap J, Hunter T. Dimerization inhibits the activity of receptor-like protein-tyrosine phosphatase-alpha. Nature. 1999;401(6753):606-10.
102. Tertoolen LG, Blanchetot C, Jiang G, Overvoorde J, Gadella TW, Jr., Hunter T, et al. Dimerization of receptor protein-tyrosine phosphatase alpha in living cells. BMC Cell Biol. 2001;2:8.
103. Johnson KG, Van Vactor D. Receptor protein tyrosine phosphatases in nervous system development. Physiol Rev. 2003;83(1):1-24.
104. Majeti R, Xu Z, Parslow TG, Olson JL, Daikh DI, Killeen N, et al. An inactivating point mutation in the inhibitory wedge of CD45 causes lymphoproliferation and autoimmunity. Cell. 2000;103(7):1059-70.
105. Desai DM, Sap J, Schlessinger J, Weiss A. Ligand-mediated negative regulation of a chimeric transmembrane receptor tyrosine phosphatase. Cell. 1993;73(3):541-54.
106. Wallace MJ, Fladd C, Batt J, Rotin D. The second catalytic domain of protein tyrosine phosphatase delta (PTP delta) binds to and inhibits the first catalytic domain of PTP sigma. Mol Cell Biol. 1998;18(5):2608-16.
107. Blanchetot C, den Hertog J. Multiple interactions between receptor protein-tyrosine phosphatase (RPTP) alpha and membrane-distal protein-tyrosine phosphatase domains of various RPTPs. J Biol Chem. 2000;275(17):12446-52.
108. Hoffmann KM, Tonks NK, Barford D. The crystal structure of domain 1 of receptor protein-tyrosine phosphatase mu. J Biol Chem. 1997;272(44):27505-8.
109. Aricescu AR, Siebold C, Choudhuri K, Chang VT, Lu W, Davis SJ, et al. Structure of a tyrosine phosphatase adhesive interaction reveals a spacer-clamp mechanism. Science. 2007;317(5842):1217-20.
110. Zondag GC, Koningstein GM, Jiang YP, Sap J, Moolenaar WH, Gebbink MF. Homophilic interactions mediated by receptor tyrosine phosphatases mu and kappa. A critical role for the novel extracellular MAM domain. J Biol Chem. 1995;270(24):14247-50.
111. Fuchs M, Wang H, Ciossek T, Chen Z, Ullrich A. Differential expression of MAM-subfamily protein tyrosine phosphatases during mouse development. Mech Dev. 1998;70(1-2):91-109.
112. McAndrew PE, Frostholm A, White RA, Rotter A, Burghes AH. Identification and characterization of RPTP rho, a novel RPTP mu/kappa-like receptor protein tyrosine phosphatase whose expression is restricted to the central nervous system. Brain Res Mol Brain Res. 1998;56(1-2):9-21.
113. Wang Z, Shen D, Parsons DW, Bardelli A, Sager J, Szabo S, et al. Mutational analysis of the tyrosine phosphatome in colorectal cancers. Science. 2004;304(5674):1164-6.
114. Burgoyne AM, Palomo JM, Phillips-Mason PJ, Burden-Gulley SM, Major DL, Zaremba A, et al. PTPmu suppresses glioma cell migration and dispersal. Neuro Oncol. 2009;11(6):767-78.

115. Bianchi C, Sellke FW, Del Vecchio RL, Tonks NK, Neel BG. Receptor-type protein-tyrosine phosphatase mu is expressed in specific vascular endothelial beds in vivo. Exp Cell Res. 1999;248(1):329-38.
116. Koop EA, Lopes SM, Feiken E, Bluyssen HA, van der Valk M, Voest EE, et al. Receptor protein tyrosine phosphatase mu expression as a marker for endothelial cell heterogeneity; analysis of RPTPmu gene expression using LacZ knock-in mice. Int J Dev Biol. 2003;47(5):345-54.
117. Ensslen-Craig SE, Brady-Kalnay SM. Receptor protein tyrosine phosphatases regulate neural development and axon guidance. Dev Biol. 2004;275(1):12-22.
118. Aricescu AR, Hon WC, Siebold C, Lu W, van der Merwe PA, Jones EY. Molecular analysis of receptor protein tyrosine phosphatase mu-mediated cell adhesion. EMBO J. 2006;25(4):701-12.
119. Campan M, Yoshizumi M, Seidah NG, Lee ME, Bianchi C, Haber E. Increased proteolytic processing of protein tyrosine phosphatase mu in confluent vascular endothelial cells: the role of PC5, a member of the subtilisin family. Biochemistry. 1996;35(12):3797-802.
120. Anders L, Mertins P, Lammich S, Murgia M, Hartmann D, Saftig P, et al. Furin-, ADAM 10-, and gamma-secretase-mediated cleavage of a receptor tyrosine phosphatase and regulation of beta-catenin's transcriptional activity. Mol Cell Biol. 2006;26(10):3917-34.
121. Gebbink MF, Zondag GC, Koningstein GM, Feiken E, Wubbolts RW, Moolenaar WH. Cell surface expression of receptor protein tyrosine phosphatase RPTP mu is regulated by cell-cell contact. J Cell Biol. 1995;131(1):251-60.
122. Burgoyne AM, Phillips-Mason PJ, Burden-Gulley SM, Robinson S, Sloan AE, Miller RH, et al. Proteolytic cleavage of protein tyrosine phosphatase mu regulates glioblastoma cell migration. Cancer Res. 2009;69(17):6960-8.
123. Brady-Kalnay SM, Mourton T, Nixon JP, Pietz GE, Kinch M, Chen H, et al. Dynamic interaction of PTPmu with multiple cadherins in vivo. J Cell Biol. 1998;141(1):287-96.
124. Sui XF, Kiser TD, Hyun SW, Angelini DJ, Del Vecchio RL, Young BA, et al. Receptor protein tyrosine phosphatase micro regulates the paracellular pathway in human lung microvascular endothelia. Am J Pathol. 2005;166(4):1247-58.
125. Mourton T, Hellberg CB, Burden-Gulley SM, Hinman J, Rhee A, Brady-Kalnay SM. The PTPmu protein-tyrosine phosphatase binds and recruits the scaffolding protein RACK1 to cell-cell contacts. J Biol Chem. 2001;276(18):14896-901.
126. Rosdahl JA, Mourton TL, Brady-Kalnay SM. Protein kinase C delta (PKCdelta) is required for protein tyrosine phosphatase mu (PTPmu)-dependent neurite outgrowth. Mol Cell Neurosci. 2002;19(2):292-306.
127. Nilsson J, Sengupta J, Frank J, Nissen P. Regulation of eukaryotic translation by the RACK1 protein: a platform for signalling molecules on the ribosome. EMBO Rep. 2004;5(12):1137-41.
128. Aricescu AR, Siebold C, Jones EY. Receptor protein tyrosine phosphatase micro: measuring where to stick. Biochem Soc Trans. 2008;36(Pt 2):167-72.
129. Ensslen-Craig SE, Brady-Kalnay SM. PTP mu expression and catalytic activity are required for PTP mu-mediated neurite outgrowth and repulsion. Mol Cell Neurosci. 2005;28(1):177-88.
130. Ensslen SE, Rosdahl JA, Brady-Kalnay SM. The receptor protein tyrosine phosphatase mu, PTPmu, regulates histogenesis of the chick retina. Dev Biol. 2003;264(1):106-18.
131. Himanen JP, Yermekbayeva L, Janes PW, Walker JR, Xu K, Atapattu L, et al. Architecture of Eph receptor clusters. Proc Natl Acad Sci U S A. 2010;107(24):10860-5.

132. Seiradake E, Harlos K, Sutton G, Aricescu AR, Jones EY. An extracellular steric seeding mechanism for Eph-ephrin signaling platform assembly. Nat Struct Mol Biol. 2010;17(4):398-402.
133. Tanaka H, Miyazaki N, Matoba K, Nogi T, Iwasaki K, Takagi J. Higher-order architecture of cell adhesion mediated by polymorphic synaptic adhesion molecules neurexin and neuroligin. Cell Rep. 2012;2(1):101-10.
134. Harrison OJ, Jin X, Hong S, Bahna F, Ahlsen G, Brasch J, et al. The extracellular architecture of adherens junctions revealed by crystal structures of type I cadherins. Structure. 2011;19(2):244-56.
135. Um JW, Kim KH, Park BS, Choi Y, Kim D, Kim CY, et al. Structural basis for LAR-RPTP/Slitrk complex-mediated synaptic adhesion. Nat Commun. 2014;5:5423.
136. Cismasiu VB, Denes SA, Reilander H, Michel H, Szedlacsek SE. The MAM (meprin/A5-protein/PTPmu) domain is a homophilic binding site promoting the lateral dimerization of receptor-like protein-tyrosine phosphatase mu. J Biol Chem. 2004;279(26):26922-31.
137. Teese MG, Langosch D. Role of GxxxG Motifs in Transmembrane Domain Interactions. Biochemistry. 2015;54(33):5125-35.
138. Aricescu AR, Lu W, Jones EY. A time- and cost-efficient system for high-level protein production in mammalian cells. Acta Crystallogr D Biol Crystallogr. 2006;62(Pt 10):1243-50.
139. Elegheert J, Behiels E, Bishop B, Scott S, Woolley RE, Griffiths SC, et al. Lentiviral transduction of mammalian cells for fast, scalable and high-level production of soluble and membrane proteins. Nat Protoc. 2018;13(12):2991-3017.
140. Reeves PJ, Callewaert N, Contreras R, Khorana HG. Structure and function in rhodopsin: high-level expression of rhodopsin with restricted and homogeneous N-glycosylation by a tetracycline-inducible N-acetylglucosaminyltransferase I-negative HEK293S stable mammalian cell line. Proc Natl Acad Sci U S A. 2002;99(21):13419-24.
141. Pardon E, Laeremans T, Triest S, Rasmussen SG, Wohlkonig A, Ruf A, et al. A general protocol for the generation of Nanobodies for structural biology. Nat Protoc. 2014;9(3):674-93.
142. Karlsson R, Katsamba PS, Nordin H, Pol E, Myszka DG. Analyzing a kinetic titration series using affinity biosensors. Anal Biochem. 2006;349(1):136-47.
143. Winter G, Lobley CM, Prince SM. Decision making in xia2. Acta Crystallogr D Biol Crystallogr. 2013;69(Pt 7):1260-73.
144. Evans P. Scaling and assessment of data quality. Acta Crystallogr D Biol Crystallogr. 2006;62(Pt 1):72-82.
145. Kantardjieff KA, Rupp B. Matthews coefficient probabilities: Improved estimates for unit cell contents of proteins, DNA, and protein-nucleic acid complex crystals. Protein Sci. 2003;12(9):1865-71.
146. Matthews BW. Solvent content of protein crystals. J Mol Biol. 1968;33(2):491-7.
147. Winn MD, Ballard CC, Cowtan KD, Dodson EJ, Emsley P, Evans PR, et al. Overview of the CCP4 suite and current developments. Acta Crystallogr D Biol Crystallogr. 2011;67(Pt 4):235-42.
148. McCoy AJ, Grosse-Kunstleve RW, Adams PD, Winn MD, Storoni LC, Read RJ. Phaser crystallographic software. J Appl Crystallogr. 2007;40(Pt 4):658-74.
149. Murshudov GN, Skubak P, Lebedev AA, Pannu NS, Steiner RA, Nicholls RA, et al. REFMAC5 for the refinement of macromolecular crystal structures. Acta Crystallogr D Biol Crystallogr. 2011;67(Pt 4):355-67.
150. Emsley P, Cowtan K. Coot: model-building tools for molecular graphics. Acta Crystallogr D Biol Crystallogr. 2004;60(Pt 12 Pt 1):2126-32.

151. Langer G, Cohen SX, Lamzin VS, Perrakis A. Automated macromolecular model building for X-ray crystallography using ARP/wARP version 7. Nat Protoc. 2008;3(7):1171-9.
152. Lamzin VS, Wilson KS. Automated refinement of protein models. Acta Crystallogr D Biol Crystallogr. 1993;49(Pt 1):129-47.
153. Adams PD, Afonine PV, Bunkoczi G, Chen VB, Davis IW, Echols N, et al. PHENIX: a comprehensive Python-based system for macromolecular structure solution. Acta Crystallogr D Biol Crystallogr. 2010;66(Pt 2):213-21.
154. Painter J, Merritt EA. Optimal description of a protein structure in terms of multiple groups undergoing TLS motion. Acta Crystallogr D Biol Crystallogr. 2006;62(Pt 4):439-50.
155. Chen VB, Arendall WB, 3rd, Headd JJ, Keedy DA, Immormino RM, Kapral GJ, et al. MolProbity: all-atom structure validation for macromolecular crystallography. Acta Crystallogr D Biol Crystallogr. 2010;66(Pt 1):12-21.
156. Yang Z, Lasker K, Schneidman-Duhovny D, Webb B, Huang CC, Pettersen EF, et al. UCSF Chimera, MODELLER, and IMP: an integrated modeling system. J Struct Biol. 2012;179(3):269-78.
157. Krissinel E, Henrick K. Inference of macromolecular assemblies from crystalline state. J Mol Biol. 2007;372(3):774-97.
158. Hayward S, Lee RA. Improvements in the analysis of domain motions in proteins from conformational change: DynDom version 1.50. J Mol Graph Model. 2002;21(3):181-3.
159. Laverty D, Desai R, Uchanski T, Masiulis S, Stec WJ, Malinauskas T, et al. Cryo-EM structure of the human alpha1beta3gamma2 GABAA receptor in a lipid bilayer. Nature. 2019;565(7740):516-20.
160. Masiulis S, Desai R, Uchanski T, Serna Martin I, Laverty D, Karia D, et al. GABAA receptor signalling mechanisms revealed by structural pharmacology. Nature. 2019;565(7740):454-9.
161. Bayburt TH, Sligar SG. Membrane protein assembly into Nanodiscs. FEBS Lett. 2010;584(9):1721-7.
162. Danev R, Buijsse B, Khoshouei M, Plitzko JM, Baumeister W. Volta potential phase plate for in-focus phase contrast transmission electron microscopy. Proc Natl Acad Sci U S A. 2014;111(44):15635-40.
163. Zheng SQ, Palovcak E, Armache JP, Verba KA, Cheng Y, Agard DA. MotionCor2: anisotropic correction of beam-induced motion for improved cryo-electron microscopy. Nat Methods. 2017;14(4):331-2.
164. Zhang K. Gctf: Real-time CTF determination and correction. J Struct Biol. 2016;193(1):1-12.
165. Scheres SH. RELION: implementation of a Bayesian approach to cryo-EM structure determination. J Struct Biol. 2012;180(3):519-30.
166. Scheres SH. A Bayesian view on cryo-EM structure determination. J Mol Biol. 2012;415(2):406-18.
167. Tang G, Peng L, Baldwin PR, Mann DS, Jiang W, Rees I, et al. EMAN2: an extensible image processing suite for electron microscopy. J Struct Biol. 2007;157(1):38-46.
168. Ader NR, Kukulski W. triCLEM: Combining high-precision, room temperature CLEM with cryo-fluorescence microscopy to identify very rare events. Methods Cell Biol. 2017;140:303-20.
169. Kukulski W, Schorb M, Welsch S, Picco A, Kaksonen M, Briggs JA. Precise, correlated fluorescence microscopy and electron tomography of lowicryl sections using fluorescent fiducial markers. Methods Cell Biol. 2012;111:235-57.

170. Mastronarde DN. Automated electron microscope tomography using robust prediction of specimen movements. J Struct Biol. 2005;152(1):36-51.
171. Schaffer M, Mahamid J, Engel BD, Laugks T, Baumeister W, Plitzko JM. Optimized cryo-focused ion beam sample preparation aimed at in situ structural studies of membrane proteins. J Struct Biol. 2016.
172. Rigort A, Bauerlein FJ, Leis A, Gruska M, Hoffmann C, Laugks T, et al. Micromachining tools and correlative approaches for cellular cryo-electron tomography. J Struct Biol. 2010;172(2):169-79.
173. Rigort A, Villa E, Bauerlein FJ, Engel BD, Plitzko JM. Integrative approaches for cellular cryo-electron tomography: correlative imaging and focused ion beam micromachining. Methods Cell Biol. 2012;111:259-81.
174. Hagen WJH, Wan W, Briggs JAG. Implementation of a cryo-electron tomography tilt-scheme optimized for high resolution subtomogram averaging. J Struct Biol. 2017;197(2):191-8.
175. Kremer JR, Mastronarde DN, McIntosh JR. Computer visualization of three-dimensional image data using IMOD. J Struct Biol. 1996;116(1):71-6.
176. Grant T, Grigorieff N. Measuring the optimal exposure for single particle cryo-EM using a 2.6 A reconstruction of rotavirus VP6. Elife. 2015;4:e06980.
177. Rohou A, Grigorieff N. CTFFIND4: Fast and accurate defocus estimation from electron micrographs. J Struct Biol. 2015;192(2):216-21.
178. Tegunov D, Cramer, P. Real-time cryo-EM data pre-processing with Warp. bioRxiv. 2018.
179. Navarro PP, Stahlberg H, Castano-Diez D. Protocols for Subtomogram Averaging of Membrane Proteins in the Dynamo Software Package. Front Mol Biosci. 2018;5:82.
180. Rasmussen SG, Choi HJ, Fung JJ, Pardon E, Casarosa P, Chae PS, et al. Structure of a nanobody-stabilized active state of the beta(2) adrenoceptor. Nature. 2011;469(7329):175-80.
181. Rasmussen SG, DeVree BT, Zou Y, Kruse AC, Chung KY, Kobilka TS, et al. Crystal structure of the beta2 adrenergic receptor-Gs protein complex. Nature. 2011;477(7366):549-55.
182. Low C, Yau YH, Pardon E, Jegerschold C, Wahlin L, Quistgaard EM, et al. Nanobody mediated crystallization of an archeal mechanosensitive channel. PLoS One. 2013;8(10):e77984.
183. Jin R, Banke TG, Mayer ML, Traynelis SF, Gouaux E. Structural basis for partial agonist action at ionotropic glutamate receptors. Nat Neurosci. 2003;6(8):803-10.
184. Scott S, Aricescu AR. A structural perspective on GABAA receptor pharmacology. Curr Opin Struct Biol. 2019;54:189-97.
185. Tribet C, Audebert R, Popot JL. Amphipols: polymers that keep membrane proteins soluble in aqueous solutions. Proc Natl Acad Sci U S A. 1996;93(26):15047-50.
186. D'Imprima E, Floris D, Joppe M, Sanchez R, Grininger M, Kuhlbrandt W. Protein denaturation at the air-water interface and how to prevent it. Elife. 2019;8.
187. Naydenova K, Russo CJ. Measuring the effects of particle orientation to improve the efficiency of electron cryomicroscopy. Nat Commun. 2017;8(1):629.
188. Noble AJ, Wei H, Dandey VP, Zhang Z, Tan YZ, Potter CS, et al. Reducing effects of particle adsorption to the air-water interface in cryo-EM. Nat Methods. 2018;15(10):793-5.
189. Chen J, Noble, A.J., Kang, J.Y., Darst, S.A. Eliminating effects of particle adsorption to the air/water interface in single-particle cryo-electron microscopy: Bacterial RNA polymerase and CHAPSO. Journal of Structural Biology. 2019.

190. Chen S, Zhao Y, Wang Y, Shekhar M, Tajkhorshid E, Gouaux E. Activation and Desensitization Mechanism of AMPA Receptor-TARP Complex by Cryo-EM. Cell. 2017;170(6):1234-46 e14.
191. Herguedas B, Watson JF, Ho H, Cais O, Garcia-Nafria J, Greger IH. Architecture of the heteromeric GluA1/2 AMPA receptor in complex with the auxiliary subunit TARP gamma8. Science. 2019;364(6438).
192. Naydenova K, Peet MJ, Russo CJ. Multifunctional graphene supports for electron cryomicroscopy. Proc Natl Acad Sci U S A. 2019;116(24):11718-24.
193. Du J, Lu W, Wu S, Cheng Y, Gouaux E. Glycine receptor mechanism elucidated by electron cryo-microscopy. Nature. 2015;526(7572):224-9.
194. Snapp EL, Hegde RS, Francolini M, Lombardo F, Colombo S, Pedrazzini E, et al. Formation of stacked ER cisternae by low affinity protein interactions. J Cell Biol. 2003;163(2):257-69.
195. Costantini LM, Fossati M, Francolini M, Snapp EL. Assessing the tendency of fluorescent proteins to oligomerize under physiologic conditions. Traffic. 2012;13(5):643-9.
196. Wu MM, Llopis J, Adams S, McCaffery JM, Kulomaa MS, Machen TE, et al. Organelle pH studies using targeted avidin and fluorescein-biotin. Chem Biol. 2000;7(3):197-209.
197. Brasch J, Goodman KM, Noble AJ, Rapp M, Mannepalli S, Bahna F, et al. Visualization of clustered protocadherin neuronal self-recognition complexes. Nature. 2019;569(7755):280-3.
198. Azubel M, Carter SD, Weiszmann J, Zhang J, Jensen GJ, Li Y, et al. FGF21 trafficking in intact human cells revealed by cryo-electron tomography with gold nanoparticles. Elife. 2019;8.
199. Azubel M, Kornberg RD. Synthesis of Water-Soluble, Thiolate-Protected Gold Nanoparticles Uniform in Size. Nano Lett. 2016;16(5):3348-51.
200. Feiken E, van Etten I, Gebbink MF, Moolenaar WH, Zondag GC. Intramolecular interactions between the juxtamembrane domain and phosphatase domains of receptor protein-tyrosine phosphatase RPTPmu. Regulation of catalytic activity. J Biol Chem. 2000;275(20):15350-6.
201. Ruiz Carrillo D, Chandrasekaran R, Nilsson M, Cornvik T, Liew CW, Tan SM, et al. Structure of human Rack1 protein at a resolution of 2.45 A. Acta Crystallogr Sect F Struct Biol Cryst Commun. 2012;68(Pt 8):867-72.
202. Hattne J, Martynowycz MW, Penczek PA, Gonen T. MicroED with the Falcon III direct electron detector. IUCrJ. 2019;6(Pt 5):921-6.
203. Herzik MA, Jr., Wu M, Lander GC. High-resolution structure determination of sub-100 kDa complexes using conventional cryo-EM. Nat Commun. 2019;10(1):1032.
204. de Jongh HH, Kosters HA, Kudryashova E, Meinders MB, Trofimova D, Wierenga PA. Protein adsorption at air-water interfaces: a combination of details. Biopolymers. 2004;74(1-2):131-5.
205. Noble AJ, Dandey VP, Wei H, Brasch J, Chase J, Acharya P, et al. Routine single particle CryoEM sample and grid characterization by tomography. Elife. 2018;7.
206. Schur FK, Obr M, Hagen WJ, Wan W, Jakobi AJ, Kirkpatrick JM, et al. An atomic model of HIV-1 capsid-SP1 reveals structures regulating assembly and maturation. Science. 2016;353(6298):506-8.
207. Hutchings J, Stancheva V, Miller EA, Zanetti G. Subtomogram averaging of COPII assemblies reveals how coat organization dictates membrane shape. Nat Commun. 2018;9(1):4154.

Figures 1-1 and 1-4 were obtained from Sudhof et al, Cell, 2017;171(4):745-69, with permissions received under license number 4901401208467.

Figures 1-2 and 1-3 were obtained from Traynelis et al, Pharmacol Rev, 2010;62(3):405-96, with permissions granted by the letters attached to this thesis. The content of figure 1-2 was originally published in Sobolevsky et al, Nature, 2009;462(7274):745-56 and reproduced here with permissions received under license number 4901930929992.

Figure 1-5 was obtained from Elegheert et al, Science, 2016;353(6296):295-9, with permissions received under license number 4901410508937.

Figure 1-7 was obtained from Johnson et al, Physiol Rev, 2003;83(1):1-24, with permissions received under license number 4904280652372.

Figure 1-8 was obtained from Fuchs et al, Mech Dev, 1998;70(1-2):91-109, with permissions received under license number 4901450106149.

Figure 1-9 was obtained from Aricescu et al, EMBO J, 2006;25(4):701-12 and Aricescu et al, Biochem Soc Trans, 2008;36(Pt 2):167-72, with permissions received under license number 4901450627269 (John Wiley and Sons for EMBO J) and license number 1061221-1 (Biochemical Society).

Council

Charles P. France
President
University of Texas Health Science Center

Margaret E. Gnegy
President-Elect
University of Michigan Medical School

Wayne L. Backes
Past President
Louisiana State University Health Sciences Center

Mary-Ann Bjornsti
Secretary/Treasurer
University of Alabama, Birmingham

Carol L. Beck
Secretary/Treasurer-Elect
Thomas Jefferson University

Jin Zhang
Past Secretary/Treasurer
University of California, San Diego

Kathryn A. Cunningham
Councilor
University of Texas Medical Branch

Namandjé N. Bumpus
Councilor
Johns Hopkins University School of Medicine

Randy A. Hall
Councilor
Emory University School of Medicine

Emily E. Scott
Chair, Board of Publications Trustees
University of Michigan

Catherine M. Davis
FASEB Board Representative
Johns Hopkins University School of Medicine

Michael W. Wood
Chair, Program Committee
Neupharm LLC

Judith A. Siuciak
Executive Officer

ASPET
Transforming Discoveries into Therapies

September 4, 2020

Christina Heroven
Nuffield Dept of Medicine – STRUBI
University of Oxford
Roosevelt Drive
Oxford OX3 7BN
United Kingdom

Email: christina.heroven@gmail.com

Dear Christina Heroven:

This is to grant you permission to include the following figure in your thesis titled "Structural studies of trans-synaptic complexes" for the University of Oxford:

> Figure 1 from SF Traynelis, LP Wollmuth, CJ McBain, FS Menniti, KM Vance, KK Ogden, KB Hansen, H Yuan, SJ Myers, and R Dingledine (2010) Glutamate Receptor Ion Channels: Structure, Regulation, and Function, *Pharmacol Rev*, 62(3): 405-496;DOI: https://doi.org/10.1124/pr.109.002451

This is a modified version of a figure owned by Spring/Nature. Permission to reproduce the modified figure is granted under the same conditions stipulated by Spring/Nature for the original version of the figure. The authors and the source of the modified figure must be cited in full, including the article title, journal title, volume, year, and page numbers. Spring/Nature may require that you also cite the original source.

Sincerely yours,

Richard Dodenhoff
Journals Director

Council

Charles P. France
President
University of Texas Health Science Center

Margaret E. Gnegy
President-Elect
University of Michigan Medical School

Wayne L. Backes
Past President
Louisiana State University Health Sciences Center

Mary-Ann Bjornsti
Secretary/Treasurer
University of Alabama, Birmingham

Carol L. Beck
Secretary/Treasurer-Elect
Thomas Jefferson University

Jin Zhang
Past Secretary/Treasurer
University of California, San Diego

Kathryn A. Cunningham
Councilor
University of Texas Medical Branch

Namandjé N. Bumpus
Councilor
Johns Hopkins University School of Medicine

Randy A. Hall
Councilor
Emory University School of Medicine

Emily E. Scott
Chair, Board of Publications Trustees
University of Michigan

Catherine M. Davis
FASEB Board Representative
Johns Hopkins University School of Medicine

Michael W. Wood
Chair, Program Committee
Neupharm LLC

Judith A. Siuciak
Executive Officer

ASPET
Transforming Discoveries into Therapies

September 4, 2020

Christina Heroven
Nuffield Dept of Medicine – STRUBI
University of Oxford
Roosevelt Drive
Oxford OX3 7BN
United Kingdom

Email: christina.heroven@gmail.com

Dear Christina Heroven:

This is to grant you permission to include the following figure in your thesis titled "Structural studies of trans-synaptic complexes" for University of Oxford:

> Figure 3 from SF Traynelis, LP Wollmuth, CJ McBain, FS Menniti, KM Vance, KK Ogden, KB Hansen, H Yuan, SJ Myers, and R Dingledine (2010) Glutamate Receptor Ion Channels: Structure, Regulation, and Function, *Pharmacol Rev*, 62(3): 405-496; DOI: https://doi.org/10.1124/pr.109.002451

Permission to reproduce the figure is granted for worldwide use in all languages, translations, and editions, and in any format or medium including print and electronic. The authors and the source of the materials must be cited in full, including the article title, journal title, volume, year, and page numbers.

Sincerely yours,

Richard Dodenhoff
Journals Director

Transforming Discoveries into Therapies
ASPET · 1801 Rockville Pike, Suite 210 · Rockville, MD 20852 · Office: 301-634-7060 · aspet.org